Examining the drivers of current and future changes in Central U.S. warm-season rainfall

A DISSERTATION
SUBMITTED TO THE FACULTY OF THE GRADUATE SCHOOL
OF THE UNIVERSITY OF MINNESOTA
BY

Keith John Iliff Harding

IN PARTIAL FULFILLMENT OF THE REQUIREMENTS
FOR THE DEGREE OF
DOCTOR OF PHILOSOPHY

Peter K. Snyder

September 2014

Acknowledgments

Thank you to everyone in my research group for promoting an ideal work and research environment. I appreciate the guidance that Dr. Peter Snyder, my advisor, has provided me ever since I came to the University of Minnesota as a Master's student in 2009. It has been enjoyable to have so many shared research interests to investigate, especially our extensive work investigating mid-afternoon boundary layer processes over the St. Paul campus of the University of Minnesota. Thank you to Dr. Tracy Twine, whose advice and guidance has been instrumental in the success of this project. I look forward to working with you both in the future.

Thank you to everyone in my research group, especially Dr. Brian Smoliak and Tom Hultquist. Our brainstorming sessions at Northbound and Lori's provided valuable feedback that has been extremely helpful for this project and other proposals.

Thank you to my committee for assisting me through this process. I appreciate your insightful comments that enhance the quality of this work. Thank you for your time and commitment Dr. Peter Snyder, Dr. Tracy Twine, Dr. Timothy Griffis, and Dr. Scott St. George.

On a personal note, I would like to thank Kelly and Jade Harding, who have been very supportive of this endeavor. It has been a joy to have people to put everything in perspective, especially in those moments that really matter. Thank you as well to my parents, Ian and Loretta Harding, who provided an environment that enabled me to thrive.

Abstract

Warm-season precipitation in the Central U.S. is highly variable, as severe droughts and flooding often occur in consecutive years or simultaneously. Some of the most highly productive agricultural lands are present within the region despite susceptibility to warm-season rainfall extremes. Climate change is expected to increase precipitation extremes globally, but how warm-season Central U.S. precipitation will be affected is unclear. In this study, I examine the drivers of current and future warm-season precipitation in the region as well as how the basic characteristics of summer rainfall may be affected by climate change through the use of gridded observations, reanalysis datasets, and dynamical downscaling of global climate models (GCMs). It is demonstrated that the negative phase of the Pacific-North American (PNA) teleconnection pattern enhances heavy precipitation events over the Upper Midwest by modulating the strength of the Great Plains Low Level Jet (GPLLJ), possibly enabling greater medium range prediction of Midwest heavy rain events. Similarly, I aim to reduce uncertainty in long-term projections of how precipitation may be affected by climate change by examining shortfalls in GCM-simulated warm-season precipitation and demonstrating improvement with dynamical downscaling. Using the Weather Research and Forecasting (WRF) model, two GCMs are dynamically downscaled in one historical and three future timeslices with varying anthropogenic forcing. Future warm-season precipitation in these simulations is more intense, less frequent, and occurs with more days between rain events, similar to trends in observations that show large increases in extreme rainfall events and rainfall intensity. The intensification of extreme rainfall events in future simulations is the strongest during the April-July, associated with a strengthening of the GPLLJ during those months. Heavier rainfall rates during extreme precipitation events are related to a stronger cold pool and mesohigh, which force stronger moisture convergence above the cold pool in the presence of additional low-level moisture and a drier mid-troposphere. Overall, the identification of plausible physical mechanisms that might contribute to the enhancement of heavy rainfall events in the region enables greater confidence in future projections of extreme rainfall events.

Table of Contents

List of Tables

List of Figures

Chapter 1

Introduction

Severe droughts and floods have often occurred in consecutive years or simultaneously in the Great Plains and Midwestern United States, which support abundant agriculture despite the frequent occurrence of warm-season precipitation extremes. Higher temperatures from an increase in greenhouse gases are expected to amplify the hydrologic cycle (Bates et al. 2008; Durack et al. 2012; Huntington 2006; O'Gorman and Schneider 2009; Trenberth et al. 2003), which will likely change the frequency and intensity of precipitation and result in more frequent extreme rainfall events (Allan and Soden 2008; Allen and Ingram 2002; Dai 2013; Held and Soden 2006; O'Gorman and Schneider 2009; Parry et al. 2007; Trenberth 1999; Trenberth et al. 2003). Increases in extreme precipitation and rainfall intensity have been observed in the Central U.S. (Groisman et al. 2005; Karl and Knight 1998), with some models suggesting that an increase in summer drought could occur in the region with climate change (Dai 2013; Seneviratne et al. 2012).

Warm-season precipitation in the Central U.S. is primarily convective in nature (Changnon 2001), with a large percentage occurring nocturnally (Higgins et al. 1997). The Great Plains Low Level Jet (GPLLJ), a nocturnal southerly wind maximum in the Central U.S., is the main driver of dynamically forced warm-season nocturnal rainfall (Means 1952, 1954; Mo and Berbery 2004). The GPLLJ provides low-level convergence, cyclonic shear, abundant moisture transport, and moisture convergence to the north of the jet maximum, which often results in the development or intensification of mesoscale convective systems (MCSs) (Bonner 1968; Helfand and Schubert 1995; Weaver and Nigam 2011). For these reasons, a significant percentage of extreme rainfall events in the region are typically associated with anomalously strong southerly flow within the GPLLJ (Arritt et al. 1997; Cook et al. 2008; Monaghan et al. 2010).

Weather forecasters tasked with conducting medium-range forecasts (i.e., 3-14 days) typically consider the behavior of the GPLLJ and its associated moisture transport when assessing the possibility of heavy precipitation. While recent work has shown some promise in predicting the large-scale flow patterns (i.e., atmospheric rivers) that are often associated with extreme precipitation several days in advance (Nayak et al. 2014), further research is needed to help reduce uncertainty in medium-range forecasting of heavy rainfall events in the region. In Chapter Two of this study, I examine how the Pacific North America (PNA) teleconnection pattern, a leading mode of Northern Hemisphere atmospheric variability, affects the strength of the GPLLJ and the development of Midwestern extreme rainfall events. I show that low-level geopotential height anomalies associated with the negative phase of the PNA can enhance the GPLLJ by strengthening the pressure gradient within the GPLLJ core. Stronger and more prolonged southerly moisture transport within the GPLLJ typically increases precipitation during strong LLJ events when the PNA is very negative compared to strong LLJ events associated with a very positive PNA. In identifying links between the PNA, GPLLJ, and heavy rainfall events, I aim to increase confidence in medium-range forecasts of heavy rainfall events over the Midwest by providing greater knowledge of the dynamical and thermodynamic drivers of heavy precipitation episodes.

Because warm-season rainfall extremes have previously caused significant economic and societal damage in the region (NCDC 2013), it is important to understand how rainfall extremes and the basic characteristics of precipitation will be affected by anthropogenic climate change. Changes in the frequency and intensity of precipitation will likely have greater societal impacts than variations in seasonal averages (Trenberth et al. 2003), so any future projections must incorporate models that can accurately simulate those aspects of summer precipitation. Projections of warm-season precipitation extremes generally rely on global climate models (GCMs), which can simulate seasonal averages of precipitation with reasonable accuracy but often struggle with the frequency and intensity of convective precipitation (Allan and Soden 2008; Dai 2006; Meehl et al. 2005) because of their coarse spatial resolution and the use of parameterized convection. High rainfall rates typically cannot be resolved by GCMs because of unresolved convective processes and spatial averaging over large grid boxes due to coarse horizontal and vertical model resolution (Chen and Knutson 2008; Gober et al. 2008). GCMs typically simulate too many light rainfall days (Allan and Soden 2008; Harding et al. 2013), causing insufficient simulation of heavy precipitation events. In addition, poorly simulated rainfall frequency can reduce the ability of GCMs to simulate the onset of droughts by inhibiting sufficient drying of soils between precipitation events.

These issues have resulted in significant uncertainty in rainfall projections in regions and seasons dominated by convective precipitation. However, the high computational cost of GCM simulations and limited computing power currently prohibit the use of high spatial resolutions to explicitly resolve convective processes. While computing power will continue to increase and help to improve the simulation of convective processes in GCMs, until then dynamical downscaling with regional models will be necessary for addressing critical questions regarding future changes in the basic characteristics of convective precipitation. Dynamical downscaling, which uses GCM output as the initial and lateral boundary conditions for a regional model, enables model simulations to be conducted over smaller domains with much higher spatial resolutions that do not require parameterized convection. In Chapter Three of this study, I show that dynamical downscaling using the Weather Research and Forecasting (WRF) model can more effectively simulate the timing, frequency, and intensity of summer convective precipitation over the Central U.S. compared to the current generation of GCMs from the Coupled Model Intercomparison Project – Phase Five (CMIP5). However, because biases in GCM data can filter through the downscaling process (Wu et al. 2005), dynamical downscaling must use GCM data that provides reasonably represents the regional climate. Therefore, I demonstrate that the accurate simulation of particular variables by CMIP5 models affects how well total summer precipitation is simulated over the Central U.S. in WRF, guiding future dynamical downscaling efforts in the region.

Because dynamical downscaling provides a more accurate simulation of summer precipitation in the Central U.S., future regional projections that incorporate dynamical downscaling have the potential to provide more reliable estimates of how the basic characteristics of warm-season rainfall will be affected by climate change. In Chapter Four, I explore how warm season rainfall in the Midwest and Great Plains could be modified by climate change using dynamical downscaling of results from two GCMs in WRF. The selection of these GCMs is guided by the results from Chapter Three, which examines the variables that can influence simulated precipitation accuracy in WRF.

Simulations that use input from two GCMs from the CMIP5 in three different future scenarios enable a realistic look into how the frequency and intensity of warm-season precipitation, the occurrence and severity of extreme precipitation events, and meteorological drought may change in the region with anthropogenic warming. Future changes in these basic characteristics of warm-season precipitation are compared to observed trends in the Climate Prediction Center's (CPC) daily precipitation dataset (Higgins et al. 2000), enabling greater confidence in future projections for simulated changes that have the same sign as observations.

While additional confidence can be gained when changes in future simulations resemble observed trends, uncertainty can be reduced further by examining possible mechanisms that contribute to altered precipitation behavior in model simulations. The identification of realistic and plausible physical mechanisms that can explain simulated precipitation changes enable greater confidence that models can provide valid future outcomes instead of results fraught with artifacts. I explore how changes in the Great Plains Low-Level Jet in future simulations can affect the frequency and intensity of extreme rainfall events in Chapter Four of this study. In Chapter Five, I examine mesoscale mechanisms that could contribute to the simulated intensification of extreme rainfall events over the Central U.S. using WRF simulations of future scenarios from Chapter Four. The atmospheric conditions adjacent to extreme rainfall events during historical and future simulations are composited, enabling an investigation into possible physical mechanisms that self-sustain convective storms and result in the intensification of extreme rainfall events in the region.

The goal of this study is to reduce the uncertainty involving projections of summer precipitation within the Central U.S. Because the Midwest and Great Plains contain considerable agricultural acreage and a large population that is prone to damage from flash flooding, it is important to understand how the basic characteristics of summer precipitation will change in the region with reasonable certainty. While the results from this study likely will not provide the final answer on the exact future changes in summer precipitation over the Central U.S., I aim to reduce uncertainty regarding how the basic characteristics of summer precipitation will be affected by climate change within the research community. The growing scientific confidence in projections of regional rainfall extremes enables greater clarity for stakeholders that are most affected, possibly reducing the potential impacts of these basic changes in summer precipitation by enabling more targeted adaptation strategies.

Chapter 2

The relationship between the Pacific - North American Teleconnection Pattern, the Great Plains Low-Level Jet, and North Central U.S. heavy rainfall events

Harding, K. J. and P. K. Snyder (2014), submitted.

2.1 Overview

In this study we demonstrate the relationship between the Pacific - North American (PNA) teleconnection pattern and the Great Plains Low-Level Jet (GPLLJ). The negative phase of the PNA, which is associated with lower heights over the Great Plains and ridging in the Southeast U.S., enhances the GPLLJ by increasing the pressure gradient within the GPLLJ on daily to monthly timescales. Strong GPLLJ events predominantly occur when the PNA is negative. Strong GPLLJ events with a very negative PNA (< -1) are associated with more persistent, longer wavelength planetary waves that increase the duration of GPLLJ events and enhance precipitation over the North Central U.S. When one considers the greatest 5-day North Central precipitation events, a large majority occur when the PNA is negative, with most exhibiting a very negative PNA. Stronger moisture transport during heavy rainfall events with a very negative PNA decreases the precipitation of locally derived moisture compared to events with a very positive PNA. The PNA becomes negative 2-12 days before heavy rainfall events and is very negative within two weeks of 78% of heavy rainfall events in the North Central U.S., a finding that could be used to improve forecasts.

2.2 Introduction

Heavy rain events and associated flash flooding routinely cause significant economic losses in the Midwestern United States and are the leading cause of weather-related deaths (NWS 2014). Because of their large societal impacts, considerable effort has been spent on improving medium-range (3-14 day) prediction of heavy rainfall events and their drivers (e.g., the Great Plains Low-Level Jet (GPLLJ), atmospheric rivers)

(Nayak et al. 2014). Recent research has identified that the PNA, which has significant variability within the medium-range forecasting window (Feldstein 2000), may have influenced the development of two heavy rainfall events with flash flooding over the Midwest by enhancing the GPLLJ (Patricola et al. 2013). In this study, we examine the monthly impact that the PNA has on the GPLLJ as well as how the PNA impacts strong jet events and North Central U.S. heavy rainfall events at daily to pentadal (5-day) timescales.

The GPLLJ, a generally southerly lower-tropospheric wind maximum that is a key feature of the Midwestern summertime hydroclimate, is the primary driver of summertime nocturnal convective precipitation in the Central U.S. (Higgins et al. 1997; Means 1954). Low-level convergence, cyclonic shear, and moisture convergence to the north of the GPLLJ maximum (Bonner 1968; Helfand and Schubert 1995; Weaver and Nigam 2011) support the development of nocturnal mesoscale convective systems (MCSs), which are responsible for a significant percentage of total summer rainfall in the region (Higgins et al. 1997). In the Midwestern United States, heavy rainfall events peak in the summer months (Dirmeyer and Kinter 2010) and are often associated with anomalously strong meridional moisture transport (i.e., atmospheric rivers) within the GPLLJ (Arritt et al. 1997; Cook et al. 2008; Lavers and Villarini 2013; Monaghan et al. 2010).

The GPLLJ typically is the strongest during July and is located between 925 hPa and 850 hPa (Cook et al. 2008). Variations in the GPLLJ are influenced by fluctuations in the 850 hPa height gradient between the North Atlantic Subtropical High (NASH) and lower heights over the Great Plains and the front range of the Rocky Mountains (Holton

1967), with stronger wind speeds at night due to the decoupling of the surface and boundary layers. Anomalous low-level ridging on the western edge of the NASH (Weaver et al. 2009) or an enhanced 850 hPa trough over the Great Plains (Mo and Berbery 2004; Weaver and Nigam 2008) can strengthen the GPLLJ by enhancing the pressure gradient across the GPLLJ core (Holton 1967).

The PNA teleconnection pattern is a prominent mode in Northern Hemispheric low-frequency variability (Wallace and Gutzler 1981) that is more pronounced during the winter (Barnston and Livezey 1987). However, the PNA exerts significant variability on daily to weekly timescales (Feldstein 2000) and can influence weather patterns over the Midwest during the summer months (Patricola et al. 2013). Previous studies have linked the PNA teleconnection pattern to diabatic heating anomalies associated with convection in the North Pacific (Yu et al. 2008), ENSO-related tropical convection (Trenberth et al. 1998), and variations in the East Asian jet (Lau and Boyle 1987; Leathers and Palecki 1992). Weaver and Nigam (2008) showed that PNA-initiated Rossby waves associated with convection in the tropical North Pacific are responsible for generating a specific pattern expressed in 200 hPa heights that ultimately affects 850 hPa height gradients and the GPLLJ in July. This suggests that precipitation, and associated diabatic heating anomalies, over the Pacific may play a role in affecting the strength of the GPLLJ. The negative phase of the PNA, which results in upper-level troughing over western North America and ridging over the Southeast U.S., has been previously linked to summer heavy rainfall events in the Midwest (Patricola et al. 2013).

In this study, we demonstrate how the PNA impacts the GPLLJ and North Central U.S. precipitation on monthly timescales using the NCEP-NCAR Reanalysis. After establishing the mechanisms linking the PNA and the GPLLJ, we investigate how the PNA influences the GPLLJ and extreme rainfall events on timescales associated with synoptic weather systems (≤ 5 days). Ultimately, the goal of this study is to improve medium-range weather prediction of extreme precipitation events in the Upper Midwest.

2.3 Methods

2.3.1 Data

The NCEP-NCAR reanalysis (Kalnay et al. 1996), which available every six hours on a 2.5° x 2.5° global grid starting in 1948, was used for all analyses except those that included daily and 5-daily precipitation over CONUS. Precipitation from the Climate Prediction Center's Daily Precipitation dataset (CPC) (Higgins et al. 2000), available starting in 1948 at 0.25° x 0.25° over CONUS, was used for all daily and 5-daily precipitation over CONUS. The heaviest 1-day and 5-day rainfall events over the North Central U.S. were determined by calculating the highest grid cell rainfall totals in the CPC dataset and eliminating duplicates. When multiple overlapping 5-day periods had the same rainfall total, the event was centered on the day with the most daily precipitation.

2.3.2 PNA calculation

All PNA values were calculated using the modified pointwise method from the Climate Prediction Center (CPC 2014), which defines the PNA as

$$\begin{aligned} PNA = Z^{*}(15^{\circ}-25^{\circ}N,180^{\circ}-140^{\circ}W)-Z^{*}(40^{\circ}-50^{\circ}N,180^{\circ}-140^{\circ}W) \\ +Z^{*}(45^{\circ}-60^{\circ}N,125^{\circ}-105^{\circ}W)-Z^{*}(25^{\circ}-35^{\circ}N,90^{\circ}-70^{\circ}W) \end{aligned} , \qquad (1)$$

where Z^* is the mean 500 hPa geopotential height anomaly from NCEP-NCAR compared to the 1981-2010 average. Calculations using the modified pointwise method are highly correlated with the original pointwise method from Wallace and Gutzler (R = 0.98) and those using an EOF analysis (R = 0.92) (CPC 2014). Daily PNA values were standardized by 1981-2010 daily means, with monthly values standardized by the 1981-2010 average of all months to enable an examination of the annual cycle of the PNA on the GPLLJ. Daily PNA values at least one standard deviation below average (PNA < -1) were classified as *very negative* and corresponding positive values (PNA > 1) were termed *very positive*.

2.3.3 Definition of other indices

The Low-Level Jet (LLJ) index is the average 850 hPa meridional wind speed within the LLJ region (27.5°-42.5°N, 102.5°-90°W; Figure 2.1), which overlaps the climatological maximum of the GPLLJ. To represent the geopotential height gradient that modulates the speed of the GPLLJ, we define the Zgrad index, which is the average 850 hPa geopotential height in the Southeast U.S. (SEUS; 25°-40°N, 95°-80°W; Figure 2.1) minus the average 850 hPa heights in the Great Plains region (GP; 35°-50°N, 110°-100°W; Figure 2.1). The Zgrad index was standardized by the 1981-2010 average and standard deviation. Both indices were calculated on monthly, daily, and 6-hourly timescales.

2.3.4 LLJ categories and strong LLJ event classification

Times with an active LLJ were determined using 6-hourly 850 hPa winds, following criteria from Arritt et al. (1997). Weak LLJs were any time the maximum wind speed within the LLJ region was between 12-16 m s^{-1}, 16-20 m s^{-1} for moderate LLJs, and over 20 m s^{-1} for strong LLJs. The identification of LLJs only considered wind directions between 135° and 225°. We classified strong LLJ *events* as discrete periods of time with a strong LLJ. If multiple strong LLJs occurred within 12 hours, they were classified as the same strong LLJ event. The average daily PNA index during strong LLJ events was calculated to enable the grouping of multiple LLJ events with the same PNA classification (e.g., *very negative, negative, positive, very positive*).

2.3.5 Precipitation recycling ratio calculation

Precipitation recycling ratios were calculated with daily data from the NCEP-NCAR reanalysis for the top 100 5-day rainfall events in the North Central U.S. from the CPC dataset, using the Quasi-Isentropic Backtrajectory Technique (QIBT) from Brubaker et al. (2001). One hundred parcels were launched for each grid cell within the North Central U.S. during each 5-day rainfall event, with each parcel representing 1/100th of the total pentad precipitation within a grid cell. Parcels were launched at the occurrence of precipitation and the horizontal and vertical location of parcel launches was randomized, with the height of launches weighted by the vertical profile of tropospheric moisture. After parcels were launched, the evaporative source of precipitation was determined by dividing the evapotranspiration for each timestep (4 hours) by the total column precipitable water. Parcels were tracked backwards using the iterative backward trajectory technique from Merrill et al. (1986) every four hours (interpolated linearly from daily data) for up to 21 days or until all the moisture was accounted for. Recycling ratios were determined by dividing the total North Central U.S. precipitation by the amount of precipitation that was locally derived. Recycling ratio calculations are calculated for the North Central region which is approximately 1.31 x 10^6 km^2, slightly larger than 1.0 x 10^6 km^2 that is recommended to capture mesoscale and synoptic moisture transport while also capturing small-scale variability (Dominguez et al. 2006; Rasmusson 1968).

2.4 Impact of the PNA on the GPLLJ at monthly timescales

To examine how the GPLLJ is affected by the PNA at monthly timescales, we consider the difference in geopotential heights, column-integrated precipitable water, precipitation, and meridional winds between the ten strongest and weakest LLJ years for each month and then average across all months. Strong 850 hPa southerly flow during strong LLJ years (Figure 2.2a) contributes to enhanced column-integrated moisture transport in the Southern Plains (Figure 2.2b). Greater meridional transport of moisture during strong LLJ years throughout the Southern Plains and Lower Mississippi Valley increases precipitation over much of the Central U.S. (Figure 2.2c), with the greatest difference in NCUS precipitation between strong and weak LLJ years in April-July (Figures 2.3a, 2.3f).

During strong LLJ years, enhanced southerly flow is coincident with higher 850 hPa geopotential heights over the Southeast U.S. and troughing over the mountain west and Great Plains (Figure 2.2d), as the stronger height gradient enhances meridional flow within the GPLLJ core. Height differences between the Great Plains and Southeast U.S. regions at 850 hPa (Zgrad index) are responsible for 90% of the variance in the LLJ index (Figure 2.4a), with the greatest relationship in April (95%). Differences in geopotential heights at 500 hPa (Figure 2.2e) are collocated with 850 hPa height differences, with a slight westward shift (negative tilt) with height. Geopotential height differences between strong and weak LLJ years at 500 hPa and 850 hPa reveal a height pattern that resembles differences between the most negative minus most positive PNA years (Figures 2.2d-e, Figures 2.5a-b). In addition, precipitation differences over the North Pacific (Figure 2.2c) are nearly identical to anomalies during the negative phase of the PNA as reported by Yu et al. [2009] (also shown in Figure 2.5c). Therefore, the difference in 500 hPa heights during strong and weak LLJ years (Figure 2.2e) is likely related to the PNA and its associated diabatic heating anomalies in the North Pacific.

For all months of the year, the PNA is negative during the strongest LLJ years and positive during the weakest LLJ years, with a statistically significant difference for all months (Figures 2.3b, 2.3f). Overall, the PNA is responsible for 42% of the total variance in the GPLLJ on monthly timescales (Figure 2.4c). The PNA principally impacts the strength of the GPLLJ by affecting 850 hPa height differences between the Great Plains and SEUS. A significant percentage (53%) of the monthly variance in the Zgrad index is related to the PNA (Figure 2.3c, 2.3g, 2.4b), with the greatest relationship in January (73%) and the weakest in June (32%). These results indicate that the negative phase of the PNA enhances the GPLLJ by increasing the low-level pressure gradient within the GPLLJ core, which lies between two opposing “centers of action” of the PNA. When the PNA is negative, troughing over the Great Plains and ridging over the Southeastern U.S. combine to enhance the height gradient within the GPLLJ core, while a positive PNA typically causes a weaker gradient by increasing heights over the Great Plains and lowering heights in the SEUS.

While the GPLLJ predominantly impacts NCUS precipitation from April-July, the PNA exerts a greater influence on the Zgrad index and GPLLJ during November-April (Figures 2.3b, 2.3c). The timing of these seasonal impacts suggests that the PNA likely has the greatest impact on NCUS precipitation in April when the strong winter influence of the PNA on the GPLLJ overlaps the warm-season impact of the GPLLJ on NCUS precipitation. In April, a large difference in PNA occurs between the ten wettest and driest years in the NCUS (Figures 2.3d, 2.3h), corresponding to the only month with a statistically significant relationship (R^2=0.26) between the PNA and NCUS precipitation. These results suggest that the PNA has a modest influence on average NCUS precipitation during April before the effect of the PNA on the GPLLJ decreases in summer due to reduced variability in the PNA (Table 2.1). However, the PNA still has a significant impact on precipitation and the LLJ during June-August as the strongest LLJ years (and the wettest years) have a significantly more negative PNA than the weakest LLJ years (and driest years) (Table 2.2).

2.5 Impact of the PNA on strong LLJ events and heavy precipitation events

In the previous section, we demonstrated how the PNA could influence the GPLLJ by strengthening the 850 hPa height gradient in the Central U.S. on monthly timescales. Here we use this knowledge to investigate how the PNA influences the GPLLJ and North Central U.S. heavy precipitation events on timescales of five days (pentads) or less.

Similar to the monthly results, geopotential height gradients within the GPLLJ core affect the strength of the GPLLJ on daily (77%) and 5-day (81%) timescales (Figure 2.4). The PNA, which can strengthen the 850 hPa height gradient within the GPLLJ core during the negative phase of the PNA on monthly timescales, is responsible for a significant percentage of the daily (30%) and pentadal (39%) variability in the Zgrad index (Figure 2.4). Because the PNA can influence height gradients that control the strength of the GPLLJ, the PNA has a modest effect on the daily and pentadal variability of GPLLJ strength (18% and 24%, respectively; Figure 2.4). During times when a strong LLJ is present, the PNA is predominantly negative and is much more likely to be very negative than very positive (Figures 2.6a-b). When no LLJ is present, the PNA is primarily positive and a large percentage of non-LLJ events are associated with positive or very positive PNA values (Figure 2.6). However, a significant number of strong LLJs (Figure 2.6b) and discrete strong LLJ *events* (defined in section 2.3.4) are associated with a positive (27% and 28%, respectively) or very positive PNA (3.3% and 4.2%).

During strong LLJ events, an 850 hPa trough is present over the Great Plains with anomalously high heights in the Southeast U.S. (Figures 2.7a-b), as suggested by the strong relationship between the LLJ and Zgrad indices (Figure 2.4g). These height anomalies occur regardless of whether the PNA is very negative or very positive (Figures 2.7a-b). However, the wavelengths of troughs/ridges at 850 hPa are much shorter in composites of strong LLJ events with a very positive PNA compared to events with a very negative PNA (Figures 2.7a-b). The same wavelength disparity occurs at 500 hPa for strong LLJ events associated with a very negative or very positive PNA (Figures 2.7c-d). Using the Rossby wave speed equation ((Rossby 1938), Appendix A), this implies that individual troughs/ridges propagate eastward faster during strong LLJ events when the PNA is very positive and upper-level flow features exhibit much shorter wavelengths. Therefore, the 850 hPa height pattern that strengthens the height gradient across the

GPLLJ core and favors the development of a strong LLJ is theoretically less persistent with a very positive PNA. Strong LLJ events are significantly longer in duration when associated with a very negative PNA compared to a very positive PNA (Table 2.1; $p < 0.05$), suggesting that the trough/ridge wavelength disparity between LLJ events with a very negative/positive PNA may play a role in controlling the duration of strong LLJ events.

In addition, more strong LLJ events associated with a very positive PNA (35%) are only six hours in duration and occur at 0600 UTC compared with very negative events (24%). These short duration LLJ events at 06 UTC are likely an artifact of the inertial oscillation of the GPLLJ and the nocturnal decoupling of the boundary and surface layers that have been shown to cause the nocturnal maximum of the GPLLJ. This implies that a significant number of strong LLJ events with a very positive PNA may instead be related to the inertial oscillation of the GPLLJ rather than a flow pattern that induces a persistent pressure gradient across the region and lingers longer than the timescale of a single weather system.

Strong LLJ events also exhibit stronger southerly flow in the LLJ region throughout the duration of events when the PNA is very negative (Table 2.3; Figures 2.7e-f (vectors)). The stronger and more persistent southerly flow enables greater moisture transport and precipitation to occur during strong LLJ events when the PNA is very negative versus very positive (Table 2.3; Figures 2.7e-h). Because anomalously strong southerly flow and enhanced moisture transport persists longer when the PNA is negative or very negative, a significant majority of the greatest 5-day rainfall totals in the North Central U.S. are associated with a negative PNA (Table 2.4). In addition, as event rainfall totals increase, the PNA becomes more negative and a greater share of heavy rainfall events occur during a negative or very negative PNA (Tables 2.4, 2.5). Of the ten highest 5-day rainfall totals, all are associated with a negative average PNA, with seven of them being very negative. These results suggest that very heavy 5-day rainfall events in the North Central U.S. are generally associated with the negative phase of the PNA, with a large number occurring when the PNA is very negative. Stronger southerly flow within the GPLLJ during heavy rainfall events with a very negative PNA increases the transport of moisture from the Gulf of Mexico compared to events with a very positive PNA (Table 2.6), reducing precipitation recycling ratios during those events (Table 2.6). Higher precipitation recycling ratios during heavy rainfall events with a very positive PNA suggests that increased locally derived moisture offsets the reduced southerly transport of moisture associated with the very positive phase of the PNA. In this manner, variations in land-atmosphere coupling might diminish the influence of the PNA on the development of heavy rainfall events by reducing the impact of advected moisture on the production of high rainfall totals.

Considering the evolution of the PNA before and after heavy rainfall events, the PNA is typically negative several days before the greatest 1-day heavy rainfall events over the North Central U.S., with the lowest value 1-2 days before events and an extended period of negative values two to twelve days prior to the top 50 and top 100 events (Figure 2.8). Out of the top 100 heavy rainfall events, 78 have a very negative PNA within two weeks prior to events, much higher than the 56.7% of all 14-day periods within the entire NCEP-NCAR Reanalysis that have a very negative PNA. Additionally, 10,000 Monte Carlo simulations comprised of 100 randomized 14-day periods indicate only a 0.006% probability (4.11 standard deviations from the mean) that 78 out of 100 randomly selected 14-day periods would have a very negative PNA by random chance. These results suggest that the very negative phase of the PNA has a significant influence on the development of heavy rainfall events over the North Central U.S. by strengthening the GPLLJ and enhancing moisture transport into the region.

2.6 Conclusions

In this study, we use the NCEP/NCAR reanalysis to demonstrate that the PNA can affect the strength of the GPLLJ on daily to monthly intervals, with a greater impact at longer timescales. Contrasting low-level height anomalies associated with two PNA "centers of action" occur on opposite sides of the GPLLJ core and modify the pressure gradient within the GPLLJ, influencing the strength of the GPLLJ. The negative phase of the PNA is shown to enhance the GPLLJ, which increases moisture transport within the GPLLJ and precipitation in the North Central U.S. We find that the PNA has a modest impact on April North Central U.S. precipitation when the cold season relationship between the PNA and GPLLJ overlaps the GPLLJ's summer effect on precipitation.

Strong LLJ events are predominantly associated with the negative phase of the PNA, with non-LLJ events mostly occurring when the PNA is positive. While strong LLJ events can occur with a positive or very positive PNA, the shorter wavelength features that are present in the upper-level flow pattern during strong LLJ events with a very positive PNA tend to be less persistent. In addition, strong LLJ events associated with a very positive PNA are also more likely to be a byproduct of the nocturnal maximum of the GPLLJ, resulting in shorter LLJ events when the PNA is very positive. Conversely, when the PNA is negative, the Rossby wave train induced by the PNA enables stronger and more sustained southerly flow within the GPLLJ. This supports more persistent moisture transport into the North Central U.S. from the Gulf of Mexico, which can result in the production of heavy precipitation over several days and a greater possibility of flash flooding than from strong GPLLJ events with a very positive PNA. Conversely, heavy rainfall events in the North Central U.S. with a very positive PNA typically are more heavily influenced by locally-derived precipitation compared to events with a very negative PNA. This demonstrates that heavy rainfall events are still possible when the PNA is positive, but the occurrence of these events is less influenced by variations in southerly moisture transport associated with the PNA. Therefore, land-atmosphere interactions (e.g., precipitation recycling from evapotranspiration) might reduce the impact of the PNA on heavy rainfall events during times with enhanced land-atmosphere coupling.

The large societal and economic cost of flash flooding in the Midwestern United States places greater importance on improving medium range forecasting of heavy rainfall events. In this study, we show that very heavy rainfall events in the region are associated with the negative phase of the PNA through a prolonged enhancement of the GPLLJ. Recent work has demonstrated promising medium-range forecasting skill for the prediction of atmospheric rivers in the Central U.S. (Nayak et al. 2014), which are associated with anomalous meridional moisture transport within the GPLLJ (Lavers and Villarini 2013). The PNA has significant variability within this forecasting window and is typically very negative within two weeks prior to North Central U.S. heavy rainfall events, suggesting that improved medium-range prediction of the PNA might enable better prediction of destructive heavy rainfall events within the region. Understanding the relationship between the PNA and GPLLJ events could improve forecast lead times with the goal of minimizing socioeconomic losses from flash flooding in the region.

2.6 Acknowledgments

Support for this study was provided by the U.S. National Science Foundation under grant no. 1029711. All data used in this study was downloaded from the NOAA-ESRL Physical Sciences Division website (http://www.esrl.noaa.gov/psd/data/gridded/). All other data and programs used to replicate the results in this study are available upon request from the corresponding author at pksnyder@umn.edu.

2.7 Appendix: Rossby wave speed equation

The zonal phase speed (c) of a Rossby wave relative to the mean flow ($\overline{u}$) is

$$c-\overline{u}=\frac{-\beta}{K^2} \tag{2.1}$$

where β is the change in the Coriolis force (*f*) with latitude ($\frac{df}{dy}$) using the midlatitude β -plane approximation) and K is the horizontal wave number ($K=\frac{2\pi}{\lambda}$, where λ is the zonal wavelength) (Holton 2004; Rossby 1938). Equation A1 implies that as the zonal wavelength decreases, Rossby waves propagate to the east faster (i.e., move more slowly westward relative to the mean flow).

2.8 Tables

Table 2.1. Average and standard deviation of LLJ index, North Central U.S. precipitation, and the PNA index (unstandardized; units of meters) for June-August (JJA) and January-March (JFM) from NCEP1.

	June-August		**January-March**	
Variable	**Average**	**Standard Deviation**	**Average**	**Standard Deviation**
LLJ index (m/s)	3.46	0.49	0.96	0.96
North Central precipitation	96.16	19.03	34.11	8.09
PNA index (m) (unstandardized)	0	1.33	0	2.74

Table 2.2. PNA index, LLJ index, and North Central U.S. precipitation during 10 wettest and driest years in North Central U.S. as well as 10 strongest LLJ years and 10 weakest LLJ years (lowest average 850 hPa meridional wind in LLJ region) for June-August and January-March.

	June-August			**January-March**		
Variable	**PNA**	**LLJ index (m/s)**	**Precipitation (mm)**	**PNA**	**LLJ index (m/s)**	**Precipitation (mm)**
10 wettest	-0.29	3.61	126.65	-0.02	1.05	47.63
10 driest	0.21	3.40	68.50	0.24	0.11	23.05
10 strongest LLJ	-0.90	4.26	105.52	-0.82	2.32	39.16
10 weakest LLJ	1.07	2.78	90.46	1.45	-0.62	28.86

Table 2.3. Duration, average meridional wind, total precipitation, maximum event total precipitation, and total moisture transport during strong LLJ events with different PNA classifications*

PNA Event Classification	Number of Events (Percent of total events)	Duration of Event (hours)	Average Meridional Wind (m s^{-1})**	Total Precipitation (mm)***	Maximum Event Rainfall (mm)***	Total Moisture Transport (m s^{-1})**
Very Negative (< -1)	1091 (32.8%)	19.85 +/- 0.98	7.72 +/- 0.01	10.19 +/- 0.99	208.26	2.80
Negative (< 0)	2386 (71.8%)	20.40 +/- 0.68	7.13 +/- 0.01	10.94 +/-0.70	208.26	2.68
Positive (> 0)	939 (28.2%)	18.10 +/- 1.03	5.70 +/- 0.01	9.68 +/-1.02	203.25	2.38
Very Positive (> 1)	138 (4.2%)	14.65 +/- 2.18	4.34 +/- 0.06	7.32 +/-2.37	89.60	2.29

*95% confidence intervals shown using standard error and *t* distribution, **LLJ region used for calculation, ***North Central region used for calculation

Table 2.4. Average PNA during the greatest 5-day precipitation events over the North Central U.S. in the CPC dataset (1948-2013)*

Number of events considered	Average Event Precipitation (mm)	Average PNA	Very Negative PNA Average	Negative PNA Average	Positive PNA Average	Very Positive PNA Average
100	225.66	-0.51	33%	76%	24%	9%
50	247.40	-0.60	40%	80%	20%	10%
25	269.76	-0.74	44%	88%	12%	8%
10	295.52	-1.21	70%	100%	0%	0%

*Percent of the highest precipitation events associated with a very negative (< -1), negative, positive, or very positive (> 1) average PNA during a 5-day precipitation event are also shown. The greatest 5-day precipitation events are determined by finding the highest 5-day rainfall for any grid cell within the North Central region in the CPC dataset, with any overlapping events (temporally and spatially) excluded.

Table 2.5. List of 100 strongest 5-day precipitation events over the North Central U.S.

Date Range	Maximum 5-day Precipitation (mm)	Average PNA	PNA Range	Average LLJ (m/s)	Recycling Ratio (%)
9/23/1959 to 9/27/1959	195.56	-0.56	-1.27 to 0.32	6.35	6.09%
7/4/2005 to 7/8/2005	195.60	0.00	-0.15 to 0.23	2.52	18.25%
7/23/1981 to 7/27/1981	196.16	-0.27	-1.17 to 0.29	4.54	19.29%
6/19/2002 to 6/23/2002	196.42	0.59	-0.36 to 1.39	5.97	16.14%
9/9/2003 to 9/13/2003	196.94	-0.03	-0.27 to 0.21	5.39	13.16%
7/13/1968 to 7/17/1968	197.06	-0.80	-1.42 to -0.3	8.76	8.38%
7/26/2001 to 7/30/2001	197.14	-1.45	-2.08 to -0.7	4.06	15.48%
7/22/1992 to 7/26/1992	197.69	-0.19	-0.53 to 0.14	4.04	19.25%
8/28/2002 to 9/3/2002	197.92	0.32	-1.14 to 1.5	1.97	13.69%
7/14/1982 to 7/18/1982	198.32	-1.22	-1.6 to -0.18	6.22	9.44%
5/23/2008 to 5/27/2008	198.45	-0.10	-0.54 to 0.35	6.87	17.80%
5/9/2002 to 5/13/2002	198.69	-1.19	-2.35 to 0.27	4.43	12.97%
6/19/2007 to 6/23/2007	199.51	-0.65	-1.41 to -0.24	2.68	10.47%
9/22/1970 to 9/26/1970	199.71	-0.65	-1.35 to 0.6	3.78	7.45%
9/10/1986 to 9/14/1986	199.86	-0.92	-1.29 to -0.55	3.73	14.26%
9/23/1986 to 9/27/1986	200.31	-1.56	-1.98 to -1.11	7.86	10.38%
8/25/1960 to 8/29/1960	200.92	-1.67	-2.04 to -0.97	6.03	8.69%
6/18/1964 to 6/22/1964	200.94	-0.58	-0.78 to -0.34	7.44	9.67%
5/17/1960 to 5/21/1960	201.22	-0.90	-1.22 to -0.63	5.79	19.92%
6/24/1998 to 6/28/1998	201.49	-1.52	-2.16 to -0.68	7.19	7.66%
6/14/1950 to 6/18/1950	201.51	1.22	0.9 to 1.45	4.76	12.74%
7/10/1992 to 7/14/1992	201.87	-1.65	-2.2 to -1.02	6.13	10.30%
5/14/1951 to 5/18/1951	202.10	1.26	0.64 to 1.57	8.75	22.57%
7/17/1977 to 7/21/1977	202.28	-1.52	-2.37 to -0.02	4.84	12.23%
8/5/1954 to 8/9/1954	202.32	-0.47	-0.89 to -0.08	1.47	28.95%
6/26/1965 to 6/30/1965	203.03	0.30	-0.32 to 1	7.39	10.17%
9/29/1995 to 10/3/1995	203.57	-0.26	-0.7 to -0.07	3.59	7.94%
6/28/1978 to 7/2/1978	203.74	-0.05	-0.49 to 0.31	3.63	15.83%
10/2/1991 to 10/6/1991	204.11	-0.19	-0.85 to 0.96	0.60	17.69%
6/21/1963 to 6/25/1963	204.25	-2.01	-2.59 to -1.47	6.40	21.45%
6/7/1953 to 6/11/1953	205.19	-0.41	-1.09 to 0.15	5.44	22.47%
9/21/2010 to 9/25/2010	205.42	0.07	-0.45 to 0.94	6.37	7.63%
5/26/2013 to 5/30/2013	205.82	-0.52	-0.74 to -0.31	10.31	7.91%
6/28/1983 to 7/2/1983	206.33	0.78	-0.02 to 1.3	5.64	13.22%
8/13/1995 to 8/17/1995	206.70	-1.81	-1.95 to -1.65	5.07	8.78%
7/7/1994 to 7/11/1994	207.23	-0.66	-1.04 to 0.16	3.60	11.92%
5/11/2006 to 5/15/2006	207.66	0.42	-0.1 to 1.12	-5.17	9.53%
7/4/1999 to 7/8/1999	208.04	-1.03	-2.57 to 0.47	4.22	10.27%
9/25/1972 to 9/29/1972	208.05	-1.26	-1.67 to -0.53	4.84	19.44%
7/12/1957 to 7/16/1957	208.83	1.14	0.45 to 1.67	2.70	21.76%

7/8/1951 to 7/12/1951	209.62	0.27	-0.24 to 0.76	5.16	7.23%
6/15/2012 to 6/19/2012	211.43	-0.40	-1.98 to 1.12	6.63	12.51%
5/31/1980 to 6/4/1980	211.59	-2.29	-2.79 to -1.78	6.81	14.91%
10/10/1969 to 10/14/1969	211.66	1.44	0.48 to 2.16	3.31	8.51%
6/14/1957 to 6/18/1957	211.72	0.08	-0.89 to 0.94	6.99	9.10%
7/20/1987 to 7/24/1987	212.43	-0.96	-1.49 to -0.25	5.23	9.70%
10/10/1954 to 10/14/1954	214.25	-0.32	-1.24 to 1.25	4.02	10.92%
9/7/1991 to 9/11/1991	214.52	0.49	0.12 to 0.67	5.37	16.09%
7/22/1990 to 7/26/1990	215.19	-0.09	-0.65 to 0.98	3.70	18.77%
10/3/2005 to 10/7/2005	215.75	-0.40	-0.91 to -0.05	2.58	5.68%
5/7/1996 to 5/11/1996	216.26	-1.17	-2.17 to 0.2	6.00	24.02%
9/12/2008 to 9/16/2008	217.00	0.58	0.37 to 0.73	0.94	12.40%
7/7/2002 to 7/11/2002	217.19	1.66	1.52 to 1.87	1.16	11.06%
8/25/1989 to 8/29/1989	217.20	-0.36	-0.8 to 0.23	3.81	17.67%
8/9/1980 to 8/13/1980	217.61	0.14	-0.46 to 0.59	3.88	19.60%
8/31/1973 to 9/4/1973	218.22	0.35	-0.92 to 1.28	7.56	4.39%
7/15/1950 to 7/19/1950	218.67	-1.02	-1.17 to -0.87	6.81	11.00%
4/15/2013 to 4/19/2013	219.12	-1.12	-1.29 to -0.92	4.31	7.87%
5/8/2005 to 5/12/2005	219.29	1.41	1.09 to 1.94	6.19	11.29%
6/13/1990 to 6/17/1990	220.78	-0.97	-1.45 to -0.68	6.12	12.20%
8/24/2004 to 8/28/2004	221.93	-0.95	-1.49 to -0.52	5.13	7.73%
8/13/1987 to 8/17/1987	223.98	-1.84	-2.04 to -1.54	4.74	12.71%
6/10/2010 to 6/14/2010	224.21	-0.05	-0.8 to 0.44	7.02	9.75%
6/8/1967 to 6/12/1967	224.73	-0.95	-1.19 to -0.71	8.57	5.75%
7/24/2011 to 7/28/2011	227.71	-1.30	-1.69 to -0.73	3.32	18.91%
8/29/1999 to 9/4/1999	228.51	-0.44	-1.11 to 0.94	3.56	34.57%
9/4/1965 to 9/8/1965	228.96	-0.64	-1.32 to 0.23	4.19	12.62%
9/19/1993 to 9/23/1993	229.34	-0.68	-0.8 to -0.51	3.91	21.62%
8/9/1966 to 8/13/1966	231.93	-1.14	-1.63 to -0.5	3.99	27.74%
6/16/1954 to 6/20/1954	232.66	-0.26	-1.2 to 0.81	5.28	5.78%
9/4/1989 to 9/8/1989	232.83	0.20	-0.02 to 0.46	4.38	7.74%
8/22/1954 to 8/26/1954	233.27	-1.28	-1.54 to -0.73	5.66	6.27%
8/30/1957 to 9/3/1957	233.42	1.41	0.47 to 1.89	3.49	17.66%
7/17/1999 to 7/21/1999	233.69	-1.28	-1.68 to -0.87	4.31	11.49%
7/5/1993 to 7/9/1993	237.44	-1.62	-1.79 to -1.52	8.48	4.24%
6/27/1975 to 7/1/1975	237.85	-0.66	-1.3 to 0.58	3.78	11.12%
6/16/2000 to 6/20/2000	238.75	-1.20	-1.5 to -0.93	5.90	12.86%
8/18/1979 to 8/22/1979	245.88	1.05	0.85 to 1.58	3.02	18.74%
7/1/1958 to 7/5/1958	246.47	0.06	-1.5 to 1.08	5.51	9.17%
8/25/1977 to 8/29/1977	246.48	-1.00	-1.3 to -0.74	7.21	16.15%
5/4/2007 to 5/8/2007	248.79	-0.17	-0.28 to -0.03	7.14	12.88%
8/4/1970 to 8/8/1970	251.81	-0.18	-0.66 to 0.23	3.10	29.72%
6/9/2002 to 6/13/2002	252.76	-0.72	-1.48 to 0.12	6.28	10.47%
6/21/2013 to 6/25/2013	253.28	-0.02	-0.43 to 0.39	8.00	9.09%
7/14/1996 to 7/18/1996	254.38	-1.51	-1.95 to -0.63	4.85	12.01%
6/15/1992 to 6/19/1992	256.87	1.24	0.64 to 2.44	5.11	9.26%
8/18/2007 to 8/22/2007	256.93	-0.40	-1.03 to 0.34	6.53	12.03%
9/12/1994 to 9/16/1994	259.71	-0.45	-1.2 to 0.88	4.73	15.39%
8/7/2010 to 8/11/2010	264.86	-0.87	-1.26 to -0.15	3.07	14.46%
7/17/1952 to 7/21/1952	273.97	-1.53	-2.27 to -1.11	8.20	6.12%
6/5/2008 to 6/9/2008	278.01	-2.02	-2.56 to -1.48	10.94	7.96%
6/27/1980 to 7/1/1980	278.36	-1.66	-1.92 to -1.26	2.50	23.79%
9/14/1992 to 9/18/1992	279.71	-1.48	-2.3 to -0.96	5.40	9.97%
7/21/2010 to 7/25/2010	282.68	-1.38	-2.3 to -0.48	4.78	8.69%
9/14/2004 to 9/18/2004	287.25	-1.51	-1.72 to -1.39	3.68	11.87%
7/24/2008 to 7/28/2008	289.21	-0.54	-0.96 to -0.2	3.26	24.34%
9/10/1972 to 9/14/1972	301.36	-0.57	-1.06 to -0.08	3.76	28.25%
7/21/1993 to 7/25/1993	304.21	-0.11	-0.89 to 0.44	4.96	14.46%
7/19/1972 to 7/23/1972	305.57	-1.84	-2.1 to -1.51	6.39	6.89%
8/30/1962 to 9/3/1962	348.80	-1.02	-1.24 to -0.77	4.76	19.09%

Table 2.6. Total precipitation (mm), average LLJ index, average moisture transport in GPLLJ region, and recycling ratio in North Central U.S. during top 100 5-day heavy rainfall events in CPC dataset*

PNA Classification	Average Event Precipitation (mm)	Average LLJ (m/s)	Moisture Transport (m/s)	Recycling Ratio
Very Negative (33)	235.02 +/- 12.83	5.65 +/- 0.58	2.87 +/- 0.27	12.67 +/- 2.00%
Very Positive (9)	221.86 +/- 12.74	4.28 +/- 1.45	2.39 +/- 0.32	14.84 +/- 3.53%

*Statistical significance determined using unpaired *t* test.

2.9 Figures

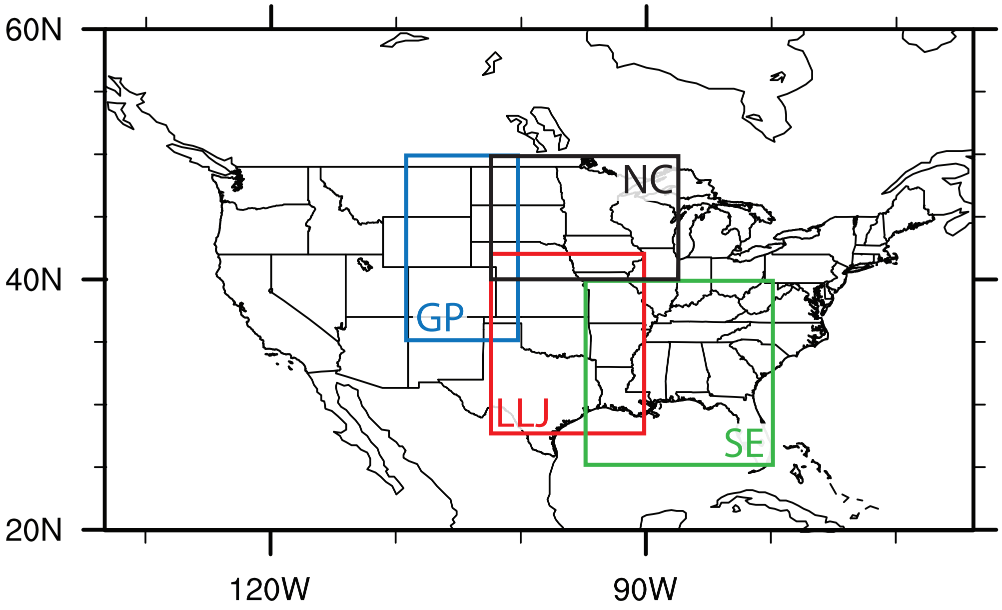

Figure 2.1. The North Central U.S. region (NCUS; 40°-50°N, 102.5°-87.5°W), the Great Plains (GP; 35°-50°N, 110°-100°W), the Southeast U.S. (SEUS; 25°-40°N, 95°-80°W), and the LLJ regions (27.5°-42.5°N, 102.5°-90°W) used in this study.

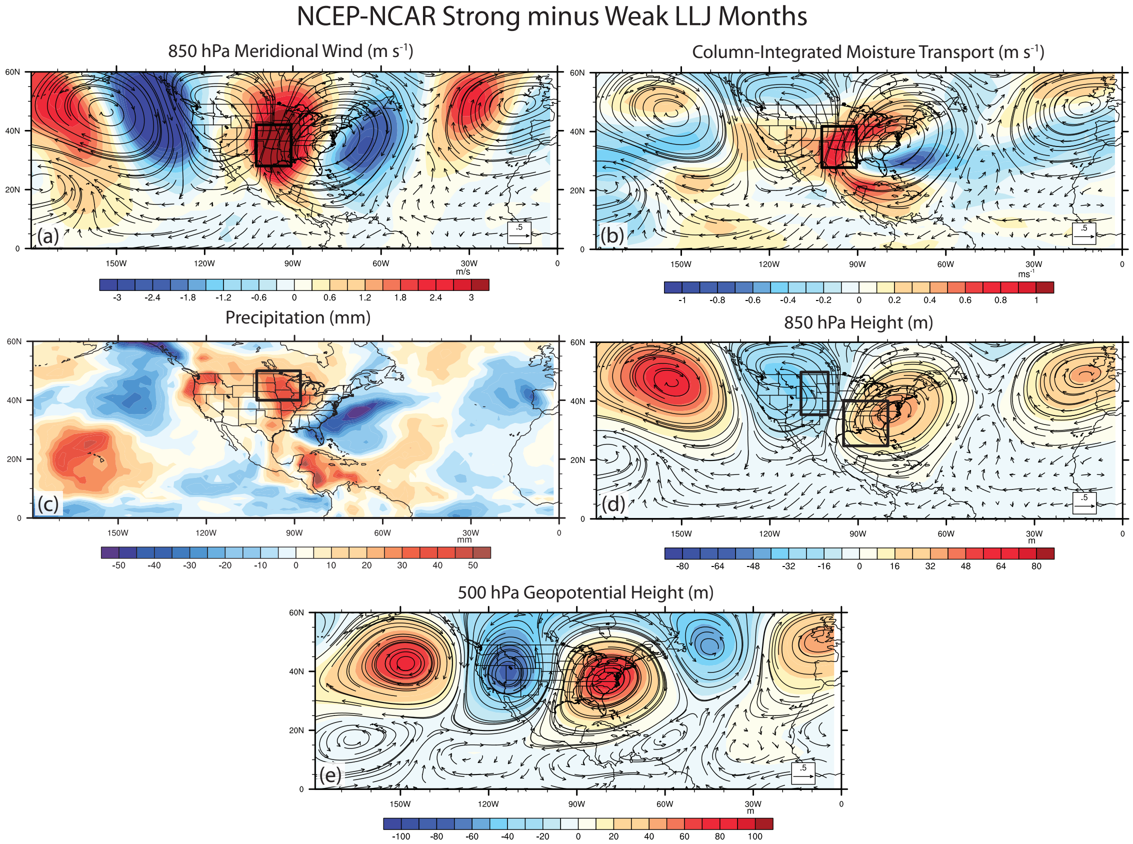

Figure 2.2. (a) 1948-2013 NCEP-NCAR 850 hPa meridional wind (m s^{-1}) during 10 strongest minus 10 weakest LLJ years for average of all calendar months. (b) as (a) but for column-integrated moisture transport (m s^{-1}), (c) as (a) but for precipitation (mm), (d) as (a) but for 850 hPa geopotential height (m), and (e) as (a) but for 500 hPa geopotential height (m).

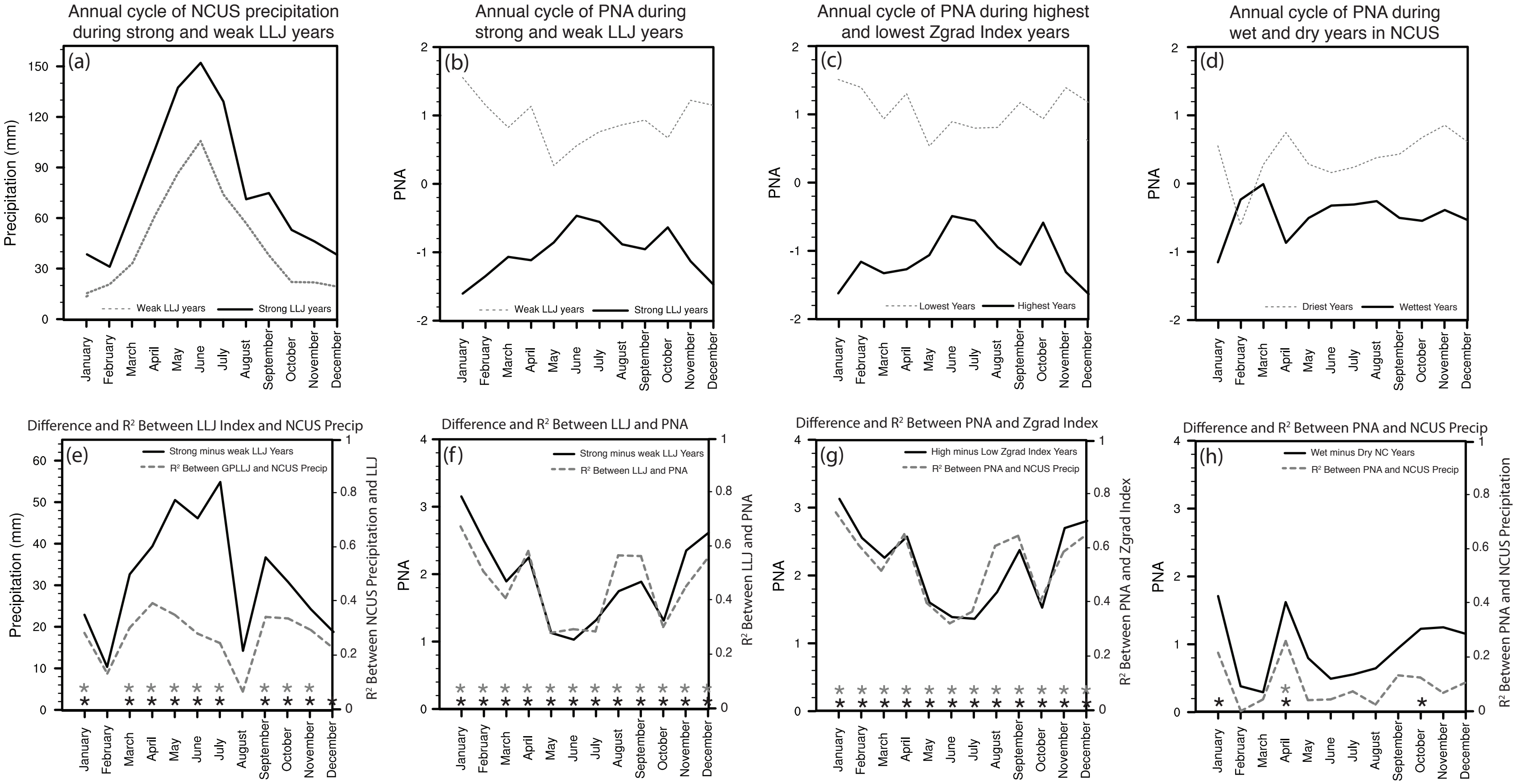

Figure 2.3. 1948-2013 Annual cycle of (a) North Central U.S. (NCUS) precipitation during 10 strongest and weakest LLJ years, (b) PNA during the 10 strongest and weakest LLJ years, (c) PNA during the 10 highest and lowest Zgrad index years, and (d) PNA during 10 wettest and driest years in NCUS. Annual cycle of (e) precipitation difference between 10 strongest and weakest LLJ years and R^2 between LLJ index and NCUS precipitation, (f) PNA difference between 10 strongest and weakest LLJ years and R^2 between LLJ index and PNA, (g) PNA difference between 10 highest and lowest Zgrad index years and R^2 between PNA and Zgrad index, and (h) PNA difference between 10 wettest and driest years in NCUS and R^2 between PNA and NCUS precipitation. Asterisks indicate 95% confidence for differences (black) using a *t* test and for coefficients of determination (R^2; gray) using an F-test.

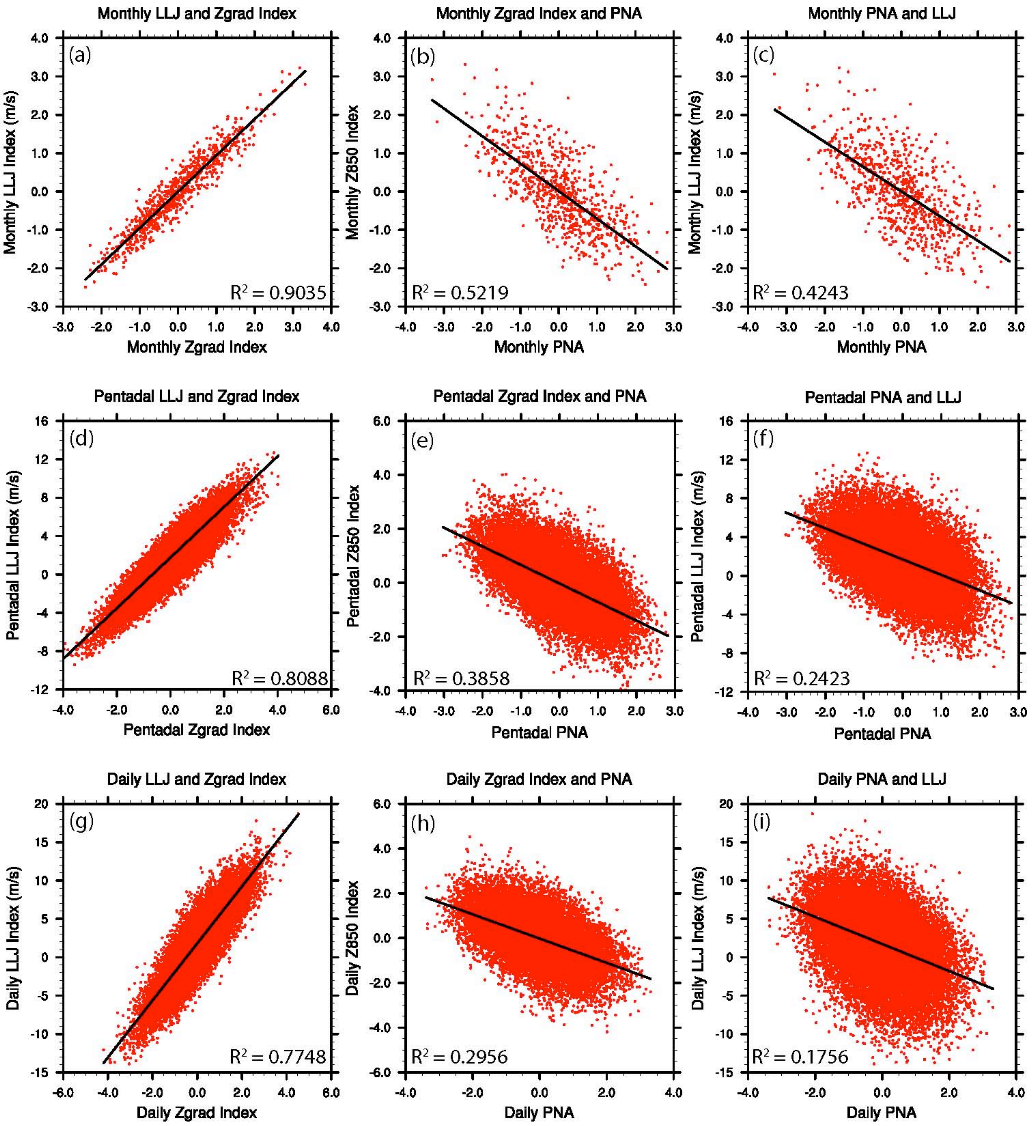

Figure 2.4. 1948-2013 scatterplots for monthly (a) LLJ index and Zgrad index, (b) Zgrad index and PNA, and (c) PNA and LLJ index from NCEP-NCAR Reanalysis. (d) through (f) as (a) to (c) but for pentads instead of monthly data. (g) to (i) as (a) to (c) but for daily data.

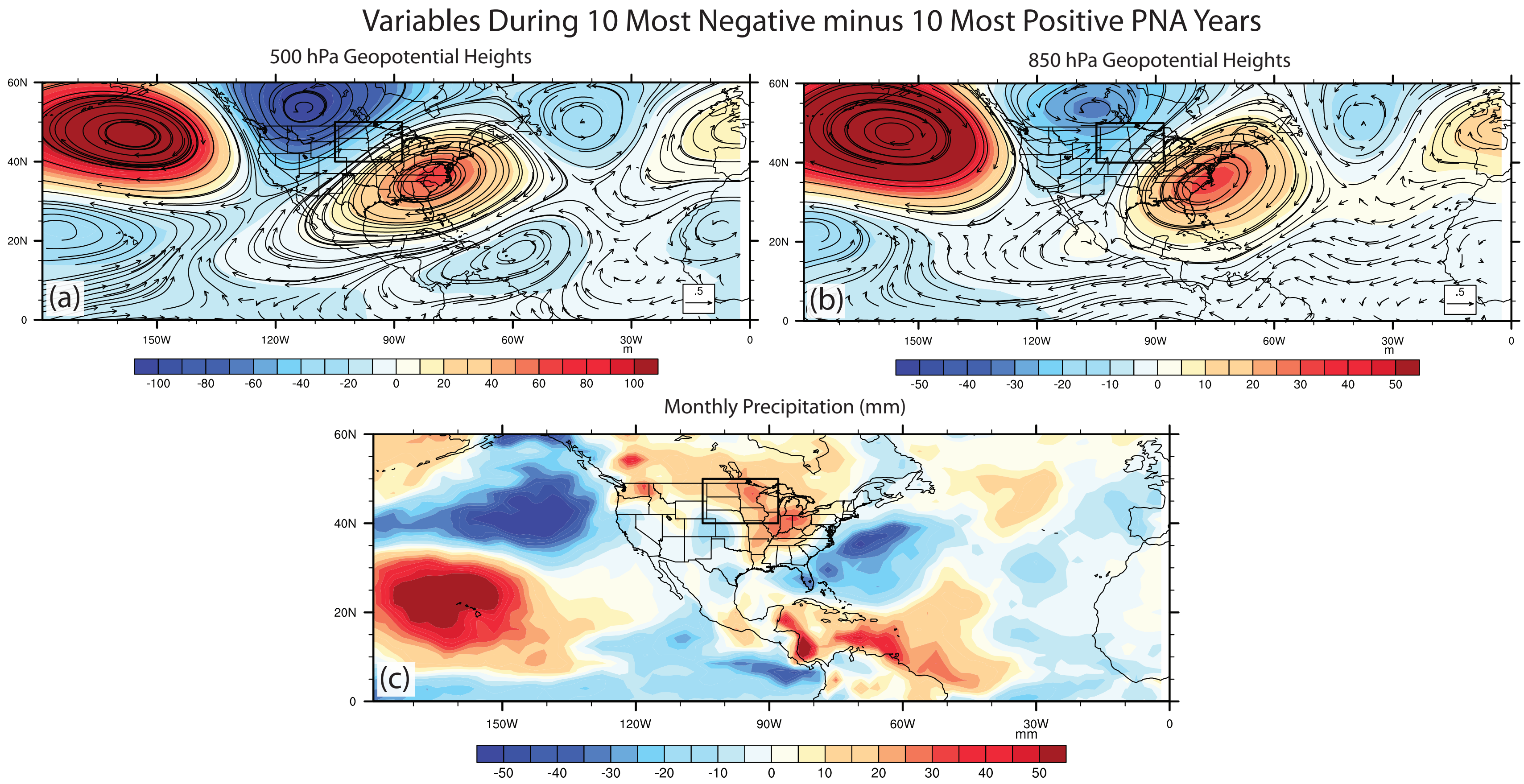

Figure 2.5. (a) 1948-2013 NCEP-NCAR 500 hPa geopotential heights (m) during 10 strongest minus 10 weakest LLJ years for the average of all calendar months. (b) as (a) but for 850 hPa. (c) as (a) but for precipitation (mm).

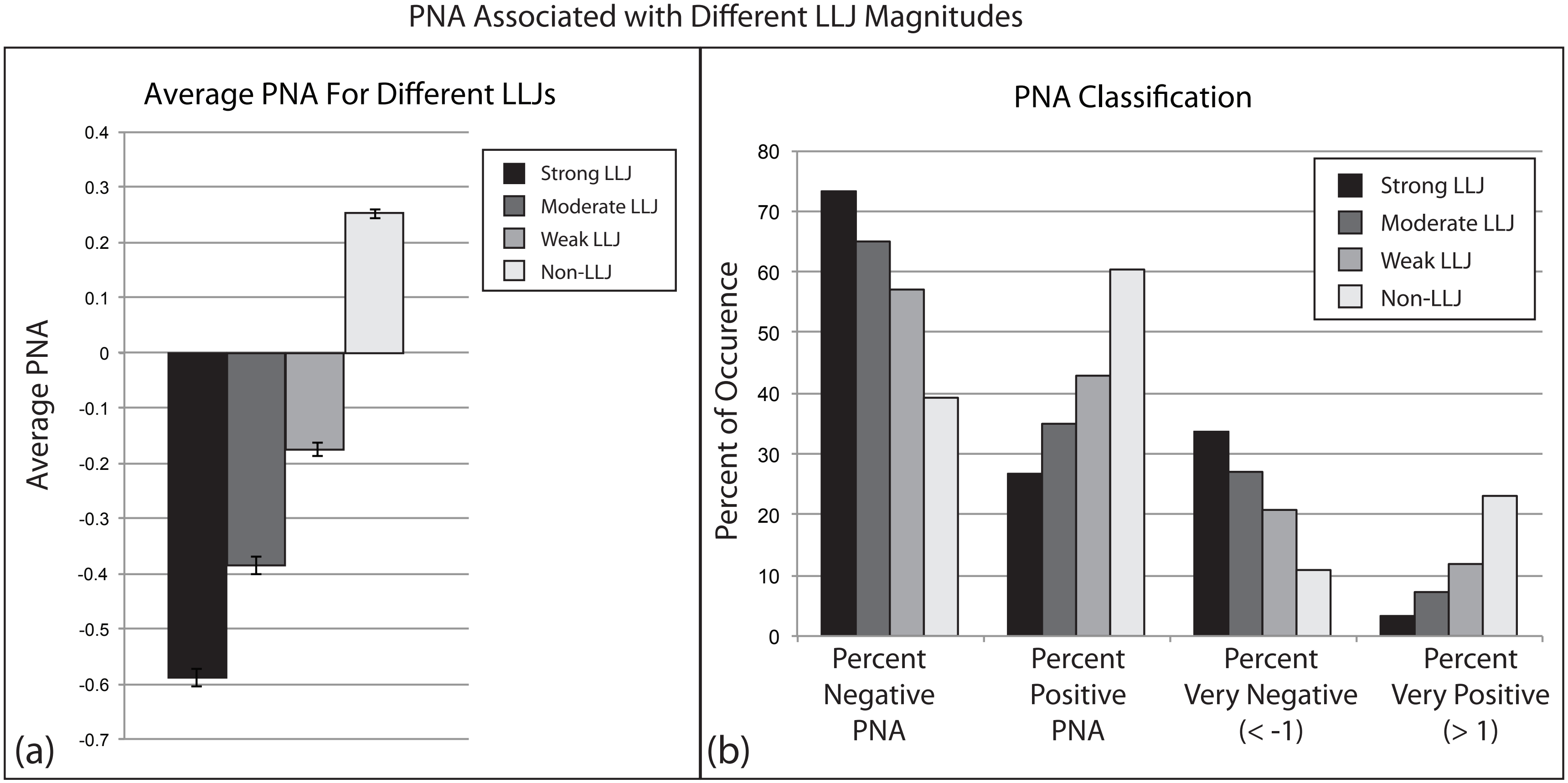

Figure 2.6. (a) 1948-2013 Average PNA for 6-hour periods within the NCEP-NCAR reanalysis with a strong LLJ, moderate LLJ, weak LLJ, or no LLJ present. (b) as (a) but for the percent of each type of LLJ associated with a negative PNA, positive PNA, very negative PNA, and very positive PNA.

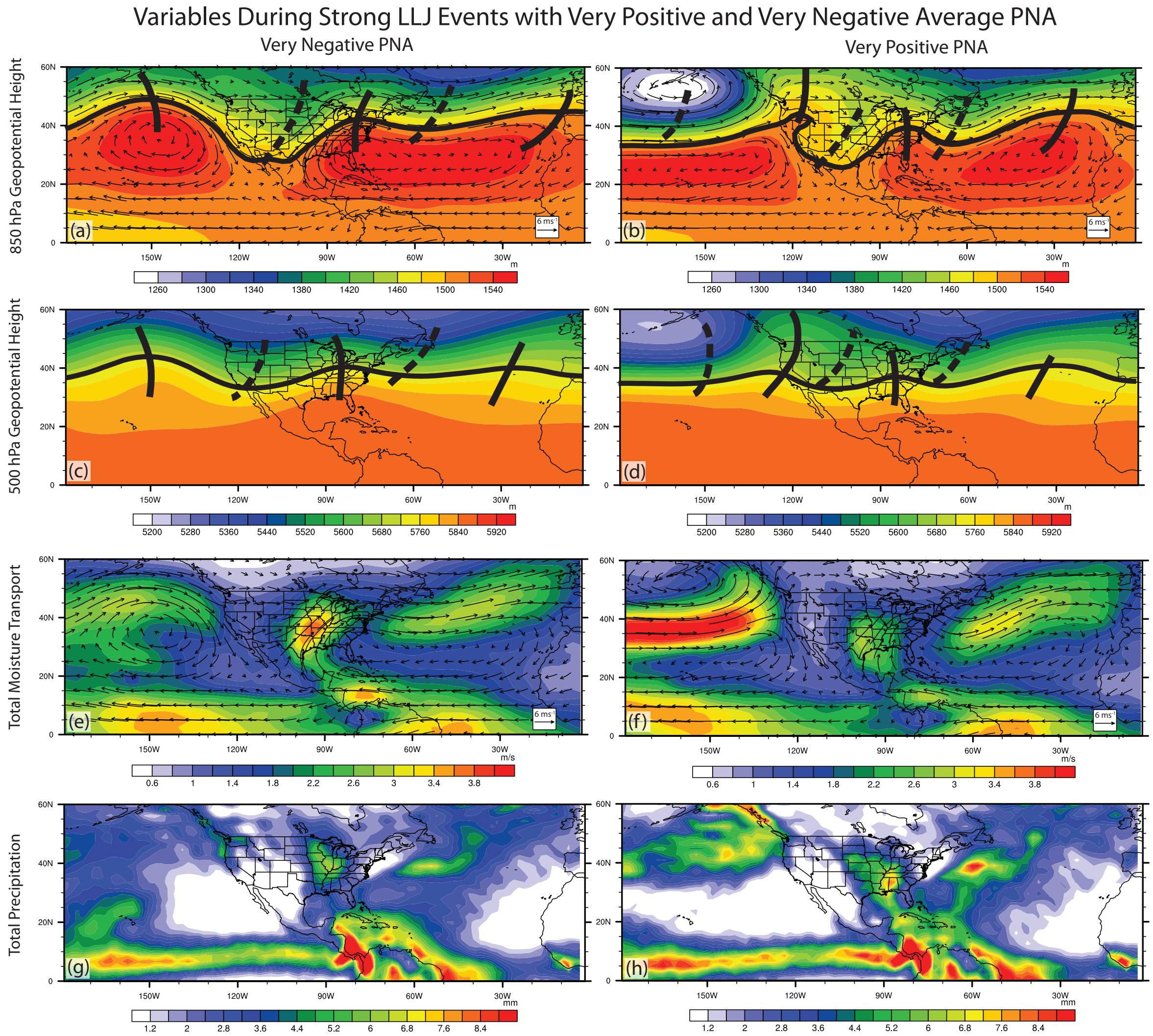

Figure 2.7. (a) 1948-2013 850 hPa geopotential height (m) during strong LLJ events associated with a very negative PNA average during the LLJ event. (b) as (a) but for a very positive PNA. (c) and (d) as (a) and (b) but for 500 hPa geopotential height (m). (e) and (f) as (a) and (b) but for the total vertically integrated moisture transport (m s^{-1}) during the duration of strong LLJ events. (g) and (h) as (e) and (f) but for total precipitation (mm). In (a) through (d), ridges/troughs are denoted and the 5720 m (500 hPa) and 1520 m (850 hPa) isoheights are outlined to highlight large-scale flow features.

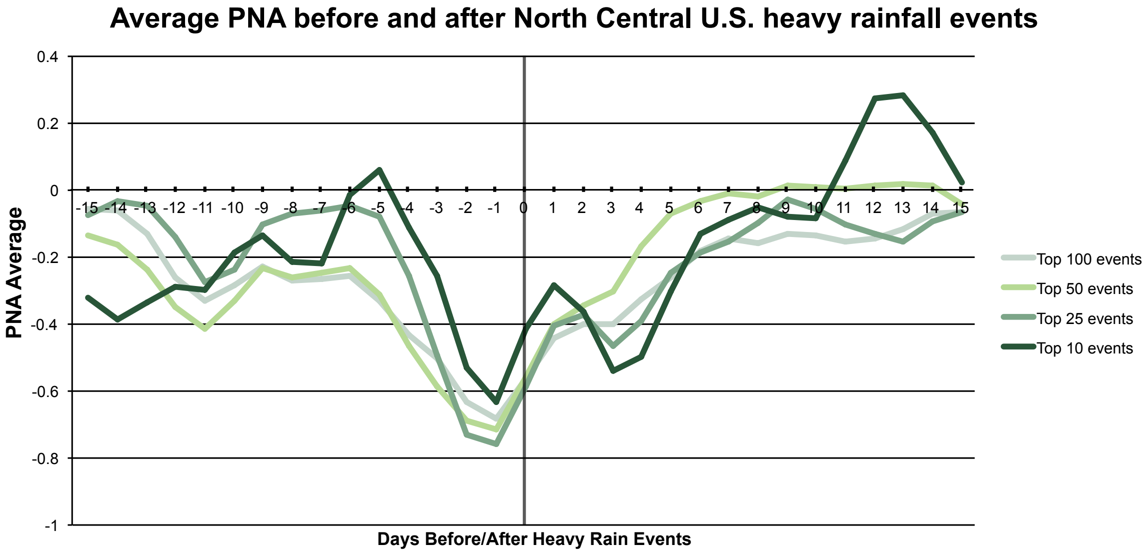

Figure 2.8. Average PNA before and after top 10, top 25, top 50, and top 100 North Central U.S. 1-day heavy rainfall events.

Chapter 3

Use of dynamical downscaling to improve the simulation of Central U.S. warm season precipitation in CMIP5 models

Harding, K. J., P. K. Snyder, and S. Liess (2013), *Journal of Geophysical Research - Atmospheres*, 118, 12,522-12,536, doi:10.1002/2013JD019994.

3.1 Overview

Despite supporting exceptionally productive agricultural lands, the Central U.S. is susceptible to severe droughts and floods. Such precipitation extremes are expected to worsen with climate change. However, future projections are highly uncertain as global climate models (GCMs) generally fail to resolve precipitation extremes. In this study, we assess how well models from the Coupled Model Intercomparison Project – Phase 5 (CMIP5) simulate summer means, variability, extremes, and the diurnal cycle of Central U.S. summer rainfall. Output from a subset of historical CMIP5 simulations are used to drive the Weather Research and Forecasting (WRF) model to determine whether dynamical downscaling improves the representation of Central U.S. rainfall. We investigate which boundary conditions influence dynamically downscaled precipitation estimates and identify GCMs that can reasonably simulate precipitation when downscaled. The CMIP5 models simulate the seasonal mean and variability of summer rainfall reasonably well, but fail to resolve extremes, the diurnal cycle, and the dynamic forcing of precipitation. Downscaling to 30 km improves these characteristics of precipitation, with the greatest improvement in the representation of extremes. Additionally, sizeable diurnal cycle improvements occur with higher (10 km) resolution and convective parameterization disabled, as the daily rainfall peak shifts four hours closer to observations than 30 km resolution simulations. This lends greater confidence that the mechanisms responsible for producing rainfall are better simulated. Because dynamical downscaling can more accurately simulate these aspects of Central U.S.

summer rainfall, policymakers can have added confidence in dynamically downscaled rainfall projections, allowing for more targeted adaptation and mitigation.

3.2 Introduction

The Great Plains and Midwestern United States include some of the most productive agricultural lands in the world, despite their vulnerability to extremes in precipitation. Historically, drought and heavy rainfall episodes have contributed to significant economic losses throughout the Midwest. The 1988-89 North American drought resulted in damages in excess of $77.8 billion (National Climatic Data Center, available at http://www.ncdc.noaa.gov/billions/) – one of the three costliest weather-related disasters in the last three decades. Increasing temperatures are generally expected to alter regional precipitation patterns (Bates et al. 2008; Huntington 2006) and lead to more frequent extreme rainfall events (Parry et al. 2007; Trenberth et al. 2003). How exactly warm season precipitation might change over the Central U.S. is still fraught with uncertainty, primarily because of the inadequacy of global climate models (GCMs) in simulating the spatial variability of convective precipitation. GCMs do a reasonable job simulating large-scale changes in precipitation (Reichler and Kim 2008), however they tend to overestimate light precipitation episodes at the expense of heavier rainfall events (Allan and Soden 2008; Dai 2006; Meehl et al. 2005) due to the presence of unresolved convective processes and averaging over large grid boxes (Chen and Knutson 2008; Gober et al. 2008). With more credible projections of future changes in warm season precipitation extremes, policymakers can better act to implement adaptation strategies to minimize the economic impacts to agricultural lands in the Central U.S.

To overcome these limitations, regional models are commonly employed because they can be run at spatial resolutions that are far higher than most GCMs and better represent regional topography and mesoscale characteristics that influence convective precipitation. However, even with these improvements, inherent biases in regional models can reduce the accuracy of dynamical downscaling. In this study we evaluate how well the Coupled Model Intercomparison Project – Phase 5 (CMIP5) global models simulate summer rainfall means, variability, extremes, and the diurnal cycle. We also assess whether these models can adequately simulate the factors contributing to the simulation of summer precipitation over the Central U.S. We then use output from the historical runs of a subset of the CMIP5 models to drive the Weather Research and Forecasting (WRF) model (Skamarock et al. 2008) to explore whether dynamical downscaling can be used to improve upon GCM-simulated warm season precipitation. We investigate whether the accuracy of specific GCM boundary conditions improves downscaled precipitation over the Central U.S. and identify specific models that accurately simulate Central U.S. summer rainfall, with the goal of providing a methodology for choosing the best models to dynamically downscale.

Precipitation over the Great Plains and Midwestern U.S. is highly variable as shown by recent severe droughts (e.g., 1930s Dust Bowl, 1950s, 1988, 2012) and floods (e.g., 1993, 2008, 2011). Several recent droughts in the Central U.S. have resulted in significant economic losses ($77.6 billion in 1988; (NCDC 2013)) because of widespread crop failure. Predicted increases in drought (Allen and Ingram 2002; Wang et al. 2011; Wetherald and Manabe 2002) and higher summertime temperatures over much of the region (Meehl and Tebaldi 2004) will likely place additional stress on crops and lead to further economic losses. The 2012 drought in the central U.S. was exacerbated by an extended period of record-breaking temperatures and could be a portent of future droughts in the region. Similarly, the continued trend toward heavier rainfall events (Kunkel et al. 1999) could cause severe agricultural losses similar to those experienced during the 2008 and 2011 Midwest floods (National Climatic Data Center, available at http://www.ncdc.noaa.gov/billions/).

The majority of warm-season precipitation over the Great Plains is convective (Changnon 2001), with a significant percentage (>25%) occurring nocturnally (Higgins et al. 1997). Numerous studies have identified the Great Plains Low Level Jet (GPLLJ) as being the prominent driver of dynamically forced summertime nocturnal precipitation (Bell and Janowiak 1995; Helfand and Schubert 1995; Higgins et al. 1997; Means 1952, 1954; Mo and Berbery 2004; Mo et al. 1995; Pitchford and London 1962) with the jet being responsible for transporting up to one-third of all moisture entering the contiguous U.S. (Bell and Janowiak 1995; Helfand and Schubert 1995; Higgins et al. 1997). GPLLJ events primarily occur from May to September between about 0600 UTC and 1200 UTC (between 12 am and 6 am local standard time) (Bonner 1968; Higgins et al. 1997; Mitchell et al. 1995), with the monthly average GPLLJ located around 910 hPa in April and 860 hPa in July according to the North American Regional Reanalysis (NARR) dataset [*Cook et al.*, 2008].

Because low-level inflow from the Gulf of Mexico is up to 45% higher than nocturnal mean values during GPLLJ events (Higgins et al. 1997), the GPLLJ is considered an important source for the development of mesoscale convective complexes (MCCs) (Tuttle and Davis 2006). Low-level convergence, cyclonic shear, and moisture convergence to the north (downstream) of the jet maximum is well documented (Bonner 1968; Helfand and Schubert 1995; Weaver and Nigam 2011) and has been shown to contribute to ascent and the occurrence of heavy precipitation events (Arritt et al. 1997; Cook et al. 2008; Monaghan et al. 2010).

The GPLLJ has been effectively replicated in reanalysis datasets (Higgins et al. 1997), regional models (Mo and Berbery 2004), and some GCMs (Cook et al. 2008; Helfand and Schubert 1995) at daily and monthly timescales. However, GCMs generally fail to simulate the observed link between moisture convergence from the GPLLJ and Midwest precipitation (Cook et al. 2008; Lee et al. 2007a; Lee et al. 2007b; Ruiz-Barradas and Nigam 2006a, 2006b). In an analysis of three GCMs, Lee et al. (2007a; 2007b) found that each reasonably simulated the GPLLJ but failed to capture the diurnal cycle of precipitation or the relationship between the GPLLJ and precipitation. The models did not adequately capture the large-scale forcing for convection, but instead initiated convection based on thermodynamic rather than dynamic forcing during the afternoon hours (Lee et al. 2007a; Lee et al. 2007b; Zhang 2003). While a clear link exists between the strength of the GPLLJ and precipitation, in this study we investigate whether such a link exists in the new suite of CMIP5 models and if dynamical downscaling can improve the simulation of precipitation using a subset of these models.

Downscaling uses statistical or dynamical approaches to produce high-resolution regional and local climate datasets from spatially and temporally coarse datasets (e.g., GCMs or reanalysis). In dynamical downscaling, GCM output is used as a lateral boundary condition to initialize a regional model, thus producing high-resolution data through physical and dynamical equations (Castro et al. 2005). However, the high computational expense of dynamical downscaling GCM data limits the number of models that can be used, potentially affecting the results because of biases in the parent GCMs. Because inaccuracies in GCM data can filter through the downscaling process (Wu et al. 2005), regional downscaling must incorporate GCM data that reasonably simulates the regional climate. Regional models ingest prognostic variables that are related to precipitation, but not precipitation itself, making accurate simulation of precipitation in a regional model dependent on the accuracy of these prognostic boundary conditions.

The goals of this study are to (1) establish whether the CMIP5 models adequately simulate seasonal means, interannual variability, extremes, and the forcing of summer precipitation over the Central U.S., (2) determine whether these precipitation characteristics are improved with dynamical downscaling, (3) evaluate which boundary conditions from GCMs are most influential in generating accurate downscaled summertime precipitation over the Central U.S., and (4) identify models that most accurately simulate summer rainfall over the Central U.S. when downscaled using WRF.

3.3 Methods

3.3.1 CMIP5 Models

The most recent model intercomparison project, CMIP5, was initiated by the World Climate Research Programme's (WCRP) Working Group on Coupled Modeling (WGCM) to provide a new generation of GCMs and earth system models (ESMs) for use in the IPCC Fifth Assessment Report (AR5) (Taylor et al. 2012). The average longitudinal and latitudinal spatial resolution of the models ranges from approximately 0.5° to 3.75°, with half of the models running at a resolution finer than 1.9° (Table 2.1).

All CMIP5 model output in this study was interpolated to a 2.5° x 2.5° grid (except for boundary condition rankings and the boundary conditions used in dynamical downscaling). Weighted-area averages for each region shown in Figure 3.1 were calculated using the 2.5° x 2.5° interpolated output. The multi-model ensemble (MME) in this study was produced by weighting all models equally.

3.3.2 Observations

Model data from the historical simulations were compared to observations for the period 1979-2005, thus overlapping the post-satellite period included in reanalysis datasets. Because model performance has been shown to be influenced by the choice of observational dataset used in the comparison (Gómez-Navarro et al. 2012), model data for each variable was tested against five datasets (datasets with monthly resolution in Table 2.2) to minimize observational bias. Reanalysis datasets were used for comparison of variables on pressure levels (Table 2.2).

The National Center for Environmental Prediction's (NCEP) Stage IV precipitation dataset and precipitation from NARR were selected for comparisons of the diurnal cycle and extreme events. Five years of heavy precipitation events in the CMIP5 models and WRF simulations (described in section 3.3.4) were compared with Stage IV (first five available years, 2002-2006) (Lin and Mitchell 2005) and NARR (1990-1994) (Mesinger et al. 2006). Stage IV compares well with other observational datasets for extreme rainfall events and is commonly used as a benchmark for sub-daily observations (AghaKouchak et al. 2011; Sapiano and Arkin 2009). Because both datasets have been shown to accurately resolve the diurnal cycle (Lee et al. 2007b) they were used to compare 3-hourly precipitation from WRF and CMIP5 simulations.

3.3.3 Model Variable Rankings

Here we describe the three different types of model rankings that were conducted for precipitation and 850-hPa meridional wind speed (which is highly correlated with N. Central U.S. summer precipitation) as well as rankings for precipitation extremes. This analysis was conducted over the North Central and South Central U.S. as shown in Figure 3.1 for June-July-August (JJA). Weighted-area averages were calculated for each region and compared with weighted-area averages of the observations or reanalysis datasets.

The mean ranking is based on the z-score of each model and the MME:

$$MZ_{vmr} = \frac{1}{N}\sum_{i=1}^{N}\frac{\overline{v_{mr}} - \overline{o_{ri}}}{\sigma_r}, \qquad (3.1)$$

where MZ is the mean model z-score for a particular simulated variable (v), model (m), and region (r) for the average of all N observational datasets; o_i is an observed variable for observational dataset i, and σ is the intermodel standard deviation for region r. The standard deviation ranking is based on the z-score of each model and the MME as shown:

$$SDZ_{vmr} = \frac{1}{N}\sum_{i=1}^{N}\frac{\zeta_{mr} - \varphi_{ri}}{\psi_r}, \qquad (3.2)$$

where SDZ is the standard deviation z-score for a particular variable (v), model (m), and region (r) for the average of all N observational datasets; ζ is the model interannual standard deviation, φ is the observed interannual standard deviation for observational dataset i, and ψ is the standard deviation of ζ across all models for region r. The mean and standard deviation z-scores are then summed to produce a combined ranking.

For the extreme precipitation rankings, all 6-hourly simulated (GCM and WRF) and observed (Stage IV and NARR) precipitation datasets were interpolated to a common 2.5° x 2.5° grid for analysis. It is worth noting that exact precipitation frequency distributions from the models and observations are more accurately represented if the native resolutions are used in lieu of a common resolution, but a common resolution is more applicable for comparison between data at different resolutions. All 6-hourly precipitation events over 0.01 mm within a region from each model were grouped into different bins with a range of 5 mm (e.g., 0.01-5 mm, 5-10 mm, etc.) and the percentage of total rainfall events in each bin were calculated. For each rainfall bin, models were given a Z-score (Z) as shown:

$$Z_{mr} = \frac{1}{B}\sum_{b=1}^{B}\frac{\eta_{bmr} - \eta_{bor}}{\omega_{br}} , \qquad (3.3)$$

where η is the percentage of total rainfall events from Stage IV (o) or each model (m) for every precipitation bin (b) in each region (r); ω is the standard deviation of η across all the models for each bin (b) and region (r), and B is the number of bins.

3.3.4 Downscaling using the WRF model

For this study the regional WRF model version 3.4 (Skamarock et al. 2008) was used with the coupled Noah Land Surface Model (LSM) (Chen and Dudhia 2001). WRF is a non-hydrostatic mesoscale meteorological model that can be used for research or operational forecasting. The Noah LSM is the coupled land-surface model that exchanges surface fluxes of energy, momentum, and mass with the WRF model and includes four soil layers and one canopy layer. The 20-category, 30-arc-second resolution MODerate Resolution Imaging Spectroradiometer (MODIS) land use dataset (Friedl et al. 2002) is assimilated into the Noah LSM and WRF. Evapotranspiration is calculated as the sum of direct ground and canopy evaporation, transpiration, and sublimation (Chen and Dudhia 2001; Hong et al. 2009), all of which are calculated empirically using soil and vegetation parameters from MODIS (Betts et al. 1997; Friedl et al. 2002; Jacquemin and Noilhan 1990; Noilhan and Planton 1989).

The model uses a terrain-following vertical coordinate system that extends from the surface to 50 hPa. Because convective processes and shallow clouds cannot be fully resolved within coarsely resolved grid cells (Skamarock et al. 2008), the development of precipitation in WRF is aided by a convective parameterization (CP) at coarse spatial resolutions. CPs are designed to resolve sub-grid scale vertical fluxes of mass, momentum, and latent heating when adequate spatial resolution prevents these processes from being resolved explicitly. The spatial resolution required to resolve convective precipitation varies by application. Deep moist convection can explicitly develop in the absence of a CP in WRF at a horizontal resolution of 10 km over the Central U.S. during the warm season (Harding and Snyder 2012b) but in some cases CPs are necessary at spatial resolutions between 5-10 km (Skamarock et al. 2008).

WRF was run in a nested grid configuration with a 90-km resolution outer domain and 30-km resolution inner domain. The outer domain was run at a time step of 5 minutes, with a 100-second time step in the inner domain. The model was run with the Morrison 2-moment microphysics scheme (Morrison et al. 2009), Kain-Fritsch cumulus parameterization (Kain 2004), YSU Planetary Boundary Layer (PBL) scheme (Hong et al. 2006), RRTM long wave radiation scheme (Mlawer et al. 1997), Dudhia shortwave radiation scheme (Dudhia 1989), and the MM5 surface-layer scheme (Skamarock et al.

2008). Model simulations were conducted from March 15 to October 1 and soil moisture was initialized using the 1981-2010 average March 15 soil moisture from the NCEP-DOE Reanalysis II (NCEP2) (Kanamitsu et al. 2002).

Analysis nudging was not used within the interior of either model domain because results from a set of sensitivity simulations using NCEP2 showed less accuracy when nudging was applied using the model configuration listed. The average RMSE increased from 45.30 to 64.12 mm over the Central U.S. in simulations that incorporated nudging parameters from Otte et al. (2012). However, it is possible that precipitation estimates could be improved with the use of different nudging parameters. Additionally, a limited number of 10-km resolution simulations with and without CP were performed to assess how the CP contributes to the diurnal cycle of precipitation.

3.3.5 Boundary Condition Rankings

Boundary condition rankings were determined by comparing all the lateral boundary conditions that are used to drive WRF. This includes temperature, specific humidity, geopotential height, meridional and zonal winds as well as sea surface temperatures (SSTs) throughout the outer WRF domain shown in Figure 3.1. Because the lateral boundary conditions used to run WRF consist of five grid cells along each side of the outer domain, only model data interpolated to those grid cells was considered. The root mean squared error (RMSE) of the 1979-2005 JJA average for each lateral boundary condition variable was calculated by comparing each model to the average of all five reanalysis datasets at standard pressure levels provided in the CMIP5 model output up to 100 hPa (1000, 925, 850, 700, 600, 500, 400, 300, 200, and 100 hPa). Average RMSE values for all the lateral boundary condition grid cells were calculated. Models were given a Z-score for each pressure level based on the standard deviation of the average RMSE for all models. For each variable, z-scores were summed for all pressure levels and models were then ranked (lowest z-score was ranked 1st).

For SSTs, individual ocean grid points within the entire domain (outer 90-km WRF grid) were considered. Average 1981-2005 JJA SSTs for each model were compared with the NOAA Optimum Interpolation SST (v2) dataset (available at 1° x 1° from 1981-2005) (Reynolds et al. 2002) and the RMSE was calculated for each grid cell in the domain. An area-weighted average RMSE was calculated for each model and z-scores were determined based on the standard deviation of the area-averaged RMSEs. Models were ranked based on their z-score, with the lowest z-score ranked 1st. Ranks were calculated over the entire domain, the Atlantic Ocean, Pacific Ocean, Gulf of Mexico, and the Atlantic Warm Pool (AWP; 10°-30°N, 100°-60°W). For the different ocean basins, only grid cells within the outer WRF domain were considered. Z-scores for the AWP SSTs are shown in Figure 3.2b.

3.4 GCM Performance of Central U.S. Precipitation and the GPLLJ

To evaluate how well the GCMs simulate Central U.S. precipitation during the warm season, we focus on the MME seasonal means, interannual variability, extremes, and the role of the GPLLJ as a forcing for precipitation. In general, the JJA MME mean rainfall is consistently overestimated by the models over the high terrain of the Great Plains and the Rocky Mountains (Figures 3.3a, 3.3b) due to orographic effects and overestimated low-level moisture (not shown). This is consistent with previous studies that have found a large precipitation bias over the Rocky Mountains and the high terrain of the western

Great Plains (Chao 2012; Lee et al. 2007a; Lee et al. 2007b; Schaller et al. 2011). However, a consistent negative precipitation bias occurs across a longitudinal band from Minnesota through Texas, despite an overestimation of low-level convergence by the models due to the weaker jet exit region (Figures 3.3e, 3.3f). The interannual variability of precipitation in the CMIP5 MME is generally similar to that of the observations, with slightly more variability than in the South Central region (Figure 3.4a) and slightly less in the North Central region (Figure 3.4b).

Considering individual model performance, the CESM1-FASTCHEM most accurately simulates the mean and interannual variability of summer rainfall over the South Central U.S., while the BCC-CSM1.1 is the most accurate over the North Central region (Figure 3.5a). Interestingly, the dynamical cores of both these models are based on the Community Atmosphere Model (CAM). Model spatial resolution results in only slight improvement in simulation of seasonal means over both regions ($R^2 = 0.095$ for South Central, $R^2 = 0.045$ for North Central), with no improvement in the interannual variability over the North Central and slight improvement in the South Central ($R^2 = 0.117$).

The GPLLJ in the MME compares well to the average of the five reanalysis datasets spatially at 850 hPa (Figure 3.3c-d) and 925 hPa (Figure 3.3g-h). While the MME captures the general strength and shape of the GPLLJ, some of the models fail to resolve the jet (GISS-E2-H, GISS-E2-R) and some models have excessively high wind speeds (CanCM4, FGOALS-s2). The 850 hPa (Figures 3.3c, 3.3d) and 925 hPa (Figures 3.3g, 3.3h) wind maxima are located slightly north of the reanalysis average in the MME, but the exit region on the north side of the jet is significantly weaker, resulting in stronger low-level convergence (Figure 3.3f) across parts of the central Great Plains. Considering individual model performance of the GPLLJ, the GFDL-ESM2M model is the most accurate when considering both the mean and interannual variability (Figure 3.5a), the NorESM1-ME model most precisely simulates the seasonal mean (Figure 3.5b), and the MIROC5 model most accurately simulates the interannual variability (Figure 3.5c).

While the spatial representation of summertime precipitation and the GPLLJ are reasonably represented in the CMIP5 models (Figure 3.3), several issues emerge when considering the forcing for precipitation and the relationship between the GPLLJ and rainfall. The models generally resolve the GPLLJ spatially, but they are less successful at simulating the physical relationship between the strength of the GPLLJ and precipitation over the North Central U.S, the primary dynamic forcing for Midwest summertime rainfall. For JJA, the model-average strength of the GPLLJ is inversely related to North Central precipitation ($R^2 = 0.397$), meaning that models with a stronger GPLLJ are more likely to simulate less North Central precipitation.

Additionally, the 850 hPa South Central meridional wind speed explains only 9.3% of the variance in North Central precipitation in the CMIP5 models, compared with 59.8% for the reanalysis datasets. This is most apparent in June and July when the 850 hPa GPLLJ explains 17.9% and 10.3% of the variance in North Central precipitation, while the strength of the GPLLJ explains 54.2% and 57.9% of the variance, respectively, in the reanalysis datasets. This behavior, exhibited by most CMIP5 models, implies that Midwest summertime rainfall is likely being developed thermodynamically rather than from dynamic forcing as discussed by Lee et al. (2007a), (2007b) and Zhang (2003). This is supported by the fact that the diurnal cycle for precipitation is out of phase with NARR and Stage IV over the North Central U.S. (Figure 3.6a), despite the fact that most models for which sub-daily data is available correctly simulate the diurnal cycle of the GPLLJ (not shown). In addition, the diurnal cycle of precipitation is more in phase with observations over regions where summertime precipitation is governed by thermodynamic forcing (e.g., the Southeast U.S.; Figure 3.6b). Therefore, the CMIP5 models are likely unable to resolve the dynamic forcing of nocturnal convective precipitation from the GPLLJ during the summer months, which highlights potential problems with convective schemes in GCMs. These results are also consistent with the CMIP3 models (Bukovsky and Karoly 2011) and other studies on GCM performance (Lee et al. 2007a; Lee et al. 2007b; Zhang 2003). However, the models exhibit more realistic correlations between the strength of the GPLLJ and precipitation when rainfall is less convective in nature during April, May, and September (not shown). During these months, the models are less likely to be overwhelmed by thermodynamic forcing. Therefore, potential future changes in dynamical forcing will likely have a more noticeable impact on GCM-simulated precipitation in the North Central U.S. during the spring months.

Heavy precipitation events in the North Central U.S. during JJA, which are associated with strong GPLLJ events (Arritt et al. 1997; Monaghan et al. 2010), are generally absent in simulations of the CMIP5 models over the North and South Central regions (Figures 3.7a, 3.7b). This likely occurs because of inadequate dynamic forcing of convection from the GPLLJ and coarse spatial resolutions, consistent with previous studies that have shown an underestimation of heavy precipitation events by GCMs in general (Wilcox and Donner 2007). This problem also appears in the high-resolution

NARR (Becker et al. 2009), suggesting that comparison of extreme events in NARR with GCMs is likely flawed. Lighter precipitation events are oversimulated at the expense of heavier rainfall episodes in the CMIP5 models (Figure 3.7a, 2.7b), with the exception of the high-resolution MIROC4h and CMCC-CM models (Figures 3.7a-c). Wehner et al. (2010) noted that higher resolution GCMs are more apt to simulate heavy rainfall events, suggesting that the fine horizontal resolution (< 0.75°) of the MIROC4h and CMCC-CM likely contributes to the accurate simulation of extreme wet episodes in all regions. All coarser resolution CMIP5 models greatly underestimate the occurrence of rainfall events over 10 mm (Figures 3.7a, 3.7b), with significant improvement as model resolution increases. That is, model horizontal resolution explains 51.6% of the variance in North Central U.S. extreme precipitation performance [R^2 between North Central U.S. extreme precipitation Z-scores (described in section 3.3.3) and spatial resolution] and 51.1% of the variance in the South Central U.S. extreme precipitation performance (Figure 3.7c).

To determine whether the averaging over large grid boxes or unresolved convective processes is responsible for the strong relationship between native model resolution and extreme rainfall performance, this analysis was also completed using the model and observational data at their original spatial resolutions. Upon analyzing the models, native model resolution still impacts the simulation of heavy rainfall events (Figure 3.8). Native spatial resolution explains 52.1% of the variance in North Central U.S. extreme precipitation performance, nearly identical to the correlation found with the 2.5° x 2.5° common grid. Because a similar relationship between native model resolution and extreme rainfall performance is found in both analyses (Figures 3.7, 3.8), it is unlikely that differences in extreme precipitation performance are due to averaging over larger grid boxes as discussed by Chen and Knutson (2008) and Göber et al. (2008). Instead, these results suggest that the inadequate simulation of heavy rainfall events in the coarse resolution GCMs is because of the inability of these models to resolve convective processes related to extreme precipitation over large areas.

3.5 Dynamical Downscaling Performance

3.5.1 WRF Precipitation Performance

Nine out of nineteen CMIP5 models with 6-hourly output (ACCESS1.3, BCC-CSM1.1, CMCC-CM, GFDL-CM3, IPSL-CM5A-LR, IPSL-CM5B-LR, MIROC5, MRI-CGCM3, and NorESM1-M) were dynamically downscaled using WRF. These models represent a range of accuracy in simulated precipitation over the Central U.S. (Figure 3.2a). Simulations for March 15-October 1 were performed over the domain shown in Figure 3.1 for five individual years (1990-1994). It is preferred that simulations be run over a longer time period (i.e., 10-30 years) to assess model performance, however, the purpose of this study was to assess whether a larger subset of CMIP5 models could reasonably simulate regional precipitation. Such an objective may be achieved on shorter time scales, especially for models that significantly deviate from a realistic climate. With computational limitations in mind, our objective supported the incorporation of more models with fewer simulated years to allow for an expanded model intercomparison. However, it is worth noting that such a short period is generally inadequate for studies that aim to estimate future changes relative to a climatological base period (i.e., NARCCAP (Mearns et al. 2012)).

Because the GCMs used to drive the WRF simulations do not represent specific observed years, WRF simulations were compared with observations from the 1981-2010 climatological period rather than the period (1990-1994) in which WRF was run. For the average of the downscaled CMIP5 models (Figure 3.9i), WRF accurately simulates the JJA precipitation mean throughout much of the Central U.S. compared with the 1981-2010 average of all five observational datasets listed in Table 2.2 (Figure 3.9k). WRF simulations forced by NCEP2 (WRF-NCEP2) produce more accurate precipitation estimates than any of the WRF simulations forced by CMIP5 models (Figure 3.9i, 2.9j). However, the top five downscaled CMIP5 models are only marginally worse than WRF-NCEP2, suggesting that the best performing CMIP5 models in this study can simulate rainfall with skill similar to NCEP2 when downscaled in WRF. Therefore, these CMIP5 models are desirable candidates for studies that incorporate dynamical downscaling to produce future projections.

Comparing WRF downscaled simulations with the original GCMs, the simulation of seasonal rainfall means in WRF is improved slightly over much of the southern Great Plains but is generally worse over the northern Plains (Figures 3.10a-b), with a 2.6% increase in RMSE over the South and North Central regions combined. Greater improvement occurs over the South Central region, where large negative biases along the Gulf Coast are eliminated and positive anomalies are reduced over the high terrain of New Mexico and west Texas (Figure 3.10c), resulting in a 22% lower average RMSE over the South Central region. In the North Central region, WRF overestimates precipitation over a rather large area of the northern Plains and Upper Midwest (Figure 9c), resulting in a 34% greater RMSE over the North Central region. The greatest accuracy in WRF is achieved along a corridor from southern Texas into south central Minnesota where rainfall biases are near zero (Figure 3.9i, 2.9b) and RMSE is reduced compared with the GCMs (Figure 3.10c). Considering individual downscaled models, the ACCESS1.3 model most accurately simulates seasonal mean precipitation over the Central U.S. (Figure 3.9a-h; 2.11) and only small performance differences exist between models ranked first to fifth in the regional RMSE ranking.

Considering the relationship between precipitation performance in GCMs and downscaled simulations, GCMs that accurately simulate seasonal rainfall means are generally more accurate when downscaled. This is supported by the fact that the rank in GCM-simulated precipitation over the Central U.S. is significantly correlated with the rank of downscaled Central U.S. rainfall ($R^2 = 0.46$; $p < 0.05$). Over the South Central region, GCM precipitation rank explains 45.9% of the variance in downscaled rainfall rank ($p < 0.05$) compared with less than 1% in the North Central U.S.

The greatest improvements with dynamical downscaling occur with the simulation of extreme rainfall events. Heavy precipitation episodes over 50 mm are simulated with greater accuracy in WRF compared with the original GCMs when analyzed at a common 2.5° x 2.5° resolution (Figures 3.7a, 3.7b) as well as at their native model resolutions (Figure 3.8). WRF-simulated precipitation frequency distributions closely match the Stage IV observations in the North (Figure 3.7a) and South Central regions (Figure 3.7b), with a slight underestimation of rainfall events over 10 mm (between 25 mm and 70 mm when analyzed at native model resolution). In general, the small spread in precipitation frequency distributions between different WRF simulations (Figures 3.7a, 3.7b) suggests that the representation of extreme rainfall episodes is generally independent of the forcing model in WRF. Additionally, the accurate representation of heavy rainfall episodes in WRF suggests that the choice of 30-km resolution in WRF is sufficient to accurately resolve extreme rainfall events.

Only slight performance enhancements occur for the diurnal cycle of rainfall in WRF. While WRF produces more nocturnal precipitation than all of the CMIP5 models, the late afternoon convective precipitation peak is still quite large in the North Central region (Figure 3.6a), suggesting that rainfall in WRF may be produced disproportionately from thermodynamic, rather than dynamic, forcing. The timing of the diurnal precipitation peak is independent of the forcing model in the North Central region, with all WRF simulations producing a peak during the same hour in the early afternoon (22 UTC; Figure 3.6c). Regardless of how accurately WRF simulates the dynamic forcing for precipitation, the strength of the GPLLJ explains only slightly more of the variance in North Central rainfall for JJA (16.5% vs. 9.3% in the GCMs; 59.8% in the reanalyses). Improvement only occurs in June (33.7% vs. 7.5% in the GCMs; 55% in the reanalyses), with no improvement in July or August. This shows that WRF, similar to CMIP5 models, overemphasizes thermodynamically driven precipitation over dynamically driven precipitation from the nocturnal GPLLJ at this spatial resolution. However, the small shift in rainfall to the overnight hours is likely related to the fact that the dynamic forcing for convective precipitation is slightly more influential in WRF, albeit still too weak.

3.5.2 *Influence of GCM boundary conditions on Central U.S. Summertime Rainfall*

Here we investigate whether certain boundary conditions influence how well Central U.S. precipitation is simulated with dynamical downscaling. GCMs are ranked based on how well they simulate boundary conditions assimilated into the WRF domain shown in Figure 3.1. SSTs over the AWP have the greatest impact on the accurate simulation of rainfall over the Central U.S. (Table 2.3), contributing to 28% of the variance in downscaled Central U.S. precipitation performance (AWP Z-scores shown in Figure 2b). Because the AWP is a significant source of moisture for summer rainfall in the Great Plains (Bosilovich and Schubert 2002; Wang et al. 2006), accurate SSTs over this region can have a sizable impact on precipitation simulated in WRF. Downscaled rainfall performance is impacted the most by accurate AWP SSTs over the South Central region ($R^2 = 0.27$), with no impact over the North Central ($R^2 = 0.01$). Considering lateral boundary conditions, geopotential height has the most influence the accurate simulation of Central U.S. summer rainfall, with a much smaller impact for specific humidity, zonal wind, and meridional wind (Table 2.3). Over the North Central region, none of the boundary conditions appeared to play a significant role in the accurate simulation of warm-season precipitation (Table 2.3).

Additionally, the rankings of AWP SSTs and GCM-simulated Central U.S. rainfall together explain 57% of the variance ($p < 0.01$) in downscaled precipitation performance over the Central U.S when z-scores from these rankings are averaged (Figure 2c; a ranking for this combination is shown in Table 2.4). This suggests that GCMs with the combination of accurate AWP SSTs and precisely simulated rainfall tend to downscale Central U.S. rainfall with significantly higher accuracy in WRF. However, the reasons behind this relationship are not entirely clear.

3.5.3 10-km sensitivity simulations

Because WRF simulations with a 30-km spatial resolution produce excessive afternoon precipitation, additional simulations were completed at a higher spatial resolution to determine whether the diurnal cycle of downscaled rainfall can be improved. CMCC-CM, a model that produced accurate downscaled precipitation estimates in the 90-30 km configuration, was also downscaled using the 50-10 km nested grid configuration shown in Figure 3.1 (dashed lines). Simulations were completed over the same period as those mentioned in section 3.3.4. To infer the impact of the CP on the diurnal cycle of precipitation, a set of simulations (1990-1994) was completed at a 10-km spatial resolution with the CP activated for both domains, while another set of simulations were completed without use of a CP in the inner domain.

The diurnal precipitation peak is shifted later in both sets of simulations, with the greatest improvement over the North Central region in simulations without a CP (Figure 3.6c). In the simulation without a CP, the peak in precipitation occurs at 01 UTC and a prolonged period of rainfall persists through the overnight hours (Figure 3.6c), generally consistent with the Stage IV observations. This is a significant improvement over the relatively narrow rainfall peak in the 30-km simulations (Figure 3.6c). Simulations with a CP also show an improved diurnal cycle compared with the 30-km simulations and the original GCMs. However, the afternoon rainfall peak is shifted only an hour later and excess afternoon rainfall still occurs compared with the observations (Figure 3.6c). This is consistent with previous studies that have found that WRF simulates the diurnal cycle of convection more accurately at higher resolution (Clark et al. 2007) in the absence of a CP (Clark et al. 2009).

The simulation of extreme rainfall events is also improved in 10-km simulations, with a slight overestimation of some extremes in simulations without a CP (Figure 3.7). More heavy rainfall events likely occur in simulations without a CP because greater convective instability can be achieved without convection being triggered by the CP, enabling stronger updraft velocities and greater precipitation rates. In simulations with a CP, rainfall is spread over more events that are generally lighter in nature.

While clear improvements in the diurnal cycle of precipitation and extreme rainfall events occur for simulations with a 10-km horizontal resolution, seasonal means are not as accurate when compared to the 30-km simulations. Precipitation is underestimated throughout much of the South Central region (not shown), with the greatest bias occurring in simulations without a CP. While the underestimation of rainfall in the non-CP simulations may occur because the 10-km resolution is still too coarse to explicitly resolve convection (Clark et al. 2009), accurate seasonal averages and the correct diurnal cycle have been produced from WRF simulations without a CP at this spatial resolution (Harding and Snyder 2012b). Overall, significant improvement in the diurnal cycle occurs in WRF at a horizontal resolution of 10-km compared with 30-km, with the greatest improvements for 10-km simulations without a CP.

3.6 Summary and Discussion

The CMIP5 models analyzed in this study accurately simulate seasonal averages and the interannual variability of rainfall over the Central U.S., but fail to resolve the diurnal cycle of precipitation and extreme rainfall events. Additionally, the models accurately resolve the GPLLJ but fail to capture the dynamic forcing of convective precipitation in the region, as evidenced by excessive afternoon rainfall and a poor relationship between strength of the GPLLJ and precipitation in the CMIP5 models. The inadequate dynamic forcing for convection may contribute to deficiencies in the representation of extreme rainfall events in the CMIP5 models, as previous studies have shown that extreme rainfall events are associated with strong GPLLJ events (Arritt et al. 1997; Monaghan et al. 2010). However, generally coarse model resolution also contributes to deficiencies in extreme rainfall events, likely due to the inability of coarse resolution GCMs to simulate processes related to extreme precipitation over large areas.

Dynamical downscaling using WRF provides significant improvements in numerous aspects of simulated summertime rainfall in the Central U.S. The greatest improvement occurs in the representation of extreme events, where precipitation frequency distributions in WRF closely match observations from NCEP's Stage IV dataset. The forcing for convection is also slightly more realistic in WRF simulations. The 30-km resolution simulations in WRF show slight improvement compared with the CMIP5 models, especially for the diurnal cycle of rainfall and extreme rainfall events. However, greater accuracy is achieved with a 10-km horizontal resolution and no cumulus parameterization.

Accurate projections from dynamical downscaling are ultimately dependent on accurate boundary conditions and significant biases can result from inaccuracies in parent GCMs. Atlantic Warm Pool SSTs have been shown previously to contribute to significant rainfall variability in the Midwest and Great Plains (Bosilovich and Schubert 2002; Wang et al. 2006) and this study also shows that accurate SSTs in this region have a significant impact on Central U.S. precipitation performance. Precise SSTs in the Atlantic Warm Pool have the greatest impact on the accuracy of Central U.S. rainfall in WRF, contributing a statistically significant improvement in performance. Additionally, while precipitation is not explicitly assimilated into WRF, models that accurately simulate rainfall over the Central U.S. are more likely to precisely simulate precipitation when downscaled. This might be related to the fact that GCMs with accurate precipitation tend to better simulate prognostic variables that are related to rainfall and that get assimilated into regional models. Regardless, CMIP5 models with accurate AWP SSTs and Central U.S. precipitation are statistically more likely to simulate rainfall over the Central U.S. with greater precision when downscaled in WRF. Because of the considerable computational cost of dynamical downscaling, downscaling efforts in the Central U.S. region may be refined by knowing how well individual GCMs simulate the boundary conditions required for downscaling. Additionally, future downscaling studies in the region may be guided by the present-day performance of these GCMs.

With extreme rainfall events expected to become more frequent, dynamical downscaling provides a more precise approach to assessing spatial and temporal changes in heavy precipitation episodes than most of the CMIP5 models because spatial resolutions of the CMIP5 models are still generally too coarse to accurately simulate such extremes. Because dynamical downscaling improves simulated extreme rainfall events and seasonal precipitation means, policymakers can have added confidence in such projections of regional precipitation, allowing for more targeted adaptation and mitigation efforts.

3.7 Acknowledgments

Support for this study was provided by the U.S. National Science Foundation under grant no. 1029711. This work was carried out in part using computing resources at the University of Minnesota Supercomputing Institute. We acknowledge the World Climate Research Programme's Working Group on Coupled Modelling, which is responsible for CMIP, and thank the climate modeling groups for producing and making available their model output. For CMIP, the U.S. Department of Energy's Program for Climate Model Diagnosis and Intercomparison provides coordinating support and led development of software infrastructure in partnership with the Global Organization for Earth System Science Portals. The authors thank three anonymous reviewers for their comprehensive and constructive comments on this manuscript.

3.8 Tables

Table 3.1. List of CMIP5 models analyzed in this study.

Number	Model	Institution	Resolution
1	ACCESS1.0	CSIRO-BOM (Australia)	1.875 x 1.25
2	ACCESS1.3	CSIRO-BOM (Australia)	1.875 x 1.25
3	BCC-CSM1.1	BCC (China)	1 x 1.33
4	BNU-ESM	GCESS (China)	2.8 x 2.8
5	CanCM4	CCCMA (Canada)	2.8 x 2.8
6	CCSM4	NCAR (USA)	0.9 x 1.25
7	CESM1-BGC	NSF-DOE-NCAR (USA)	0.9 x 1.25
8	CESM1-CAM5	NSF-DOE-NCAR (USA)	0.9 x 1.25
9	CESM1-FASTCHEM	NSF-DOE-NCAR (USA)	0.9 x 1.25
10	CESM1-WACCM	NSF-DOE-NCAR (USA)	1.9 x 2.5
11	CMCC-CM	CMCC (Italy)	0.75 x 0.75
12	CNRM-CM5	CNRM-CERFACS (France)	1.5 x 1.5
13	CSIRO-Mk3.6.0	CSIRO-QCCCE (Australia)	1.875 x 1.875
14	FGOALS-g2	LASG-CESS (China)	3 x 2.8
15	FGOALS-s2	LASG-IAP (China)	1.67 x 2.8
16	FIO-ESM	FIO (China)	2.8 x 2.8
17	GFDL-CM3	NOAA GFDL (USA)	2 x 2.5
18	GFDL-ESM2G	NOAA GFDL (USA)	2 x 2.5
19	GFDL-ESM2M	NOAA GFDL (USA)	2 x 2.5
20	GISS-E2-H	NASA GISS (USA)	2 x 2.5
21	GISS-E2-R	NASA GISS (USA)	2 x 2.5
22	HadCM3	MOHC (UK)	2.5 x 3.75
23	HadGEM2-AO	MOHC (UK)	1.25 x 1.875
24	HadGEM2-CC	MOHC (UK)	1.25 x 1.875
25	HadGEM2-ES	MOHC (UK)	1.25 x 1.875
26	INM-CM4	INM (Russia)	1.5 x 2.0
27	IPSL-CM5A-LR	IPSL (France)	1.875 x 3.75
28	IPSL-CM5A-MR	IPSL (France)	1.25 x 2.5
29	IPSL-CM5B-LR	IPSL (France)	1.875 x 3.75
30	MIROC-ESM	MIROC (Japan)	2.8x 2.8
31	MIROC-ESM-CHEM	MIROC (Japan)	2.8 x 2.8
32	MIROC4h	MIROC (Japan)	0.56 x 0.56
33	MIROC5	MIROC (Japan)	2.8 x 2.8
34	MPI-ESM-LR	MPI (Germany)	1.875 x 1.875
35	MPI-ESM-P	MPI (Germany)	1.875 x 1.875
36	MPI-ESM-MR	MPI (Germany)	1.875 x 1.875
37	MRI-CGCM3	MRI (Japan)	1.125 x 1.125
38	NorESM1-M	NCC (Norway)	1.875 x 2.5
39	NorESM1-ME	NCC (Norway)	1.875 x 2.5

Table 3.2. Observational precipitation datasets and reanalysis datasets used in this study[a]

Precipitation Observations	Spatial Resolution	Temporal Resolution
Global Precipitation Climatology Project (GPCP) v2.2 (Adler et al. 2003)	2.5° x 2.5°	Monthly
CPC Merged Analysis of Precipitation (CMAP) (Xie and Arkin 1997)	2.5° x 2.5°	Monthly
Climate Research Unit (CRU) Time-Series dataset v3.0 (Mitchell and Jones 2005)	0.5° x 0.5°	Monthly
University of Delaware v2.01 (Matsuura and Willmott 2009)	0.5° x 0.5°	Monthly
Global Precipitation Climatology Centre (GPCC) (Rudolf et al. 2005)	2.5° x 2.5°	Monthly
Stage IV Precipitation (Lin and Mitchell 2005)	4-km	Hourly
Reanalysis	**Spatial Resolution**	**Temporal Resolution**
ERA-Interim (ECMWF) (Dee et al. 2011)	1.5° x 1.5°	Monthly
MERRA (NASA-NCCS) (Rienecker et al. 2011)	1.25° x 1.25°	Monthly
NARR (NCEP) (Mesinger et al. 2006)	32-km	Monthly, 3-hourly
NCEP/NCAR Reanalysis I [*Kalnay et al.*, 1996]	2.5° x 2.5°	Monthly
NCEP/DOE Reanalysis II (Kanamitsu et al. 2002)	2.5° x 2.5°	Monthly

[a] Corresponding spatial and temporal resolutions also listed. NARR 3-hourly data and Stage IV precipitation data were used for the diurnal cycle of precipitation and extreme rainfall events.

Table 3.3. Correlation between ranking for JJA WRF Central U.S. RMSE and JJA boundary condition rankings[b]

Variable	Central R^2	S. Central R^2	N. Central R^2
SST (Atlantic Warm Pool)	0.278	0.269	0.010
Geopotential Height	0.274	0.010	0.018
SST (entire domain)	0.156	0.034	0.004
SST (Atlantic)	0.123	0.052	0.000
Temperature	0.104	0.338	0.079 (-)
SST (Pacific)	0.075	0.161	0.134 (-)
Specific Humidity	0.052	0.003	0.087 (-)
Meridional Wind	0.033	0.007	0.014 (-)
SST (Gulf of Mexico)	0.029	0.116	0.000
Zonal Wind	0.012	0.002	0.110 (-)

[b] SST ranks consider the averages SSTs over the regions mentioned in parentheses, while other variables consider the lateral boundary conditions. A (-) sign indicates a negative correlation coefficient. Statistical significance at the 95% confidence level (assessed with an F-test) is denoted as follows: * ($p < 0.10$) and ** ($p < 0.05$).

Table 3.4. CMIP5 model rankings for AWP SSTs and Central U.S. rainfall[c]

Model	Rank
ACCESS1.0	8
ACCESS1.3	**6**
BCC-CSM1.1	**2**
CMCC-CM	**1**
CNRM-CM5	5
FGOALS-g2	11
GFDL-CM3	**18**
GFDL-ESM2G	15
GFDL-ESM2M	9
HadGEM2-ES	12
IPSL-CM5A-LR	**7**
IPSL-CM5A-MR	17
IPSL-CM5B-LR	**16**
MIROC-ESM	14
MIROC-ESM-CHEM	13
MIROC4h	3
MIROC5	**10**
MRI-CGCM3	**4**
NorESM1-M	**19**

[c] Rankings were determined by averaging the z-scores from Atlantic Warm Pool SSTs and GCM-simulated Central U.S. rainfall and then re-ranking. Z-scores are based on a comparison of GCMs with reanalysis datasets and observations (see section 3.3.5). Bolded models were downscaled. Only models with available data for downscaling were included.

3.9 Figures

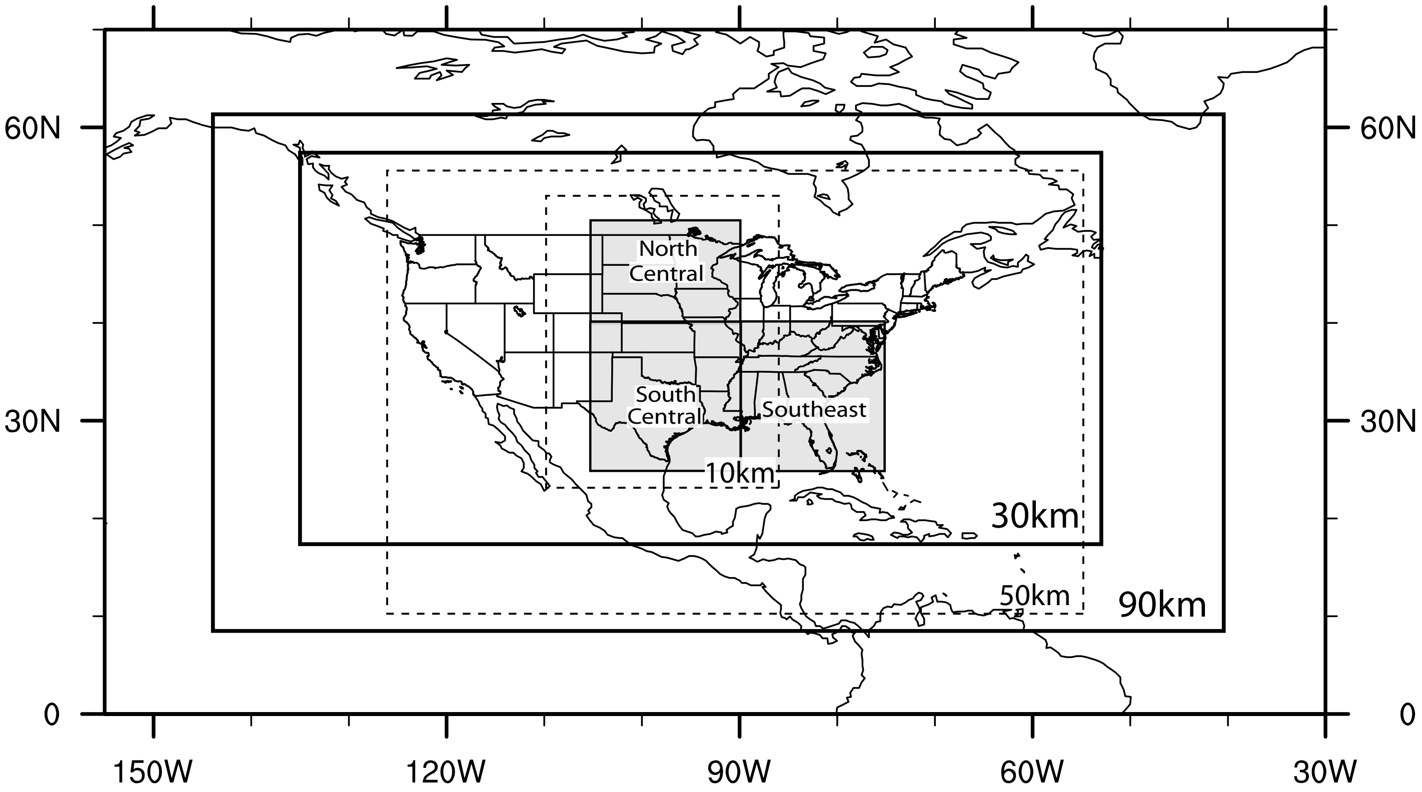

Figure 3.1. WRF 90-km outer domain, 30-km inner domain, 50-km outer domain (dashed), 10-km inner domain (dashed), and regions used to calculate weighted averages and rankings (shaded). North Central and South Central regions were used for averages and rankings and the Southeast region is included for comparison of diurnal precipitation.

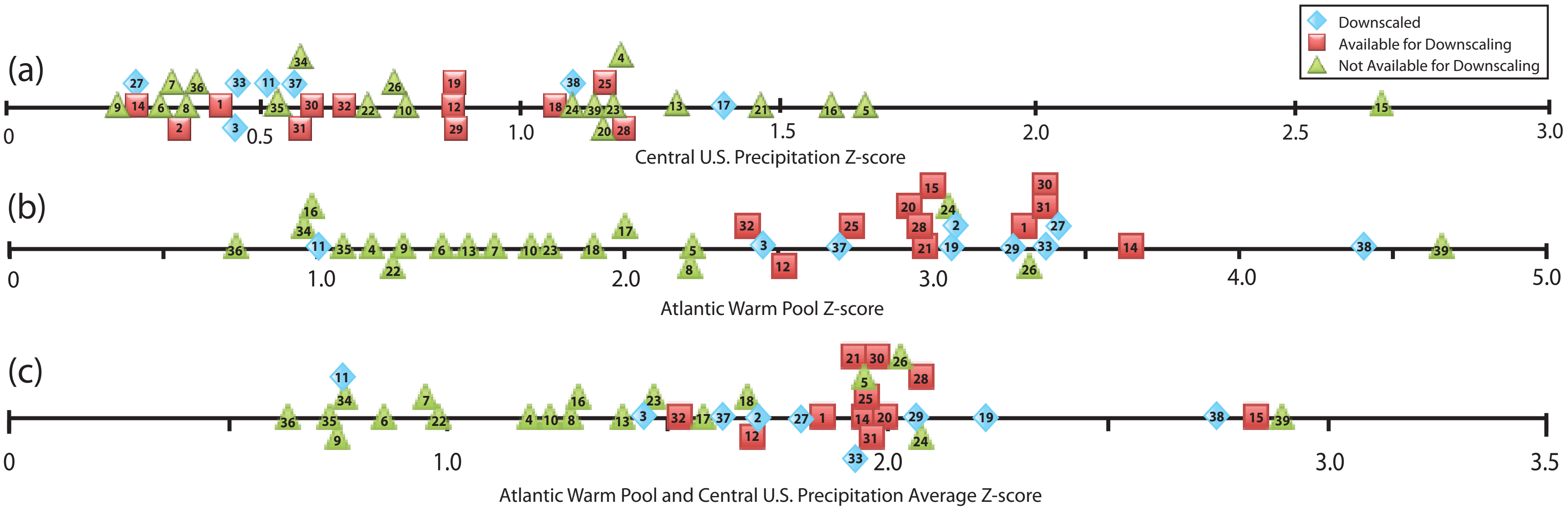

Figure 3.2. Z-scores of (a) Central U.S. precipitation (average z-score for North Central and South Central), (b) AWP SSTs, and (c) the average of (a) and (b). Lower z-scores indicate greater accuracy of CMIP5 models compared with observations, with reduced accuracy for higher z-scores. Blue triangles indicate models that were downscaled, red squares are models that were not downscaled but had 6-hourly forcing data available for downscaling as of December 1, 2012, and green triangles are models that did not have 6-hourly data available for downscaling. Numbers within shapes correspond to the model number in Table 3.1. Calculations of Z-scores are explained in sections 3.3.3 and 3.3.5.

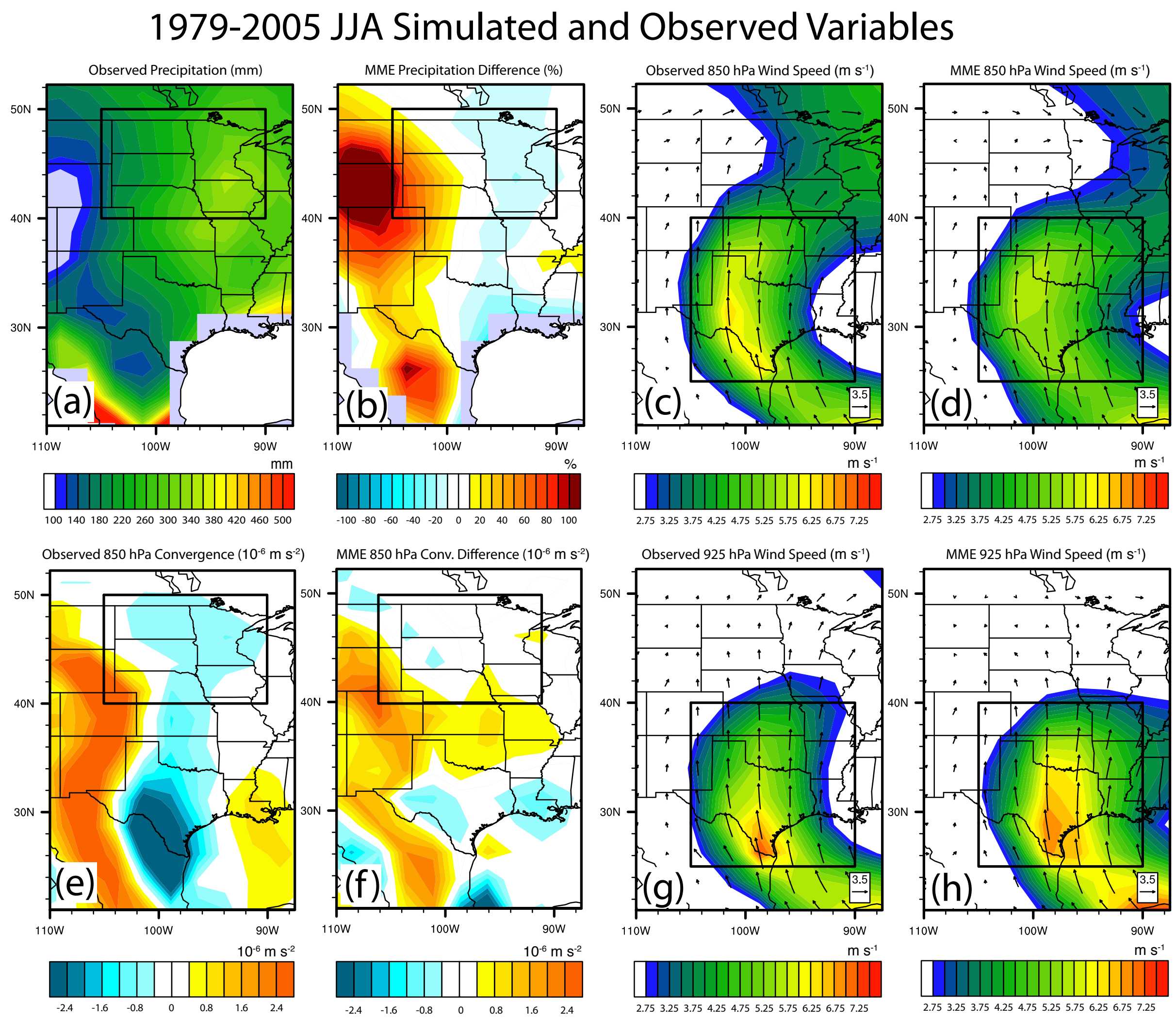

Figure 3.3. 1979-2005 JJA (a-b) precipitation (mm), (c-d) 850 hPa wind speed (m s^{-1}), (e-f) 850 hPa convergence (10^{-6} m s^{-2}), and (g-h) 925 hPa wind speed (m s^{-1}). (a), (c), (e), and (g) show the average of all observational (or reanalysis) datasets for each variable. (b) and (f) show the MME mean minus observations, while (d) and (h) show the MME mean.

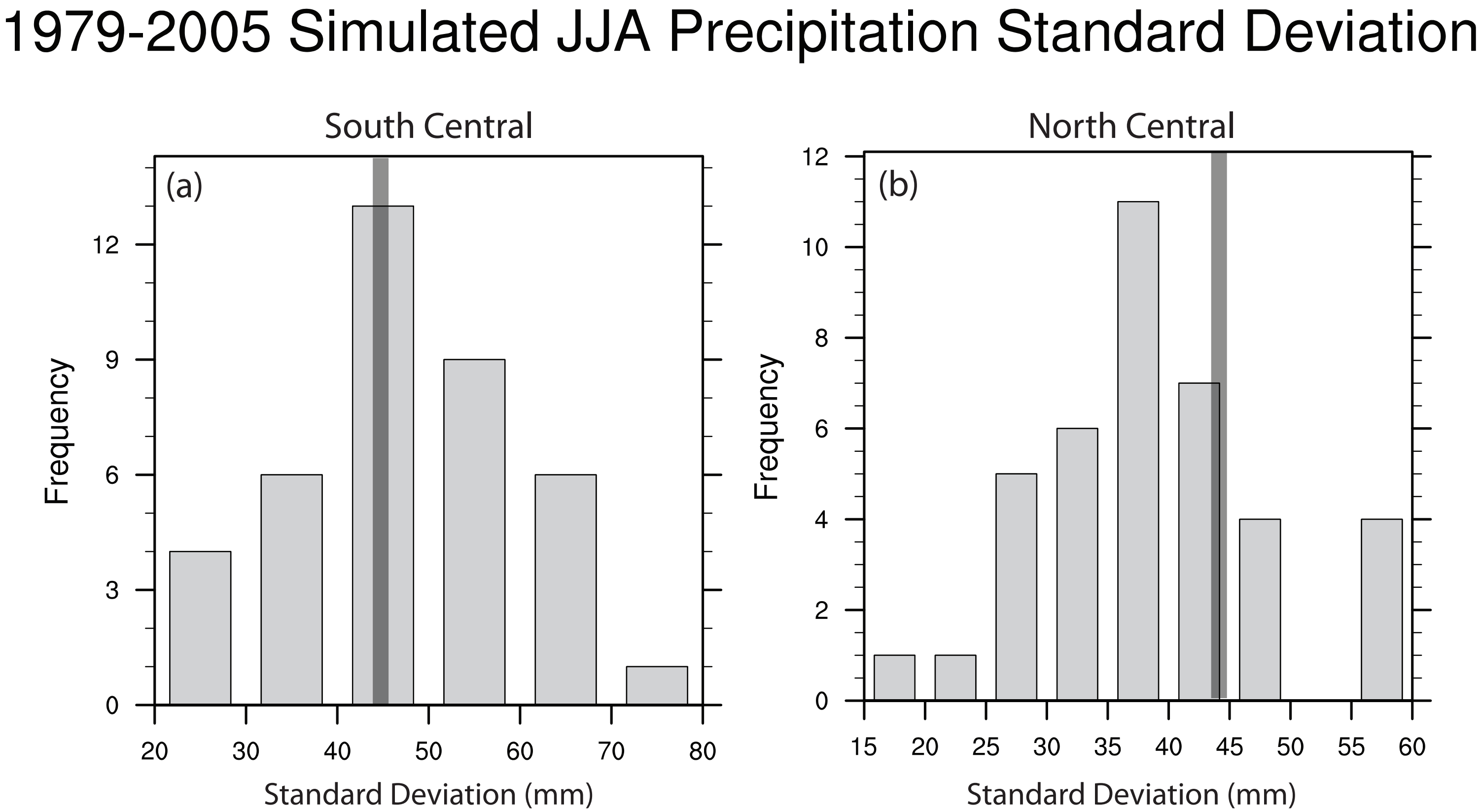

Figure 3.4. Histogram of 1979-2005 JJA interannual precipitation standard deviations from all CMIP5 models over the (a) South Central and (b) North Central regions outlined in Figure 3.1. The gray vertical line indicates the average observed standard deviation from the five precipitation observational datasets with monthly data listed in Table 3.2.

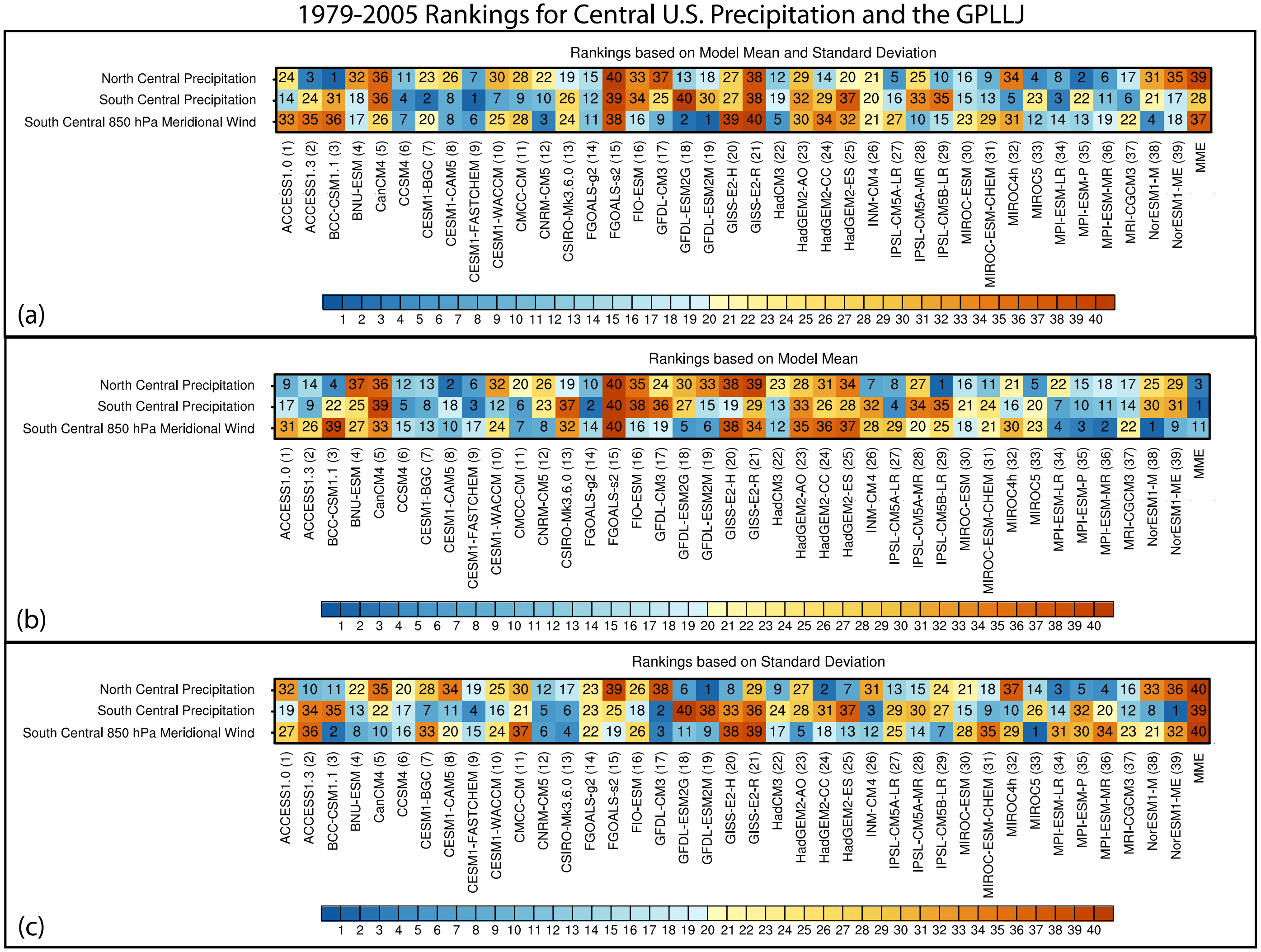

1979-2005 Rankings for Central U.S. Precipitation and the GPLLJ

Rankings based on Model Mean and Standard Deviation

	ACCESS1.0 (1)	ACCESS1.3 (2)	BCC-CSM1.1 (3)	BNU-ESM (4)	CanCM4 (5)	CCSM4 (6)	CESM1-BGC (7)	CESM1-CAM5 (8)	CESM1-FASTCHEM (9)	CESM1-WACCM (10)	CMCC-CM (11)	CNRM-CM5 (12)	CSIRO-Mk3.6.0 (13)	FGOALS-g2 (14)	FGOALS-s2 (15)	FIO-ESM (16)	GFDL-CM3 (17)	GFDL-ESM2G (18)	GFDL-ESM2M (19)	GISS-E2-H (20)	GISS-E2-R (21)	HadCM3 (22)	HadGEM2-AO (23)	HadGEM2-CC (24)	HadGEM2-ES (25)	INM-CM4 (26)	IPSL-CM5A-LR (27)	IPSL-CM5A-MR (28)	IPSL-CM5B-LR (29)	MIROC-ESM (30)	MIROC-ESM-CHEM (31)	MIROC4h (32)	MIROC5 (33)	MPI-ESM-LR (34)	MPI-ESM-P (35)	MPI-ESM-MR (36)	MRI-CGCM3 (37)	NorESM1-M (38)	NorESM1-ME (39)	MME
North Central Precipitation	24	3	1	32	36	11	23	26	7	30	28	22	19	15	40	33	37	13	18	27	38	12	29	14	20	21	5	25	10	16	9	34	4	8	2	6	17	31	35	39
South Central Precipitation	14	24	31	18	36	4	2	8	1	7	9	10	26	12	39	34	25	40	30	27	38	19	32	29	37	20	16	33	35	15	13	5	23	3	22	11	6	21	17	28
South Central 850 hPa Meridional Wind	33	35	36	17	26	7	20	8	6	25	28	3	24	11	38	16	9	2	1	39	40	5	30	34	32	21	27	10	15	23	29	31	12	14	13	19	22	4	18	37

Rankings based on Model Mean

	ACCESS1.0 (1)	ACCESS1.3 (2)	BCC-CSM1.1 (3)	BNU-ESM (4)	CanCM4 (5)	CCSM4 (6)	CESM1-BGC (7)	CESM1-CAM5 (8)	CESM1-FASTCHEM (9)	CESM1-WACCM (10)	CMCC-CM (11)	CNRM-CM5 (12)	CSIRO-Mk3.6.0 (13)	FGOALS-g2 (14)	FGOALS-s2 (15)	FIO-ESM (16)	GFDL-CM3 (17)	GFDL-ESM2G (18)	GFDL-ESM2M (19)	GISS-E2-H (20)	GISS-E2-R (21)	HadCM3 (22)	HadGEM2-AO (23)	HadGEM2-CC (24)	HadGEM2-ES (25)	INM-CM4 (26)	IPSL-CM5A-LR (27)	IPSL-CM5A-MR (28)	IPSL-CM5B-LR (29)	MIROC-ESM (30)	MIROC-ESM-CHEM (31)	MIROC4h (32)	MIROC5 (33)	MPI-ESM-LR (34)	MPI-ESM-P (35)	MPI-ESM-MR (36)	MRI-CGCM3 (37)	NorESM1-M (38)	NorESM1-ME (39)	MME
North Central Precipitation	9	14	4	37	36	12	13	2	6	32	20	26	19	10	40	35	24	30	33	38	39	23	28	31	34	7	8	27	1	16	11	21	5	22	15	18	17	25	29	3
South Central Precipitation	17	9	22	25	39	5	8	18	3	12	6	23	37	2	40	38	36	27	15	19	29	13	33	26	28	32	4	34	35	21	24	16	20	7	10	11	14	30	31	1
South Central 850 hPa Meridional Wind	31	26	39	27	33	15	13	10	17	24	7	8	32	14	40	16	19	5	6	38	34	12	35	36	37	28	29	20	25	18	21	30	23	4	3	2	22	1	9	11

Rankings based on Standard Deviation

	ACCESS1.0 (1)	ACCESS1.3 (2)	BCC-CSM1.1 (3)	BNU-ESM (4)	CanCM4 (5)	CCSM4 (6)	CESM1-BGC (7)	CESM1-CAM5 (8)	CESM1-FASTCHEM (9)	CESM1-WACCM (10)	CMCC-CM (11)	CNRM-CM5 (12)	CSIRO-Mk3.6.0 (13)	FGOALS-g2 (14)	FGOALS-s2 (15)	FIO-ESM (16)	GFDL-CM3 (17)	GFDL-ESM2G (18)	GFDL-ESM2M (19)	GISS-E2-H (20)	GISS-E2-R (21)	HadCM3 (22)	HadGEM2-AO (23)	HadGEM2-CC (24)	HadGEM2-ES (25)	INM-CM4 (26)	IPSL-CM5A-LR (27)	IPSL-CM5A-MR (28)	IPSL-CM5B-LR (29)	MIROC-ESM (30)	MIROC-ESM-CHEM (31)	MIROC4h (32)	MIROC5 (33)	MPI-ESM-LR (34)	MPI-ESM-P (35)	MPI-ESM-MR (36)	MRI-CGCM3 (37)	NorESM1-M (38)	NorESM1-ME (39)	MME
North Central Precipitation	32	10	11	22	35	20	28	34	19	25	30	12	17	23	39	26	38	6	1	8	29	9	27	2	7	31	13	15	24	21	18	37	14	3	5	4	16	33	36	40
South Central Precipitation	19	34	35	13	22	17	7	11	4	16	21	5	6	23	25	18	2	40	38	33	36	24	28	31	37	3	29	30	27	15	9	10	26	14	32	20	12	8	1	39
South Central 850 hPa Meridional Wind	27	36	2	8	10	16	33	20	15	24	37	6	4	22	19	26	3	11	9	38	39	17	5	18	13	12	25	14	7	28	35	29	1	31	30	34	23	21	32	40

Figure 3.5. June-July-August (JJA) rankings for South Central and North Central U.S. precipitation as well as South Central 850 hPa meridional wind speed for the (a) model mean and standard deviation, (b) model mean, and (c) model interannual standard deviation for all CMIP5 models and the MME.

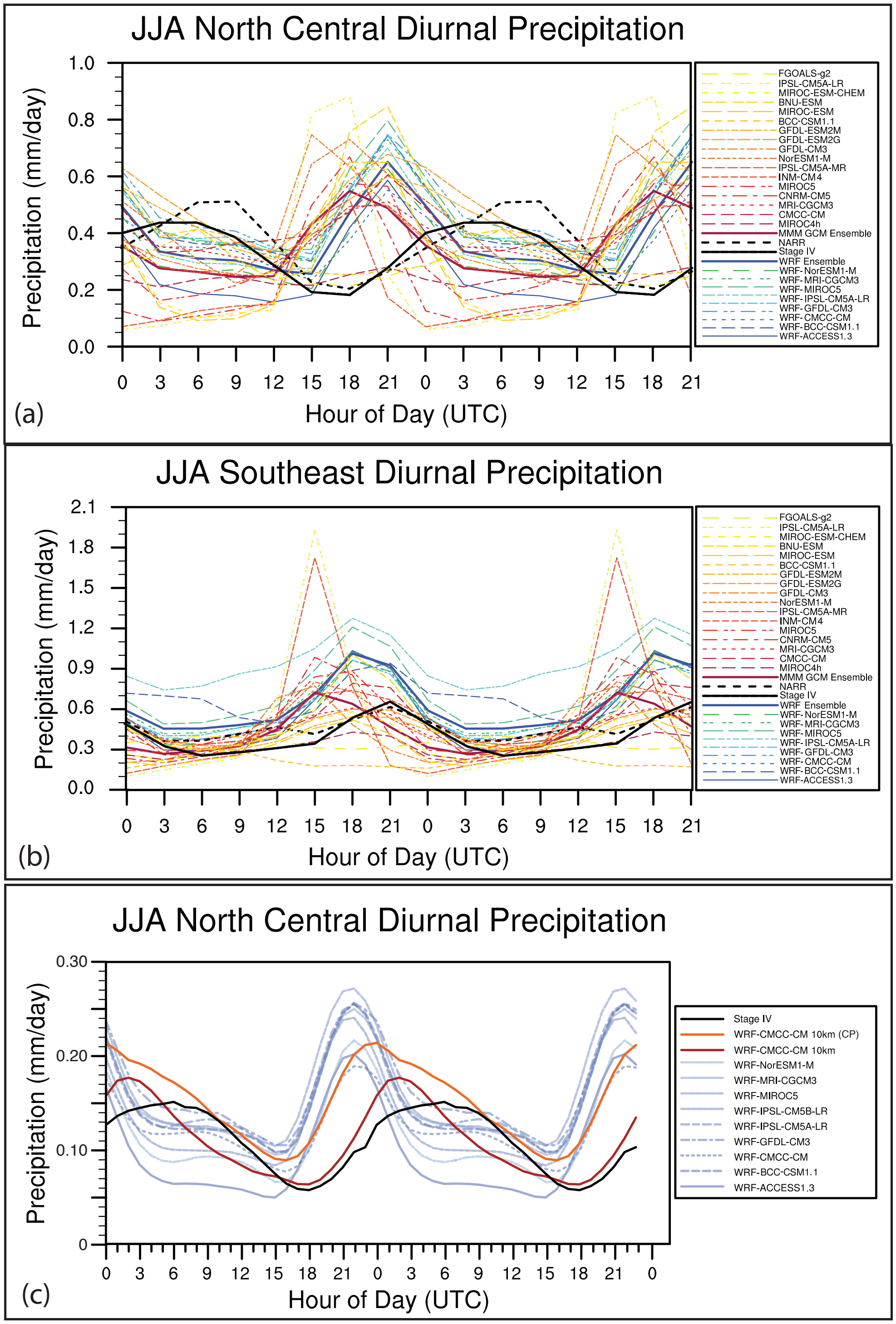

Figure 3.6. Diurnal cycle of JJA precipitation from 1990-1994 in the North American Regional Reanalysis (NARR; black and thick dashed), 2002-2006 (first five available years) of the Stage IV precipitation (black solid), 1990-1994 of all CMIP5 models with available 3-hourly precipitation in the historical period (dashed; yellow to red), 1990-1994 of the ensemble of all available CMIP5 models (red solid), 1990-1994 of all WRF 30-km simulations (dashed; blue to green), and the average of all WRF 30-km simulations (blue solid) for (a) North Central and (b) Southeast regions. (c) JJA diurnal cycle using hourly data for 2002-2006 Stage IV precipitation (solid and black), 1990-1994 30-km WRF simulations (light blue), and 1990-1994 10-km simulations (solid, orange and red).

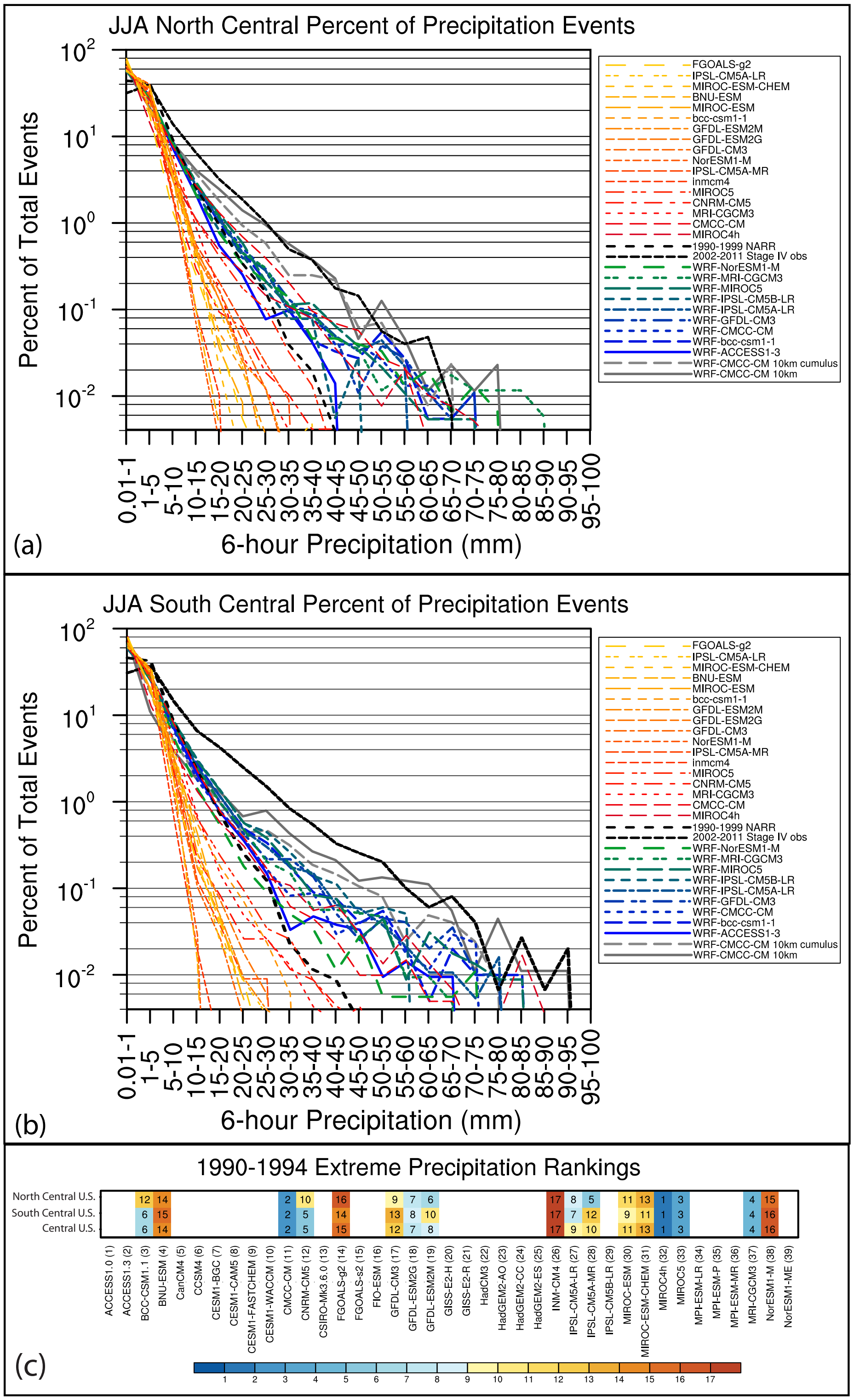

Figure 3.7. Percent of total 6-hourly precipitation events (over 0.01 mm) for each rainfall bin, calculated for the first five years of the Stage IV precipitation dataset (2002-2006; black), NARR (1990-1994; black), 30-km WRF simulations (1990-1994; blue and green), 10-km WRF simulations (gray), and CMIP5 models (1990-1994; yellow to red, sorted by resolution) for the (a) North Central and (b) South Central regions. (c) Extreme precipitation rankings for North Central, South Central, and Central U.S. (average of z-scores

from North Central and South Central). Extreme precipitation rankings determined using methods from section 3.3.3. 6-hourly data was interpolated to a common 2.5° x 2.5° grid for all observational and model datasets.

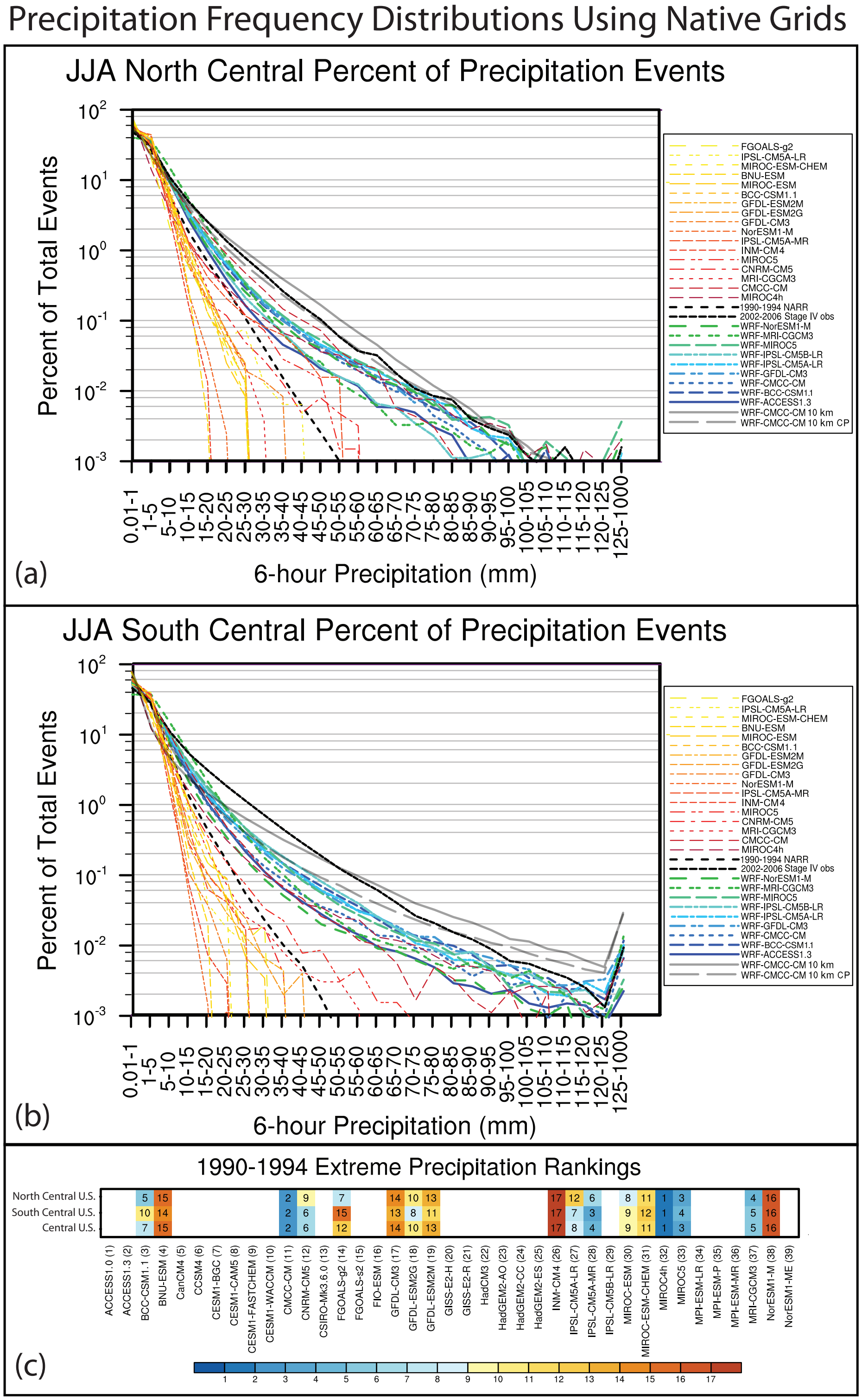

	ACCESS1.0 (1)	ACCESS1.3 (2)	BCC-CSM1.1 (3)	BNU-ESM (4)	CanCM4 (5)	CCSM4 (6)	CESM1-BGC (7)	CESM1-CAM5 (8)	CESM1-FASTCHEM (9)	CESM1-WACCM (10)	CMCC-CM (11)	CNRM-CM5 (12)	CSIRO-Mk3.6.0 (13)	FGOALS-g2 (14)	FGOALS-s2 (15)	FIO-ESM (16)	GFDL-CM3 (17)	GFDL-ESM2G (18)	GFDL-ESM2M (19)	GISS-E2-H (20)
North Central U.S.			5	15							2	9		7			14	10	13	
South Central U.S.			10	14							2	6		15			13	8	11	
Central U.S.			7	15							2	6		12			14	10	13	

	GISS-E2-R (21)	HadCM3 (22)	HadGEM2-AO (23)	HadGEM2-CC (24)	HadGEM2-ES (25)	INM-CM4 (26)	IPSL-CM5A-LR (27)	IPSL-CM5A-MR (28)	IPSL-CM5B-LR (29)	MIROC-ESM (30)	MIROC-ESM-CHEM (31)	MIROC4h (32)	MIROC5 (33)	MPI-ESM-LR (34)	MPI-ESM-P (35)	MPI-ESM-MR (36)	MRI-CGCM3 (37)	NorESM1-M (38)	NorESM1-ME (39)
North Central U.S.						17	12	6		8	11	1	3				4	16	
South Central U.S.						17	7	3		9	12	1	4				5	16	
Central U.S.						17	8	4		9	11	1	3				5	16	

Figure 3.8. Percent of total 6-hourly precipitation events (over 0.01 mm) for each rainfall bin, calculated for the first five years of the Stage IV precipitation dataset (2002-2006; black), NARR (1990-1994; black),

30-km WRF simulations (1990-1994; blue and green), 10-km WRF simulations (gray), and CMIP5 models (1990-1994; yellow to red, sorted by resolution) for the (a) North Central and (b) South Central regions. (c) Extreme precipitation rankings for North Central, South Central, and Central U.S. (average of z-scores from North Central and South Central). Extreme precipitation rankings determined using methods from section 3.3.3. *6-hourly data was kept in its native resolution for this analysis.* This figure is the same as Figure S1 from Harding and Snyder (2013).

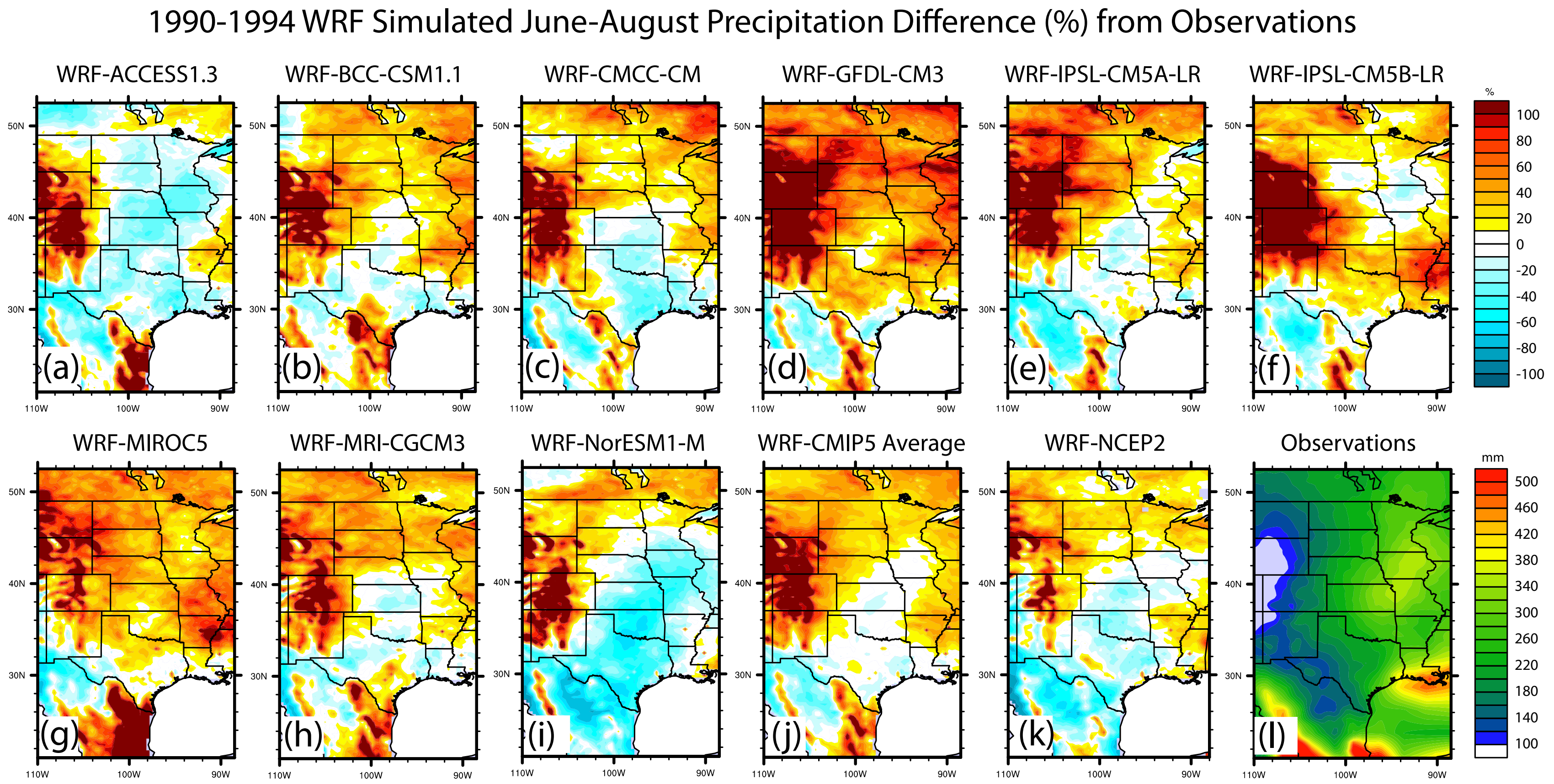

1990-1994 WRF Simulated June-August Precipitation Difference (%) from Observations

WRF-ACCESS1.3

WRF-BCC-CSM1.1

WRF-CMCC-CM

WRF-GFDL-CM3

WRF-IPSL-CM5A-LR

WRF-IPSL-CM5B-LR

WRF-MIROC5

WRF-MRI-CGCM3

WRF-NorESM1-M

WRF-CMIP5 Average

WRF-NCEP2

Observations

Figure 3.9. (a) through (i) 1990-1994 WRF simulated JJA precipitation difference (%) from the 1990-1994 JJA average of five observational datasets listed in Table 3.2 for individual models and (j) the average of all WRF simulations forced by CMIP5 models completed over the 30 km nested domain shown in Figure 1. (k) 1990-1994 as for (a) through (i) but for WRF simulations forced by the NCEP-DOE reanalysis (Kanamitsu et al. 2002). (k) 1990-1994 June-August precipitation from the average of five observational datasets listed in Table 3.2. The color scale for (a) through (k) is adjacent to (f).

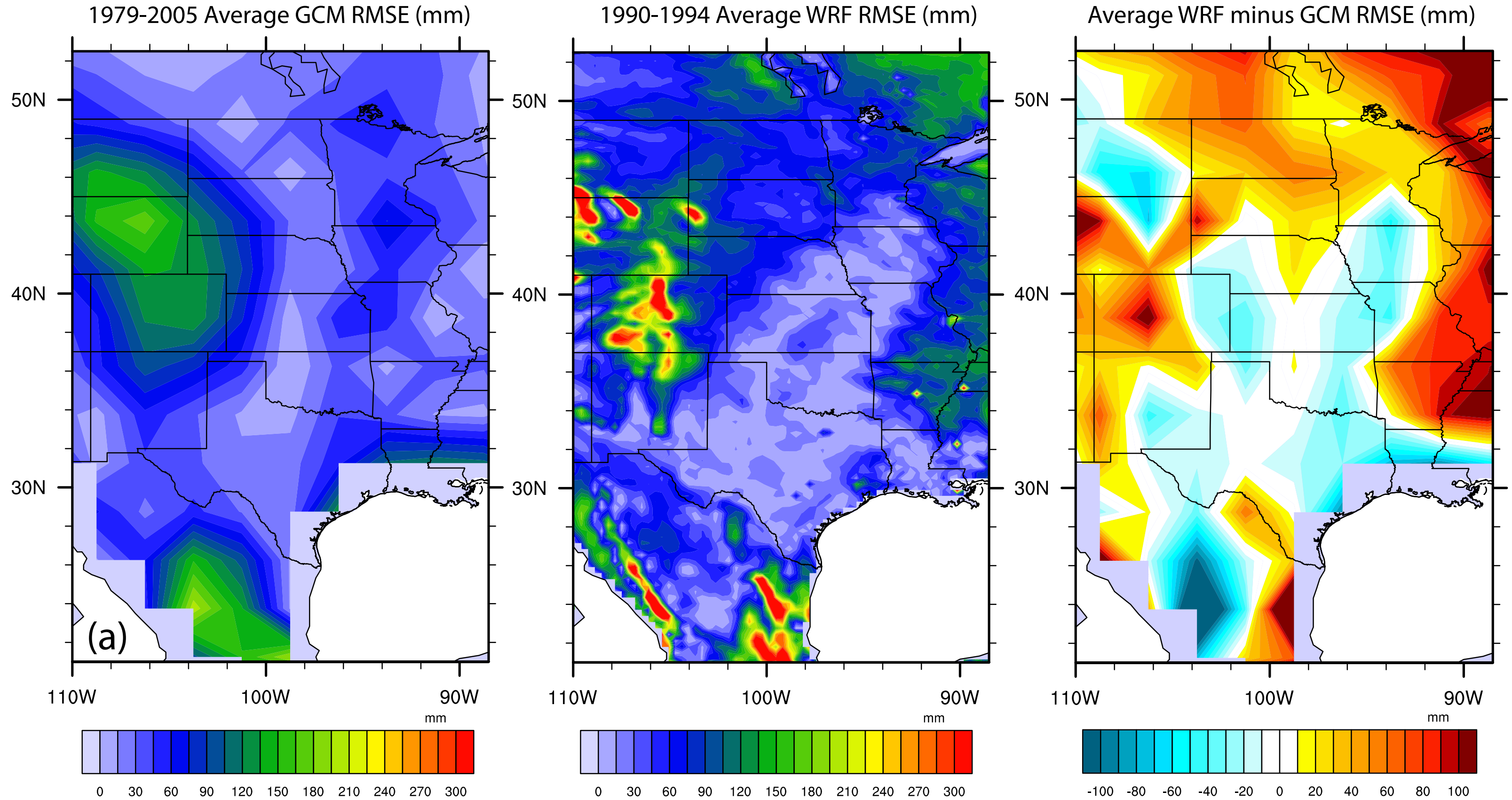

1979-2005 Average GCM RMSE (mm)

1990-1994 Average WRF RMSE (mm)

Average WRF minus GCM RMSE (mm)

Figure 3.10. June-August precipitation RMSE (mm) for (a) 1979-2005 average of all CMIP5 models, (b) 1990-1994 average of all 30-km WRF simulations, (c) 1990-1994 WRF Average RMSE (interpolated to 2.5° x 2.5° grid) minus 1979-2005 average RMSE from CMIP5 models. All RMSEs calculated based on average of five monthly precipitation observation datasets listed in Table 3.2.

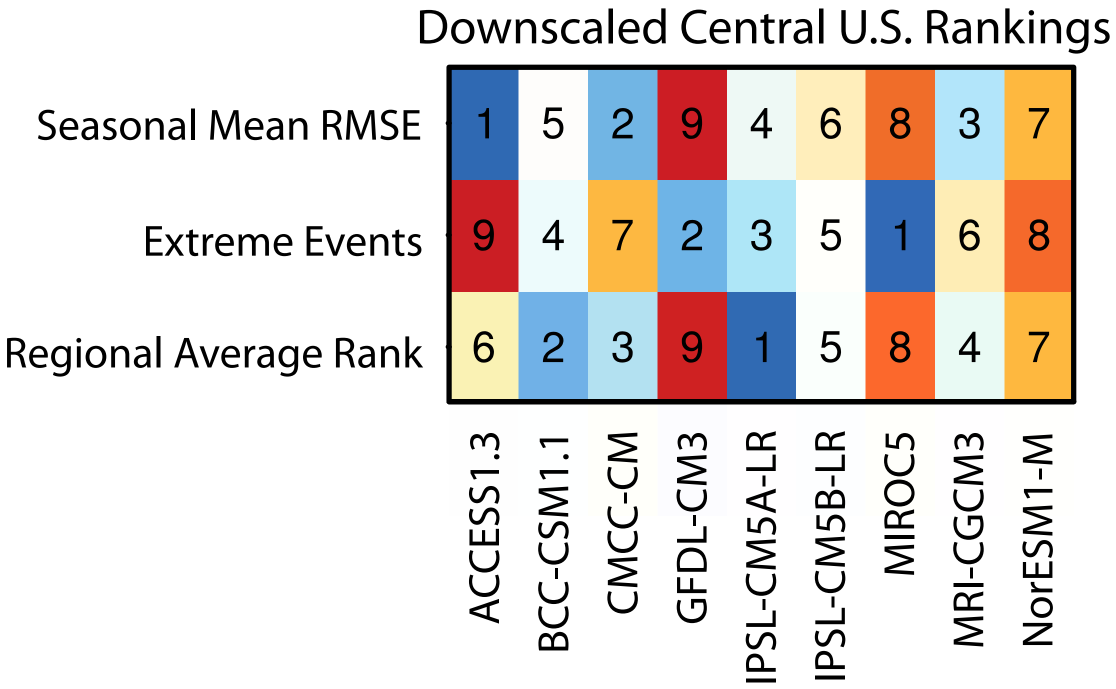
Downscaled Central U.S. Rankings

	ACCESS1.3	BCC-CSM1.1	CMCC-CM	GFDL-CM3	IPSL-CM5A-LR	IPSL-CM5B-LR	MIROC5	MRI-CGCM3	NorESM1-M
Seasonal Mean RMSE	1	5	2	9	4	6	8	3	7
Extreme Events	9	4	7	2	3	5	1	6	8
Regional Average Rank	6	2	3	9	1	5	8	4	7

Figure 3.11. Rankings for 30-km WRF simulations forced with CMIP5 models over model domain shown in Figure 3.1. Rankings are shown for the RMSE, extreme events, and the combination of RMSE and extreme event ranks over the Central U.S. from 1990-1994.

Chapter 4

Examining future changes in the character of Midwestern U.S. warm-season precipitation using dynamical downscaling

Harding, K. J. and P. K. Snyder, *submitted.*

4.1 Overview

Climate change is expected to increase the frequency of hydrological extremes, producing more droughts and heavy rainfall events globally. How warm-season precipitation extremes will change over the Central U.S. is unclear because most coarse spatial resolution GCMs inadequately simulate hydrological extremes resulting from convective precipitation. However, the higher spatial resolution from dynamical downscaling potentially enables improved projections of future changes in extreme rainfall events. In this study, we downscaled two models from the Coupled Model Intercomparison Project – Phase 5 (CMIP5) using the Weather Research and Forecasting (WRF) model for one historical period (1990-1999), two future periods (2040-2049, 2090-2099) in a mid-range (RCP4.5) scenario, and one period (2090-2099) in a high emissions (RCP8.5) scenario. The diurnal cycle, extremes, and averages of precipitation in historical simulations compare well with observations. While the future change in the total amount of precipitation is unclear, model simulations suggest that summer rainfall will be less frequent, but more intense when precipitation does occur. Significant intensification of the heaviest rainfall events occurs in the models, with the greatest changes in the early warm-season (April). Increases in total April-July rainfall and the enhancement of extreme rainfall events in the RCP8.5 2090s is related to a stronger Great Plains Low Level Jet (GPLLJ) during those months. Conversely, late warm-season drying over the North Central U.S. is present in nearly all future simulations, with increased drought in August-September associated with a slight weakening of the GPLLJ. Simulated trends generally increase with stronger greenhouse gas forcing.

4.2 Introduction

Higher temperatures with anthropogenic climate change are generally expected to amplify the hydrologic cycle globally (Bates et al. 2008; Durack et al. 2012; Huntington 2006; O'Gorman and Schneider 2009; Trenberth et al. 2003), driving more frequent extreme rainfall events and changes in the intensity and frequency of precipitation (Allan and Soden 2008; Allen and Ingram 2002; Dai 2013; Held and Soden 2006; O'Gorman and Schneider 2009; Parry et al. 2007; Trenberth 1999; Trenberth et al. 2003), the effects of which have already been observed at regional and global scales (Dai et al. 2004; Groisman et al. 2005; Karl and Knight 1998; Polson et al. 2013; Seneviratne et al. 2012; Villarini et al. 2012). Simulations from global climate models (GCMs) suggest that the observed increase in heavy rainfall events will continue throughout the remainder of the century (Seneviratne et al. 2012; Sillmann et al. 2013; Wuebbles et al. 2014). However, in what manner warm season precipitation might change over the Central U.S. is still fraught with uncertainty, primarily because GCMs have trouble simulating heavy rainfall events, the intensity and frequency of precipitation (Allan and Soden 2008; Dai 2006; Harding et al. 2013; Meehl et al. 2005), and the drivers of summertime convective precipitation (Harding et al. 2013) due to their coarse spatial resolution and convective parameterizations (Duffy et al. 2003; Moncrieff and Liu 2006). Regional stakeholders demand reasonably accurate and quantitative projections of the character of future precipitation to make decisions for adaptation and mitigation purposes (Collins et al. 2012; Knutti et al. 2010), but these limitations make regional predictions of rainfall extremes from GCMs inadequate for practical use. Recently, dynamical downscaling of GCMs has shown promise by accurately simulating heavy rainfall events and the dynamical drivers of extremes over the Central U.S. (Harding et al. 2013). Studies using dynamical downscaling of models from the Coupled Model Intercomparison Project - Phase Three (CMIP3) have shown that extreme rainfall events may increase with climate change in the Central U.S. (Alexander et al. 2013; Bukovsky and Karoly 2011; Mahoney et al. 2013; Vavrus and Behnke 2014; Wehner 2013) and elsewhere (Argueso et al. 2012; Gao et al. 2012; Lee et al. 2014). In this study, we dynamically downscaled two models from the next generation of CMIP models (CMIP5) using the Weather Research and Forecasting (WRF) model to examine how extreme rainfall events and the overall character of Central U.S. warm-season precipitation may be altered with climate change in a mid-range emissions scenario [Representative Concentration Pathway 4.5 (RCP4.5)] and a high emissions scenario (RCP8.5).

A significant percentage of agricultural production in the United States occurs within the Great Plains and Midwestern United States despite the commonality of warm-season precipitation extremes. Midwestern heavy rainfall events occur most frequently in the summer months (Dirmeyer and Kinter 2010; Hitchens et al. 2013; Villarini et al. 2011a; Villarini et al. 2011b) and are closely related to fluctuations in the Great Plains Low Level Jet (GPLLJ), a lower tropospheric southerly wind maximum that is a key feature of the summertime hydroclimate of the Central United States (Arritt et al. 1997;

Cook et al. 2008; Monaghan et al. 2010). Variations in the strength of the GPLLJ are related to pressure differences between the North Atlantic Subtropical High (NASH) and lower heights over the Great Plains and mountain west as well as the decoupling of the surface and boundary layers at night (Markowski and Richardson 2010; Stull 1988). Previous studies have suggested that the observed intensification of the GPLLJ (Barandiaran et al. 2013) is related to a recent westward movement of the NASH with global warming (Li et al. 2011).

Abundant moisture transport within the GPLLJ as well as low-level convergence, cyclonic shear, and moisture convergence to the north of the GPLLJ maximum contribute to the nocturnal development of mesoscale convective systems (MCSs) (Arritt et al. 1997; Bonner 1968; Tuttle and Davis 2006; Weaver and Nigam 2011). The majority of warm-season (April-September) precipitation over the Central U.S. is convective (Changnon 2001), with a significant percentage (>25%) occurring overnight (Higgins et al. 1997) and coinciding with the nocturnal southerly wind maximum of the GPLLJ (Bonner 1968; Means 1954). Up to one-third of all moisture entering the contiguous U.S. is transported by the GPLLJ (Bell and Janowiak 1995; Helfand and Schubert 1995; Higgins et al. 1997) and low-level inflow from the Gulf of Mexico is up to 45% higher than nocturnal means during strong GPLLJ events (> 20 ms^{-1}), a significant reason why heavy precipitation episodes are often associated with strong jet events (Arritt et al. 1997; Cook et al. 2008; Higgins et al. 1997; Monaghan et al. 2010).

Historically, drought and heavy rainfall episodes have contributed to large economic losses throughout the Midwest. Damages in excess of \$77.8 billion and \$30.3 billion occurred during the 1988-89 and 2012 North American droughts, respectively (National Climatic Data Center, available at http://www.ncdc.noaa.gov/billions/). Flash flooding events cause the most weather related fatalities in the U.S. (National Weather Service, available at http://www.nws.noaa.gov/os/hazstats.shtml) and are responsible for considerable economic damage (\$33.8 billion in 1993 and \$16.2 billion in 2008) even though they are less widespread than droughts. Changes in the frequency and intensity of precipitation are likely to cause far greater economic impacts in the region than changes in average precipitation (Trenberth et al. 2003). Because extreme rainfall events may become more prevalent in the future, it is important that we understand how and why they might change so that we can plan and adapt.

Predictions of changes in extreme rainfall events with climate change have typically invoked broad thermodynamic arguments involving the Clausius-Clapeyron equation (Allen and Ingram 2002; Trenberth et al. 2003). While this argument can be used to explain theoretical and global-scale changes in precipitation extremes, such mechanisms will likely be overwhelmed by regional-scale dynamic processes, especially in regions where precipitation is governed by dynamically-derived convective precipitation. Better representation of fine-scale processes will generally result in spatially heterogeneous regional and local changes in rainfall extremes that cannot be predicted by broad thermodynamic arguments or using coarse resolution GCMs. Over the Midwest and Great Plains, changes in extreme rainfall events will likely be influenced by changes in dynamical mechanisms (i.e., GPLLJ) that currently influence convective precipitation in the region. Cook et al. [2008] showed that a strengthening of the GPLLJ in GCM simulations of a high emissions scenario might increase the frequency of extreme rainfall events with climate change. Coarse resolution GCMs tend to inadequately simulate the dynamic forcing of convective precipitation from the GPLLJ (Harding et al. 2013) making future projections of Central U.S. warm-season precipitation from GCMs challenging. Because most CMIP5 GCMs cannot resolve heavy rainfall events, future changes will require use of other tools such as regional dynamical downscaling.

Several recent studies have used dynamical downscaling over the Central U.S. to estimate how extreme rainfall events or the basic characteristics of summer precipitation may be affected by climate change (Alexander et al. 2013; Bukovsky and Karoly 2011; Mahoney et al. 2013; Pryor et al. 2013; Vavrus and Behnke 2014; Wehner 2013). Bukovsky and Karoly (2011) showed that heavy rainfall events over the region are expected to increase at the expense of light events using 30-km WRF downscaled simulations of a GCM. Dynamically downscaled simulations of CMIP3 models from the North American Regional Climate Change Assessment Program (NARCCAP) (Mearns et al. 2012) have been used to examine how different characteristics of summer precipitation in the Central U.S. may be affected by climate change in several studies (Alexander et al. 2013; Mahoney et al. 2013; Pryor et al. 2013; Vavrus and Behnke 2014; Wehner 2013). These studies have either analyzed NARCCAP data that was generated using 50-km simulations (Alexander et al. 2013; Pryor et al. 2013; Vavrus and

Behnke 2014; Wehner 2013) or further downscaled NARCCAP simulations to a resolution suitable for non-parameterized convection over a limited area (Mahoney et al. 2013). While previous studies using dynamical downscaling over the region have all suggested an increase in extreme rainfall events with climate change, they were limited either by the use of convective parameterizations (Bukovsky and Karoly 2011; Vavrus and Behnke 2014; Wehner 2013) or the use of short model simulations over small areas (Mahoney et al. 2013).

In this study, we dynamically downscaled two CMIP5 models for four 10-year timeslices (one historical and three future) using a sufficiently fine spatial resolution (10-km) to adequately simulate summertime precipitation and heavy rainfall events in the Central U.S. without a convective parameterization. We evaluate these changes by examining derived precipitation variables as suggested by the Expert Team on Climate Change Detection Indices (ETCCDI) as outlined by Klein Tank et al. (2009) and Zhang et al. (2011) to enable direct comparison with other studies.

4.3 Methods

4.3.1 WRF Model

For this study the regional WRF model version 3.4 (Skamarock et al. 2008) was used with the coupled Noah Land Surface Model (LSM) (Chen and Dudhia 2001). WRF is a non-hydrostatic mesoscale meteorological model that can be used for research or operational forecasting. The Noah LSM is the coupled land-surface model responsible for exchanging surface fluxes of energy, momentum, and mass with the WRF model and includes four soil layers and one vegetation canopy layer. The 20-category, 30-arc-second resolution MODerate Resolution Imaging Spectroradiometer (MODIS) land use dataset (Friedl et al. 2002) is assimilated into the Noah LSM and WRF.

The atmosphere model uses a terrain-following vertical coordinate system that extends from the surface to 50 hPa. Because convective processes and shallow clouds cannot be fully resolved within coarsely resolved grid cells (Skamarock et al. 2008), the development of precipitation is aided by a convective parameterization (CP) at coarse spatial resolutions (typically greater than 10 km). CPs are designed to resolve sub-grid scale vertical fluxes of mass, momentum, and latent heating when inadequate spatial resolution prevents these processes from being resolved explicitly. The spatial resolution required to resolve convective precipitation varies by application. Deep moist convection can explicitly develop without a CP in 10-km WRF simulations over the Central U.S. during the warm season (Harding and Snyder 2012b), but in some cases CPs are necessary at spatial resolutions between 5-10 km without a strong dynamical forcing for convection (Skamarock et al. 2008).

4.3.2 WRF Simulations

Model simulations were completed for March 15-October 1 for each year in the historical period (using the Historical CMIP5 scenario; 1990-99), two future periods (2040-49, 2090-99) in the mid-range RCP4.5 scenario and one future period (2090-99) in the high emissions RCP8.5 scenario. A nested grid configuration was used with a 50-km resolution outer domain, 10-km resolution inner domain (Figure 4.1), and 34 vertical levels. Soil moisture was initialized from the 1981-2010 average March 15 soil moisture from the National Center for Environmental Prediction – Department of Energy (NCEP-DOE) Reanalysis II (Kanamitsu et al. 2002). The outer domain was run at a time step of 150 seconds, with a 30-second time step in the inner domain. The Morrison 2-moment Microphysics scheme (Morrison et al. 2009), YSU Planetary Boundary Layer (PBL) scheme (Hong et al. 2006), RRTM long wave radiation scheme (Mlawer et al. 1997), Dudhia shortwave radiation scheme (Dudhia 1989), and the MM5 surface-layer scheme (Skamarock et al. 2008) were employed. No cumulus parameterization (CP) was used because 10-km simulations without a CP in Harding et al. (2013) more accurately simulated the diurnal cycle of central U.S. precipitation than simulations with a CP activated. Additionally, a sensitivity simulation representing May-September 2004 driven by the North American Regional Reanalysis (Mesinger et al. 2006) (not shown) simulated the diurnal cycle of precipitation with reasonable accuracy compared with NCEP's Stage IV hourly precipitation dataset (Lin and Mitchell 2005), hereafter referred to as Stage IV.

Accurate average Atlantic Warm Pool (AWP) sea surface temperatures (SSTs) in the CMIP5 models have been previously shown to significantly impact the precision of downscaled Central U.S. summer precipitation in WRF (Harding et al. 2013). WRF simulations were forced by two GCMs from the CMIP5 (CMCC-CM and CNRM-CM5) that accurately resolve the seasonality and structure of the GPLLJ and simulate AWP SSTs and other variables that influence the accuracy of simulated precipitation in WRF (Harding et al. 2013).

In this study, analysis nudging of momentum, temperature, and moisture was incorporated into the WRF simulations above the boundary layer because it can improve the simulation of rainfall in WRF without dampening precipitation extremes (Otte et al. 2012). Because Otte (2008) more accurately simulated meteorological fields with reduced moisture nudging, coefficients were reduced for moisture compared with other variables. Additionally, nudging was reduced in the inner domain because previous studies have shown that model simulations with nested grids achieve greater accuracy when nudging is reduced in the inner domain (Otte et al. 2012; Stauffer and Seaman 1994). To reduce the possibility of dampened precipitation extremes, we further reduced nudging parameters for moisture compared to Otte et al. [2012] in the inner domain because it is significantly smaller (one-third of the size) and nudging is not as critical for smaller domains. In addition, precipitation fields were more realistic in sensitivity simulations of WRF-CMCC-CM and WRF-CNRM-CM5 with analysis nudging than for those without nudging (not shown). While nudging applied throughout the atmospheric column for all variables in all nested domains has the potential to hamper the production of extremes, the fact that nudging was turned off in the boundary layer and was greatly reduced for moisture in the inner model domain reduces this possibility.

4.3.3 Observational Datasets

Performance of the diurnal cycle of precipitation and extreme rainfall events was determined by comparing WRF with the Stage IV precipitation dataset (Lin and Mitchell 2005), which is available hourly at a 4-km spatial resolution from 2002-present. Stage IV compares well with other datasets for the diurnal cycle of precipitation (Lee et al.

2007b) and heavy rainfall events and is commonly used as a benchmark for sub-daily observations (AghaKouchak et al. 2011; Sapiano and Arkin 2009). The use of Stage IV to compare precipitation frequency distributions is more appropriate than NARR as has been done in previous studies (Bukovsky and Karoly 2011), because NARR is unable to simulate the heaviest rain events that are present in Stage IV (Harding et al. 2013). Because Stage IV is not available before 2002, the Climate Research Unit (CRU) (Mitchell and Jones 2005) 0.5° x 0.5° monthly precipitation dataset was used to validate seasonal averages of WRF precipitation. Observed trends in daily rainfall characteristics were calculated using the Climate Prediction Center (CPC) 0.25° x 0.25° daily precipitation dataset, which provides a long-term and high-resolution record of daily precipitation over the contiguous United States. CPC data from 1961-2012 was used to assess trends over five full decades. While regional trends in observed precipitation are influenced by numerous natural (e.g., internal variability, dust, volcanoes, solar forcing) and anthropogenic factors (e.g., aerosols and land use change) besides greenhouse gas increases, we compare the sign of observed trends with simulated changes to enable increased confidence in simulated future changes.

4.3.4 Extreme Indices

The ETCCDI suggests consistent use of particular variables when analyzing trends in extreme precipitation from observations or model data (Klein Tank et al. 2009). In this study, we used several of the recommended variables from ETCCDI to analyze trends in precipitation extremes in WRF simulations and the CPC dataset. Rainy days represent the number of days with at least 1 mm of precipitation, while the precipitation intensity (i.e., simple daily intensity index in Klein Tank et al. (2009)) is the annual warm-season average precipitation on rainy days. Consecutive dry days refers to the average maximum number of consecutive days with less than 1 mm of precipitation in a year, while the maximum one-day precipitation refers to the average annual warm-season maximum in total daily rainfall. Additionally, the classification of 95th percentile rainfall events uses daily rainfall totals (of all days ≥ 1 mm) in the 1990-99 historical period in WRF and the climatological averaging period of 1961-1990 in the CPC dataset. All indices are calculated for each grid cell and regional means consider weighted area averages of all grid cells within a region. Additional information on ETCCDI indices and recommendations is available in Klein Tank et al. (2009). All variables were analyzed for April-September, unless otherwise noted. Statistical testing for differences between extreme indices and other variables in WRF simulations were conducted using a two-tailed, paired *t* test.

4.3.5. Great Plains Low Level Jet Event Classification

The strength of the GPLLJ was determined by averaging the meridional wind speed over the GPLLJ region (28°N-38°N, 102°W-92°W; Figure 4.1), which overlaps the climatological maximum in the GPLLJ and closely matches the GPLLJ region from Cook et al. (2008). GPLLJ events were determined using hourly WRF as well as 3-hourly output from the North American Regional Reanalysis (NARR) (Mesinger et al. 2006). Following jet criteria from Arritt et al. (1997), weak LLJ events occurred when the maximum wind speed in the GPLLJ region was between 12 and 16 knots, 16-20 knots for moderate events, and > 20 knots for strong events. GPLLJ events were only considered for grid cells with a wind direction between 135° and 225°. The 850 hPa wind speed was used to determine GPLLJ events because it is the closest standard level to the observed GPLLJ maximum (Arritt et al. 1997).

4.4 Model Validation

Both climate models reasonably simulate average warm-season (April-September) precipitation when downscaled in WRF compared with the 1981-2010 CRU average (Figure 4.2; Table 4.1). While the strength of the GPLLJ is overestimated by both models (especially in late summer), they capture the general shape and strength of the jet as well as the seasonal cycles of 850 hPa meridional wind speed and GPLLJ events (Figure 4.3). The overestimation of the GPLLJ in WRF-CMCC-CM likely explains the overestimation of North Central U.S. precipitation and the strong dry bias south of the GPLLJ maximum in those simulations (Figure 4.2, Table 4.1). WRF-CNRM-CM5 produces generally small precipitation errors of opposing sign throughout most of the Central U.S., except for the lee side of the Rocky Mountains where an exaggerated rain shadow is present (Figure 4.2). Overall, WRF-CNRM-CM5 more accurately simulates total seasonal precipitation in general compared to WRF-CMCC-CM when considering root mean squared errors (RMSEs), pattern correlations (Santer and Wigley 1990), and weighted area averages (Table 4.1).

While too much afternoon precipitation is present in the North Central region in both models, the general shape of the diurnal cycle is adequately simulated (Figure 4.4a). The rainfall peak is still a few hours earlier than the observations in the North Central region, but WRF captures the prolonged period of nocturnal precipitation associated with the GPLLJ as well as the minimum around 18 UTC in the Stage IV dataset (Figure 4.4a). In addition, simulated convective systems tend to propagate eastward throughout the overnight hours during the GPLLJ maximum as observed (Figure 4.5). This indicates that the configuration of WRF used in this study can simulate the development and eastward progression of mesoscale convective systems that dominate nocturnal summer rainfall over the North Central U.S. (Figure 4.5).

Over the South Central region, the diurnal peak in both WRF simulations matches the observed peak, but the prolonged period of observed nocturnal rainfall is generally absent from WRF simulations (Figure 4.4b). Hovmöller diagrams reveal that both WRF simulations struggle with the eastward propagation of nocturnal convective precipitation in the South Central region during the overnight hours, especially in WRF-CNRM-CM5 (Figure 4.5). This likely occurs because much weaker forcing for convection (e.g., moisture convergence) is present in the South Central (Figure 4.6), which limits convective development in the region without a convective parameterization. While the eastward movement of MCSs appears to be problematic in the South Central region due to the weak convective forcing, the reasonable agreement between the diurnal cycle of precipitation in WRF and the Stage IV observations in the North Central region suggests that WRF can adequately simulate the dynamic forcing for warm-season convective precipitation over the North Central with the model configuration used herein.

WRF simulations generally match the shape of observed precipitation frequency distributions from Stage IV except for a slight but consistent overestimation of 6-hourly events over 25 mm (Figures 4.7a, c). Six-hourly rainfall events of 5-10 mm produce the most seasonal precipitation in WRF and 1-5 mm events produce the most rainfall in Stage IV, with a slow decline in rainfall totals as precipitation events decrease in magnitude (Figure 4.7a, c). The fact that precipitation frequency distributions in this study are comparable to Stage IV rather than NARR, which has been shown to underestimate heavy rainfall events (Harding et al. 2013), suggests that the frequency and intensity of simulated precipitation is an improvement over simulations reported by Bukovsky and Karoly (2011).

In the North Central region, average precipitation intensities are also slightly overestimated, as the 11.16 mm precipitation intensity in WRF-CMCC-CM and 11.45 mm in CNRM-CM5 (Table 4.2) are larger than the 9.21 mm observed in Stage IV. The average April-September 1-day maximum precipitation total over the North Central region is 60.89 mm in WRF-CMCC-CM and 58.05 mm in WRF-CNRM-CM5, greater than the Stage IV average of 49.31 mm. WRF simulations match the number of rainy days in the Stage IV dataset relatively well over the North Central U.S., with an average of 49.33 rainy days in WRF-CMCC-CM and 40.78 days in WRF-CNRM-CM5, compared with 48.34 days in Stage IV.

In the South Central region, WRF precipitation frequency distributions more closely match the Stage IV (Figure 4.7c). WRF simulated maximum 1-day rainfall (60.55 mm and 69.03 mm for WRF-CMCC-CM and WRF-CNRM-CM5, respectively) is in greater agreement with Stage IV (62.24 mm). Both downscaled models simulate slightly less frequent but more intense rainy days in the South Central U.S. Average precipitation intensities of 13.00 mm and 14.48 mm are simulated in WRF-CMCC-CM and WRF-CNRM-CM5 (Table 4.3), compared with 11.99 mm in Stage IV. While an average of 42.03 rainy days occur in the Stage IV dataset in April-September, only 30.04 rainy days are simulated in WRF-CMCC-CM and 34.15 rainy days occur in WRF-CNRM-CM5.

Although simulated precipitation in WRF occurs slightly less often and with marginally greater intensity than the observations, WRF can generally simulate the observed frequency and intensity of warm-season rainfall as well as heavy rainfall events in the Central U.S. While there are inherent biases present in WRF and the assimilated GCMs, simulations of future periods can provide reasonable estimates of how the general character of regional precipitation might be altered by climate change. However, significant issues with the development of nocturnal convective precipitation south of 40°N reduces confidence in results from the South Central region.

4.5 Projections of Central U.S. Precipitation

4.5.1 North Central region

Although there is no clear difference in total seasonal precipitation (Figure 4.8; Table 4.2), significant changes in numerous precipitation metrics are present in WRF simulations of the future. As documented in Bukovsky and Karoly (2011), a general shift towards more frequent heavy rainfall events at the expense of lighter events is prominent in all WRF simulations of future periods, with a greater shift with stronger climate forcing (Figure 4.7a). While a clear trend towards more heavy precipitation episodes is present in the CPC dataset over the last few decades, no reduction in the frequency of light events is observed (Figure 4.7b).

As suggested by the simulated decline in light precipitation events in the precipitation frequency distributions (Figure 4.7a), a consistent decrease in the number of rainy days (days with ≥1 mm precipitation) occurs throughout most of the North Central in all future simulations (Figure 4.9; Table 4.2). Similarly, the annual maximum number of consecutive dry days increases throughout the North Central region in all future periods and models (Figure 4.10; Table 4.2), with the greatest increase in the RCP8.5 2090s ($p < 0.05$) and in the western Great Plains (Figure 4.10). However, large increases in consecutive dry days in WRF-CNRM-CM5 might be a product of the simulated dry bias in the western Great Plains (Figure 4.2c), which can exaggerate drought through reduced precipitation recycling. These results are similar to NARCCAP simulations (Alexander et al. 2013; Wehner 2013) but smaller than values from downscaled simulations reported in Bukovsky and Karoly (2011). The greatest increase in consecutive dry days occurs in the late summer months (Figure 4.11h), coincident with the largest decreases in the number of rainy days (Figure 4.11i) and total precipitation (Figure 4.11f).

While the models simulate a clear decrease in rainy days and an increase in consecutive dry days for April-September, the opposite trend is present in the CPC dataset. For April-September, the observed number of rainy days increases throughout much of the North Central region ($p < 0.05$; Figures 4.12c, h), coincident with a decline in consecutive dry days ($p < 0.05$; Figures 4.12d, i). While WRF and CPC yield differing results for total warm-season changes in rainy days and consecutive dry days, CPC trends exhibit similar seasonality as WRF (Figure 4.11d). The observed number of rainy days (Figure 4.11d) and total precipitation (Figure 4.11a) decrease significantly in September, similar to the late season drying in WRF. These results suggest that the observed late warm-season drying of the North Central U.S. may continue, with a possible acceleration of this trend with greater climate forcing.

Fewer simulated rainy days and a shift towards heavier events in future precipitation frequency distributions are coincident with increases in daily precipitation intensity as found by Bukovsky and Karoly (2011), with the greatest increase in the RCP8.5 2090s ($p < 0.01$; Table 4.2). The average observed daily precipitation intensity over the region has also increased over the last five decades (not shown). This suggests that increases in precipitation intensity could continue if anthropogenic climate change is principally responsible for this change, with a possible future acceleration. The CPC observations and WRF simulations both exhibit a pattern of early warm-season increases and late summer declines in precipitation intensity (not shown), indicating that the greatest increases in rainfall rates might continue to occur in the early warm-season.

Increases in the maximum 1-day rainfall totals and 95th percentile events are the largest in the early warm season (April-June) in all WRF simulations (Figure 4.11g, j) and the CPC dataset (Figure 4.11b, e), consistent with increases in early warm-season total precipitation (Figures 4.11a, 4.11f). On average for both models, an additional 1.1 rainfall events over 20.47 mm (average 95th percentile event in 1990s simulations) occur each year in the RCP8.5 2090s (Figure 4.14). Simulated increases in 1-day rainfall totals are coincident with significant changes in atmospheric moisture, as increases in precipitable water are also larger with stronger warming (Table 4.2). Changes in WRF-CMCC-CM precipitable water and 2-m mixing ratio are similar to the 7% per °C increase as dictated by the Clausius-Clapeyron relationship (Table 4.2). However, increases in maximum 1-day rainfall totals and precipitation intensities are significantly smaller than changes in atmospheric moisture and the 7% per °C increase from the Clausius-Clapeyron relationship (Table 4.2), as expected based on previous work (Bukovsky and Karoly 2011; O'Gorman and Schneider 2009).

4.5.2 South Central region

Precipitation frequency distributions exhibit a significant shift towards more rainfall from heavier events in the South Central region in the observed record (Figure 4.7d) and in all future simulations (Figure 4.7c). While precipitation from light rainfall events (< 25 mm) decreases in future simulations (Figure 4.7c), no decline in rainfall from lighter events is observed (Figure 4.7d). Total warm-season precipitation increases over the South Central region in both models for both RCP4.5 periods, but the change in the RCP8.5 simulations is unclear (Table 4.3; Figure 4.8). No significant seasonality is present in the WRF simulations (Figure 4.11k), but large precipitation increases have occurred in April with significant September drying in the observations (Figure 4.11a).

A generally consistent decline in the number of rainy days occurs in all future simulations, especially in the western Plains (Figure 4.9) where observed decreases in rainy days have occurred. Declines in the number of rainy days in future simulations are coincident with clear increases in precipitation intensity (Table 4.3). Less frequent but more intense simulated future precipitation is consistent with increases in the number of consecutive dry days are simulated throughout the South Central region (Table 4.3), with the greatest increase in the western Great Plains (Figure 4.10). A significant increase in consecutive dry days is observed in September (Figure 4.11c), but no clear seasonal pattern is present in the WRF simulations (Figure 4.11m).

Considering heavy rainfall events, an increase in the annual maximum 1-day rainfall occurs in all WRF simulations (Table 4.3; Figure 4.13) and the CPC dataset (Figure 4.12b), with consistent increases in 95th percentile events as well (Figures 4.12e, 4.14). Much larger increases in observed extreme rain events occur in April than September (Figure 4.11b,e), with similar seasonality for 95th percentile events in WRF (Figure 4.11o). Considering the regional average, an additional 0.59 events (36.2%) over 22.98 mm (average 95th percentile event in the region) occur each year in RCP8.5 2090s simulations, compared to 0.39 events/year (23.0%) in the RCP4.5 2090s and 0.43 events/year (25.9%) in the RCP4.5 2040s (Figure 4.14). More intense 1-day maximum rainfall totals are generally coincident with increased atmospheric moisture in future simulations (Table 4.3). While precipitable water changes in the region generally match the expected change based on Clausius-Clapeyron, the percent change in the 1-day maximum rainfall totals and precipitation intensities are significantly smaller (Table 4.3), suggesting that changes in extreme precipitation over the region may not directly scale with the Clausius-Clapeyron relationship as expected from previous work (O'Gorman and Schneider 2009).

4.5.3 Future changes in the GPLLJ and its effect on warm-season precipitation

Model simulations of future scenarios suggest that heavy precipitation events will become more frequent and intense primarily during the early warm-season, with a tendency towards enhanced drought conditions in late summer. In this section, we examine how these changes may be related to the GPLLJ with a focus on the RCP8.5 2090s, which exhibits the strongest seasonality of GPLLJ changes.

Increases in 850 hPa meridional wind speed within the GPLLJ core primarily occur during April-July in future simulations, especially in the RCP4.5 2090s and RCP8.5 2090s (Figure 4.15). A stronger GPLLJ during April-July in the RCP4.5 2090s and RCP8.5 2090s is associated with higher 850 hPa heights over the southeast U.S. and stronger troughing over the Great Plains (Figure 4.16), which enhances the pressure gradient across the GPLLJ. Conversely, a weaker GPLLJ occurs in most future scenarios during August-September (Figure 4.15), driven by a weaker 850 hPa trough over the Upper Midwest and Great Plains in most future timeslices (Figure 4.16). This is particularly true in WRF-CNRM-CM5 simulations of the RCP4.5 2090s and RCP8.5 2090s that show significant weakening of the GPLLJ during August-September (Figure 4.15) caused by height rises over the North Central U.S. and a weakening of the western edge of the NASH over the Southeast (Figure 4.16).

Future changes in moderate and strong GPLLJ events have the same seasonality as changes in average GPLLJ strength, with the greatest increases in moderate and strong GPLLJ event frequency during April-July and much smaller changes in August-September (Figure 4.17). A stronger GPLLJ during April-July in future simulations enhances moisture convergence over the North Central region (Figure 4.18), especially in the RCP8.5 2090s. Stronger moisture convergence over the North Central U.S. is also coincident with greater moisture divergence south of the enhanced GPLLJ maximum during April-July (Figure 4.18) which drives slight decreases in spring rainfall south of 35°N (Figures 4.19a, f). In the RCP8.5 2090s, stronger moisture convergence over the North Central region is primarily associated with moderate and strong GPLLJ events during April-July, with little to no change during non-GPLLJ events and weak events (Figure 4.20). Similarly, precipitation increases (Figures 4.19, 4.21) and heavier rainfall rates (not shown) over the North Central region in the RCP8.5 2090s occur almost entirely during moderate and strong GPLLJ events. These results suggest that early warm-season increases in total precipitation during RCP8.5 simulations are driven by additional moisture convergence from more frequent moderate and strong GPLLJ events. Because rainfall rates are typically higher during moderate and strong GPLLJ events due to enhanced moisture convergence, additional precipitation and higher rainfall rates during these events in future simulations suggest that the strengthening of the GPLLJ may also increase the frequency and intensity of heavy rain events. This is supported by the fact that an additional 10.6% of maximum 1-day rainfall events in the North Central region are associated with strong GPLLJ events in the RCP8.5 2090s compared with the historical simulations for both models (66.9% in the RCP8.5 2090s, 60.1% in the RCP4.5 2090s, 58.7% in the RCP4.5 2040s, and 56.3% in the 1990s). The large increase in the intensity of heavy rainfall events in future simulations is likely due to an intensification of the GPLLJ, especially during April-July.

Conversely, reductions in total precipitation during August-September in both models over the North Central U.S. (Figure 4.19) are likely related to declines (or smaller changes) in moisture convergence during those months (Figure 4.18). Smaller increases in moisture convergence over the North Central U.S. occur during August-September for all future periods in WRF-CMCC-CM compared with April-July (Figure 4.18a-h), with decreases across most of the North Central region in WRF-CNRM-CM5 simulations during August-September (Figure 4.18i-p). Reduced moisture convergence is associated with a reduction in the number of moderate and strong GPLLJ events (Figure 4.17) and a general weakening of the GPLLJ during those months (Figure 4.15), as a weaker 850 hPa trough over the Great Plains and less ridging over the Southeast U.S. reduces the pressure gradient across the GPLLJ (Figure 4.16). Significant declines in precipitation from moderate and strong GPLLJ events occur in August-September for both models in the RCP8.5 2090s (Figure 4.19), suggesting that the reduced frequency of these moderate and strong GPLLJ events during the late summer may be responsible for reduced rainfall and a tendency towards enhanced drought during those months. On the other hand, decreased August-September moisture divergence south of the weaker GPLLJ maximum (Figure 4.18) is likely related to an increase in late summer precipitation in parts of the South Central U.S. (Figure 4.19).

4.6 Discussion and Conclusions

In this study, we have demonstrated that dynamical downscaling using WRF forced by two GCMs can reasonably replicate the timing, frequency, and intensity of Central U.S. precipitation, thereby enabling reasonable confidence in future projections. While no clear change occurs in total simulated warm-season precipitation amount, changes in the timing, intensity, and frequency of precipitation will ultimately have more profound societal impacts than changes in total warm-season rainfall (Trenberth et al. 2003). Clear and generally consistent changes in the basic character of warm-season precipitation are simulated, with larger changes in scenarios that include stronger anthropogenic forcing. While precipitation frequency distributions are improved compared to Bukovsky and Karoly [2011], the general conclusions involving projections of precipitation are very similar. WRF simulations of future periods indicate that more heavy rainfall events will likely occur at the expense of lighter events, thereby resulting in fewer days with rainfall, additional time between precipitation events, and an increase in the magnitude of the heaviest rainfall episodes. Our results show that the observed intensification of extreme rainfall events in the Central U.S. likely will continue and that this trend may accelerate with greater climate forcing.

Changes in the character of North Central U.S. precipitation have a distinct seasonal cycle in model simulations that is in general agreement with previous studies and observed trends since the mid-20th century. Increased heavy rainfall events occur primarily in the early warm-season (April-July), with a tendency towards enhanced drought in August-September. We demonstrate that the seasonality of changes in extreme precipitation over the North Central U.S. in RCP8.5 2090s is linked to an intensification of the GPLLJ which primarily occurs during the early warm-season, as found by Cook et al. (2008). More frequent moderate and strong GPLLJ events provide additional moisture convergence that increases the production of heavy rainfall events and total precipitation during April-July. A slightly weaker GPLLJ during August-September is related to increases in drought during the RCP8.5 2090s, with significant reductions in soil moisture and latent heating during those months (not shown). It is unclear whether this mechanism may drive a similar seasonality of drought and heavy rainfall events with a smaller increase in radiative forcing, as the external forcing during model simulations of the RCP4.5 scenario may have been too weak to overcome the large internal variability from such short timeslices.

WRF simulations indicate that the semi-arid Great Plains will experience the greatest increase in drought with climate change, with reduced effects elsewhere in the region. However, because the development of Central U.S. drought is dependent on sea surface temperatures in the tropical Pacific and Atlantic Warm Pool as well as soil moisture conditions several months prior (Schubert et al. 2004; Schubert et al. 2008; Seager et al. 2013), additional research is needed to enhance confidence in projections of late-summer drought and its related mechanisms. Additionally, the use of dynamic vegetation in models with longer integrations may allow for more realistic projections of drought in the region by capturing the strong hydrologic coupling on longer timescales (Ford and Quiring 2013; Koster et al. 2004). While the assessment of future drought requires longer time integrations, the simulation of extreme rainfall events is not solely dependent on the inclusion of SSTs and soil moisture several months prior, but also from dynamical drivers such as the GPLLJ.

While many model results presented in this study are robust because of the strength of the anthropogenic forcing in the late century, the simulated ten-year periods are generally too short to overcome multi-decadal climate variability that can significantly impact regional warm-season precipitation, especially for individual grid cells and regional averages during simulations with weaker climate forcing. Because extreme events are inherently rare, longer simulations that include more events may more accurately predict future trends. The use of longer future periods and/or larger ensembles can also reduce the impacts of internal variability on such climate projections (Deser et al. 2014), enabling better insights into the precise changes that are likely to occur in the basic characteristics of Central U.S. precipitation, however this comes at a considerable computational cost.

Observations over the region display changes in precipitation intensity and the occurrence of extreme rainfall events that are typically the same sign as model simulations, suggesting that such changes in the basic character of precipitation in the region will likely continue and may accelerate with stronger climate forcing. However, observed precipitation trends occur due to multiple factors besides anthropogenic climate change that are natural and human-caused (e.g., internal variability, solar forcing, land use change, volcanoes, aerosols, dust, and irrigation), making any comparison between the magnitude of observed trends and simulated future changes inappropriate. In cases where observed trends and simulated future changes are the same sign, the consistency in sign between the observations and model simulations enables greater confidence in future projections. Similarly, changes in future simulations that oppose observed trends may just be model artifacts, as is the case for changes in April-September consecutive dry days.

Although there is low confidence in the outlook for total warm-season precipitation in the Central U.S. by GCMs, our observational and modeling analysis indicates that changes in the overall timing and character of precipitation are likely to occur. Further advances in high resolution regional modeling and the use of large model ensembles (Deser et al. 2014) may allow for even more specific and targeted climate projections than were done here. Regardless, observations show that a trend towards more intense rainfall has occurred since the mid 20th century and WRF simulations here and in previous studies (Bukovsky and Karoly 2011; Wehner 2013) indicate this trend will likely continue. Warm-season precipitation will generally be more intense, occur less often, and have longer periods between events over the Central U.S. in the future due to climate change, with a greater acceleration of this trend the stronger the climate forcing. Model simulations from this study and others (Alexander et al. 2013; Bukovsky and Karoly 2011) also indicate an overall increase in drought, with simulations from this study indicating that the strongest drying will likely be in the late warm-season.

These projected changes in the timing, frequency, and intensity of precipitation would have greater societal impacts than variations in total seasonal precipitation amount alone, significantly affecting agriculture, water availability, and hydrologic infrastructure in the region. Even with no change in total seasonal rainfall, more intense but less frequent rainfall would increase runoff during precipitation events and reduce soil moisture between rainfall episodes. Additional runoff from heavier rainfall could negatively impact hydrologic infrastructure (i.e., storm sewers, culverts, bridges, etc.) while also reducing infiltration into severely depleted groundwater aquifers in the region (e.g., the Ogallala Aquifer). Reduced soil moisture between rainfall events may also reduce agricultural yields and further promote the use of irrigation, which has been linked to the depletion of regional aquifers (Gutentag et al. 1984; McGuire 2013). For these reasons, the projected increased intensity and reduced frequency of future precipitation may impose significant societal and economic costs. However, continued research in this area may provide policymakers and stakeholders better guidance for mitigating the potential problems that may be caused by the changing character of precipitation in the region.

4.7 Acknowledgments

Support for this study was provided by the U.S. National Science Foundation under grant no. 1029711. This work was carried out in part using computing resources at the University of Minnesota Supercomputing Institute. We acknowledge the World Climate Research Programme's Working Group on Coupled Modelling, which is responsible for CMIP, and we thank the climate modeling groups for producing and making available their model output. For CMIP, the U.S. Department of Energy's Program for Climate Model Diagnosis and Intercomparison provides coordinating support and led development of software infrastructure in partnership with the Global Organization for Earth System Science Portals. The WRF model used herein can be acquired from the

WRF home page at http://www2.mmm.ucar.edu/wrf/users/download/get_source.html. The parent climate model data that were downscaled can be obtained from the Earth System Grid Federation at http://pcmdi9.llnl.gov/. All other data and programs used to replicate the results in this study are available upon request from the corresponding author at pksnyder@umn.edu. The authors thank three anonymous reviewers for their comprehensive and thoughtful suggestions on this manuscript.

4.8 Tables

Table 4.1. Comparison of WRF historical simulations and 1981-2010 CPC precipitation for April-September (mm/day)

	Weighted Area Difference			Pattern Correlation			RMSE		
	North Central	South Central	Central	North Central	South Central	Central	North Central	South Central	Central
WRF-CMCC-CM	+0.52 (20.4%)	-0.53 (-19.2%)	0.08 (-3.1%)	0.750	0.852	0.626	0.63	0.59	0.61
WRF-CNRM-CM5	+0.09 (3.6%)	0.12 (4.4%)	0.10 (3.9%)	0.831	0.806	0.820	0.48	0.65	0.55

Table 4.2. Select North Central April-September hydroclimatological variables for historical simulations and the differences between future and historical simulations. Significance values for two-tailed, paired *t* tests are as follows: $^{\&}$ ($p < 0.1$), ^ ($p < 0.05$), * ($p < 0.01$).

	WRF-CMCC-CM				**WRF-CNRM-CM5**			
	1990s	**RCP4.5 2040s**	**RCP4.5 2090s**	**RCP8.5 2090s**	**1990s**	**RCP4.5 2040s**	**RCP4.5 2090s**	**RCP8.5 2090s**
Precipitation (mm)	565.94	+15.17 (2.7%)	+9.39 (-4.9%)	+39.87* (7.0%)	484.53	-30.21 (-6.2%)	-27.47 (-5.7%)	-64.42 (-13.3%)
1-day Max Precipitation (mm)	60.89	+5.17^ (8.5%)	+9.01* (14.8%)	+18.86* (31.0%)	58.05	+1.24 (2.1%)	+3.40$^{\&}$ (5.9%)	+6.06* (10.4%)
Max Consecutive Dry Days	17.71	+0.83* (4.7%)	+2.17^ (12.3%)	+2.04* (11.5%)	25.68	+4.62 (18.0%)	+4.67^ (18.2%)	+6.90^ (26.9%)
Rainy Days (≥ 1 mm)	49.33	-1.26 (2.6%)	-5.93^ (12.0%)	-2.80 (5.7%)	40.78	-5.41* (13.3%)	-6.01* (14.7%)	-7.26* (17.8%)
95th Percentile Events (events/year)	2.34	+0.65 (27.8%)	+0.52* (22.3%)	+1.97* (84.6%)	2.07	+0.10 (4.9%)	+0.24 (11.4%)	+0.21 (10.3%)
Precipitation Intensity (Rainfall on days with ≥ 1 mm) (mm)	11.16	+0.95* (8.5%)	+1.77* (15.8%)	+3.22* (28.8%)	11.45	+0.84* (7.3%)	+1.19* (10.4%)	+1.51* (13.2%)
2-m Temperature (°C)	14.67	+1.71*	+3.11*	+5.36*	16.95	+1.87*	+2.77*	+5.10*
Expected Clausius-Clapeyron Moisture Change (%)	-	+12.0%	+21.8%	+37.5%	-	+13.1%	+19.4%	+35.7%
Column-Integrated Precipitable Water (mm)	20.19	+2.67* (13.2%)	+4.44* (22.0%)	+10.16* (50.3%)	19.19	+1.12$^{\&}$ (5.8%)	+2.46* (12.8%)	+5.33* (+27.8%)
2-m Mixing Ratio (g kg^{-1})	7.38	+0.95 (12.8%)	+1.39* (18.9%)	+2.92* (39.6%)	7.69	+0.27* (3.5%)	+0.66* (8.6%)	1.60* (20.7%)

Table 4.3. Select South Central April-September hydroclimatological variables for historical simulations and the differences between future and historical simulations. Significance values for two-tailed, paired *t* tests are as follows: + ($p < 0.1$), ^ ($p < 0.05$), * ($p < 0.01$)

	WRF-CMCC-CM				**WRF-CNRM-CM5**			
	1990s	**RCP4.5 2040s**	**RCP4.5 2090s**	**RCP8.5 2090s**	**1990s**	**RCP4.5 2040s**	**RCP4.5 2090s**	**RCP8.5 2090s**
Precipitation (mm)	407.86	+60.23 (14.8%)	+20.47 (5.0%)	+2.02 (0.5%)	527.49	+26.43 (5.0%)	+29.90 (5.7%)	-24.90 (-4.7%)
1-day Max Precipitation (mm)	60.55	+9.42^ (15.6%)	+10.27* (17.0%)	+17.45* (28.8%)	69.03	+3.75 (5.4%)	+4.29^ (6.2%)	+8.12^ (11.8%)
Max Consecutive Dry Days	29.30	+0.87 (3.0%)	+2.11 (7.2%)	+4.35* (14.9%)	34.15	+1.85 (5.4%)	+2.23 (6.5%)	+2.52 (7.4%)
Rainy Days (≥ 1 mm)	30.04	+1.35 (4.5%)	-1.54 (-5.1%)	-3.97* (-13.2%)	34.45	-0.39 (-1.1%)	-0.70 (-2.0%)	-2.71 (-7.9%)
95th Percentile Events (events/year)	1.61	+0.54^ (33.2%)	+0.37^{+} (22.8%)	+0.81^ (50.5%)	1.71	+0.32^ (18.6%)	+0.40^ (23.2%)	+0.37 (21.8%)
Precipitation Intensity (Rainfall on days with ≥ 1 mm) (mm)	13.00	+1.80* (13.9%)	+1.51* (11.6%)	+3.30* (25.4%)	14.48	+0.60^{+} (4.1%)	+1.03* (7.1%)	+1.54* (10.6%)
2-m Temperature (°C)	21.45	+1.38*	+2.59*	+6.04*	21.31	+1.52*	+2.37*	+4.35*
Expected Clausius-Clapeyron Moisture Change (%)	-	+9.7%	+18.13%	+42.3%	-	+10.6%	+16.6%	+30.5%
Column-Integrated Precipitable Water (mm)	25.02	+2.96* (11.8%)	+4.77* (19.1%)	+11.41* (45.6%)	22.31	+2.00* (9.0%)	+3.41* (15.3%)	+6.26* (28.0%)
2-m Mixing Ratio (g kg^{-1})	8.84	+0.99* (11.2%)	+1.39* (15.7%)	+2.99* (33.9%)	8.50	+0.72* (8.4%)	+1.04* (12.2%)	+1.78* (21.0%)

4.9 Figures

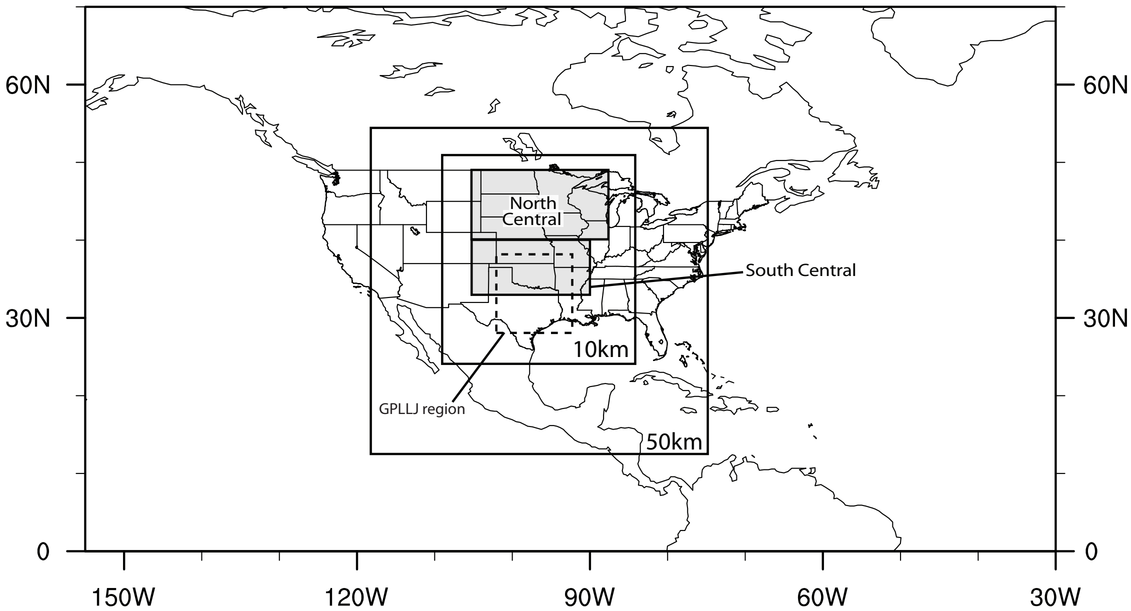

Figure 4.1. WRF 50-km outer domain and 10-km inner domain used in this study. The North Central (40°-49°N, 105°-88°W), South Central (33°-40°N, 105°-90°W), and GPLLJ analysis regions (28°-38°N, 102°-92°W) are also shown. The Central region is the North Central and South Central regions combined.

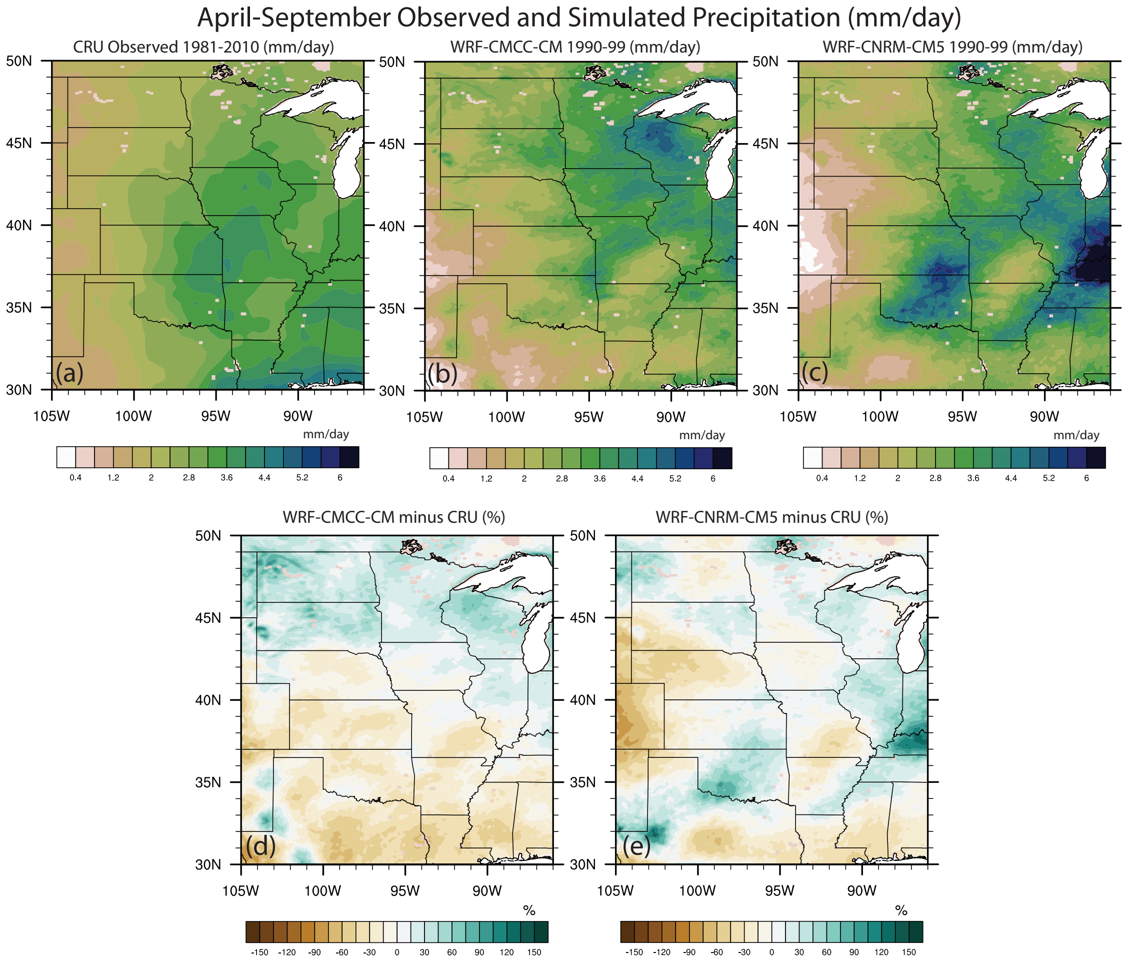

Figure 4.2. (a) Observed 1981-2010 April-September precipitation (mm/day) from the CRU dataset (Mitchell and Jones 2005). (b) as (a) but for 1990-1999 WRF-CMCC-CM simulations. (c) as (b) but for WRF-CNRM-CM5. (d) Percent difference between 1990-99 WRF-CMCC-CM April-September simulated precipitation and 1981-2010 CRU observed precipitation, and (e) as (d) but for 1990-99 WRF-CNRM-CM5.

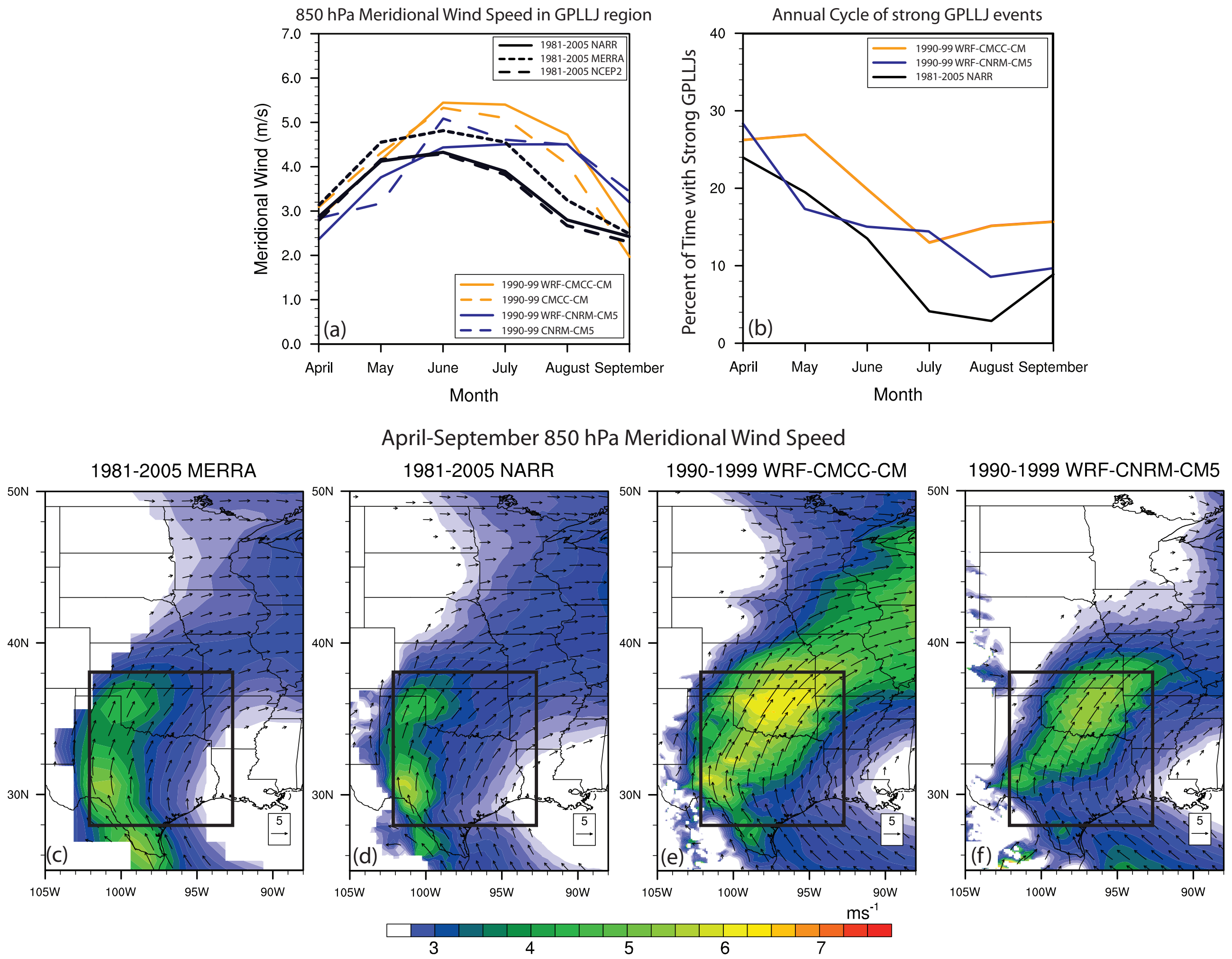

Figure 4.3. (a) 850 hPa meridional wind speed (m/s) averaged over the GPLLJ region by month from 1981-2005 for NARR, MERRA, and NCEP-DOE (NCEP2) as well as for 1990-1999 from CMCC-CM, WRF-CMCC-CM, CNRM-CM5, and WRF-CNRM-CM5 simulations. (b) Percent of times with a strong GPLLJ event within the GPLLJ region by month for NARR (1981-2005) and WRF simulations (1990-99). (c) 1981-2005 April-September average 850 hPa meridional wind speed (m/s) from MERRA, (d) from NARR, (e) from WRF-CMCC-CM for 1990-99, and (f) from WRF-CNRM-CM5 for 1990-99.

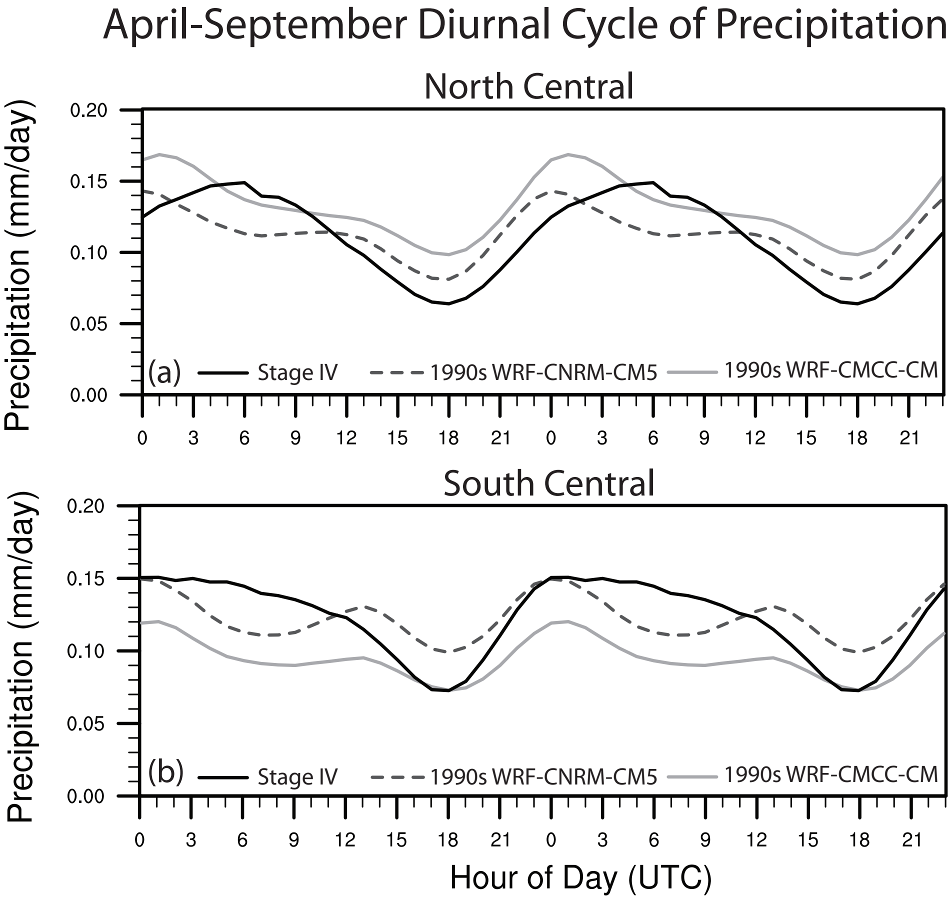

Figure 4.4. April-September diurnal cycle of precipitation for the Stage IV precipitation dataset (2002-2011), WRF-CNRM-CM5 (1990-1999), and WRF-CMCC-CM (1990-1999) over the (a) North Central and (b) South Central regions.

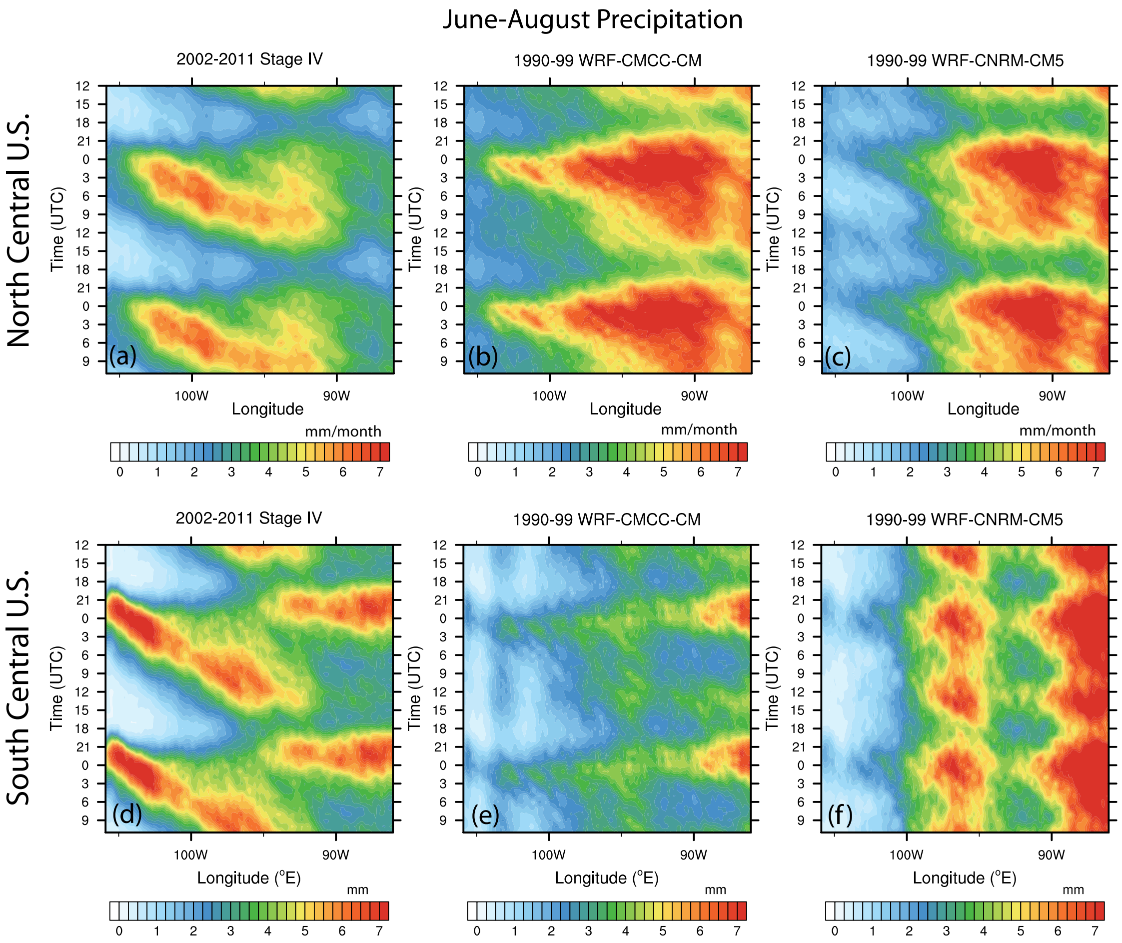

Figure 4.5. Hovmöller Diagrams of June-August North Central U.S. precipitation from (a) Stage IV observations for 2002-2011, (b) WRF-CMCC-CM for 1990-99, and (c) WRF-CNRM-CM5 for 1990-99. (d) through (f) as (a) through (c) but for the South Central region.

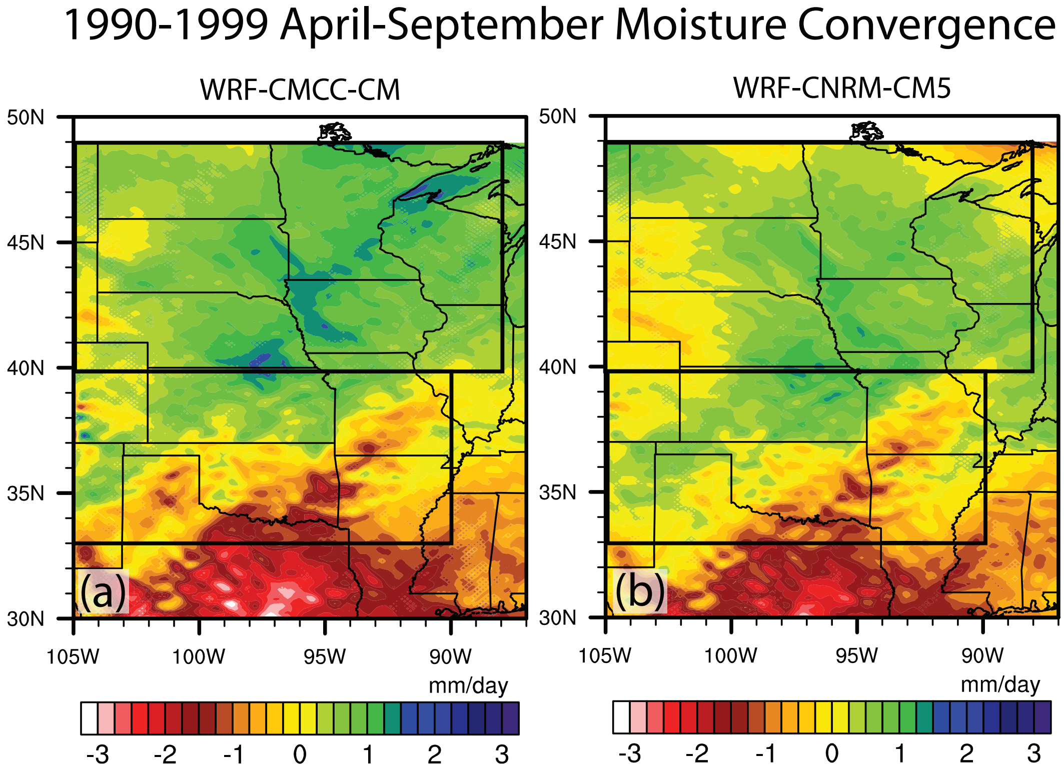

Figure 4.6. 1990-1999 April-September column-integrated moisture convergence (mm/day) from (a) WRF-CMCC-CM and (b) WRF-CNRM-CM5 simulations.

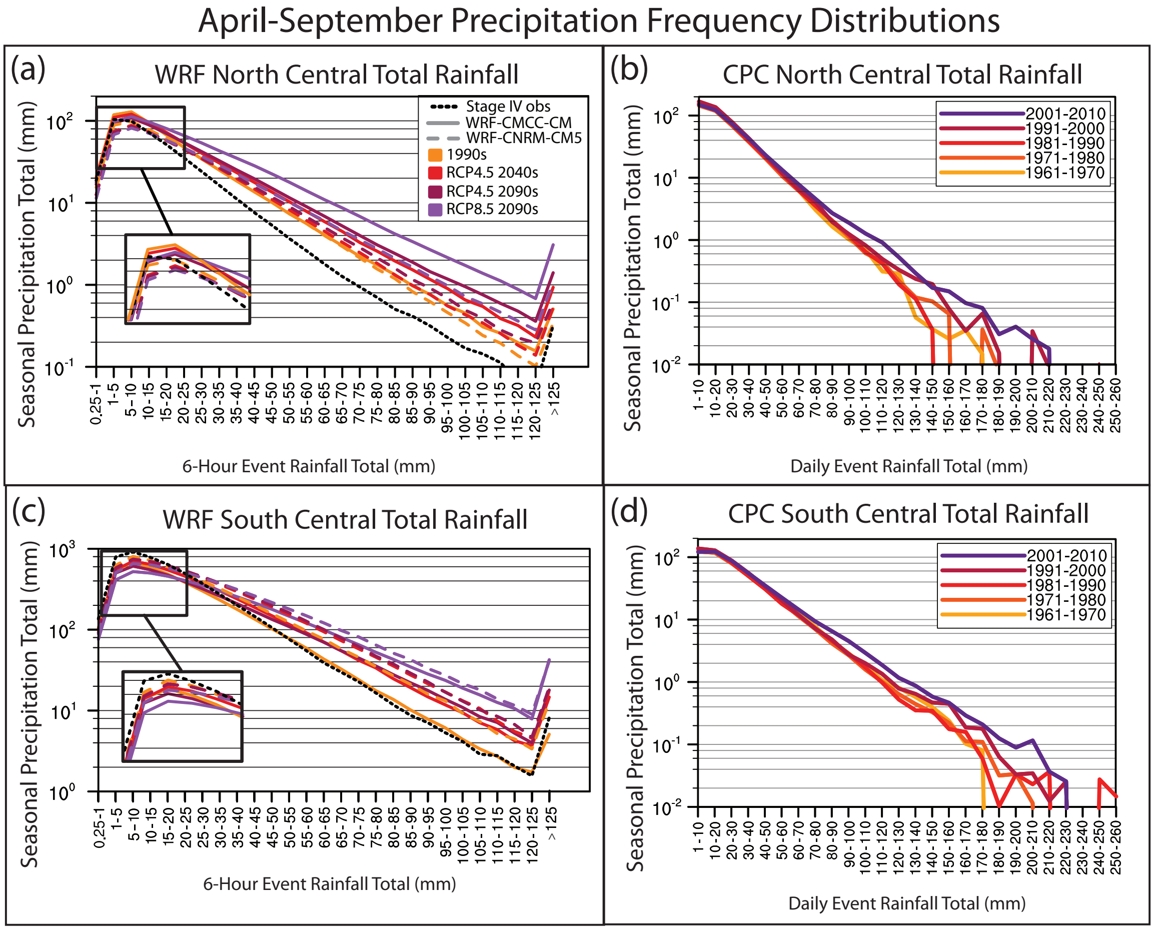

Figure 4.7. (a) Total seasonal North Central April-September precipitation from different 6-hourly rainfall event totals (over 0.25 mm), calculated from the first ten years of the Stage IV precipitation dataset (Lin and Mitchell 2005) (2002-2011; black dashed) and WRF simulations. (b) Total seasonal North Central precipitation from different daily precipitation events (over 1 mm) from the CPC precipitation dataset (Higgins et al. 2000) for five different 10-year periods. (c) and (d) as (a) and (b) but for the South Central region.

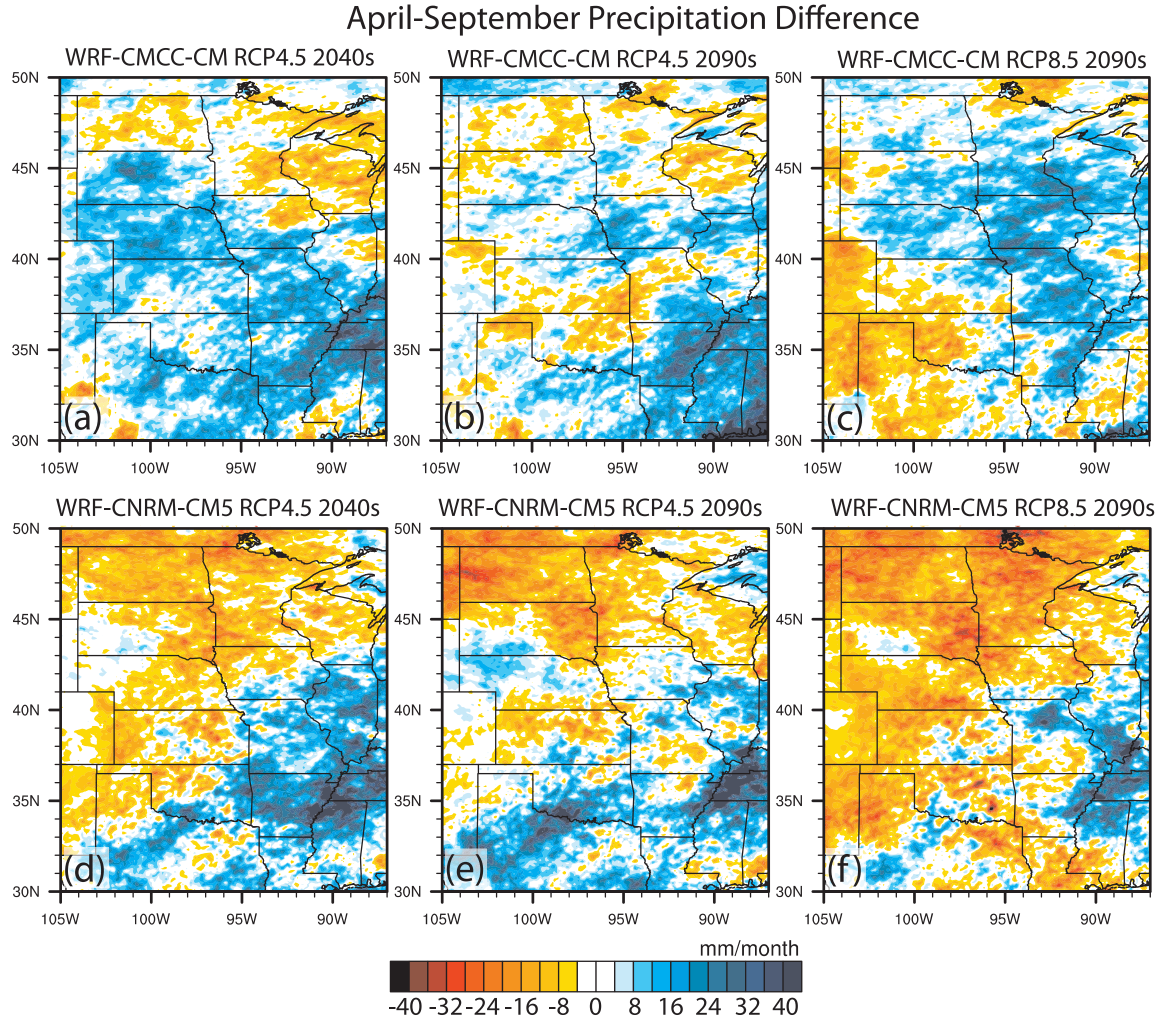

Figure 4.8. (a) RCP4.5 2040-49 WRF-CMCC-CM April-September precipitation difference (mm/month) from 1990-99, (b) as (a) but for RCP4.5 2090-99, (c) as (a) but for RCP8.5 2090-99. (d) through (f) as (a) through (c) but for WRF-CNRM-CM5.

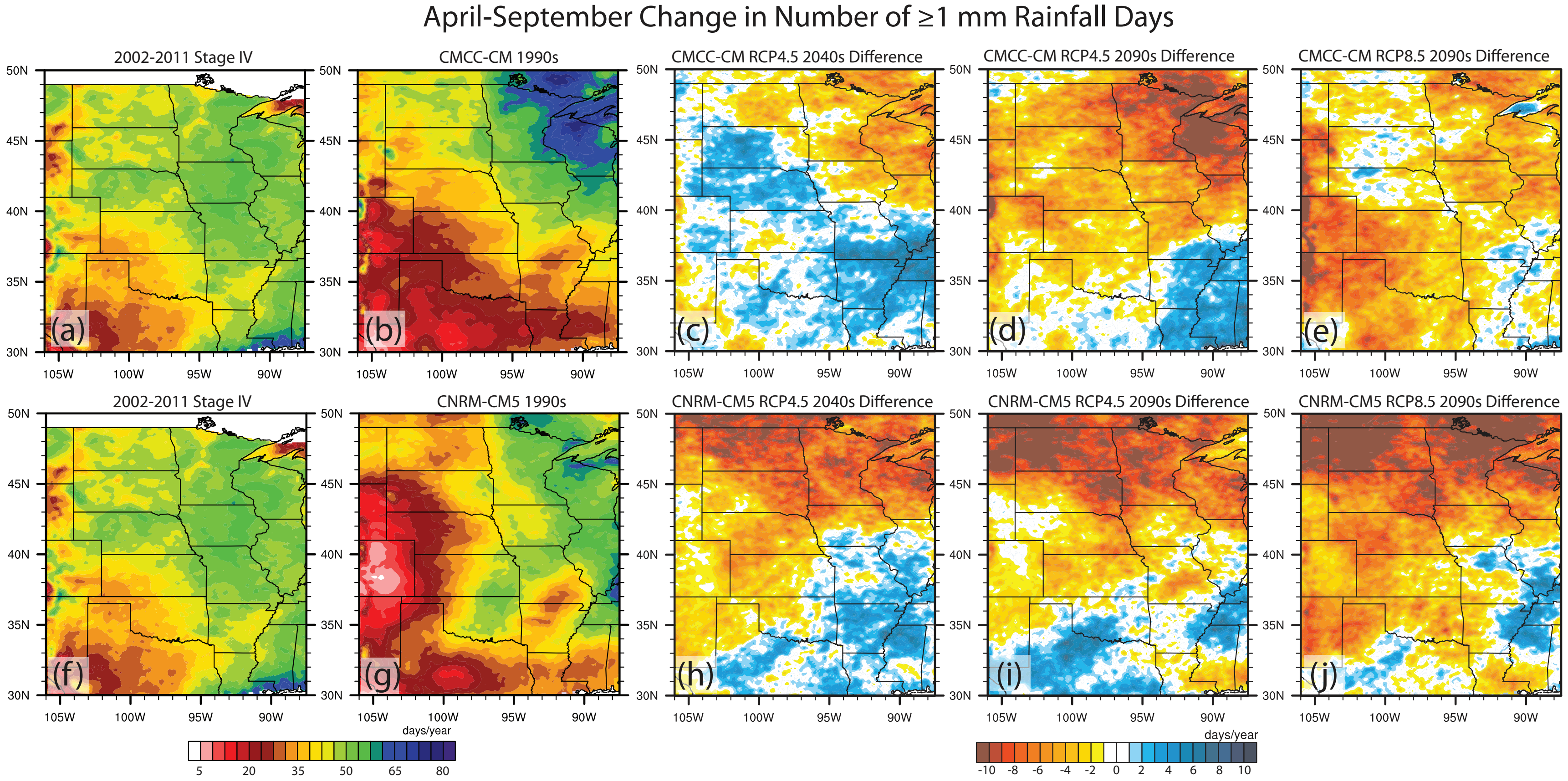

Figure 4.9. Average April-September number of rainy days (≥ 1 mm precipitation) in (a) 2002-2011 Stage IV precipitation dataset, (b) 1990-1999 WRF-CMCC-CM simulations. (c) RCP4.5 2040-49 WRF-CMCC-CM minus 1990-99 WRF-CMCC-CM, (d) as (c) but for RCP4.5 2090-99 WRF-CMCC-CM, (e) as (c) but for RCP8.5 2090-99 WRF-CMCC-CM. (g) through (j) as (b) through (e) but for WRF-CNRM-CM5.

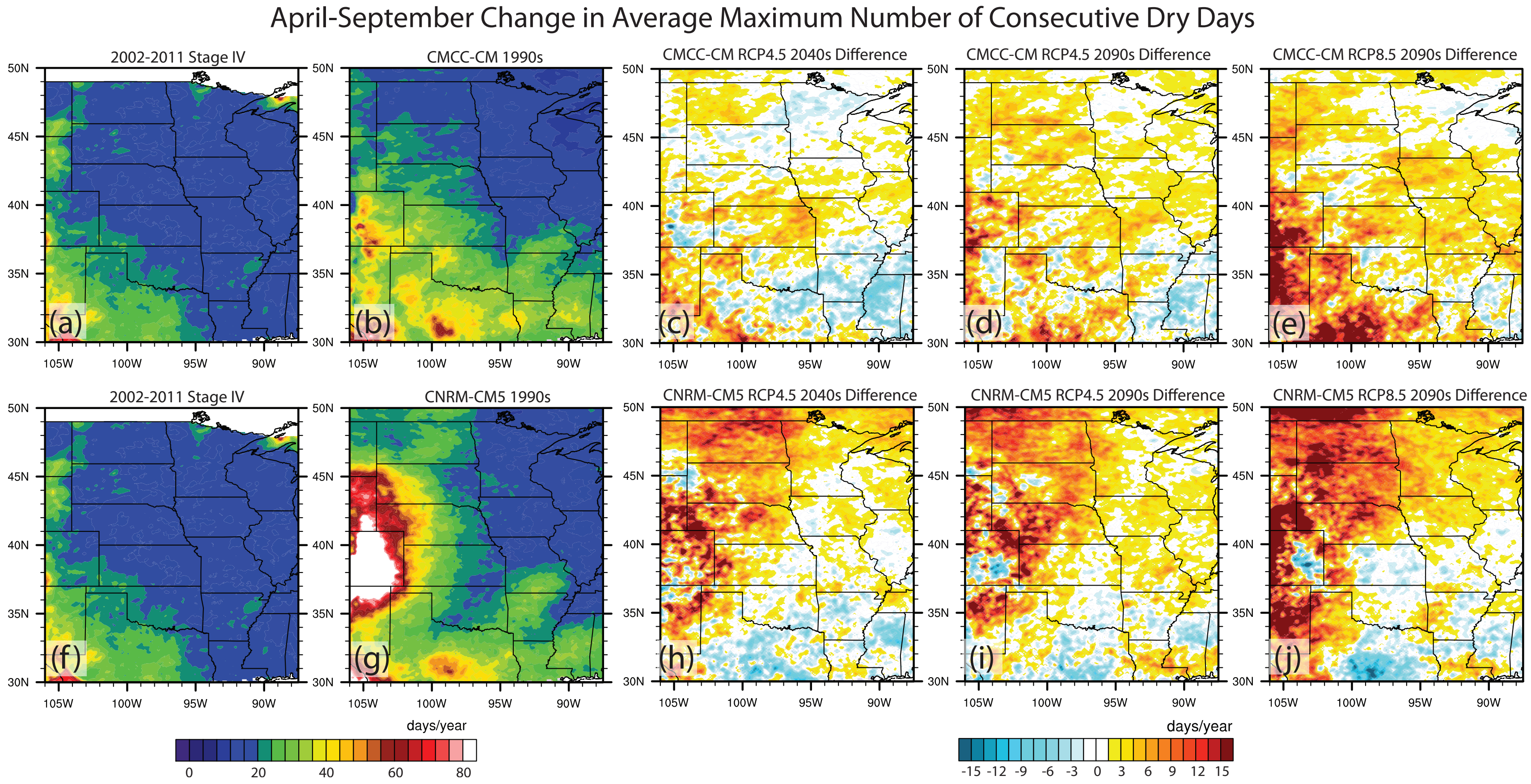

Figure 4.10. Same as Figure 4.9 but for the average maximum number of consecutive dry days (precipitation < 1 mm).

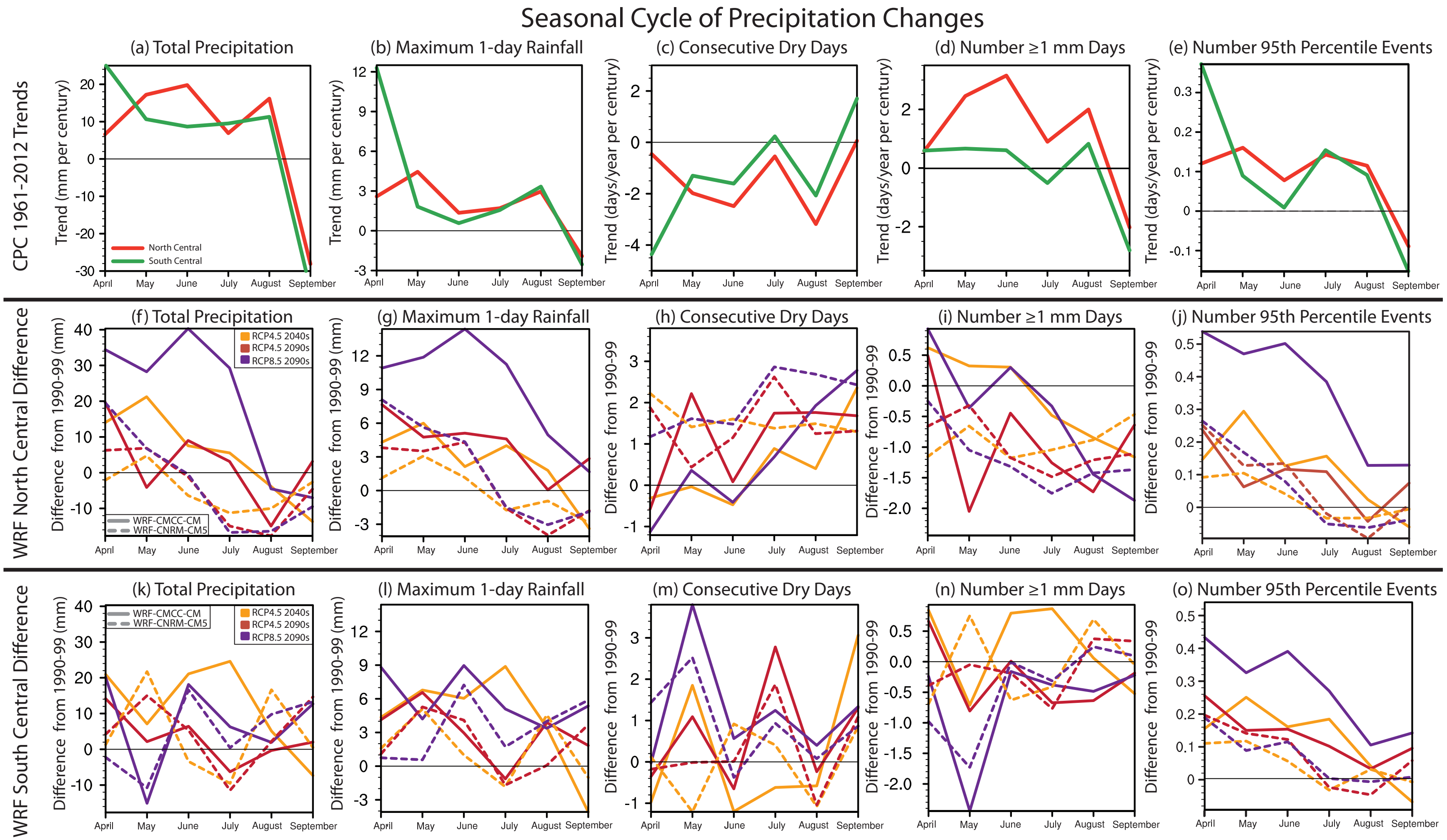

Figure 4.11: April-September seasonal cycle of 1961-2012 CPC trends (per century) of (a) total precipitation, (b) maximum 1-day rainfall, (c) number of consecutive dry days, (d) number of ≥1 mm days, and (e) number of 95th percentile events for North and South Central regions. (f) through (j) as (a) through (e) but for WRF-simulated North Central differences compared with 1990-99. (k) through (o) as (f) through (j) but for South Central region.

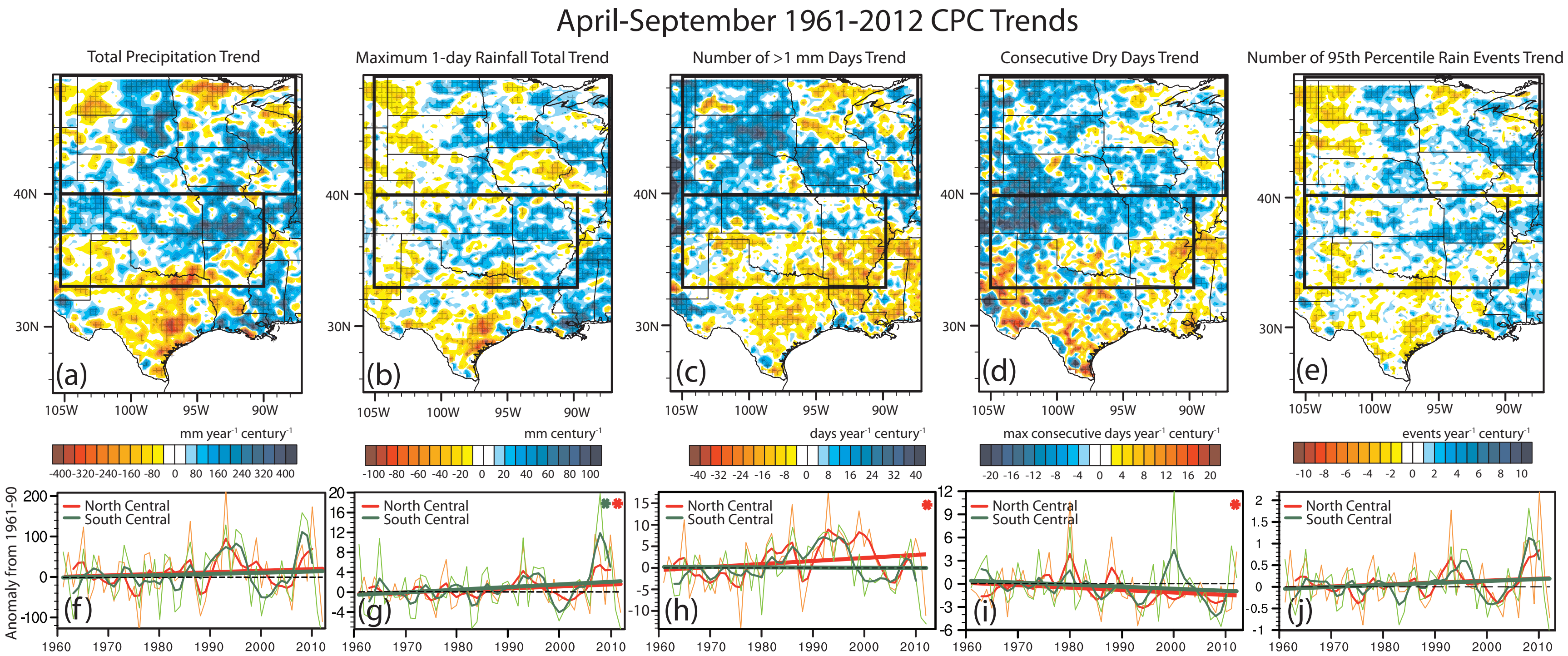

Figure 4.12. (a) 1961-2012 trend in April-September precipitation (mm/decade) from CPC dataset. (b) as (a) but for maximum 1-day rainfall total (mm/decade). (c) as (a) but for number of days in April-September with at least 1 mm of precipitation. (d) as (a) but for the annual April-September maximum number of consecutive dry days. (e) as (a) but for the number of April-September 95th percentile daily rainfall events. (f) North Central and South Central weighted area averages of yearly April-September precipitation, 5-year weighted averages, and linear trends from CPC dataset. (g) as (f) but for maximum 1-day rainfall total. (h) as (f) but for number of 1 mm rainfall days. (i) as (f) but for annual maximum number of consecutive dry days. (j) as (f) but for number of 95th percentile events. Stippling in (a) through (e) denote where the trend is statistically significant at the 95% confidence level. Asterisks in (f) through (j) indicate the trend is statistically different from zero with 95% confidence.

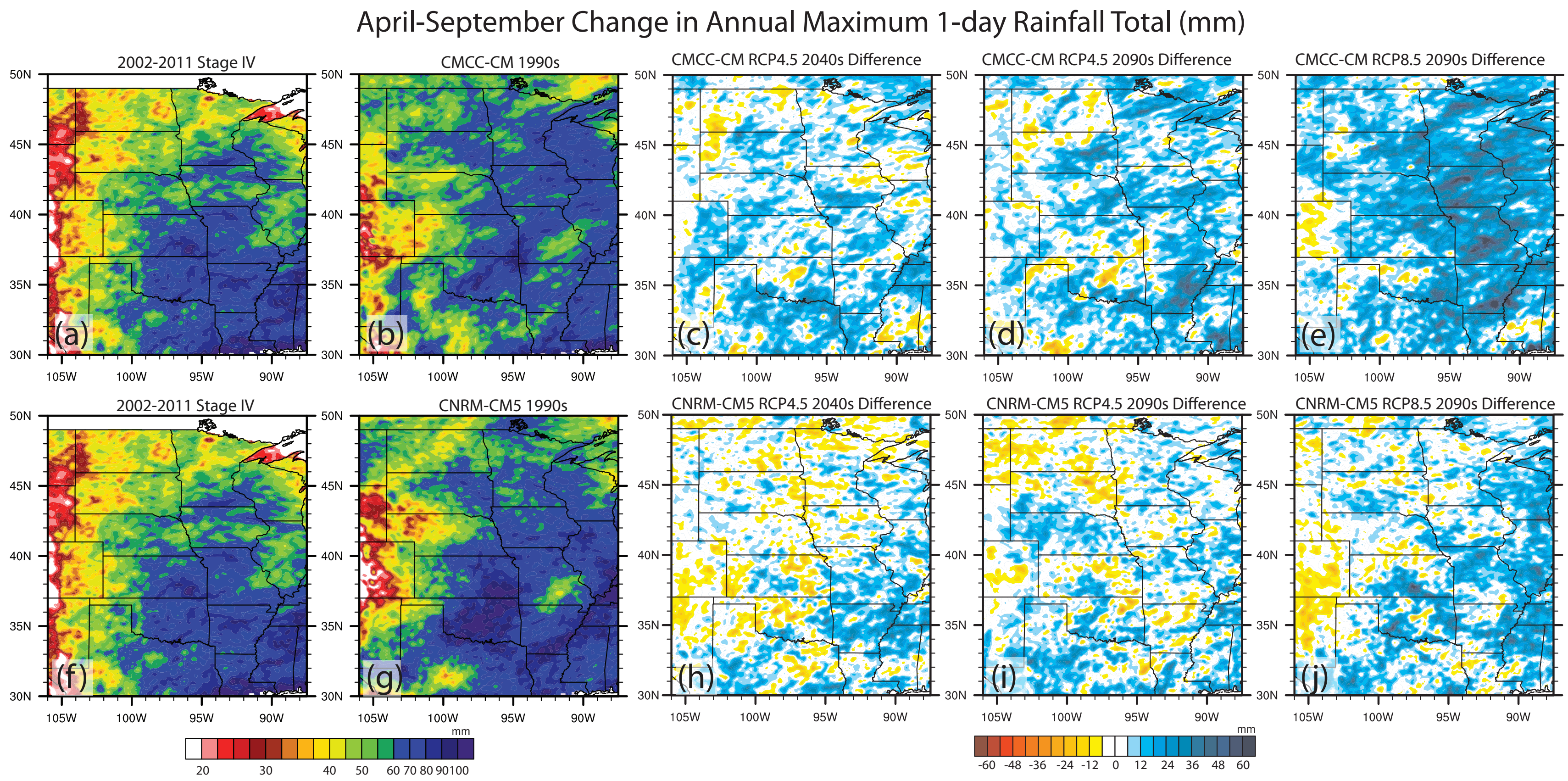

Figure 4.13. Same as Figure 4.9 but for the average maximum 1-day rainfall total (mm).

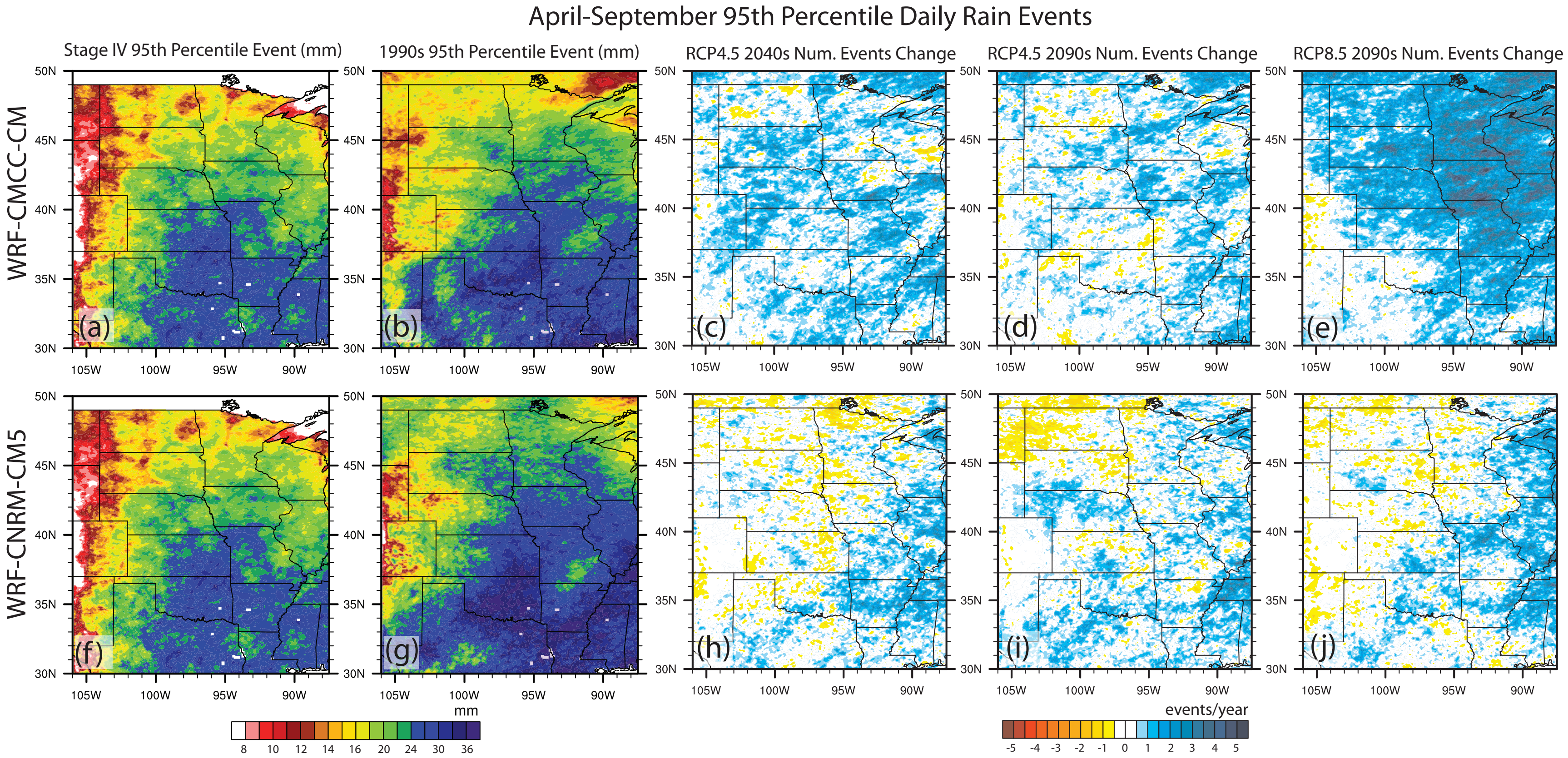

Figure 4.14. April-September 95th percentile daily rainfall total in (a) 1990-1999 WRF-CMCC-CM simulations. (b) RCP4.5 2040-49 WRF-CMCC-CM minus 1990-99 WRF-CMCC-CM average April-September number of 95th percentile daily rainfall events per year, (c) as (b) but for RCP4.5 2090-99 WRF-CMCC-CM, (d) as (b) but for RCP8.5 2090-99 WRF-CMCC-CM. (e) through (h) as (a) through (d) but for WRF-CNRM-CM5.

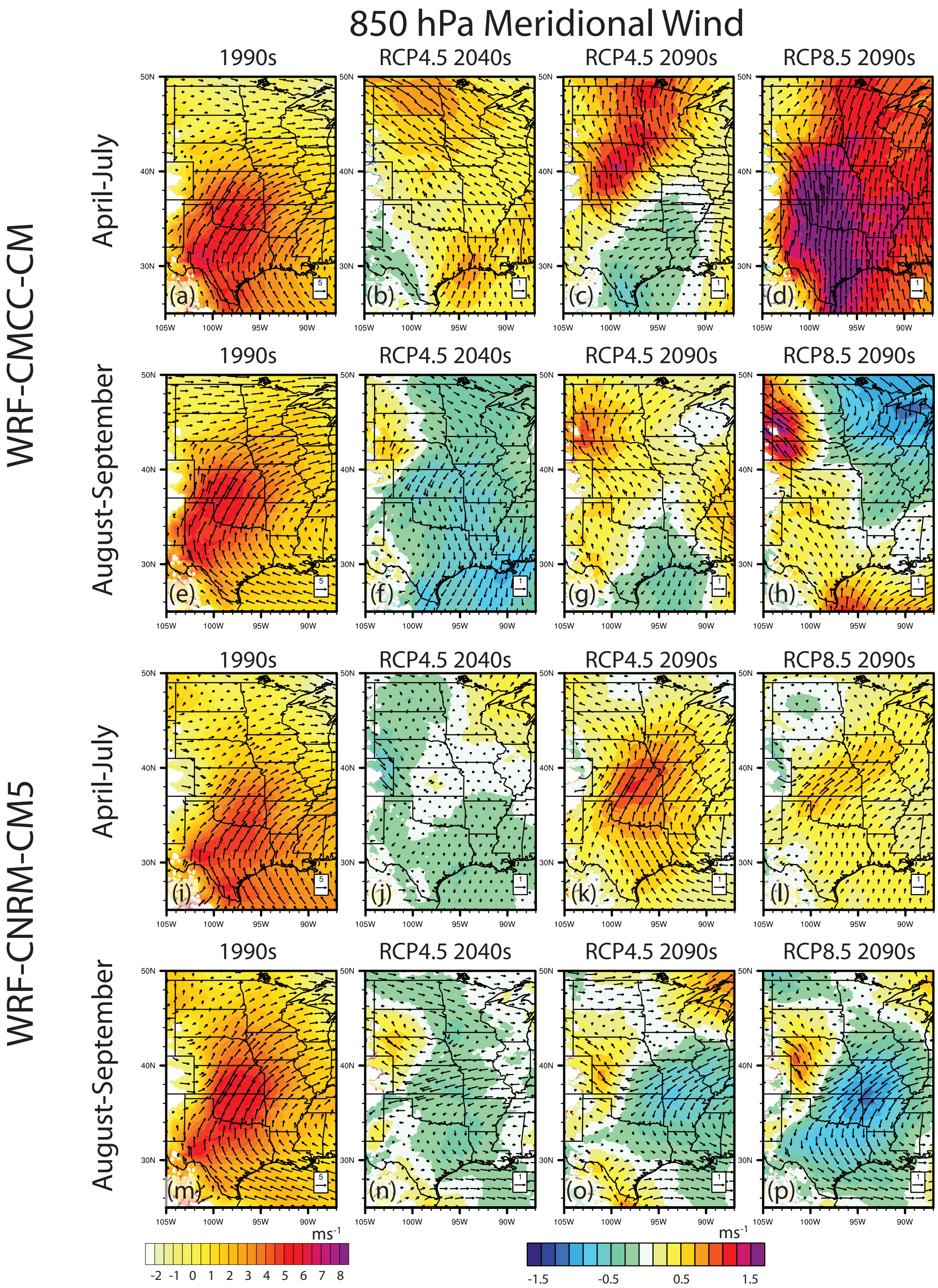

Figure 4.15. (a) April-July 850 hPa meridional wind (m/s) from WRF-CMCC-CM 1990s simulations. (b) as (a) but for RCP4.5 2040s minus 1990s. (c) as (b) but for RCP4.5 2090s. (d) as (b) but for RCP8.5 2090s. (e) through (h) as (a) through (d) but for August-September. (i) through (p) as (a) through (h) but for WRF-CNRM-CM5.

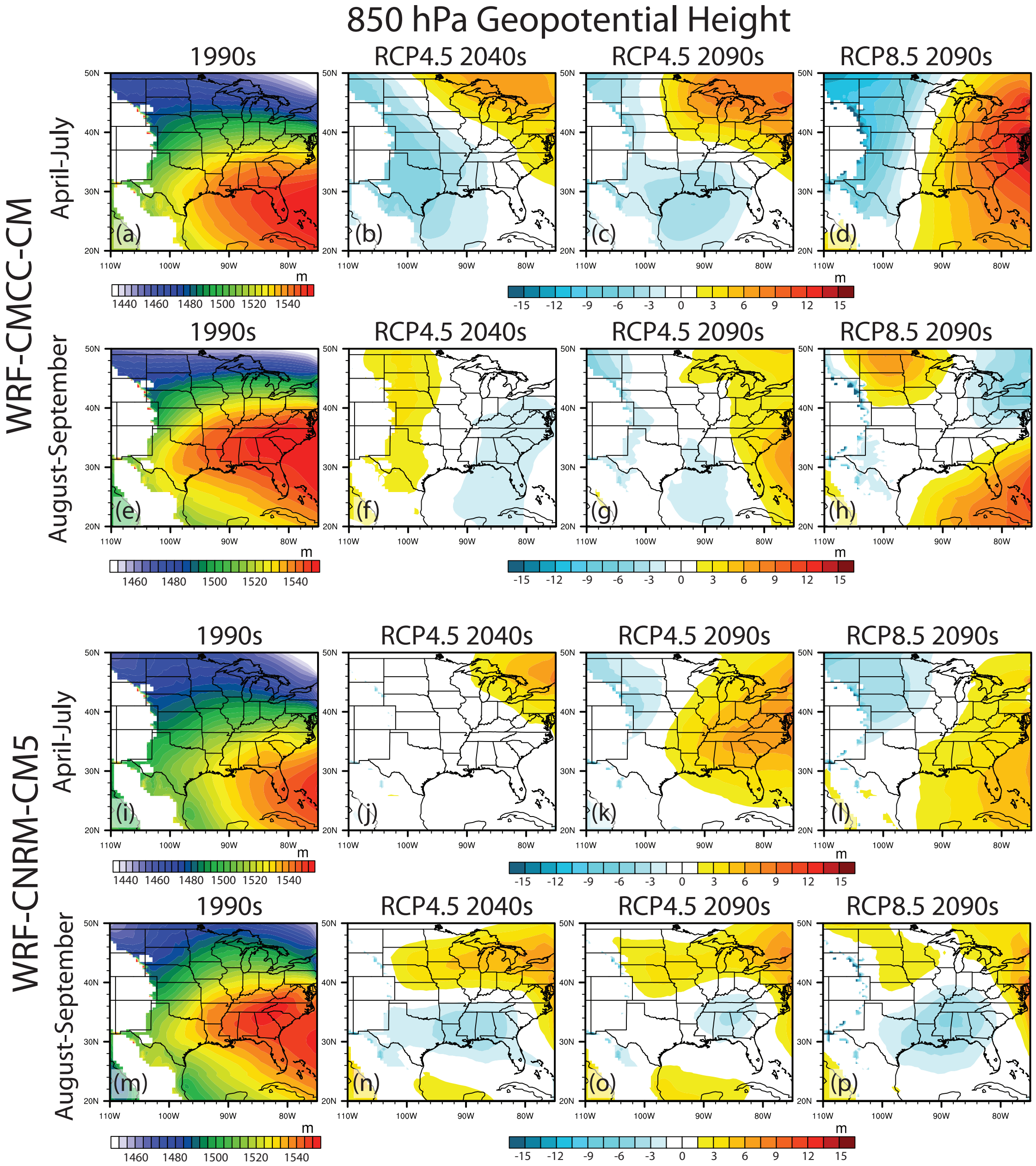

Figure 4.16. (a) April-July 850 hPa geopotential height from WRF-CMCC-CM 1990s simulations. (b) as (a) but for RCP4.5 2040s minus 1990s. (c) as (b) but for RCP4.5 2090s. (d) as (b) but for RCP8.5 2090s. (e) through (h) as (a) through (d) but for August-September. (i) through (p) as (a) through (h) but for WRF-CNRM-CM5. Differences in future scenarios show the normalized differences in geopotential height compared with historical simulations (i.e., average change removed) to emphasize spatial variations in differences.

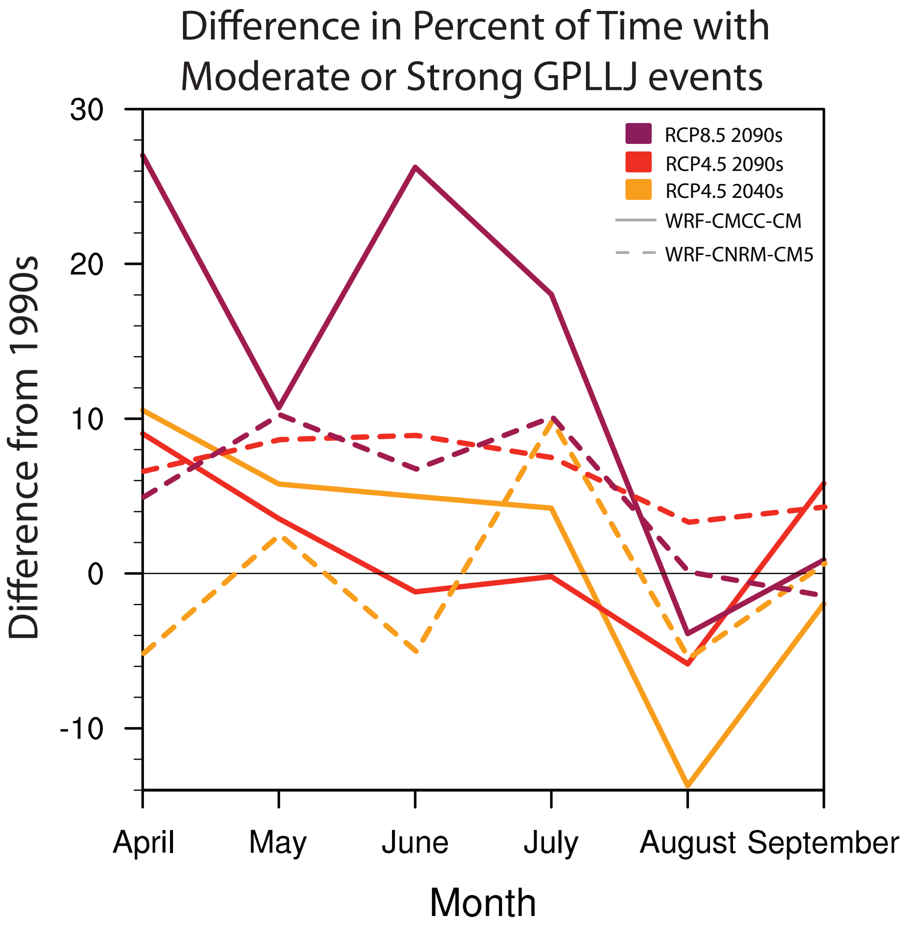

Figure 4.17. Seasonal Cycle of difference in percent of time when a moderate (≥ 16 ms^{-1}) or strong GPLLJ event (≥ 20 ms^{-1}) occurred within the GPLLJ region, compared to historical simulations.

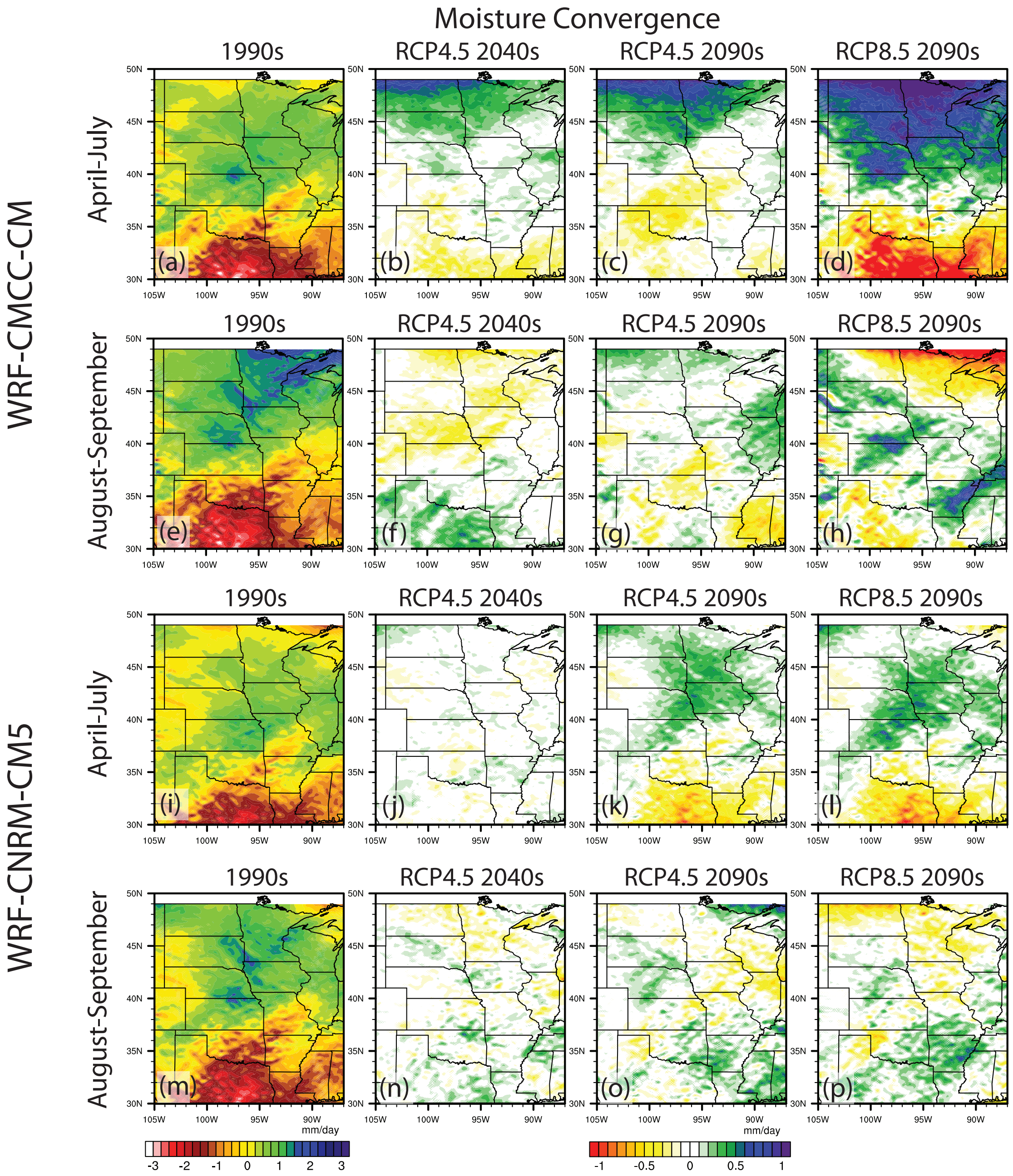

Figure 4.18. April-July column-integrated moisture convergence (mm/day) during (a) WRF-CMCC-CM simulations of the 1990s. (b) RCP4.5 2040s minus 1990s from WRF-CMCC-CM, (c) as (b) but for RCP4.5 2090s, (d) as (b) but for RCP8.5 2090s. (e) through (h) but for August-September. (i) through (p) for WRF-CNRM-CM5 simulations.

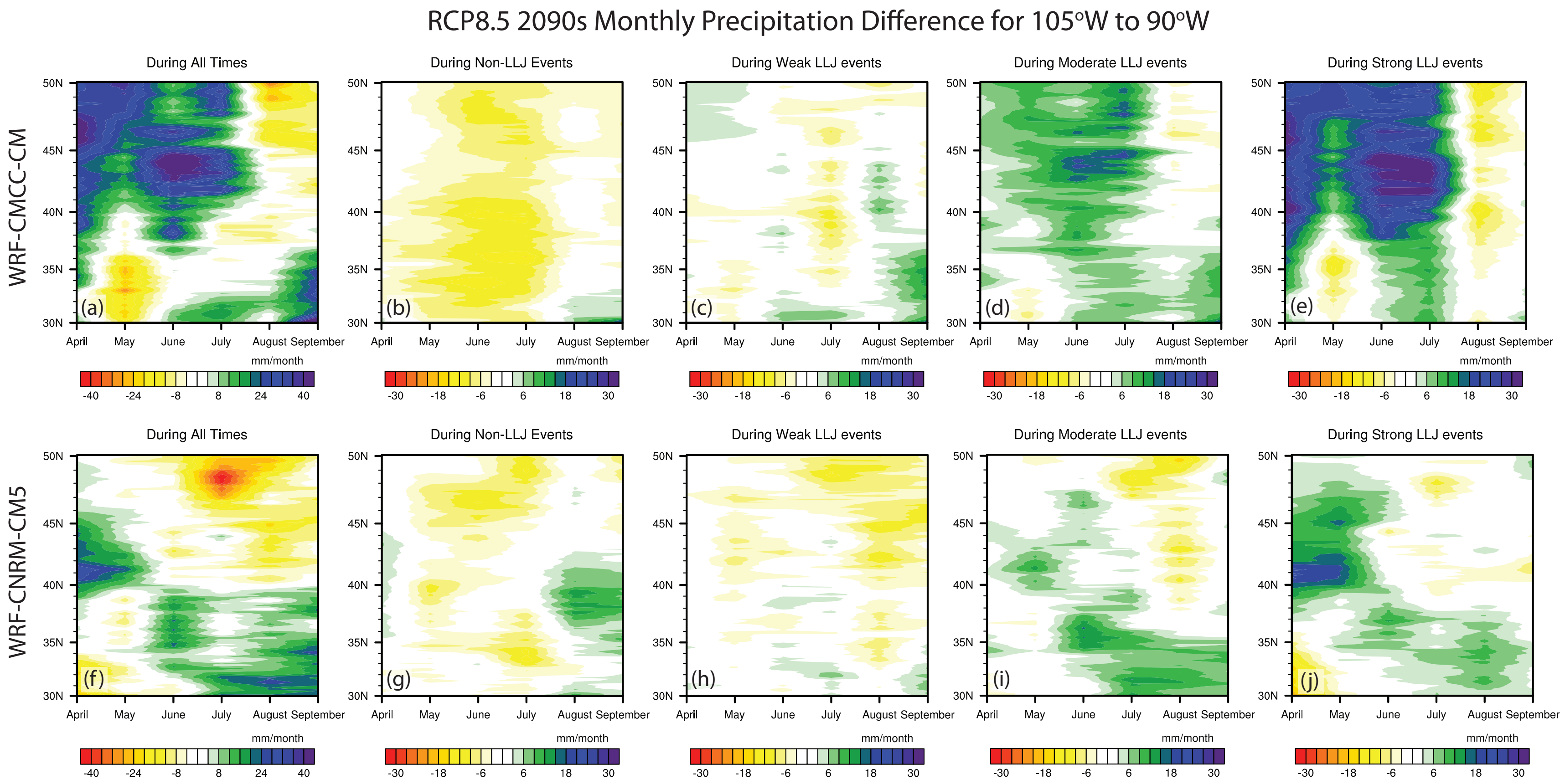

Figure 4.19. Difference in monthly precipitation from WRF-CMCC-CM simulations of the RCP8.5 2090s compared with simulations of the 1990s for (a) all times, (b) times without a GPLLJ event, (c) weak GPLLJ events, (d) moderate GPLLJ events, and (e) strong GPLLJ events by latitude, averaged across 105°W to 90°W. (f) to (j) as (a) to (e) but for WRF-CNRM-CM5 simulations.

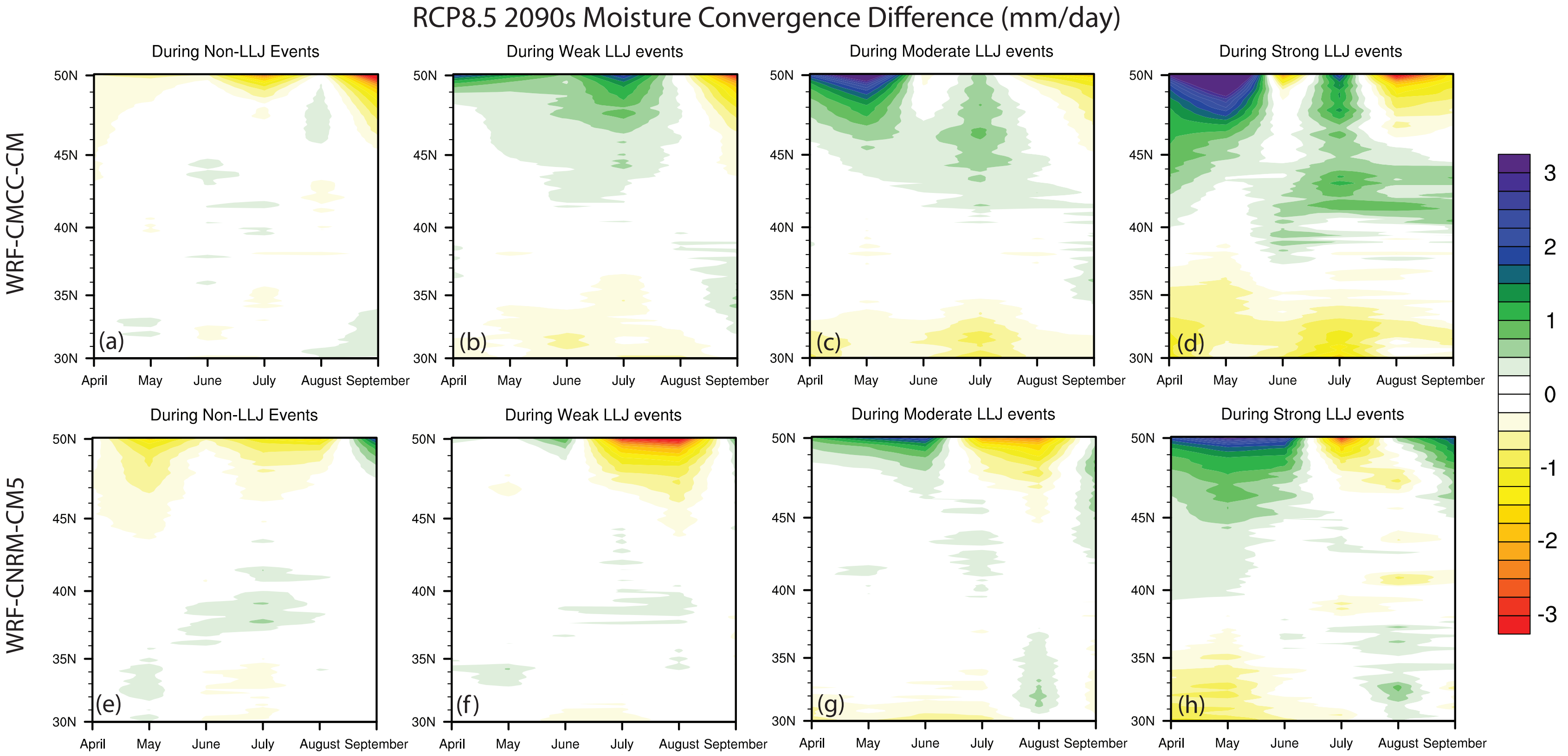

Figure 4.20. Moisture convergence (mm/day) difference between RCP8.5 2090s and 1990s by month from WRF-CMCC-CM simulations. Difference during (a) non-GPLLJ events, (b) weak GPLLJ events, (c) moderate GPLLJ events, and (d) strong GPLLJ events. (e) to (h) as (a) to (d) but for WRF-CNRM-CM5 simulations.

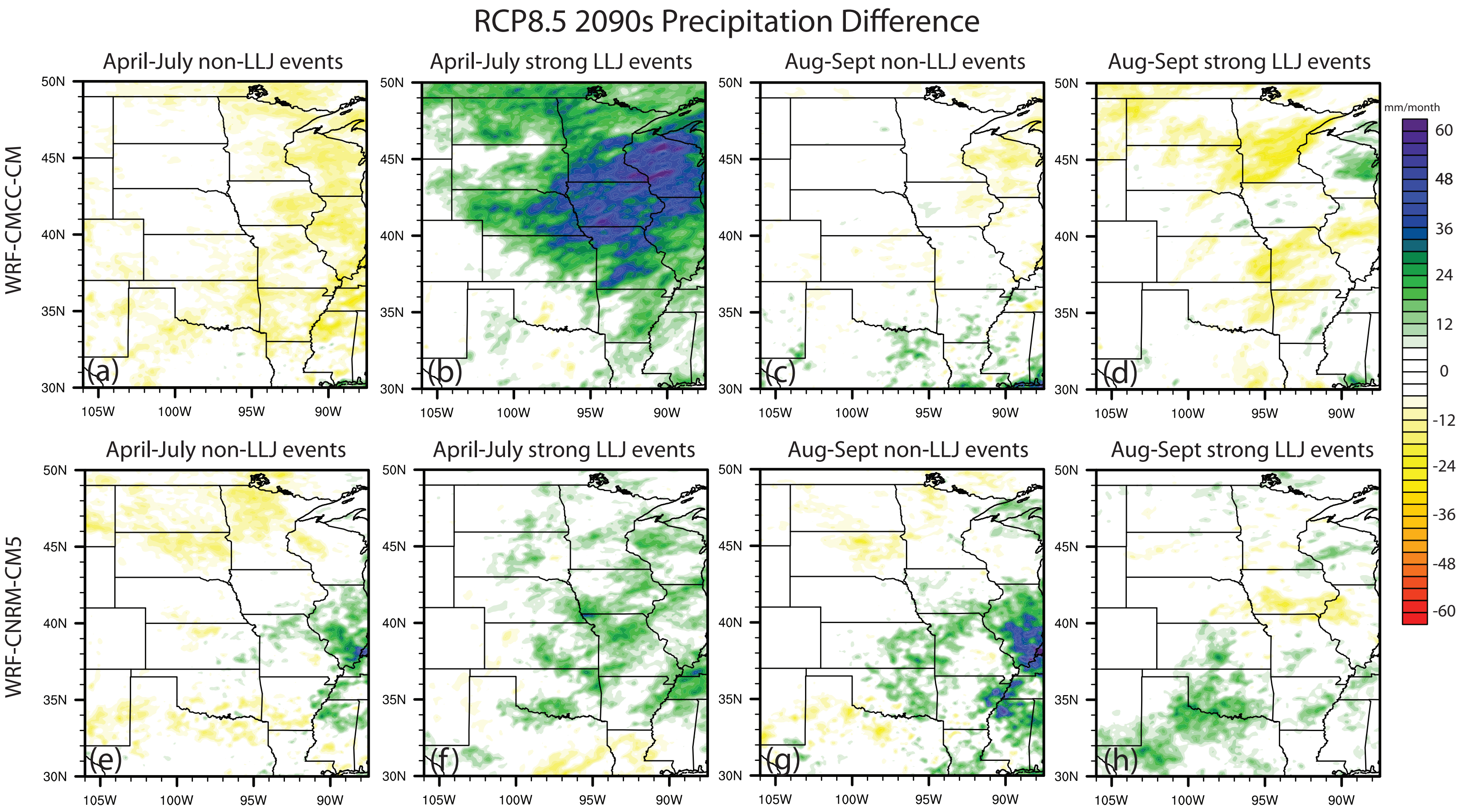

Figure 4.21. April-July precipitation (mm/month) difference between RCP8.5 2090s and 1990s by month from WRF-CMCC-CM simulations during (a) non-GPLLJ events and (b) strong GPLLJ events. (c) to (d) as (a) to (b) but for August-September. (e) to (h) as (a) to (d) but for WRF-CNRM-CM5 simulations.

Chapter 5

Mechanisms associated with the intensification of Midwest extreme rainfall events using dynamical downscaling

Harding, K. J. and P. K. Snyder, in preparation.

5.1 Overview

The frequency and intensity of heavy rainfall events have increased in the Central United States over the last several decades and model projections from dynamical downscaling suggest a continued increase with climate change. In this study, we examine how the mechanisms that are related to the development of heavy rainfall events over the Central United States might be affected by climate change. To accomplish these goals, we incorporate dynamical downscaled simulations of two CMIP5 models in WRF that accurately simulate heavy rainfall events. For each model, a set of extreme rainfall events that match the frequency, timing, and intensity of observed heavy rainfall events are objectively identified in historical and future simulations. We then examine multi-model composites of the environmental conditions during these events in simulations of historical and future scenarios, enabling an identification of possible physical mechanisms that could contribute to the intensification of extreme rainfall events over the Central U.S. with climate change. The simulations show that additional moisture is transported into convective updrafts during heavy rain events in future simulations, driving stronger evaporative cooling from the entrainment of drier mid-tropospheric air. This results in the formation of a stronger low-level cold pool, which enhances moisture convergence above the cold pool and increases rainfall rates during future heavy precipitation events. In addition, a warmer temperature profile in future simulations may allow for heavier rainfall rates as a deeper atmospheric column can support collision-coalescence of liquid hydrometeors.

5.2 Introduction

Extreme rainfall events across the Great Plains and Midwestern United States consistently cause significant societal and economic damage, with over \$33.8 billion and \$16.2 billion in losses from summer flooding in 1993 and 2008, respectively (NCDC). Climate change is expected to enhance precipitation extremes globally (Allan and Soden 2008; Allen and Ingram 2002; Dai 2013; Held and Soden 2006; O'Gorman and Schneider 2009; Trenberth 1999) due to an acceleration of the hydrologic cycle (Durack et al. 2012; Huntington 2006; O'Gorman and Schneider 2009; Trenberth et al. 2003). An increase in heavy rainfall events has already been documented in observations across the United States (Groisman et al. 2005; Karl and Knight 1998) and globally (Fischer and Knutti 2014). Model projections from GCMs (Kunkel et al. 2013; O'Gorman and Schneider 2009; Sillmann et al. 2013) and dynamical downscaling (Bukovsky and Karoly 2011; Mahoney et al. 2013; Wehner 2013) all suggest an increase in extreme rainfall events in the region will occur with climate change.

Broad thermodynamic arguments invoking the Clausius-Clapeyron equation have generally been used to explain projected increases in extreme rainfall events with climate change (Allen and Ingram 2002; Trenberth et al. 2003). While the expected increase in moisture may explain global changes in precipitation extremes, fine-scale dynamic processes will likely overwhelm such mechanisms on smaller scales. Additional atmospheric moisture could increase rainfall rates by enhancing latent heating and driving additional convergence of moisture into convective storms

(Trenberth et al. 2003). Similarly, stronger latent heat release from additional moisture ingested into convective updrafts could enhance vertical velocities. While GCM simulations have found little to no change in updrafts during mid-latitude extreme rainfall events (O'Gorman and Schneider 2009), slightly enhanced updraft velocities in the upper troposphere associated with higher rainfall rates have been simulated with a warmer climate in idealized cloud-resolving simulations (Muller et al. 2011). In regions and seasons dominated by dynamically derived convective precipitation such as the Central U.S., enhanced fine-scale processes will likely cause spatially heterogeneous regional and local changes in rainfall extremes that cannot be predicted by broad thermodynamic arguments.

Over the Midwestern United States, heavy rainfall events peak in the summer months (Dirmeyer and Kinter 2010; Hitchens et al. 2013; Villarini et al. 2011a; Villarini et al. 2011b), with over 80% of heavy rainfall events in the contiguous U.S. occurring from April-September (Hitchens et al. 2013). Numerous recent severe flooding events in the region have caused over $1 billion in damage, including the 1993 Great Mississippi River Flood (Kunkel et al. 1994), 2008 Iowa Flooding (Smith et al. 2013), and 2010 Tennessee flood (Moore et al. 2012). A large majority of flash flooding events in the Midwest originate from Mesoscale Convective Systems (MCSs) (Doswell et al. 1996; Schumacher and Johnson 2005, 2006), large (> 100 km) and persistent (3-24 hours) convective structures (Corfidi 2003; Orlanski 1975; Parker and Johnson 2000; Schumacher and Johnson 2006). Future changes in Central U.S. extreme rainfall events will likely be influenced by changes in dynamical mechanisms that currently influence

MCS development. In this study, we explore how the mechanisms that are responsible for the development of heavy rainfall events as well as the timing and intensity of these events may be affected by climate change. To accomplish these objectives, we use two CMIP5 models that were dynamically downscaled in WRF as discussed in Chapter Four.

While the synoptic and mesoscale atmospheric conditions associated with individual extreme rainfall events in the Central U.S. can be widely varied, the presence of a strong southerly low level jet (LLJ) (Arritt et al. 1997), abundant moisture, low-level convergence, conditional instability, weak vertical wind shear, and a sufficiently thick warm-cloud layer have all been identified as important precursors to extreme rainfall events (Bluestein and Jain 1985; Corfidi 2003; Davis 2001; Doswell et al. 1996; Funk 1991; Maddox et al. 1979). Strong moisture transport (Maddox et al. 1979) and moisture convergence associated with the Great Plains Low Level Jet (GPLLJ) typically enable greater precipitation rates than allowed by antecedent column-integrated precipitable water content (Funk 1991; Trenberth et al. 2003). The GPLLJ is a key factor in MCS development (Coniglio et al. 2010) and is the primary driver of nocturnal summer precipitation in the region (Bell and Janowiak 1995; Helfand and Schubert 1995; Higgins et al. 1997; Means 1952, 1954; Mo and Berbery 2004; Mo et al. 1995; Pitchford and London 1962) by providing moisture transport, low-level shear, and convergence. Low-level inflow from the Gulf of Mexico is up to 45% higher during strong LLJ events (≥ 20 ms^{-1}), a significant reason why the GPLLJ is associated with heavy rainfall events (Arritt et al. 1997; Cook et al. 2008; Monaghan et al. 2010). The strength of the GPLLJ is related to pressure differences between the North Atlantic Subtropical High (NASH) and the Great Plains. Previous studies have suggested that the observed intensification of the GPLLJ (Barandiaran et al. 2013) is related to a recent westward movement of the NASH due to anthropogenic forcing (Li et al. 2011). Simulations of future periods using dynamical downscaling indicate that a stronger GPLLJ during April-July may increase the frequency and intensity of heavy rainfall events during those months by modifying the pressure gradient across the GPLLJ (see Chapter 4).

While moisture transported within the GPLLJ can be critical for establishing heavy rainfall rates, the presence of an anomalously thick warm layer can significantly increase the efficiency of convective precipitation (Wallace and Hobbs 1977). Collision-coalescence is the most effective method for converting cloud water into precipitation, operating more efficiently than the Bergeron process where ice crystals accumulate at temperatures below -10°C (Ryan and Vitale 2008; Wallace and Hobbs 1977). The efficiency of collision-coalescence increases significantly in convective clouds with temperatures warmer than -10°C, enhancing rainfall rates as generally occurs in deep tropical convection (Davis 2001). Increasing temperatures with climate change may enhance the efficiency of warm-season convective precipitation as a greater vertical depth of convective clouds can support collision-coalescence processes in lieu of less efficient hydrometeor formation.

While antecedent synoptic conditions enable the development of heavy rain producing MCSs, mesoscale dynamics during convective development are critical for prolonging heavy precipitation. The accumulation of evaporatively cooled air from convective outflows enables the development of a surface mesohigh and low-level cold pool, which are typically observed beneath mid-latitude MCSs (Atlas et al. 1969; Fujita 1959; Johnson 2001; Maddox et al. 1979). Cold pools are characterized as a local minimum in surface temperature and are a critical component in the organization and continuation of convective precipitation (Fovell and Ogura 1989; Parker and Johnson 2004; Rotunno et al. 1988; Thorpe et al. 1982; Weisman and Rotunno 2004). Density gradients caused by the low-level cold pool are associated with the development of a surface mesohigh, a mesoscale region of high pressure that has been shown to occur during a large percentage of warm-season flash flooding events (Maddox et al. 1979). While evaporative cooling enables surface mesohigh development, hydrometeor loading and non-hydrostatic pressure increases from the impingement of the downdraft on the surface also contribute (Nicholls et al. 1988; Sanders and Paine 1975).

In the presence of a strong southerly LLJ, cold pools can drive continuous deep convection at the southern edge of the cold pool where low-level moisture convergence from the LLJ is maximized, enabling continuation of heavy rainfall rates over several hours (Coniglio et al. 2010). Additional available moisture with climate change may enhance precipitation loading and evaporative cooling within downdrafts (assuming no increase in the relative humidity of entrained air), possibly enabling the development of stronger low-level cold pools and mesohighs. Greater low-level convergence at cold pool boundaries would likely result, enabling greater moisture inflow into convective updrafts and potentially heavier rainfall rates.

In this study, we examine how the mechanisms that are related to the development of heavy rainfall events as well as the timing and intensity of events may be affected by climate change. To accomplish these goals, we use dynamical downscaled simulations of two CMIP5 models in WRF from Chapter Four that accurately simulate regional precipitation extremes. For each model, we identify a set of extreme rainfall events in historical simulations that match the frequency, timing, and intensity of observed heavy rainfall events that were associated with flashing flooding in Schumacher and Johnson (2006), as well as the Stage IV dataset (Lin and Mitchell 2005). We examine multi-model composites of the environmental conditions during these events in simulations of historical and future scenarios, enabling us to identify possible physical mechanisms that could contribute to the intensification of extreme rainfall events over the Central U.S. with climate change.

5.3 Methods

5.3.1 WRF model

WRF simulations from Chapter Four were based on the regional WRF model version 3.4 (Skamarock et al. 2008) with the coupled Noah Land Surface Model (LSM) (Chen and Dudhia 2001). The Noah LSM exchanges surface fluxes of energy, momentum, and mass with WRF and includes four soil layers and one canopy layer. WRF uses a terrain-following vertical coordinate system that extends from the surface to 50 hPa. Because convective processes and shallow clouds cannot be fully resolved within coarsely resolved grid cells (Skamarock et al. 2008), precipitation development is aided by a convective parameterization (CP) at coarse spatial resolutions. CPs are designed to resolve sub-grid scale vertical fluxes of mass, momentum, and latent heating when adequate spatial resolution prevents explicit resolution of these processes. The spatial resolution required to resolve convective precipitation varies by application. Deep moist convection can explicitly develop in the absence of a CP in 10-km WRF simulations over the Central U.S. during the warm season where deep convection is dynamically forced by the GPLLJ (Harding and Snyder 2012b) but in some cases CPs are necessary at spatial resolutions between 5-10 km without a strong dynamical forcing (Skamarock et al. 2008).

5.3.2 WRF simulations

Model simulations were completed from March 15-October 1 for each year in the historical period (1990-1999), two future periods (2040-2049, 2090-2099) in the mid-range RCP4.5 scenario, and one future period (2090-2099) in the RCP8.5 (high forcing) scenario. Soil moisture was initialized using the 1981-2010 average March 15 soil moisture from the NCEP-DOE Reanalysis II (Kanamitsu et al. 2002). A nested grid configuration was used with a 50-km resolution outer domain, 10-km resolution inner domain (Figure 5.1), and 34 vertical levels. The outer domain was run at a time step of 150 seconds, with a 30 second inner domain time step. The Morrison 2-moment Microphysics scheme (Morrison et al. 2009) was used because multi-moment microphysics schemes more accurately simulate surface cold pool development in MCSs (Dawson et al. 2010; Mansell 2008). In addition, the YSU Planetary Boundary Layer scheme (Hong et al. 2006), RRTM long wave radiation scheme (Mlawer et al. 1997), Dudhia shortwave radiation scheme (Dudhia 1989), and MM5 surface-layer scheme (Skamarock et al. 2008) were employed. No cumulus parameterization (CP) was used because 10-km simulations without a CP in Harding et al. (2013) more accurately simulated the diurnal cycle than simulations with a CP activated. While the potential for convective feedback issues exist in WRF when conducting 10-km simulations without a CP, the limited model domain and the use of nudging reduces the likelihood of these problems.

Accurate average Atlantic Warm Pool (AWP) sea surface temperatures (SSTs) in the CMIP5 models have been shown to significantly improve downscaled Central U.S. summer precipitation in WRF (Harding et al. 2013). WRF simulations were forced by two GCMs from the CMIP5 (CMCC-CM and CNRM-CM5) that accurately simulate AWP SSTs and resolve the seasonality and spatial variability of the GPLLJ. To enable accurate simulation of meteorological fields, nudging of temperature, moisture, and momentum was used above the boundary layer. While nudging has the potential to hamper the production of precipitation extremes when applied throughout the atmospheric column, Otte et al. [2012] showed that nudging above the boundary layer and with reduced coefficients (from standard WRF values) do not suppress the production of heavy rainfall. Therefore, reduced nudging coefficients were used for all variables in the inner domain and for moisture in the outer domain, with no nudging within the boundary layer (Otte 2008; Otte et al. 2012; Stauffer and Seaman 1994). Nudging parameters for moisture were reduced further compared to Otte et al. [2012] in the inner domain because it is significantly smaller (one-third of the size) and nudging is not as critical for smaller domains.

5.3.3 Observational datasets

To examine the performance of the diurnal cycle of precipitation and extreme rainfall events, WRF simulations were compared to the National Center for Environmental Prediction's Stage IV hourly precipitation dataset (Lin and Mitchell 2005), which is available from 2002-present. Stage IV is commonly used as a benchmark for sub-daily observations (AghaKouchak et al. 2011; Sapiano and Arkin 2009) and compares well with other datasets for the diurnal cycle of precipitation (Lee et al. 2007b) and heavy rainfall events. Because Stage IV is only available starting in 2002, 30-year averages of the Climate Research Unit (CRU) (Mitchell and Jones 2005) 0.5° x 0.5° monthly precipitation dataset were used to validate seasonal averages of WRF precipitation.

5.3.4 Extreme event classification

Schumacher and Johnson (2005) and (2006) examined the timing and structure of heavy rainfall events that exceeded 50-year rainfall recurrence intervals and were associated with flash flooding. In this study, we applied a similar approach with the goal of examining how the timing and frequency of extreme rainfall events may be affected by climate change. By classifying extreme rainfall events in dynamical downscaling simulations, we can also identify possible mechanisms that could contribute to an increased frequency of Central U.S. heavy rainfall events by examining the environmental conditions of these events.

Extreme rainfall events were identified in the Stage IV dataset (interpolated to the WRF inner domain in Figure 5.1) and dynamical downscaled simulations with the goal of representing the frequency and timing of events in Schumacher and Johnson (2006), hereafter referred to as SJ2006. For all dynamical downscaled simulations, an event was identified if at least 10 grid cells (5%) within any 10 x 10 grid cell box (100 x 100 km, the average MCS length scale (Houze 1993; Parker and Johnson 2000)) had the greatest 1-day precipitation within the historical period on any given day. If this threshold was exceeded on consecutive days, the day with the greatest precipitation total was identified as the event. The event center was the highest 1-day precipitation total near where the grid cell threshold was reached. While SJ2006 used archived radar reflectivity to examine the time evolution of events, we used simulated and observed precipitation rates. The start of an event occurred when a grid cell within 20 km (2 grid cells) of the event center recorded a 12.5 mm/hour rainfall rate, lower than the 45 dBZ (~24 mm/hour) threshold from SJ2006. The event peak was the time when the highest hourly rainfall rate was present within 20 km of the event center, similar to SJ2006, which used the hour when the highest reflectivities were "most persistent over the area." Because stratiform precipitation tends to persist well after the highest rainfall rates in MCSs, a lower threshold for the end of the event was used in SJ2006 and here. For the end of the event, SJ2006 used the time when all radar echoes ended or moved out of the area, while we used the first time after the event peak without any >2.5 mm/hour rainfall rates within 20 km. These procedures were used for the historical period of WRF simulations as well as the first ten years of Stage IV observations for validation (Lin and Mitchell 2005). For future WRF simulations, we used 1-day precipitation thresholds from the historical period for each model to allow detection of changes in event frequency.

Atmospheric variables were analyzed throughout the duration of extreme rainfall events to determine the physical mechanisms related to the simulation of extreme events and how these mechanisms may be modified with climate change. The average environmental conditions within a fixed radius of events were composited for variables in the North and South Central regions individually (as shown in Figure 5.1), as well as for the two regions combined (Central region).

5.4 Validation

5.4.1 WRF simulations

Both models simulate the average April-September precipitation with reasonable accuracy compared with the 1981-2010 CRU average (Figures 5.2a-c). WRF-CMCC-CM tends to overestimate rainfall over the North Central U.S. and has a dry bias over the South Central region (Figure 5.2b), while WRF-CNRM-CM5 underestimates precipitation in the lee of the Rocky Mountains (Figure 5.2c). Both models generally match the diurnal cycle of precipitation the Stage IV dataset (Figure 5.2d), with a slight overestimation of afternoon precipitation in the North Central U.S. and too little nocturnal rainfall in the South Central region (Figure 5.3). Eastward propagating MCSs, which dominate nocturnal warm-season convective precipitation, are simulated reasonably well north of 40°N (Figure 5.3) where the forcing for convection (i.e., moisture convergence) is strong (Figure 5.4). This indicates that the configuration of WRF used in this study can simulate the development and eastward progression of mesoscale convective systems that dominate nocturnal summer rainfall over the North Central U.S. However, WRF poorly simulates eastward moving MCSs in the South Central region as the lack of a convective parameterization hinders the ability to adequately force nocturnal convection in such a weakly forced environment (i.e., weak moisture convergence). Similar precipitation frequency distributions in WRF downscaled simulations and Stage IV (Figure 5.2e) suggest that WRF can simulate the frequency and intensity of warm-season precipitation in the region with considerable accuracy.

5.4.2 Extreme event classification

Our technique for classifying discrete heavy rainfall events yields similar event frequencies in the Stage IV dataset, WRF simulations, and SJ2006 (when normalized to a longer period; Table 5.1). Compared with SJ2006, approximately the same number of events is identified in WRF for both models over the North Central U.S., with more events in the Stage IV dataset. Model simulations correctly identify the observed mid-summer maximum in extreme events in the North Central U.S. (Maddox et al. 1979; Schumacher and Johnson 2006), with the greatest number of extreme rainfall events in July (Figure 5.5a). Over the South Central region, both model simulations produce more events than SJ2006, with a significant overestimation of events in the Stage IV dataset (Figure 5.5d).

Considering the intensity of extreme events, simulated events are compared with Stage IV because average event rainfall totals are not available in SJ2006. Peak hourly rainfall rates, 24-hour rainfall totals, and event totals are generally larger in the WRF simulations compared with Stage IV in both regions (Table 5.2), but are approximately the same magnitude. However, higher rainfall totals in WRF compared with Stage IV may be related to the identification of more light events in the Stage IV dataset. Rainfall totals also had little dependence on the downscaled model even with large differences in their native resolutions (0.75° x 0.75° for CMCC-CM, 1.5° x 1.5° for CNRM-CM5), similar to results from Peters and Roebber (2014) which suggest the parent model resolution has little impact on the simulation of heavy rainfall events in WRF (Harding et al. 2013).

The timing of North Central discrete heavy rainfall events in WRF simulations generally compares well with Stage IV and SJ2006 (Figures 5.6a-c). For the start of events, the broad maximum between 23Z and 04Z is at approximately the same time in WRF simulations, Stage IV, and SJ2006 (Figures 5.6a-c). Simulated event peak times consistently occur slightly after the typical event start, consistent with Stage IV and SJ2006. WRF simulations, Stage IV, and SJ2006 all exhibit a broad tail of event end times that occurs several hours after the typical event peak. Most simulated events are between 4-12 hours in duration, similar to events from Stage IV (Figure 5.6d) (SJ2006 event durations not available).

The diurnal cycle of South Central events is less coherent (Figures 5.6e-g) but follows a similar pattern as the North Central region. In the South Central U.S., the greatest number of events start at 00Z in Stage IV and WRF, generally consistent with SJ2006 (Figures 5.6e-g). Simulated event peak times are similar to the Stage IV and SJ2006 maxima between 01Z and 09Z, with later peak rainfall times than the North Central region despite issues with the development of nocturnal precipitation in the South Central region. Extreme rainfall events typically last longer over the South Central region, with an average event duration of around ten hours for WRF and Stage IV.

In general, extreme rainfall events classified in WRF simulations using the methods described in Section 6.3.4 produce a similar magnitude and timing as those from Stage IV and SJ2006. Therefore, simulated extreme rainfall events in this study provide a reasonable representation of heavy precipitation events in the region. While future simulations are limited by any biases present in WRF and the assimilated GCMs, simulated changes in extreme events in future scenarios provide a realistic estimate of how the frequency, magnitude, and timing of extreme rainfall events may be affected by climate change.

5.4.3 Atmospheric conditions during extreme events

Both models simulate more frequent extreme rainfall events over the North and South Central regions in all future scenarios (Table 5.3), with statistically significant increases in the intensity of events in the RCP8.5 2090s. Over the North Central region, extreme rainfall events increase in all months and scenarios except for July in WRF-CNRM-CM5 simulations of the RCP4.5 2040s (Figures 5.5b-c). Both models simulate the greatest increase in North Central U.S. extreme events in the RCP8.5 2090s and the smallest change in the RCP4.5 2040s (Table 5.3), suggesting that increases in extreme rainfall events in the North Central U.S. are related to the strength of the climate forcing. North Central U.S. extreme rainfall events have the largest increase in the early warm-season, with the greatest change in May (Figures 5.5b, 5.5c).

Over the South Central region, more extreme events are simulated in all months for every future scenario except for September in WRF-CNRM-CM5 simulations of the RCP4.5 2040s (Figure 5.5f). The greatest increase in events occurs during April-June in WRF-CMCC-CM simulations, but no clear change in seasonality is present in WRF-CNRM-CM5 (Figures 5.5e-f). Increases in the frequency of extreme rain events are only marginally larger in the RCP8.5 2090s compared with the RCP4.5 2040s and RCP4.5 2090s, suggesting that the strength of the anthropogenic forcing may have a smaller impact over the South Central region.

Statistically significant increases in rainfall rates occur in many of the future scenarios, with the most consistent changes in the RCP8.5 2090s (Tables 5.4-5.5). Over the North Central region, increases in hourly, daily, and event rainfall totals occur in both models during the RCP8.5 2090s, but no clear changes occur in the RCP4.5 simulations (Table 5.4). Hourly and daily rainfall increases are statistically significant for both models in the RCP8.5 2090s, with changes in event totals only significant for WRF-CMCC-CM (Table 5.4). Hourly rainfall rates increase by 9.8% in the RCP8.5

2090s on average for both models, with 10.0% and 9.9% increases in daily and event rainfall totals, respectively (Table 5.4). Changes in other future scenarios are less consistent, with some periods experiencing slight decreases in average rainfall totals (Table 5.5). However, heavier events (≥ 200 mm) have much larger percent increases than light events (< 200 mm) in all future scenarios (Table 5.6), with a 200% average increase in heavier events and just a 79.3% increase in lighter events in the RCP8.5 2090s.

Over the South Central region, clear increases in rainfall rates are present in nearly all future scenarios with statistical significance for hourly, daily, and event rainfall rates in the RCP8.5 2090s (Table 5.5). On average for both models, hourly rainfall rates during events in the South Central U.S. increase by 26.5% in the RCP8.5 2090s, maximum 24-hour rainfall totals increase by 19.9%, and event totals increase by 21.9% ($p < 0.05$; Table 5.4). Events with at least 200 mm of rainfall have a much greater increase than lighter events (< 200 mm) in all future scenarios over the South Central region, especially in scenarios with stronger climate forcing (Table 5.6). In the RCP8.5 2090s, events with ≥ 200 mm increase by 342% on average (from 17.5 to 62.5 events) for both models, compared to a 55% increase in events with less than 200 mm (Table 5.6).

5.5 Extreme rainfall events in future simulations

5.5.1 Changes in extreme events

Both models simulate more frequent extreme rainfall events over the North and South Central regions in all future scenarios (Table 5.3), with statistically significant increases in the intensity of events in the RCP8.5 2090s. Over the North Central region, extreme rainfall events increase in all months and scenarios except for July in WRF-CNRM-CM5 simulations of the RCP4.5 2040s (Figures 5.5b-c). Both models simulate the greatest increase in North Central U.S. extreme events in the RCP8.5 2090s and the smallest change in the RCP4.5 2040s (Table 5.3), suggesting that increases in extreme rainfall events in the North Central U.S. are related to the strength of the climate forcing. North Central U.S. extreme rainfall events have the largest increase in the early warm-season, with the greatest change in May (Figures 5.5b, 5.5c).

Over the South Central region, more extreme events are simulated in all months for every future scenario except for September in WRF-CNRM-CM5 simulations of the RCP4.5 2040s (Figure 5.5f). The greatest increase in events occurs during April-June in WRF-CMCC-CM simulations, but no clear change in seasonality is present in WRF-CNRM-CM5 (Figures 5.5e-f). Increases in the frequency of extreme rain events are only marginally larger in the RCP8.5 2090s compared with the RCP4.5 2040s and RCP4.5 2090s, suggesting that the strength of the anthropogenic forcing may have a smaller impact over the South Central region.

Statistically significant increases in rainfall rates occur in many of the future scenarios, with the most consistent changes in the RCP8.5 2090s (Tables 5.4-5.5). Over the North Central region, increases in hourly, daily, and event rainfall totals occur in both models during the RCP8.5 2090s, but no clear changes occur in the RCP4.5 simulations (Table 5.4). Hourly and daily rainfall increases are statistically significant for both models in the RCP8.5 2090s, with changes in event totals only significant for WRF-CMCC-CM (Table 5.4). Hourly rainfall rates increase by 9.8% in the RCP8.5 2090s on average for both models, with 10.0% and 9.9% increases in daily and event rainfall totals, respectively (Table 5.4). Changes in other future scenarios are less consistent, with some periods experiencing slight decreases in average rainfall totals (Table 5.5). However, heavier events (≥ 200 mm) have much larger percent increases than light events (< 200 mm) in all future scenarios (Table 5.6), with a 200% average increase in heavier events and just a 79.3% increase in lighter events in the RCP8.5 2090s.

Over the South Central region, clear increases in rainfall rates are present in nearly all future scenarios with statistical significance for hourly, daily, and event rainfall rates in the RCP8.5 2090s (Table 5.5). On average for both models, hourly rainfall rates during events in the South Central U.S. increase by 26.5% in the RCP8.5 2090s, maximum 24-hour rainfall totals increase by 19.9%, and event totals increase by 21.9% ($p < 0.05$; Table 5.4). Events with at least 200 mm of rainfall have a much greater increase than lighter events (< 200 mm) in all future scenarios over the South Central region, especially in scenarios with stronger climate forcing (Table 5.6). In the RCP8.5 2090s, events with ≥ 200 mm increase by 342% on average (from 17.5 to 62.5 events) for both models, compared to a 55% increase in events with less than 200 mm (Table 5.6).

5.5.2 Changes in atmospheric conditions during extreme events

For simplicity, here we investigate mesoscale dynamics of extreme rainfall events over the entire Central U.S. More abundant precipitable water and low-level moisture occur adjacent to the center of extreme rainfall events in all future scenarios, with larger changes in simulations with stronger climate forcing (Figures 5.9a-h). Additional moisture is simulated throughout the troposphere, with the greatest changes near the surface (Figures 5.9e-h). Changes in atmospheric moisture are generally smaller than expected mixing ratio increases from Clausius-Clapeyron (C-C) in the lower troposphere, resulting in reduced relative humidity during extreme rainfall events in future simulations, especially in the middle to upper troposphere (Figures 5.9i-l). However, additional low-level moisture in future simulations increases moisture transport adjacent to the center of events (Figures 5.10a-h) and enhances moisture convergence to the south of the event center (Figures 5.10i-p), even though weaker southerly low-level inflow occurs during events (Figures 5.11a-h).

Enhanced moisture convergence during extreme rainfall events primarily occurs from 900-700 hPa (Figures 5.10m-p), with increases generally simulated above the low-level cold pool where convergence is maximized. Increased moisture divergence occurs within the cold pool (Figures 5.10m-p) due to stronger divergent flow from the low-level mesohigh (Figures 5.10i-l). Competing changes in moisture convergence with height

(Figures 5.10i-l) result in no change in column-integrated moisture convergence in many locations adjacent to the event center where moisture convergence and divergence are vertically stacked (Figures 5.10m-p).

Stronger updrafts occur (Figures 5.12i-p) above the enhanced moisture convergence that is present atop the cold pool in future simulations (Figures 5.10m-p), driving higher rainfall rates over the center of extreme events (Figures 5.12a-d). Increased updraft velocities above 500 hPa (Figures 5.12i-p) are associated with additional CAPE to the south of the event center (Figures 5.11i-p) where slantwise vertical motion is initiated. Higher rainfall rates are generally co-located with increased 850 hPa downdraft velocities in future simulations (Figures 5.11e-h). The intensification of downdrafts becomes more prominent with stronger greenhouse warming, as a 44% increase in maximum 850 hPa downdraft velocity occurs in simulations of the RCP8.5 2090s compared with a 16% increase in the RCP4.5 2040s (Figures 5.11i-l).

Heavier rainfall rates and stronger downdrafts are likely related to the addition of more moisture into convective updrafts, but changes in temperature profiles with anthropogenic warming may also impact the efficiency of convective rainfall rates and the strength of downdrafts. Significant warming in future simulations causes higher freezing levels and greater warm-cloud thicknesses (vertical depths of clouds warmer than -10°C; Figures 5.11m-p), supporting collision-coalescence throughout a much deeper atmospheric column. This likely enhances rainfall rates and drives greater precipitation loading in future simulations, strengthening downdrafts. However, a complete examination of the impact of increased warm-cloud thicknesses on droplet sizes and rainfall rates in future simulations would require model simulations with much higher spatial resolution.

Heavier precipitation rates from additional moisture ingested into deep convective thunderstorms and greater warm-cloud thicknesses also enable the development of a stronger low-level cold pool through increases in evaporative cooling. Lower relative humidity throughout the troposphere in future simulations (Figures 5.9i-l) enhances evaporative cooling as drier air is entrained into thunderstorms, driving the development of stronger downdrafts as the entrained air becomes more negatively buoyant (Figures 5.12i-l). This is especially apparent in the RCP8.5 2090s when significantly drier air is present on the north side of storms and air with much lower relative humidity is present within downdraft columns (Figure 5.9l), enhancing evaporative cooling. A stronger temperature gradient occurs on the southern edge of the cold pool occur at the surface (Figures 5.13a-d) and in vertical cross sections (Figures 5.13e-h) in future simulations, suggesting the presence of stronger cold pools. Stronger density gradients from the enhanced cold pool and greater non-hydrostatic surface pressure increases from a stronger downdraft combine to develop a stronger surface mesohigh, as shown by increased gradients in sea-level pressure (Figures 5.13i-l) and low-level geopotential height (Figures 5.13m-p). Changes in the mesohigh are also expressed in changes in the low-level wind field, as the flow within the cold pool becomes more divergent and anti-cyclonic in future simulations, especially in the RCP8.5 2090s (Figures 5.13i-l). A stronger surface mesohigh enhances low-level moisture convergence above the cold pool (Figure 5.10m-p) where the diverging flow from the mesohigh meets the southerly LLJ (Figures 5.13i-l), possibly enhancing heavy precipitation rates during events. Greater moisture convergence is simulated above the enhanced cold pool throughout the duration of extreme rainfall events, suggesting that higher rainfall rates during extreme events may be related to a strengthening of the low-level cold pool and mesohigh.

While the low-level cold pool and surface mesohigh are clearly enhanced in future simulations, it is unclear whether the enhanced low-level cold pool and surface mesohigh have any effect on the duration of extreme rainfall events. No significant change in the duration of events is present in any future simulations, suggesting that enhancements in the low-level cold pool and mesohigh do not effect the length of heavy rainfall events in future simulations. However, because the period where low-level convergence is maximized along the surface cold pool is related to the fixed inertial oscillation of the LLJ (Blackadar 1957) and the nocturnal decoupling of the surface and boundary layers (Stull 1988), any changes in the strength and persistence of the cold pool and mesohigh may not impact the duration of extreme rainfall events. Changes in the strength of the cold pool and surface mesohigh may enhance precipitation rates while convergence between the LLJ and winds associated with the cold pool and mesohigh are maximized, possibly explaining the large increases in rainfall rates during simulated extreme events in the RCP8.5 2090s.

5.6 Discussion and Conclusions

In this study, model simulations realistically represent the basic characteristics of warm-season rainfall in the Central U.S. In addition, extreme rainfall events identified from historical simulations match the timing and intensity of events in the Stage IV precipitation dataset as well as observed events associated with flash flooding in Schumacher and Johnson [2006]. Therefore, while the projections in this study may be limited by inherent model biases, they provide a projection of how extreme precipitation in the region may be affected by climate change.

Increases in the frequency and intensity of heavy rainfall events occur in future simulations over both regions throughout the warm-season, with a disproportionate increase in the frequency of heavy rainfall events over 200 mm (7.87") compared to lighter events. Because simulated extreme rainfall events are similar to observed events that were associated with flash flooding in SJ2006, these results suggest that the occurrence of flash flooding in the Central U.S. may increase with climate change.

The realistic simulation of mesoscale conditions during extreme rainfall events enables an examination of potential mesoscale mechanisms that may contribute to the intensification of extreme rainfall events in the region. In future simulations, increased lower tropospheric moisture enables greater moisture transport into the center of deep convection. However, lower mid-tropospheric relative humidity enhances evaporative cooling as the additional moisture in convective updrafts encounters drier entrained air, causing the development of a stronger downdraft and low-level cold pool. Greater density gradients associated with the cold pool and larger non-hydrostatic pressure increases from enhanced downdrafts enhance the mesohigh and its associated circulation. Stronger moisture convergence occurs above the enhanced low-level cold pool where the northerly flow from the mesohigh opposes the southerly flow from the LLJ, causing stronger upward motion above the event center. While no change in the duration of heavy rainfall events is present in future simulations, heavier simulated rainfall rates during events are likely associated with the enhanced moisture convergence above the low-level cold pool and mesohigh. In addition, greater warm-cloud thicknesses associated with warming of the lower troposphere may enable collision-coalescence to operate throughout a thicker atmospheric column, possibly contributing to heavy rainfall rates in future simulations.

Intensification of extreme rainfall events that are associated with additional atmospheric moisture content, enhanced moisture convergence above a stronger low-level cold pool and mesohigh, and greater warm-cloud thicknesses are present in simulations of the RCP4.5 2040s, but are the clearest in the RCP8.5 2090s when anthropogenic forcing is stronger. In simulations of the RCP8.5 2090s, greenhouse warming is sufficient to overwhelm internal variability within the models, enabling a much clearer signal to emerge from the noise of natural variability that is present within the relatively short simulation periods.

In this study, we have identified possible mesoscale mechanisms that explain how additional atmospheric moisture could contribute to the intensification of extreme rainfall events over the Central U.S. While model simulations were aided by the use of a sophisticated microphysics scheme, higher resolution simulations may be required to accurately simulate meso-gamma-scale (2-20 km) and microscale (<1 km) processes that contribute to extreme rainfall events and were not explicitly resolved in these model simulations. Therefore, results from this study will likely need to be replicated using composites of simulated extreme rainfall events from model simulations with higher spatial resolution.

While future studies that incorporate higher spatial resolution are needed to confirm whether these mechanisms are likely to operate in a warmer climate, our results provide insights for further studies investigating the mesoscale mechanisms responsible for the increased frequency of extreme rainfall events. In addition, the knowledge of specific and realistic mechanisms that can contribute to the intensification of extreme rainfall events enables confidence in future projections of extreme precipitation from models. Because the Great Plains and Midwest are highly susceptible to warm-season precipitation extremes, an increased frequency in extreme rainfall events in the future could have significant societal and economic impacts. However, the growing scientific confidence in projections of regional rainfall extremes enables greater clarity for policymakers and stakeholders that consider adaptation, possibly reducing the potential impacts of increased precipitation extremes.

5.7 Acknowledgments

Support for this study was provided by the U.S. National Science Foundation under grant no. 1029711. This work was carried out in part using computing resources at the University of Minnesota Supercomputing Institute. We acknowledge the World Climate

Research Programme's Working Group on Coupled Modelling, which is responsible for CMIP, and we thank the climate modeling groups for producing and making available their model output. For CMIP, the U.S. Department of Energy's Program for Climate Model Diagnosis and Intercomparison provides coordinating support and led development of software infrastructure in partnership with the Global Organization for Earth System Science Portals. The authors thank Tom Hultquist for reviewing an early version of the manuscript.

5.8 Tables

Table 5.1. Number of extreme rainfall events identified in each dataset*

Dataset	North Central Events	South Central Events
SJ2006 (1999-2003)*	132	70
WRF-CMCC-CM (1990-1999)	124	97
WRF-CNRM-CM5 (1990-1999)	135	110
Stage IV (2002-2011)	171	144

*Multiplied by two to normalize by number of years; considered over approximately the same area as this study

Table 5.2. Precipitation totals for extreme rainfall events in North Central and South Central regions for Stage IV observations (2002-11) and WRF simulations of Historical scenario (1990-99)

	Average Hourly Max (mm)		Average 24-hour Max (mm)		Average Event Total (mm)	
	N. Central	S. Central	N. Central	S. Central	N. Central	S. Central
Stage IV	43.06	47.66	132.94	155.25	112.91	128.30
WRF-CMCC-CM	49.92	48.10	162.89	159.19	133.02	131.80
WRF-CNRM-CM5	51.70	56.20	157.42	192.88	124.75	151.15

Table 5.3. Number of extreme rainfall events in North Central and South Central regions from WRF simulations

	North Central				South Central			
	1990s	RCP4.5 2040s	RCP4.5 2090s	RCP8.5 2090s	1990s	RCP4.5 2040s	RCP4.5 2090s	RCP8.5 2090s
CMCC-CM	124	225	232	261	97	197	206	211
CNRM-CM5	135	173	207	227	110	170	174	175

Table 5.4. North Central U.S. simulated maximum hourly precipitation rates (mm/hour), daily precipitation rates (mm/day), and total event precipitation (mm) for heavy rainfall events in WRF simulations. Statistical significance as follows:
*90% confidence, ** 95% confidence, ***99% confidence.

North Central	Hourly Rainfall (mm/hour)				24-hour Rainfall (mm/day)				Event Rainfall (mm)			
	1990s	RCP4.5 2040s	RCP4.5 2090s	RCP8.5 2090s	1990s	RCP4.5 2040s	RCP4.5 2090s	RCP8.5 2090s	1990s	RCP4.5 2040s	RCP4.5 2090s	RCP8.5 2090s
CMCC-CM	49.92	52.02	51.80	55.47**	162.89	159.76	166.12	178.90**	133.02	127.62	135.82	147.82**
CNRM-CM5	51.70	49.08	51.58	56.14**	157.41	166.41	164.49	173.19***	124.75	127.06	124.09	133.64

Table 5.5. As Table 5.4 but for the South Central region.

South Central	Hourly Rainfall (mm)				24-hour Rainfall (mm)				Event Rainfall (mm)			
	1990s	RCP4.5 2040s	RCP4.5 2090s	RCP8.5 2090s	1990s	RCP4.5 2040s	RCP4.5 2090s	RCP8.5 2090s	1990s	RCP4.5 2040s	RCP4.5 2090s	RCP8.5 2090s
CMCC-CM	48.10	53.76**	55.52***	64.97***	159.19	176.01**	183.67***	199.57***	131.80	144.16	149.35**	170.15***
CNRM-CM5	56.20	56.73	57.72	66.94***	192.88	201.51	194.26	222.55***	151.15	155.46	150.06	174.81**

Table 5.6. Percent change in extreme rainfall events with event totals < 200 mm and ≥ 200 mm for the North Central and South Central regions.

	North Central						South Central					
	RCP4.5 2040s		RCP4.5 2090s		RCP8.5 2090s		RCP4.5 2040s		RCP4.5 2090s		RCP8.5 2090s	
	< 200 mm	≥ 200 mm	< 200 mm	≥ 200 mm	< 200 mm	≥ 200 mm	< 200 mm	≥ 200 mm	< 200 mm	≥ 200 mm	< 200 mm	≥ 200 mm
CMCC-CM	+88.0%	+31.3%	+86.1%	+93.8%	+105%	+150%	+91.9%	+220%	+90.7%	+320%	+70.9%	+540%
CNRM-CM5	+20.8%	+120%	+48.8%	+110%	+53.6%	+250%	+58.5%	+60.0%	+67.1%	+48.0%	+39.0%	+144%
Average	+54.4%	+75.7%	+67.5%	+102%	+79.3%	+200%	+75.2%	+140%	+78.9%	+184%	+55.0%	+342%

5.9 Figures

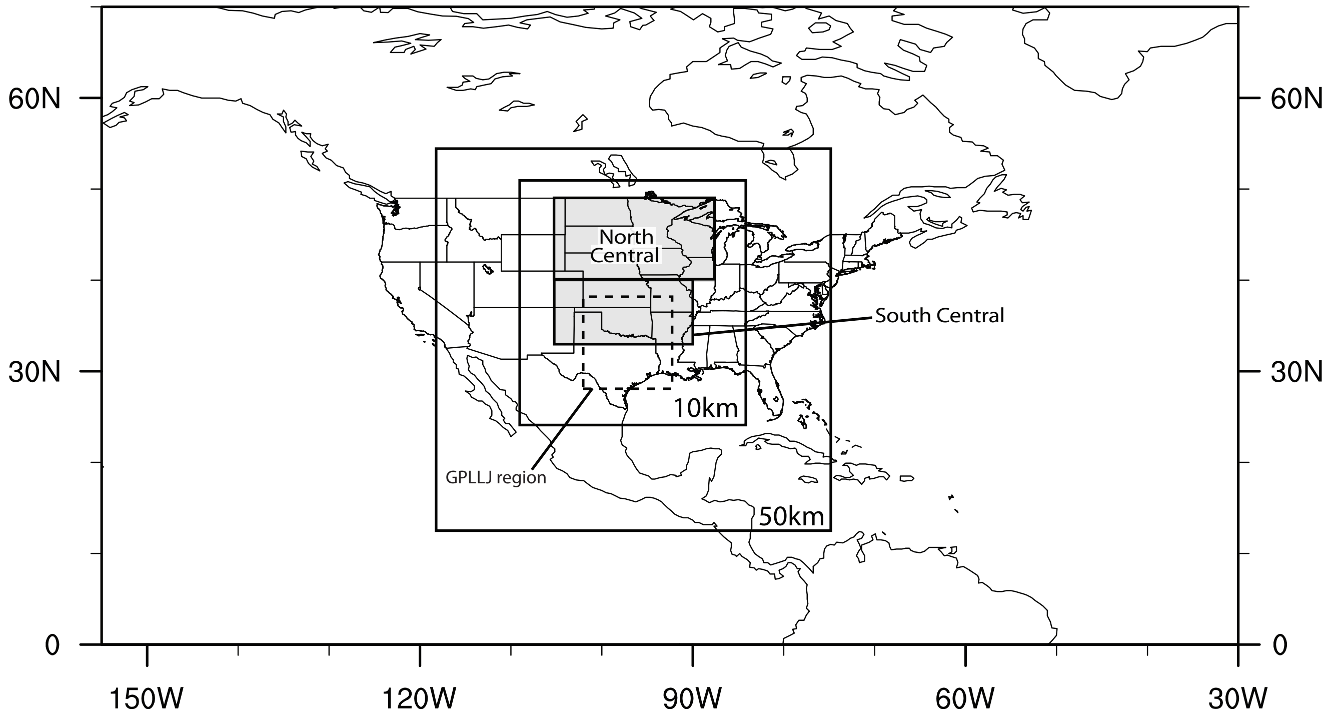

Figure 5.1. WRF 50-km outer domain and 10-km inner domain used in this study. The North Central (40°-49°N, 105°-88°W), South Central (33°-40°N, 105°-90°W), and GPLLJ regions (28°-38°N, 102°-92°W) are also shown. The Central region is the North Central and South Central regions combined.

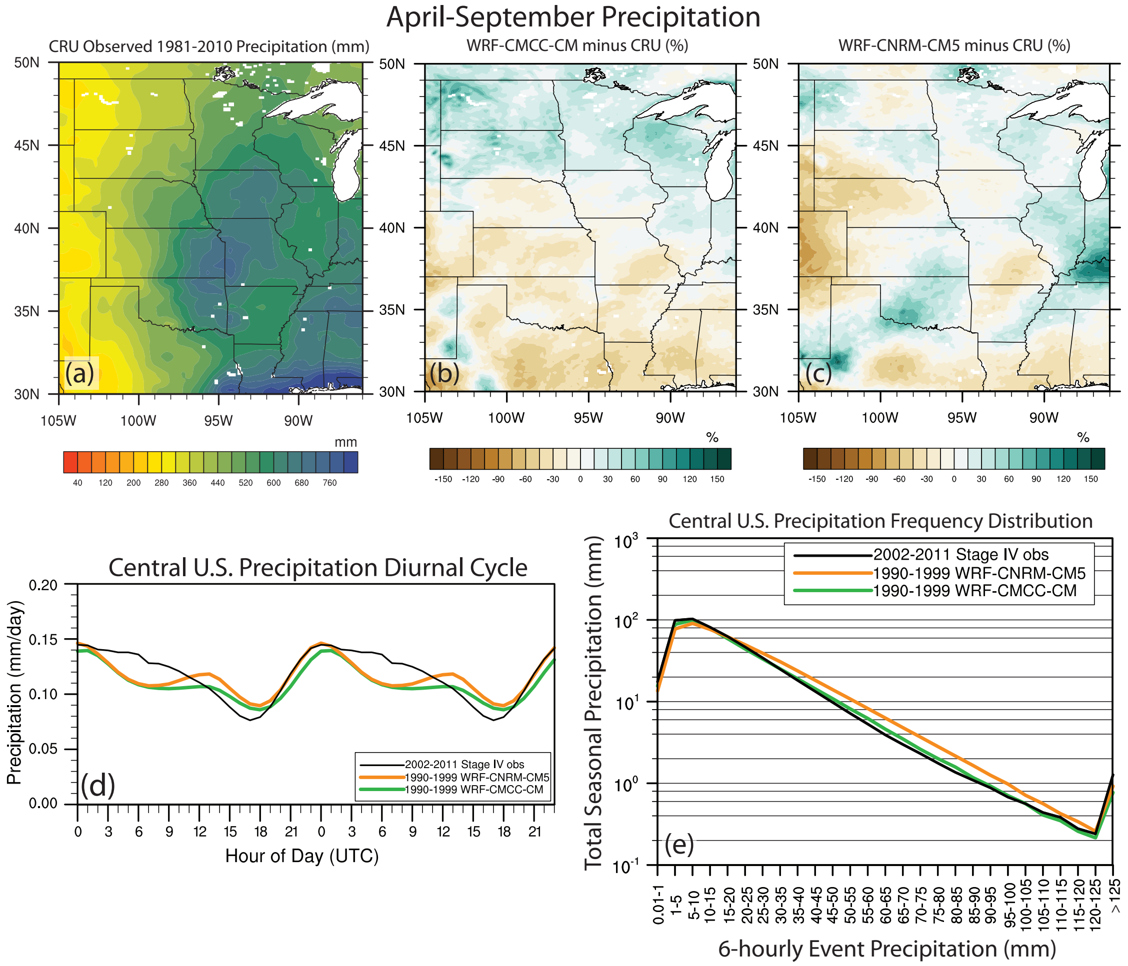

Figure 5.2. (a) Observed 1981-2010 April-September precipitation (mm) from the CRU dataset (Mitchell and Jones 2005). (b) Percent difference between 1990-99 WRF-CMCC-CM April-September simulated precipitation and 1981-2010 CRU observed precipitation, and (c) as (b) but for 1990-99 WRF-CNRM-CM5. (d) Diurnal cycle of April-September precipitation from WRF simulations and Stage IV (Lin and Mitchell 2005) precipitation dataset over the Central U.S. (e) Average Central U.S. total April-September precipitation from different 6-hourly precipitation events for WRF and Stage IV (Lin and Mitchell 2005).

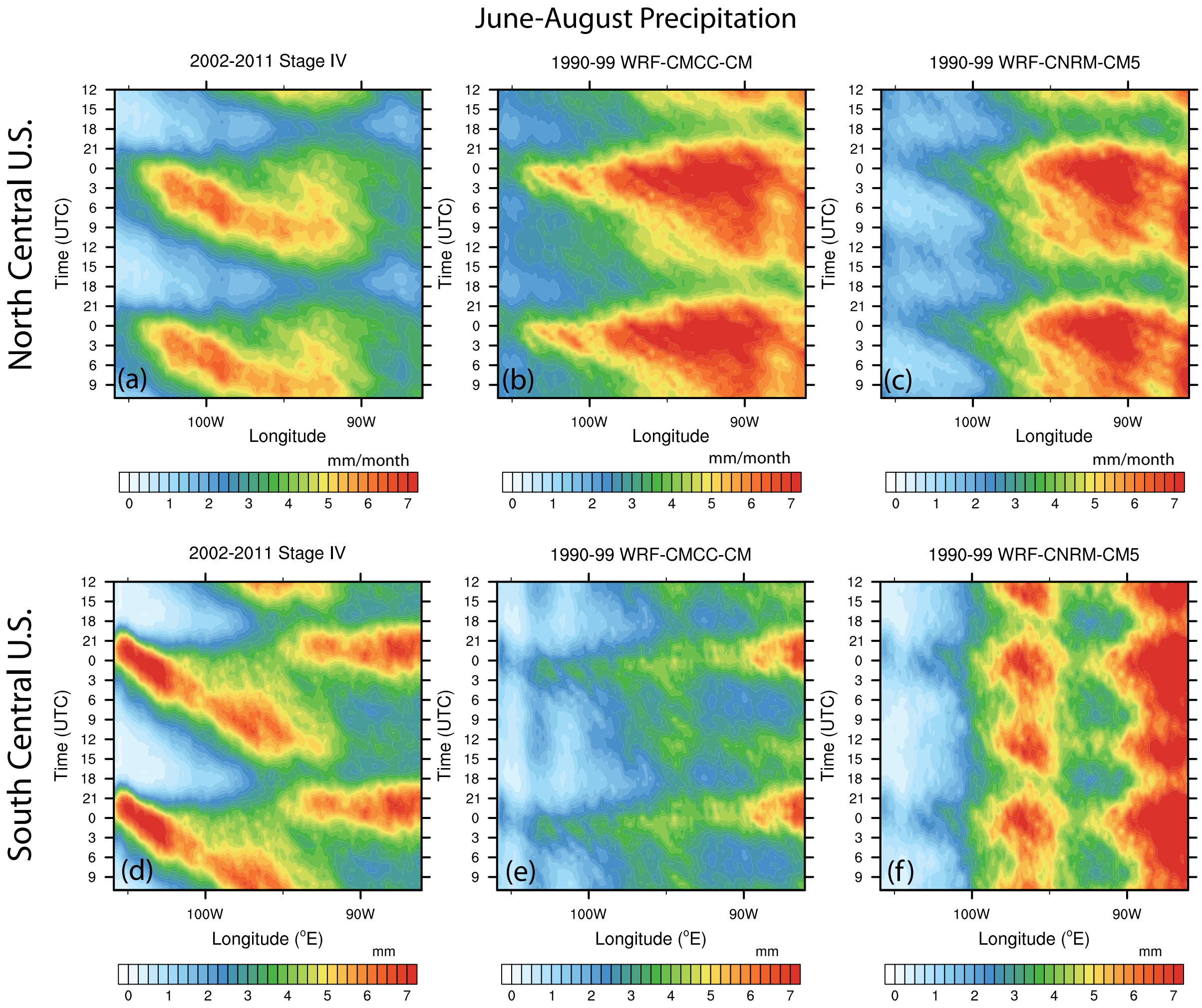

Figure 5.3. Hovmöller Diagrams of June-August North Central U.S. precipitation from (a) Stage IV observations for 2002-2011, (b) WRF-CMCC-CM for 1990-99, and (c) WRF-CNRM-CM5 for 1990-99. (d) through (f) as (a) through (c) but for the South Central region.

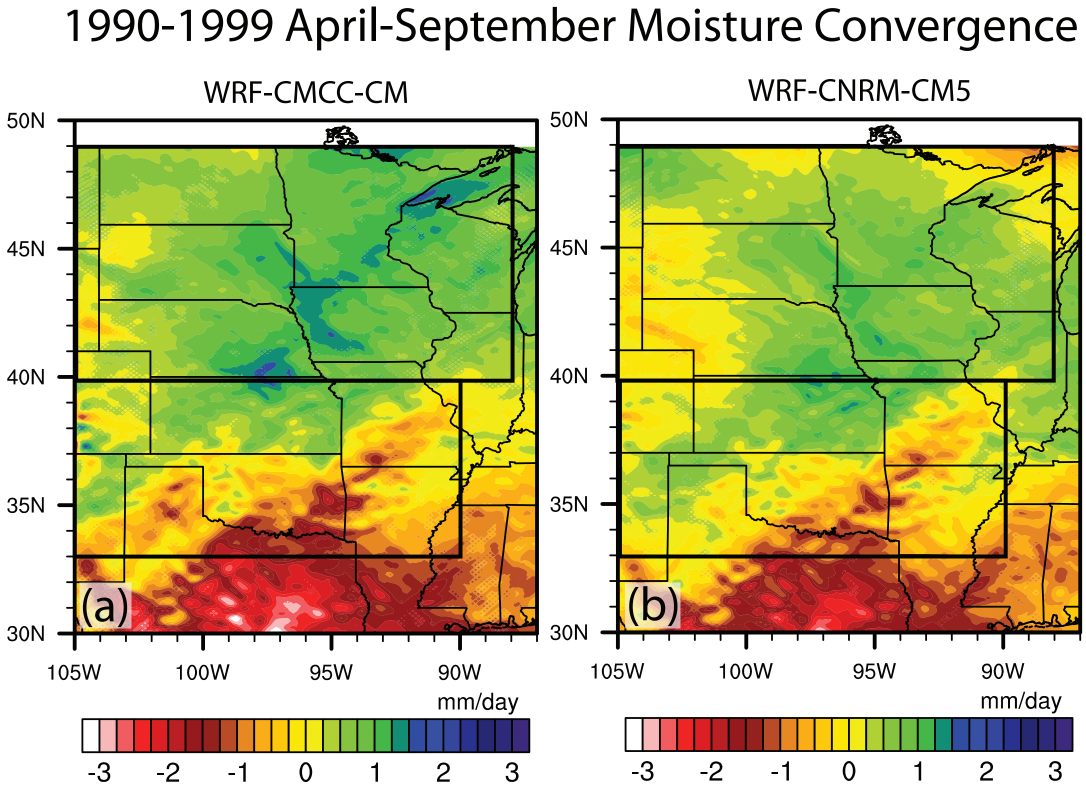

Figure 5.4. 1990-1999 April-September column-integrated moisture convergence (mm/day) from (a) WRF-CMCC-CM and (b) WRF-CNRM-CM5 simulations.

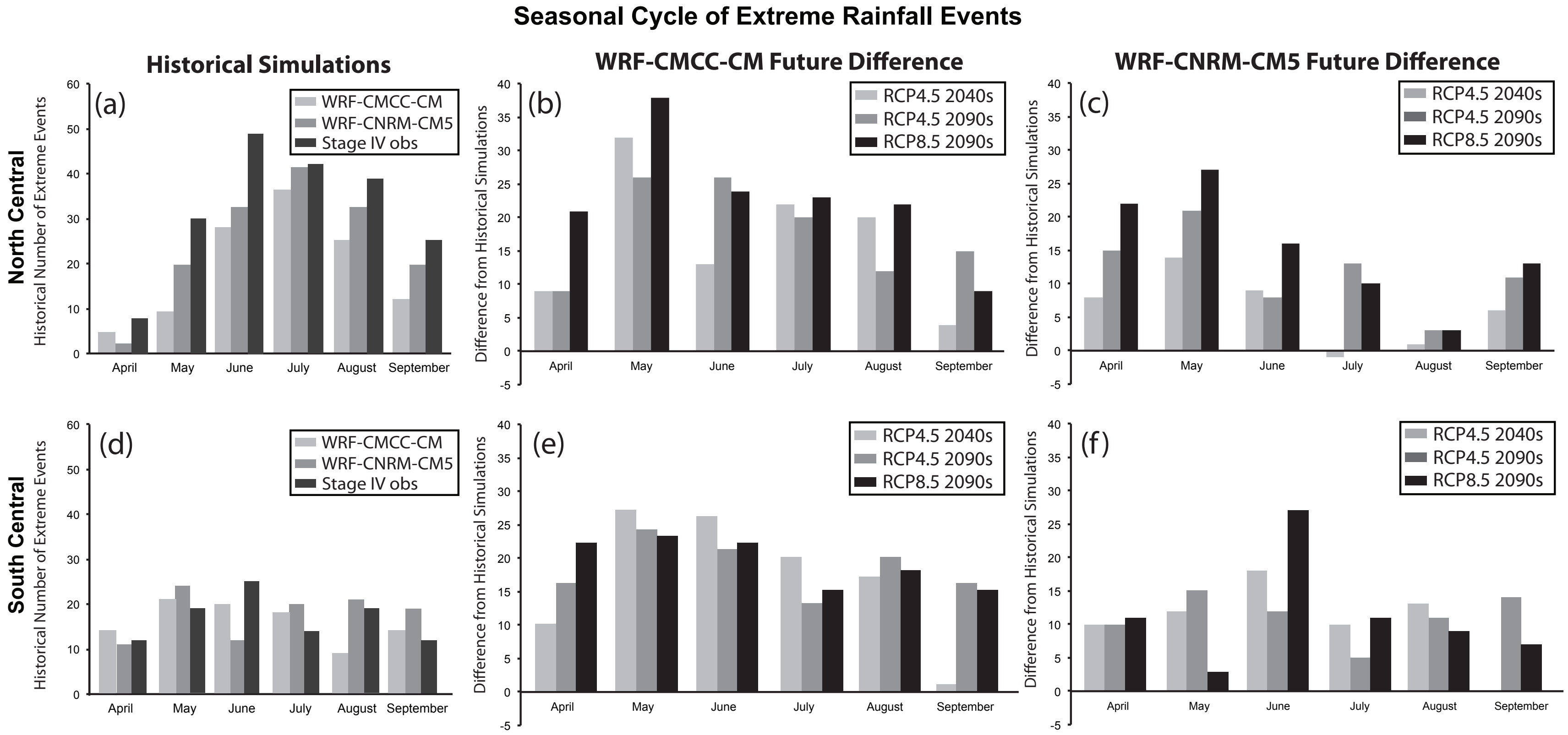

Figure 5.5. (a) Seasonal cycle of North Central extreme rainfall events for WRF simulations and Stage IV observations. Change in the occurrence of (b) North Central U.S. extreme rainfall events in future simulations compared with historical simulations from WRF-CMCC-CM and (c) WRF-CNRM-CM5. (d) through (f) as (a) through (c) but for the South Central U.S.

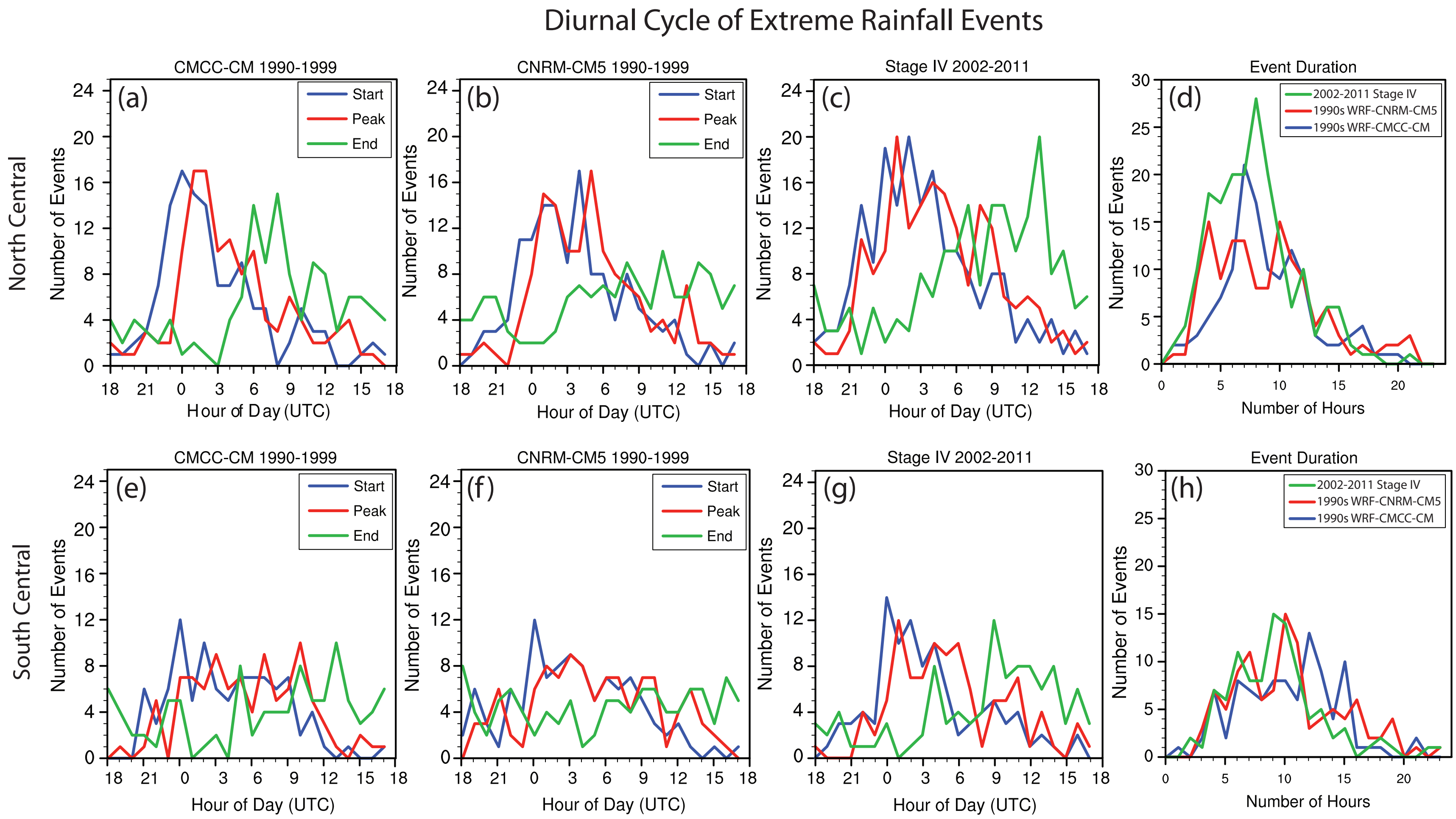

Figure 5.6. Diurnal cycle of the start, peak, and end times (UTC) of North Central discrete extreme rainfall events for (a) 1990-1999 WRF-CMCC-CM, (b) 1990-99 WRF-CNRM-CM5, and (c) 2002-2011 Stage IV observations. (d) North Central discrete extreme event duration (hours). (e) through (g) as (a) through (c) but for the South Central region. (h) South Central extreme event duration (hours).

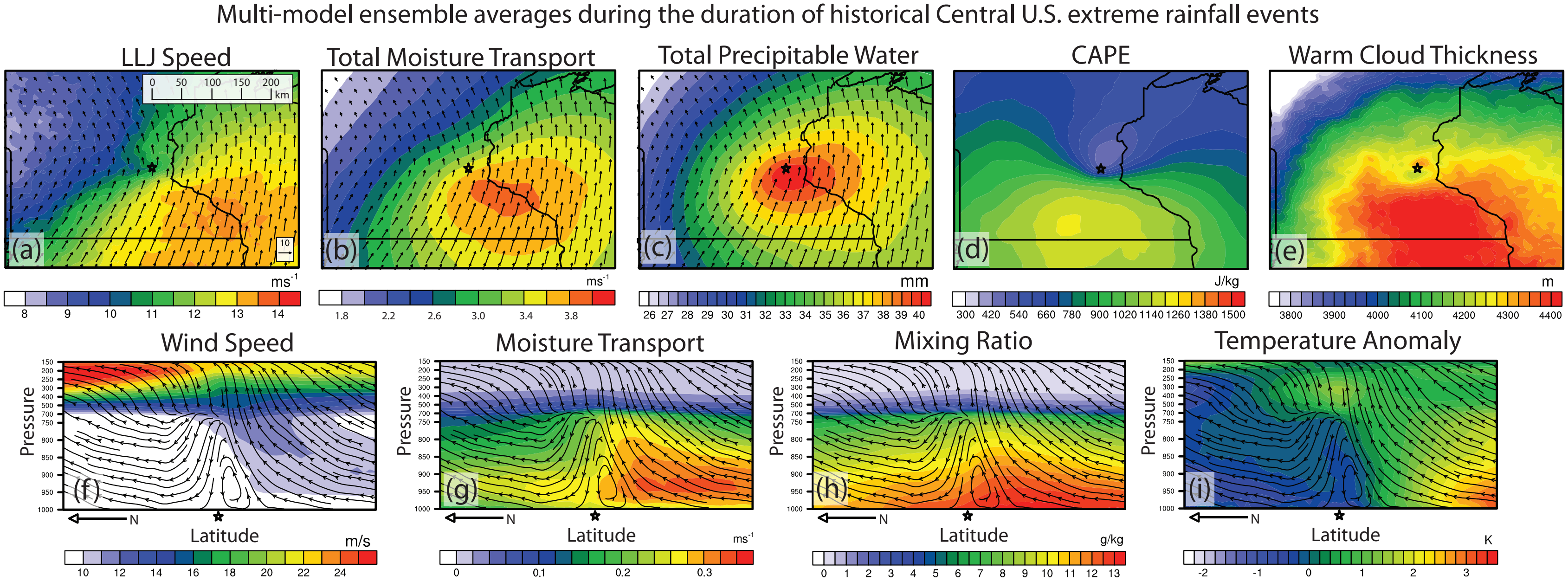

Figure 5.7. Multi-model ensemble (MME) of historical average (a) LLJ speed and LLJ vectors (m s^{-1}), (b) column-integrated moisture transport (kg m^{-1} s^{-1}) and LLJ vectors (m s^{-1}), (c) column-integrated precipitable water (mm) and LLJ vectors (m s^{-1}), (d) maximum parcel convective available potential energy (CAPE; J kg^{-1}), and (e) warm cloud thickness (m) during the duration of Central U.S. extreme rainfall events. Historical average latitude-pressure cross section of (f) wind speed (m s^{-1}), (g) moisture transport (kg m^{-1} s^{-1}), (h) mixing ratio (g kg^{-1}), and (i) temperature anomaly (K; anomaly from pressure level averages) during the duration of Central U.S. extreme rainfall events from MME. The composites are relative to the center of the event (largest 1-day rainfall total), which is indicated by a star. (a) through (e) are plotted on a map for visual reference. Cross sections intersect the center of events and include the same latitudinal area as (a) to (e). LLJ vectors represent the average wind field at the level of the low-level wind maximum. Vertical velocity component of cross section vectors were multiplied by a factor of ten.

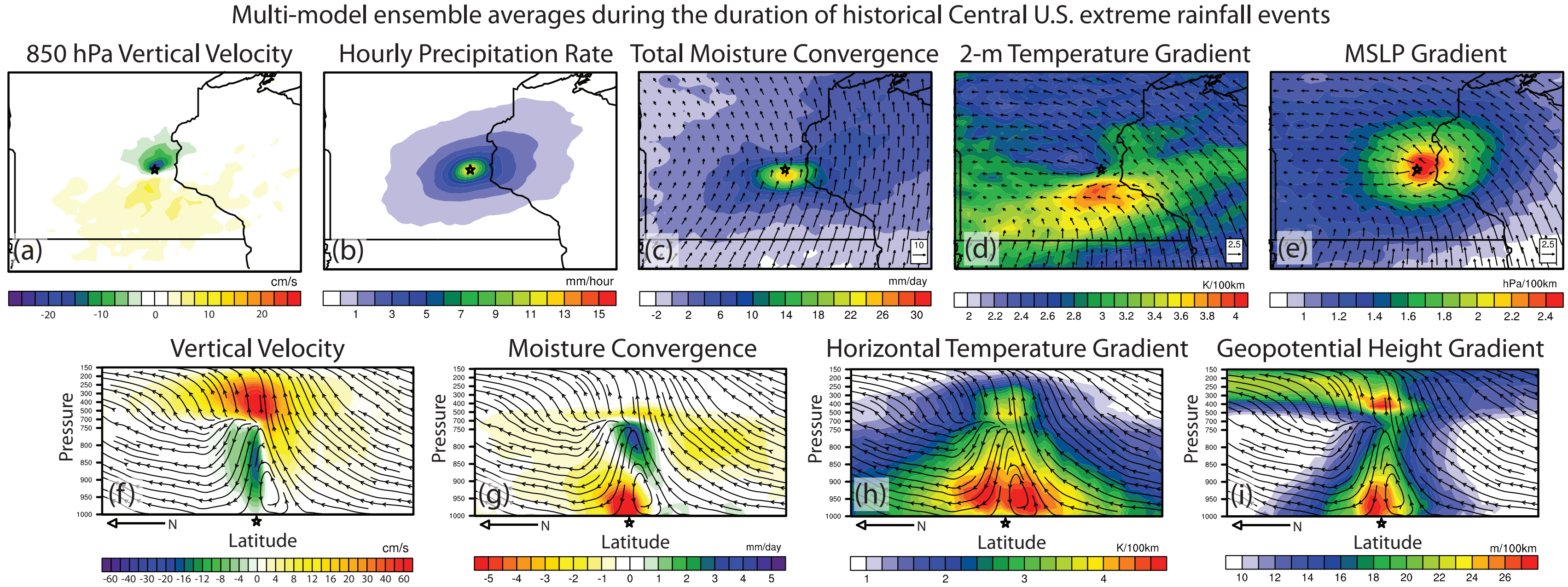

Figure 5.8. As Figure 5.7 but for (a) 850 hPa vertical velocity (cm s^{-1}), (b) hourly precipitation rate (mm hour^{-1}), (c) column-integrated moisture convergence (mm day^{-1}), (d) 2-m temperature gradient (K / 100 km), (e) sea level pressure gradient (hPa / 100 km), (f) vertical velocity (cm s^{-1}), (g) moisture convergence (mm/day), (h) horizontal temperature gradient (K / 100 km), and (h) geopotential height gradient (m / 100 km).

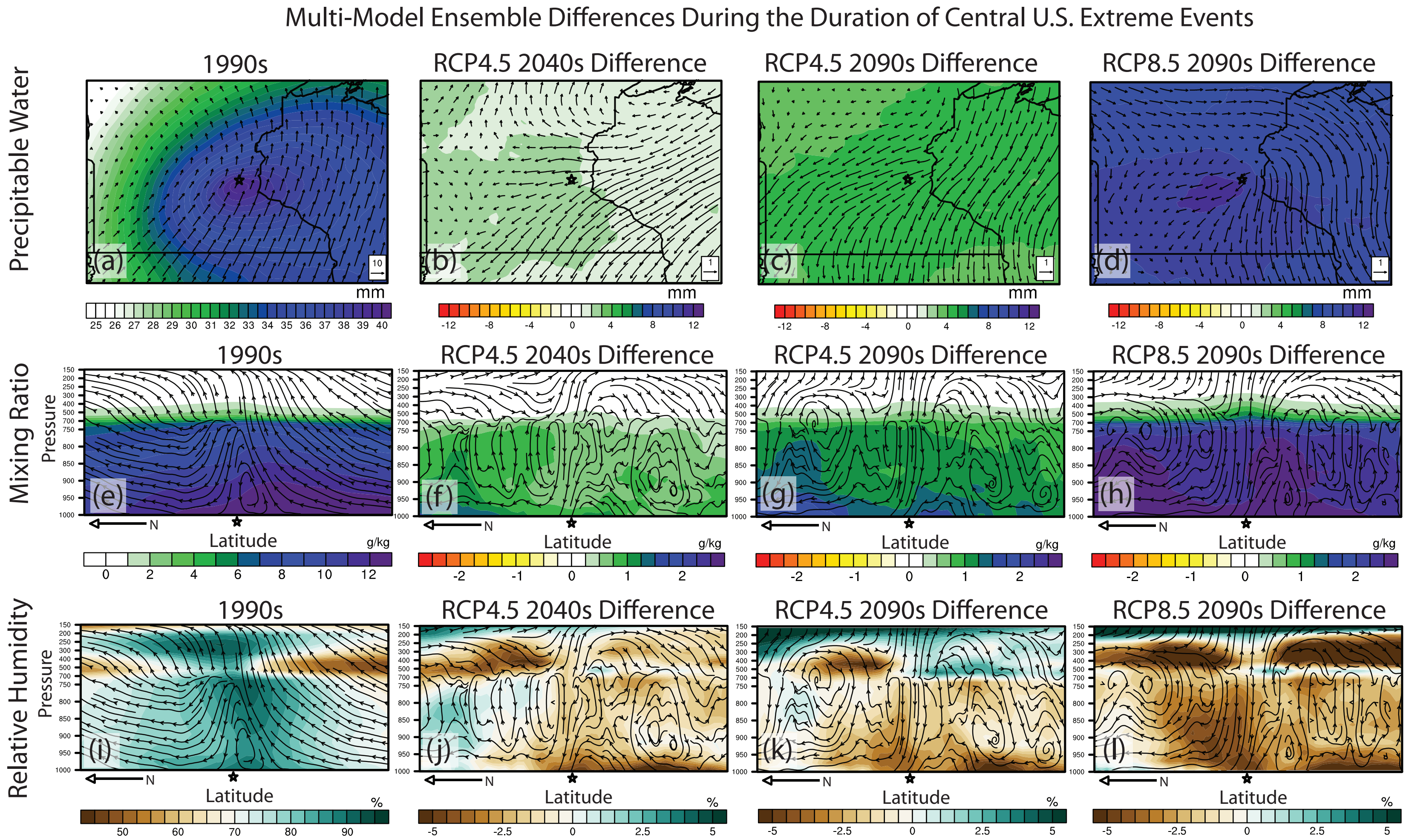

Figure 5.9. (a) Historical average column-integrated precipitable water (mm) and LLJ vectors (m s^{-1}) from MME during the duration of extreme rainfall events. (b) Difference from (a) in RCP4.5 2040s. (c) as (b) but for RCP4.5 2090s. (d) as (b) but for RCP8.5 2090s. (e) through (h) as (a) to (d) but for cross sections of mixing ratio (g kg^{-1}). (i) through (l) as (e) to (h) but for relative humidity (%).

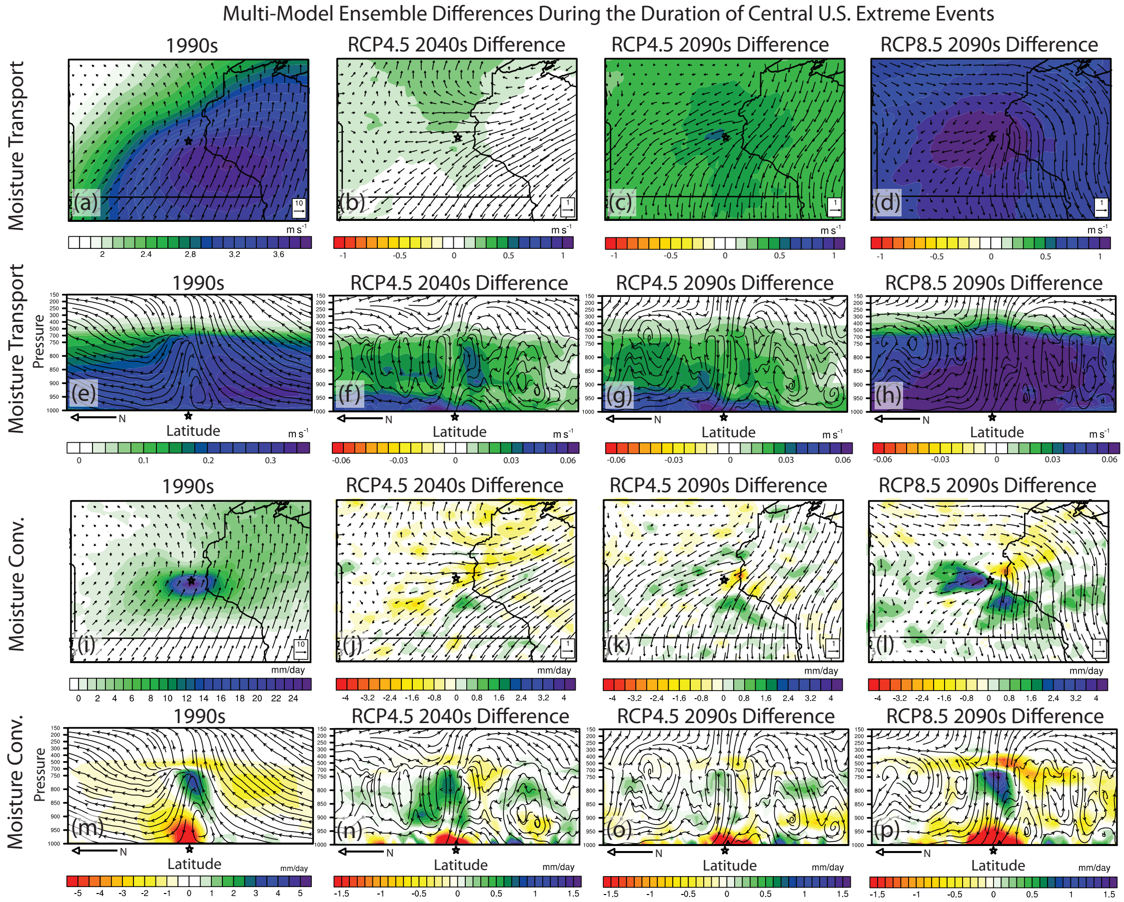

Figure 5.10. As Figure 5.9 but for column-integrated moisture transport (m s^{-1}) and LLJ vectors (m s^{-1}) in (a) to (d), cross sections of moisture transport (m s^{-1}) in (e) to (h), column-integrated moisture convergence (mm/day) and LLJ vectors (m s^{-1}) in (i) to (l), and cross sections of moisture convergence (mm/day) in (m) to (p).

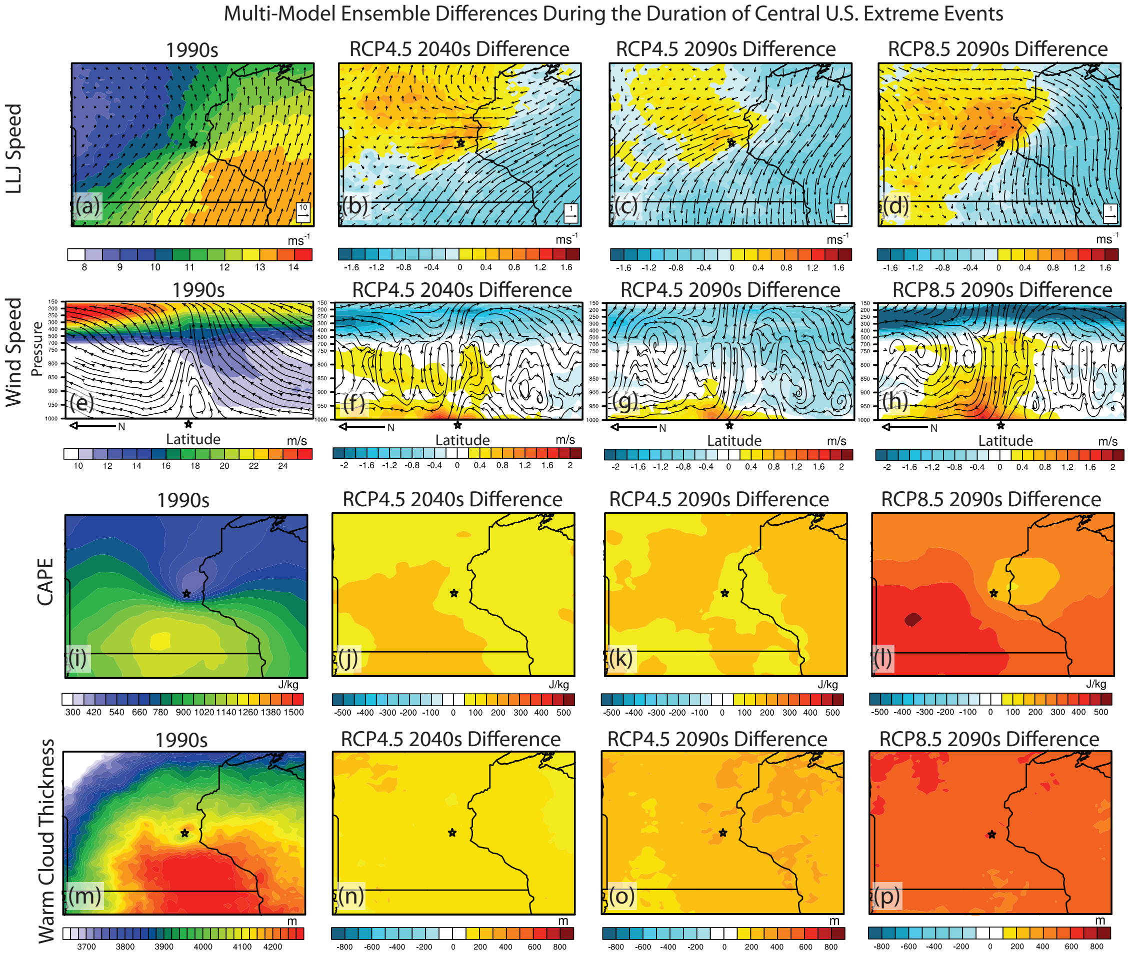

Figure 5.11. As Figure 5.9 but for LLJ speed and LLJ vectors (m s^{-1}) in (a) through (d), cross sections of wind speed (m s^{-1}) in (e) to (h), convective available potential energy (CAPE; J kg^{-1}) in (i) to (l), and warm cloud thickness (meters) in (m) through (p).

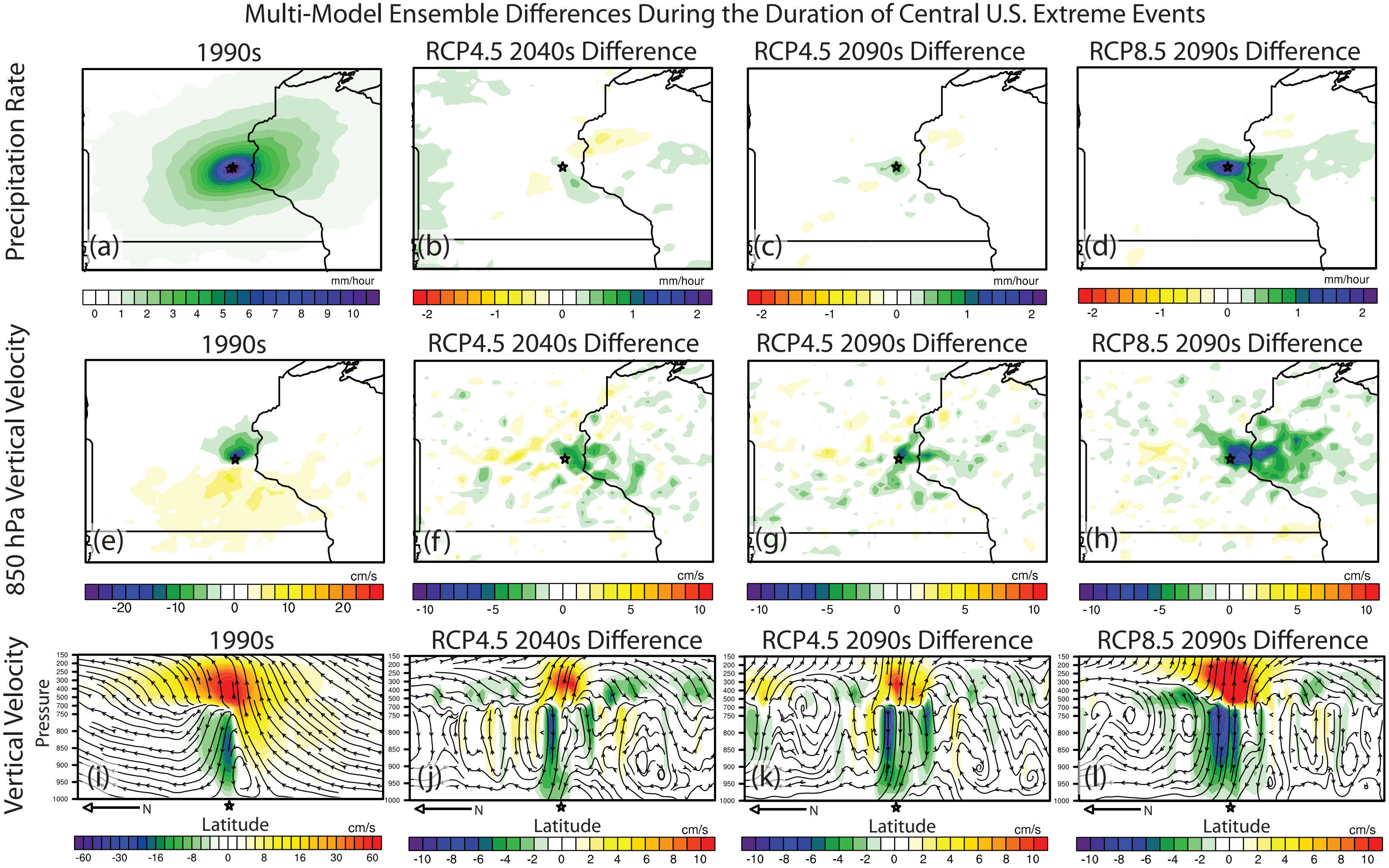

Figure 5.12. As Figure 5.9 but for hourly precipitation rate (mm/hour) in (a) through (d), 850 hPa vertical velocity (cm s^{-1}) in (e) through (h), and vertical velocity (cm s^{-1}) in (i) through (l).

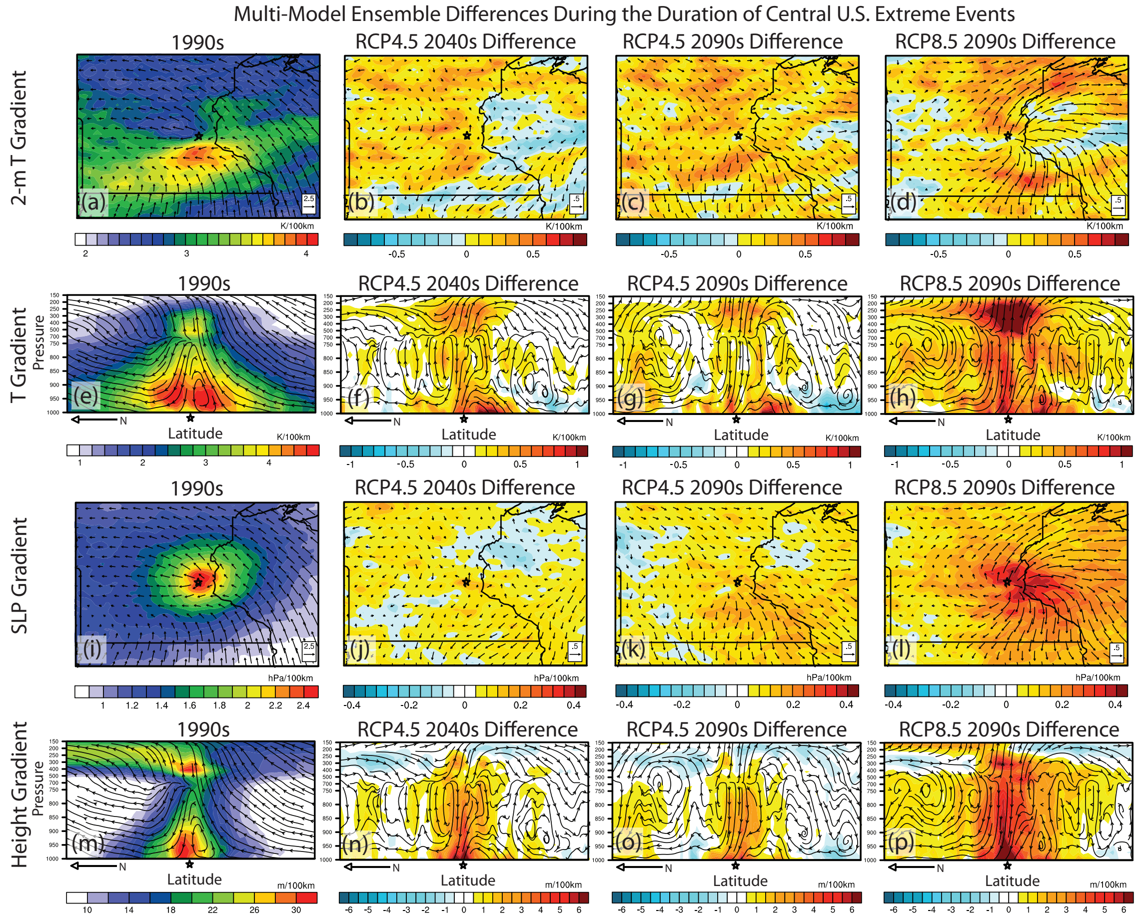

Figure 5.13. As Figure 5.9 but for 2-m temperature gradient (K / 100 km) and 10-m wind vectors (m s^{-1}) in (a) to (d), horizontal temperature gradient (K / 100 km) in (e) to (h), sea-level pressure gradient (hPa / 100 km) and 10-m wind vectors (m s^{-1}) in (i) to (l), and geopotential height gradient (m / 100 km) in (m) to (p).

Chapter 6

Conclusion

Climate change is expected to have significant societal impacts over the remainder of this century at local, regional, and global scales. Because the frequency and intensity of droughts and heavy rainfall events are expected to increase, the greatest impacts from climate change will likely involve both the scarcity and overabundance of water. Globally, droughts and heavy rainfall events have become more frequent over the last several decades with further acceleration as the climate warms. Recent severe droughts and widespread flooding from heavy rain events in the Central United States have caused significant socioeconomic damage over the last three decades. Because highly productive agricultural lands and critical infrastructure within the region are vulnerable to damage from changes in extreme precipitation events, it is critical that we understand how they might be affected by anthropogenic warming. Reducing uncertainty in future projections enables policy planners and regional stakeholders to determine the best practices for adapting to these changes with greater confidence.

Climate projections principally rely on simulations by GCMs that are conducted at resolutions too coarse to reliably produce long-term predictions of rainfall extremes. Simulated precipitation in GCMs is typically too light and occurs too often, greatly hampering the simulation of heavy rainfall events and the development of droughts in GCMs. In this study, it is demonstrated that dynamical downscaling of GCMs in WRF can improve the simulation of summer precipitation in the region. The simulation of heavy rainfall events and the basic timing, frequency, and intensity of precipitation can be significantly improved over the Central U.S. with dynamical downscaling in WRF compared to GCMs.

Using this knowledge, two of the newest generation of GCMs that can accurately simulate the drivers of regional precipitation were dynamically downscaled in historical and future scenarios. While uncertain changes in future seasonal rainfall totals occur in simulations of future periods, changes in the timing and frequency of precipitation typically have much greater socioeconomic impacts than variations in seasonal averages. Model simulations of future periods suggest that rainfall over the region will likely become less frequent and more intense, with more days between rainfall events. Increases in heavy rainfall events primarily occur during April-July, associated with a strengthening of the Great Plains Low Level Jet during those months. Conversely, a slight weakening of the Great Plains Low Level Jet during August-September drives increased drought in future simulations. Despite significant differences in the magnitude of these changes across the downscaled models, simulated future changes across large areas in both model simulations enables reasonable confidence in these results. In addition, the fact that precipitation rates and the occurrence of extreme rainfall events have also increased in the observed record lends considerable credibility to these model results.

While the agreement between model simulations and observational trends reduces the uncertainty of future projections, the inclusion of plausible future mechanisms further bolsters confidence in model results. Demonstrating that plausible physical mechanisms could be responsible for the simulated changes in precipitation provides assurance that results are not just model artifacts. In this study, we identified multiple mechanisms that appear to contribute to the increased frequency and intensity of extreme rainfall events in future simulations. Increases in extreme rainfall events in model simulations of the future are related to an intensification of the low-level cold pool and mesohigh, which drive greater ingestion of moisture into convective updrafts, enabling the development of higher rainfall rates. Tropospheric warming resulting from an increase in greenhouse gases may also enable collision-coalescence processes to operate throughout a thicker atmospheric column, driving higher rainfall rates. However, model simulations at cloud-resolving resolutions would be required to determine whether this theoretical process could be responsible for higher precipitation rates in extreme rainfall events. Much of the early warm-season intensification of heavy rainfall events over the North Central U.S. could be related to a stronger GPLLJ. Increases in precipitation during the early warm-season primarily are related to the increased frequency of moderate and strong GPLLJ events, which provide additional moisture convergence for the development of convective precipitation. While additional mechanisms could be responsible, the identification of physical mechanisms that drive the intensification of extreme rainfall events enables confidence that model projections from this study are not strictly artifacts.

While this study has increased confidence in projections of precipitation in the Central U.S., further work is required to fully understand how the basic character of rainfall in the region will be affected by climate change. A limited number of model simulations were completed in this study because of the finite availability of computing power, meaning that model results could be heavily influenced by internal variability. While the inclusion of multiple downscaled GCMs reduced the influence of internal variability on model results, the simulated 10-year timeslices were still heavily influenced by internal variability, especially in the RCP4.5 2040s when the anthropogenic forcing was considerably weaker than later in the century or for the stronger scenario. This likely explains why many results in this study were only statistically significant in the RCP8.5 2090s when the signal from anthropogenic forcing overwhelmed the noise of natural variability for many variables. The use of longer future timeslices and/or larger initial condition or multi-model ensembles can reduce the impacts of internal variability on such climate projections (Deser et al. 2014), enabling better insights into the precise changes that are likely to occur in the basic characteristics of Central U.S. precipitation. In addition, nocturnal convective precipitation may not be fully resolved without a convective parameterization in WRF in model simulations with a 10-km spatial resolution where the large-scale forcing is weak, placing limitations on some results in this study (i.e., South Central U.S. projections). While higher resolution simulations would have provided a more physically realistic representation of convective precipitation (especially in the South Central U.S.), increasing spatial resolution would have greatly reduced the number of model simulations that could have been completed. Furthermore, large model ensembles conducted at higher resolutions might enable more definitive predictions of how the basic characteristics of precipitation will be affected by climate change.

Regardless, the projected changes in the timing, frequency, and intensity of precipitation based on model simulations described in this study would have significant socioeconomic impacts in the region, especially involving agriculture, water availability, and the hydrologic infrastructure. Even with no change in total seasonal precipitation, more intense but less frequent rainfall would increase runoff during precipitation events and reduce soil moisture between rainfall episodes. These basic changes in the character of summer precipitation will likely have significant impacts on regional agriculture, requiring changes in water and crop management to enable the agricultural yields that we have all come to expect. The continued development of drought-tolerant crops could enable further cultivation of traditional crops in the region, but changes in the regional hydroclimate might eventually necessitate the planting of completely different crop varieties. Reduced soil moisture between rainfall events might also reduce agricultural yields without supplemental irrigation, which will likely further promote the expansion of irrigation in the Great Plains, which has been linked to the depletion of regional aquifers (Gutentag et al. 1984; McGuire 2013). Because such a small percentage of irrigated water is returned to the region as rainfall (Harding and Snyder 2012a) despite small increases in precipitation from irrigation (Harding and Snyder 2012b), further groundwater depletion could reduce yields as groundwater drilling becomes prohibitively expensive and large areas of land are taken out of production.

While the scarcity of water will likely have large socioeconomic impacts, so will the overabundance of water associated with higher precipitation rates. Additional runoff from heavier rainfall rates would negatively impact hydrologic infrastructure (i.e., storm sewers, culverts, bridges, dams, etc.) while also reducing infiltration into severely depleted groundwater aquifers in the region (e.g., the Ogallala Aquifer). Substantial effort will likely be required to modify the design of infrastructure to withstand greater demands not only from heavier rainfall rates and greater surface flows, but also from reduced surface and near-surface water during longer stretches without precipitation. Industries that are dependent on abundant surface water (e.g. power plant cooling, channel navigation, hydroelectric power generation) may incur significant costs to preserve stable streamflows and lake levels. Because these future changes pose a socioeconomic risk, dissemination of research results from the scientific community to stakeholders is necessary for reducing potential future harm. Effective communication between scientists and policymakers can enable better guidance for those responsible for mitigating the potential problems that may be caused by the changing character of precipitation in the region.

6.1 Future Work

While the results of this study will contribute to improving confidence in future projections of extreme rainfall in the Central United States, further study is needed to provide stakeholders the information that they need to develop strategies for climate adaptation and mitigation of future losses. It is expected that rainfall will be more intense but occur less often with more severe periods of drought between rainfall events. A future intensification of drought, which may primarily occur in the late summer, would be particularly damaging over semi-arid regions of the Great Plains where agriculture is already heavily dependent on irrigation. However, model simulations in this study incorporated static vegetation that does not respond to changes in temperature or moisture availability. Therefore, future projections of drought did not resolve land-atmosphere interactions (i.e., the phenological response to drought and its impact on precipitation recycling) that can prolong and intensify drought conditions (Wang et al. 2003) and future increases in drought in this study could be underestimated. Additional modeling efforts should include dynamic vegetation, enabling more realistic projections of drought that include low-frequency variability related to the response of vegetation to drought. Doing so would require continuous simulations over multiple decades instead of simulations over individual years as were conducted in this study, likely resulting in a significant increase in the computing required if model simulations are to be completed at a similar spatial resolution.

The expected increase in the frequency and intensity of heavy rainfall events might be driven by a number of physical processes, some of which were identified in this study. The simulated increases in rainfall rates associated with strengthening of the low-level cold pool and mesohigh that were present in this study will need to be replicated in simulations that include a finer spatial resolution that can better resolve these storm-scale processes. The simulations of individual storms in this study could be further downscaled, significantly reducing the computing demands that would be required for such a study. While the Great Plains Low-Level Jet has been identified as a potential driver of more frequent and intense extreme rainfall events in future simulations, variations in the GPLLJ are heavily influenced by decadal variability (e.g., AMO and PDO) which modulate the strength and position of the GPLLJ. Therefore, future studies must include longer timeslices that can negate the influence that internal variability can have on the GPLLJ on decadal timescales. Because the GPLLJ can be heavily influenced by the variations in geopotential height over the North Pacific (as demonstrated in Chapter Two of this study), conducting model simulations over a larger model domain would enable the general circulation-scale influences of the GPLLJ to be included. Therefore, future studies should also use model simulations that can sufficiently resolve these influences, enabling an investigation into why the GPLLJ may be enhanced with anthropogenic warming.

Bibliography

Adler, R. F., and Coauthors, 2003: The version-2 global precipitation climatology project (GPCP) monthly precipitation analysis (1979-present). *J Hydrometeorol*, **4,** 1147-1167.

AghaKouchak, A., A. Behrangi, S. Sorooshian, K. Hsu, and E. Amitai, 2011: Evaluation of satellite-retrieved extreme precipitation rates across the central United States. *J Geophys Res-Atmos*.

Alexander, M. A., J. D. Scott, K. Mahoney, and J. Barsugli, 2013: Greenhouse Gas-Induced Changes in Summer Precipitation over Colorado in NARCCAP Regional Climate Models. *J Climate*, **26,** 8690-8697.

Allan, R. P., and B. J. Soden, 2008: Atmospheric warming and the amplification of precipitation extremes. *Science*, **321,** 1481-1484.

Allen, M. R., and W. J. Ingram, 2002: Constraints on future changes in climate and the hydrologic cycle. *Nature*, **419,** 224-232.

Argueso, D., J. M. Hidalgo-Munoz, S. R. Gamiz-Fortis, M. J. Esteban-Parra, and Y. Castro-Diez, 2012: High-resolution projections of mean and extreme precipitation over Spain using the WRF model (2070-2099 versus 1970-1999). *J Geophys Res-Atmos*, **117**.

Arritt, R. W., T. D. Rink, M. Segal, D. P. Todey, C. A. Clark, M. J. Mitchell, and K. M. Labas, 1997: The great plains low-level jet during the warm season of 1993. *Mon Weather Rev*, **125,** 2176-2192.

Atlas, D., R. Tatehira, R. C. Srivastava, W. Marker, and R. E. Carbone, 1969: Precipitation-induced mesoscale wind perturbations in the melting layer. *Quarterly Journal of the Royal Meteorological Society*, **95,** 544-560.

Barandiaran, D., S.-Y. Wang, and K. Hilburn, 2013: Observed trends in the Great Plains low-level jet and associated precipitation changes in relation to recent droughts. *Geophysical Research Letters*, **40,** 2013GL058296.

Barnston, A. G., and R. E. Livezey, 1987: Classification, Seasonality and Persistence of Low-Frequency Atmospheric Circulation Patterns. *Mon Weather Rev*, **115,** 1083-1126.

Bates, B. C., S. Kundzewicz, and J. P. Palutikof, 2008: *Climate Change and Water. Technical Paper of the Intergovernmental Panel on Climate Change.* IPCC Secretariat, 210 pp.

Becker, E. J., E. H. Berbery, and R. W. Higgins, 2009: Understanding the Characteristics of Daily Precipitation over the United States Using the North American Regional Reanalysis. *J Climate*, **22,** 6268-6286.

Bell, G. D., and J. E. Janowiak, 1995: Atmospheric Circulation Associated with the Midwest Floods of 1993. *B Am Meteorol Soc*, **76,** 681-695.

Betts, R. A., P. M. Cox, S. E. Lee, and F. I. Woodward, 1997: Contrasting physiological and structural vegetation feedbacks in climate change simulations. *Nature*, **387,** 796-799.

Blackadar, A. K., 1957: Boundary layer wind maxima and their significance for the growth of nocturnal inversions. *B Am Meteorol Soc*, **38,** 283-290.

Bluestein, H. B., and M. H. Jain, 1985: Formation of Mesoscale Lines of Precipitation - Severe Squall Lines in Oklahoma during the Spring. *Journal of the Atmospheric Sciences*, **42,** 1711-1732.

Bonner, W. D., 1968: Climatology of the low-level jet. *Mon Weather Rev*, **96,** 833-850.

Bosilovich, M. G., and S. D. Schubert, 2002: Water vapor tracers as diagnostics of the regional hydrologic cycle. *J Hydrometeorol*, **3,** 149-165.

Brubaker, K. L., P. A. Dirmeyer, A. Sudradjat, B. S. Levy, and F. Bernal, 2001: A 36-yr climatological description of the evaporative sources of warm-season precipitation in the Mississippi River basin. *J Hydrometeorol*, **2,** 537-557.

Bukovsky, M. S., and D. J. Karoly, 2011: A Regional Modeling Study of Climate Change Impacts on Warm-Season Precipitation in the Central United States. *J Climate*, **24,** 1985-

2002.

Castro, C. L., R. A. Pielke, and G. Leoncini, 2005: Dynamical downscaling: Assessment of value retained and added using the regional atmospheric modeling system (RAMS). *J Geophys Res-Atmos*, **110**.

Changnon, S. A., 2001: Thunderstorm rainfall in the conterminous United States. *B Am Meteorol Soc*, **82,** 1925-1940.

Chao, W. C., 2012: Correction of Excessive Precipitation over Steep and High Mountains in a GCM. *Journal of the Atmospheric Sciences*, **69,** 1547-1561.

Chen, C. T., and T. Knutson, 2008: On the verification and comparison of extreme rainfall indices from climate models. *J Climate*, **21,** 1605-1621.

Chen, F., and J. Dudhia, 2001: Coupling an advanced land surface-hydrology model with the Penn State-NCAR MM5 modeling system. Part I: Model implementation and sensitivity. *Mon Weather Rev*, **129,** 569-585.

Clark, A. J., W. A. Gallus, and T. C. Chen, 2007: Comparison of the diurnal precipitation cycle in convection-resolving and non-convection-resolving mesoscale models. *Mon Weather Rev*, **135,** 3456-3473.

Clark, A. J., W. A. Gallus, M. Xue, and F. Y. Kong, 2009: A Comparison of Precipitation Forecast Skill between Small Convection-Allowing and Large Convection-Parameterizing Ensembles. *Weather Forecast*, **24,** 1121-1140.

Collins, M., R. E. Chandler, P. M. Cox, J. M. Huthnance, J. Rougier, and D. B. Stephenson, 2012: Quantifying future climate change. *Nat Clim Change*, **2,** 403-409.

Coniglio, M. C., J. Y. Hwang, and D. J. Stensrud, 2010: Environmental Factors in the Upscale Growth and Longevity of MCSs Derived from Rapid Update Cycle Analyses. *Mon Weather Rev*, **138,** 3514-3539.

Cook, K. H., E. K. Vizy, Z. S. Launer, and C. M. Patricola, 2008: Springtime Intensification of the Great Plains Low-Level Jet and Midwest Precipitation in GCM

Simulations of the Twenty-First Century. *J Climate*, **21,** 6321-6340.

Corfidi, S. F., 2003: Cold pools and MCS propagation: Forecasting the motion of downwind-developing MCSs. *Weather Forecast*, **18,** 997-1017.

CPC, cited 2014: Teleconnections: Pacific/North American Pattern. Monthly Mean PNA Index. [Available online at http://www.cpc.ncep.noaa.gov/products/precip/CWlink/pna/month_pna_index2.shtml.]

Dai, A., 2006: Precipitation characteristics in eighteen coupled climate models. *J Climate*, **19,** 4605-4630.

Dai, A., 2013: Increasing drought under global warming in observations and models. *Nat Clim Change*, **3,** 52-58.

Dai, A., K. E. Trenberth, and T. T. Qian, 2004: A global dataset of Palmer Drought Severity Index for 1870-2002: Relationship with soil moisture and effects of surface warming. *J Hydrometeorol*, **5,** 1117-1130.

Davis, R. S., 2001: Flash Flood Forecast and Detection Methods. *Meteorological Monographs*, **28,** 481-526.

Dawson, D. T., M. Xue, J. A. Milbrandt, and M. K. Yau, 2010: Comparison of Evaporation and Cold Pool Development between Single-Moment and Multimoment Bulk Microphysics Schemes in Idealized Simulations of Tornadic Thunderstorms. *Mon Weather Rev*, **138,** 1152-1171.

Dee, D. P., and Coauthors, 2011: The ERA-Interim reanalysis: configuration and performance of the data assimilation system. *Quarterly Journal of the Royal Meteorological Society*, **137,** 553-597.

Deser, C., A. S. Phillips, M. A. Alexander, and B. V. Smoliak, 2014: Projecting North American Climate Over the Next 50 Years: Uncertainty due to Internal Variability. *J Climate*.

Dirmeyer, P. A., and J. L. Kinter, 2010: Floods over the US Midwest: A Regional Water

Cycle Perspective. *J Hydrometeorol*, **11,** 1172-1181.

Dominguez, F., P. Kumar, X. Z. Liang, and M. F. Ting, 2006: Impact of atmospheric moisture storage on precipitation recycling. *J Climate*, **19,** 1513-1530.

Doswell, C. A., H. E. Brooks, and R. A. Maddox, 1996: Flash flood forecasting: An ingredients-based methodology. *Weather Forecast*, **11,** 560-581.

Dudhia, J., 1989: Numerical Study of Convection Observed during the Winter Monsoon Experiment Using a Mesoscale Two-Dimensional Model. *Journal of the Atmospheric Sciences*, **46,** 3077-3107.

Duffy, P. B., and Coauthors, 2003: High-resolution simulations of global climate, part 1: present climate. *Climate Dynamics*, **21,** 371-390.

Durack, P. J., S. E. Wijffels, and R. J. Matear, 2012: Ocean Salinities Reveal Strong Global Water Cycle Intensification During 1950 to 2000. *Science*, **336,** 455-458.

Feldstein, S. B., 2000: The timescale, power spectra, and climate noise properties of teleconnection patterns. *J Climate*, **13,** 4430-4440.

Fischer, E. M., and R. Knutti, 2014: Detection of spatially aggregated changes in temperature and precipitation extremes. *Geophysical Research Letters***,** 2013GL058499.

Ford, T. W., and S. M. Quiring, 2013: Influence of MODIS-derived dynamic vegetation on VIC-simulated soil moisture in Oklahoma. *J Hydrometeorol*.

Fovell, R. G., and Y. Ogura, 1989: Effect of Vertical Wind Shear on Numerically Simulated Multicell Storm Structure. *Journal of the Atmospheric Sciences*, **46,** 3144-3176.

Friedl, M., and Coauthors, 2002: Global land cover mapping from MODIS: algorithms and early results. *Remote Sens Environ***,** 287-302.

Fujita, T. T., 1959: Precipitation and cold air production in mesoscale thunderstorm systems. *Journal of Meteorology*, **16,** 454-466.

Funk, T. W., 1991: Forecasting Techniques Utilized by the Forecast Branch of the National-Meteorological-Center during a Major Convective Rainfall Event. *Weather Forecast*, **6,** 548-564.

Gao, Y., J. S. Fu, J. B. Drake, Y. Liu, and J. F. Lamarque, 2012: Projected changes of extreme weather events in the eastern United States based on a high resolution climate modeling system. *Environ Res Lett*, **7**.

Gober, M., E. Zsoter, and D. S. Richardson, 2008: Could a perfect model ever satisfy a naive forecaster? On grid box mean versus point verification. *Meteorol Appl*, **15,** 359-365.

Gómez-Navarro, J. J., J. P. Montávez, S. Jerez, P. Jiménez-Guerrero, and E. Zorita, 2012: What is the role of the observational dataset in the evaluation and scoring of climate models? *Geophysical Research Letters*, **39**.

Groisman, P. Y., R. W. Knight, D. R. Easterling, T. R. Karl, G. C. Hegerl, and V. A. N. Razuvaev, 2005: Trends in intense precipitation in the climate record. *J Climate*, **18,** 1326-1350.

Gutentag, E. D., F. J. Heimes, N. C. Krothe, R. R. Luckey, and J. B. Weeks, 1984: Geohydrology of the High Plains aquifer in parts of Colorado, Kansas, Nebraska, New Mexico, Oklahoma, South Dakota, Texas, and Wyoming. 1400-B, 63 pp.

Harding, K., and P. Snyder, 2012a: Modeling the Atmospheric Response to Irrigation in the Great Plains. Part II: The Precipitation of Irrigated Water and Changes in Precipitation Recycling. *J Hydrometeorol*, **13,** 1687-1703.

Harding, K., and P. Snyder, 2012b: Modeling the Atmospheric Response to Irrigation in the Great Plains. Part I: General Impacts on Precipitation and the Energy Budget. *J Hydrometeorol*, **13,** 1667-1686.

Harding, K. J., P. K. Snyder, and S. Liess, 2013: Use of Dynamical Downscaling to Improve the Simulation of Central U.S. Warm-Season Precipitation in CMIP5 Models. *J*

Geophys Res-Atmos.

Held, I. M., and B. J. Soden, 2006: Robust responses of the hydrological cycle to global warming. *J Climate*, **19,** 5686-5699.

Helfand, H. M., and S. D. Schubert, 1995: Climatology of the Simulated Great-Plains Low-Level Jet and Its Contribution to the Continental Moisture Budget of the United-States. *J Climate*, **8,** 784-806.

Higgins, R. W., W. Shi, E. Yarosh, and R. Joyce, 2000: Improved United States Precipitation Quality Control System and Analysis. *NCEP/Climate Prediction Center ATLAS*, **7,** 40 pp.

Higgins, R. W., Y. Yao, E. S. Yarosh, J. E. Janowiak, and K. C. Mo, 1997: Influence of the Great Plains low-level jet on summertime precipitation and moisture transport over the central United States. *J Climate*, **10,** 481-507.

Hitchens, N. M., H. E. Brooks, and R. S. Schumacher, 2013: Spatial and Temporal Characteristics of Heavy Hourly Rainfall in the United States. *Mon Weather Rev*.

Holton, J. R., 1967: The diurnal boundary layer wind oscillation above sloping terrain. *Tellus A*, **19,** 199-205.

Holton, J. R., 2004: *An Introduction to Dynamic Meteorology.* 4th ed. Elsevier Academic Press.

Hong, S. B., V. Lakshmi, E. E. Small, F. Chen, M. Tewari, and K. W. Manning, 2009: Effects of vegetation and soil moisture on the simulated land surface processes from the coupled WRF/Noah model. *J Geophys Res-Atmos*, **114,** D18118.

Hong, S. Y., Y. Noh, and J. Dudhia, 2006: A new vertical diffusion package with an explicit treatment of entrainment processes. *Mon Weather Rev*, **134,** 2318-2341.

Houze, R. A., 1993: *Cloud Dynamics.* Academic Press.

Huntington, T. G., 2006: Evidence for intensification of the global water cycle: Review and synthesis. *J Hydrol*, **319,** 83-95.

Jacquemin, B., and J. Noilhan, 1990: Sensitivity Study and Validation of a Land Surface Parameterization Using the Hapex-Mobilhy Data Set. *Bound-Lay Meteorol*, **52,** 93-134.

Johnson, R. H., 2001: Surface mesohighs and mesolows. *B Am Meteorol Soc*, **82,** 13-31.

Kain, J. S., 2004: The Kain-Fritsch convective parameterization: An update. *J Appl Meteorol*, **43,** 170-181.

Kalnay, E., and Coauthors, 1996: The NCEP/NCAR 40-year reanalysis project. *B Am Meteorol Soc*, **77,** 437-471.

Kanamitsu, M., W. Ebisuzaki, J. Woollen, S. K. Yang, J. J. Hnilo, M. Fiorino, and G. L. Potter, 2002: Ncep-Doe Amip-Ii Reanalysis (R-2). *B Am Meteorol Soc*, **83,** 1631-1643.

Karl, T. R., and R. W. Knight, 1998: Secular trends of precipitation amount, frequency, and intensity in the United States. *B Am Meteorol Soc*, **79,** 231-241.

Klein Tank, A. M. G., F. W. Zwiers, and X. Zhang, 2009: Guidelines on analysis of extremes in a changing climate in support of informed decision for adaptation. , 56 pp.

Knutti, R., R. Furrer, C. Tebaldi, J. Cermak, and G. A. Meehl, 2010: Challenges in Combining Projections from Multiple Climate Models. *J Climate*, **23,** 2739-2758.

Koster, R. D., and Coauthors, 2004: Regions of strong coupling between soil moisture and precipitation. *Science*, **305,** 1138-1140.

Kunkel, K., T. R. Karl, D. R. Easterling, K. Redmond, J. Young, Y. Xungang, and P. Hennon, 2013: Probable maximum precipitation and climate change. *Geophysical Research Letters*, **40,** 1402-1408.

Kunkel, K. E., S. A. Changnon, and J. R. Angel, 1994: Climatic Aspects of the 1993 Upper Mississippi River Basin Flood. *B Am Meteorol Soc*, **75,** 811-822.

Kunkel, K. E., K. Andsager, and D. R. Easterling, 1999: Long-term trends in extreme precipitation events over the conterminous United States and Canada. *J Climate*, **12,** 2515-2527.

Lau, K. M., and J. S. Boyle, 1987: Tropical and Extratropical Forcing of the Large-Scale Circulation - a Diagnostic Study. *Mon Weather Rev*, **115,** 400-428.

Lavers, D. A., and G. Villarini, 2013: Atmospheric Rivers and Flooding over the Central United States. *J Climate*.

Leathers, D. J., and M. A. Palecki, 1992: The Pacific North-American Teleconnection Pattern and United-States Climate .29 Temporal Characteristics and Index Specification. *J Climate*, **5,** 707-716.

Lee, J. W., S. Y. Hong, E. C. Chang, M. S. Suh, and H. S. Kang, 2014: Assessment of future climate change over East Asia due to the RCP scenarios downscaled by GRIMs-RMP. *Climate Dynamics*, **42,** 733-747.

Lee, M. I., and Coauthors, 2007a: An analysis of the warm-season diurnal cycle over the continental united states and northern Mexico in general circulation models. *J Hydrometeorol*, **8,** 344-366.

Lee, M. I., and Coauthors, 2007b: Sensitivity to horizontal resolution in the AGCM simulations of warm season diurnal cycle of precipitation over the United States and northern Mexico. *J Climate*, **20,** 1862-1881.

Li, W. H., L. F. Li, R. Fu, Y. Deng, and H. Wang, 2011: Changes to the North Atlantic Subtropical High and Its Role in the Intensification of Summer Rainfall Variability in the Southeastern United States. *J Climate*, **24,** 1499-1506.

Lin, Y., and K. Mitchell, 2005: The NCEP stage II/IV hourly precipitation analyses: Development and applications. *19th Conference on Hydrology*, San Diego, CA, American Meteorological Society.

Maddox, R. A., C. F. Chappell, and L. R. Hoxit, 1979: Synoptic and Meso-Alpha Scale Aspects of Flash Flood Events. *B Am Meteorol Soc*, **60,** 115-123.

Mahoney, K., M. Alexander, J. D. Scott, and J. Barsugli, 2013: High-Resolution Downscaled Simulations of Warm-Season Extreme Precipitation Events in the Colorado Front Range under Past and Future Climates. *J Climate*, **26,** 8671-8689.

Mansell, E. R., 2008: EnKF analysis and forecast predictability of a tornadic supercell storm. *24th Conference on Severe Local Storms*, A. M. Society, Ed., P5.2.

Markowski, P., and Y. Richardson, 2010: *Mesoscale Meteorology in Midlatitudes.* Wiley-Blackwell, 407 pp.

Matsuura, K., and C. J. Willmott, 2009: Terrestrial Precipitation: 1900-2008 Gridded Monthly Time Series (Version 2.01). D. o. G. Center for Climatic Research, University of Delaware, Ed.

McGuire, V. L., 2013: Water-level and storage changes in the High Plains aquifer, predevelopment to 2011 and 2009–11. , 15 pp.

Means, L. L., 1952: On thunderstorm forecasting in the central United States. *Mon Weather Rev*, **80,** 165-189.

Means, L. L., 1954: A study of the mean southerly wind—Maximum in low levels associated with a period of summer precipitation in the Middle West. *B Am Meteorol Soc*, **35,** 166-170.

Mearns, L. O., and Coauthors, 2012: The North American Regional Climate Change Assessment Program Overview of Phase I Results. *B Am Meteorol Soc*, **93,** 1337-1362.

Meehl, G. A., and C. Tebaldi, 2004: More intense, more frequent, and longer lasting heat waves in the 21st century. *Science*, **305,** 994-997.

Meehl, G. A., J. M. Arblaster, and C. Tebaldi, 2005: Understanding future patterns of increased precipitation intensity in climate model simulations. *Geophysical Research Letters*, **32**.

Merrill, J. T., R. Bleck, and D. Boudra, 1986: Techniques of Lagrangian Trajectory

Analysis in Isentropic Coordinates. *Mon Weather Rev*, **114,** 571-581.

Mesinger, F., and Coauthors, 2006: North American regional reanalysis. *B Am Meteorol Soc*, **87,** 343-360.

Mitchell, M. J., R. W. Arritt, and K. Labas, 1995: A Climatology of the Warm-Season Great-Plains Low-Level Jet Using Wind Profiler Observations. *Weather Forecast*, **10,** 576-591.

Mitchell, T., and P. Jones, 2005: An improved method of constructing a database of monthly climate observations and associated high-resolution grids. *Int J Climatol*, **25,** 693-712.

Mlawer, E. J., S. J. Taubman, P. D. Brown, M. J. Iacono, and S. A. Clough, 1997: Radiative transfer for inhomogeneous atmospheres: RRTM, a validated correlated-k model for the longwave. *J Geophys Res-Atmos*, **102,** 16663-16682.

Mo, K. C., and E. H. Berbery, 2004: Low-level jets and the summer precipitation regimes over North America. *J Geophys Res-Atmos*, **109**.

Mo, K. C., J. Noguespaegle, and J. Paegle, 1995: Physical-Mechanisms of the 1993 Summer Floods. *Journal of the Atmospheric Sciences*, **52,** 879-895.

Monaghan, A. J., D. L. Rife, J. O. Pinto, C. A. Davis, and J. R. Hannan, 2010: Global Precipitation Extremes Associated with Diurnally Varying Low-Level Jets. *J Climate*, **23,** 5065-5084.

Moncrieff, M. W., and C. H. Liu, 2006: Representing convective organization in prediction models by a hybrid strategy. *Journal of the Atmospheric Sciences*, **63,** 3404-3420.

Moore, B. J., P. J. Neiman, F. M. Ralph, and F. E. Barthold, 2012: Physical Processes Associated with Heavy Flooding Rainfall in Nashville, Tennessee, and Vicinity during 1-2 May 2010: The Role of an Atmospheric River and Mesoscale Convective Systems. *Mon Weather Rev*, **140,** 358-378.

Morrison, H., G. Thompson, and V. Tatarskii, 2009: Impact of Cloud Microphysics on the Development of Trailing Stratiform Precipitation in a Simulated Squall Line: Comparison of One- and Two-Moment Schemes. *Mon Weather Rev*, **137,** 991-1007.

Muller, C. J., P. A. O'Gorman, and L. E. Back, 2011: Intensification of Precipitation Extremes with Warming in a Cloud-Resolving Model. *J Climate*, **24,** 2784-2800.

Nayak, M. A., G. Villarini, and D. A. Lavers, 2014: On the skill of numerical weather prediction models to forecast atmospheric rivers over the central United States. *Geophysical Research Letters*.

NCDC, cited 2013: Billion-Dollar Weather/Climate Disasters. [Available online at https://http://www.ncdc.noaa.gov/billions/events.]

Nicholls, M. E., R. H. Johnson, and W. R. Cotton, 1988: The Sensitivity of Two-Dimensional Simulations of Tropical Squall Lines to Environmental Profiles. *Journal of the Atmospheric Sciences*, **45,** 3625-3649.

Noilhan, J., and S. Planton, 1989: A Simple Parameterization of Land Surface Processes for Meteorological Models. *Mon Weather Rev*, **117,** 536-549.

NWS: Natural Hazard Statistics. [Available online at http://www.nws.noaa.gov/om/hazstats.shtml.]

O'Gorman, P. A., and T. Schneider, 2009: The physical basis for increases in precipitation extremes in simulations of 21st-century climate change. *Proceedings of the National Academy of Sciences of the United States of America*, **106,** 14773-14777.

Orlanski, I., 1975: Rational Subdivision of Scales for Atmospheric Processes. *B Am Meteorol Soc*, **56,** 527-530.

Otte, T. L., 2008: The impact of nudging in the meteorological model for retrospective air quality simulations. Part I: Evaluation against national observation networks. *J Appl Meteorol Clim*, **47,** 1853-1867.

Otte, T. L., C. G. Nolte, M. J. Otte, and J. H. Bowden, 2012: Does nudging squelch the extremes in regional climate modeling? *J Climate*, **25,** 7046-7066.

Parker, M. D., and R. H. Johnson, 2000: Organizational modes of midlatitude mesoscale convective systems. *Mon Weather Rev*, **128,** 3413-3436.

Parker, M. D., and R. H. Johnson, 2004: Structures and dynamics of quasi-2D mesoscale convective systems. *Journal of the Atmospheric Sciences*, **61,** 545-567.

Parry, M. L., O. F. Canziani, J. P. Palutikof, P. J. van der Linden, and C. E. Hanson, 2007: IPCC. Summary for Policymakers. In: Climate Change 2007: Impacts, Adaptation and Vulnerability. , 7-22 pp.

Patricola, C. M., P. Chang, and R. Saravanan, 2013: Impact of Atlantic SST and high frequency atmospheric variability on the 1993 and 2008 Midwest floods: Regional climate model simulations of extreme climate events. *Climatic Change*.

Peters, J., and P. Roebber, 2014: Synoptic Control of Heavy-Rain-Producing Convective Training Episodes. *Mon Weather Rev*.

Pitchford, K. L., and J. London, 1962: The low-level jet as related to nocturnal thunderstorms over midwest United States. *J Appl Meteorol*, **1,** 43-47.

Polson, D., G. C. Hegerl, R. P. Allan, and B. Balan Sarojini, 2013: Have greenhouse gases intensified the contrast between wet and dry regions? *Geophysical Research Letters*, **40,** 4783-4787.

Pryor, S. C., R. J. Barthelmie, and J. T. Schoof, 2013: High-resolution projections of climate-related risks for the Midwestern USA. *Climate Res*, **56,** 61-79.

Rasmusson, E. M., 1968: Atmospheric Water Vapor Transport and the Water Balance of North America. Part 2. Large-scale water balance investigations. *Mon Weather Rev*, **96,** 720-734.

Reichler, T., and J. Kim, 2008: How well do coupled models simulate today's climate? *B Am Meteorol Soc*, **89,** 303-311.

Reynolds, R. W., N. A. Rayner, T. M. Smith, D. C. Stokes, and W. Q. Wang, 2002: An improved in situ and satellite SST analysis for climate. *J Climate*, **15,** 1609-1625.

Rienecker, M. M., and Coauthors, 2011: MERRA: NASA's Modern-Era Retrospective Analysis for Research and Applications. *J Climate*, **24,** 3624-3648.

Rossby, C. G., 1938: On the mutual adjustment of pressure and velocity distributions in certain simple current systems. II. *Journal of Marine Research*, **2,** 239-263.

Rotunno, R., J. B. Klemp, and M. L. Weisman, 1988: A Theory for Strong, Long-Lived Squall Lines. *Journal of the Atmospheric Sciences*, **45,** 463-485.

Rudolf, B., C. Beck, J. Grieser, and U. Schneider, 2005: Global Precipitation Analysis Products. Global Precipitation Climatology Centre (GPCC). *DWD*, 1-8.

Ruiz-Barradas, A., and S. Nigam, 2006a: Great plains hydroclimate variability: The view from North American regional reanalysis. *J Climate*, **19,** 3004-3010.

Ruiz-Barradas, A., and S. Nigam, 2006b: IPCC's twentieth-century climate simulations: Varied representations of north American hydroclimate variability. *J Climate*, **19,** 4041-4058.

Ryan, T. M., and J. D. Vitale, 2008: Operational recognition of high precipitation efficiency and low echo centroid convection. *24th Conference on Severe Local Storms*.

Sanders, F., and R. J. Paine, 1975: Structure and Thermodynamics of an Intense Mesoscale Convective Storm in Oklahoma. *Journal of the Atmospheric Sciences*, **32,** 1563-1579.

Santer, B. D., and T. M. L. Wigley, 1990: Regional Validation of Means, Variances, and Spatial Patterns in General-Circulation Model Control Runs. *J Geophys Res-Atmos*, **95,** 829-850.

Sapiano, M. R. P., and P. A. Arkin, 2009: An Intercomparison and Validation of High-Resolution Satellite Precipitation Estimates with 3-Hourly Gauge Data. *J Hydrometeorol*,

10, 149-166.

Schaller, N., I. Mahlstein, J. Cermak, and R. Knutti, 2011: Analyzing precipitation projections: A comparison of different approaches to climate model evaluation. *J Geophys Res-Atmos*, **116**.

Schubert, S. D., M. J. Suarez, P. J. Pegion, R. D. Koster, and J. T. Bacmeister, 2004: On the cause of the 1930s Dust Bowl. *Science*, **303,** 1855-1859.

Schubert, S. D., M. J. Suarez, P. J. Pegion, R. D. Koster, and J. T. Bacmeister, 2008: Potential Predictability of Long-Term Drought and Pluvial Conditions in the U.S. Great Plains. *J Climate*, **21,** 802-816.

Schumacher, R. S., and R. H. Johnson, 2005: Organization and environmental properties of extreme-rain-producing mesoscale convective systems. *Mon Weather Rev*, **133,** 961-976.

Schumacher, R. S., and R. H. Johnson, 2006: Characteristics of US extreme rain events during 1999-2003. *Weather Forecast*, **21,** 69-85.

Seager, R., L. Goddard, J. Nakamura, N. Henderson, and D. Eun Lee, 2013: Dynamical Causes of the 2010/11 Texas-northern Mexico drought. *J Hydrometeorol*.

Seneviratne, S. I., and Coauthors, 2012: Changes in climate extremes and their impacts on the natural physical environment. In: Managing the Risks of Extreme Events and Disasters to Advance Climate Change Adaptation. A Special Report of Working Groups I and II of the Intergovernmental Panel on Climate Change (IPCC). 109-230 pp.

Sillmann, J., V. V. Kharin, F. W. Zwiers, X. Zhang, and D. Bronaugh, 2013: Climate extreme indices in the CMIP5 multi-model ensemble. Part 2: Future climate projections. *J Geophys Res-Atmos*.

Skamarock, W. C., and Coauthors, 2008: A description of the Advanced Research WRF version 3.

Smith, J. A., M. L. Baeck, G. Villarini, D. B. Wright, and W. Krajewski, 2013: Extreme

Flood Response: The June 2008 Flooding in Iowa. *J Hydrometeorol*, **14,** 1810-1825.

Stauffer, D. R., and N. L. Seaman, 1994: Multiscale 4-Dimensional Data Assimilation. *J Appl Meteorol*, **33,** 416-434.

Stull, R. B., 1988: *An Introduction to Boundary Layer Meteorology.* Kluwer Academic Publishers, 666 pp.

Taylor, K. E., R. J. Stouffer, and G. A. Meehl, 2012: An Overview of Cmip5 and the Experiment Design. *B Am Meteorol Soc*, **93,** 485-498.

Thorpe, A. J., M. J. Miller, and M. W. Moncrieff, 1982: Two-Dimensional Convection in Non-Constant Shear - a Model of Mid-Latitude Squall Lines. *Quarterly Journal of the Royal Meteorological Society*, **108,** 739-762.

Trenberth, K. E., 1999: Conceptual framework for changes of extremes of the hydrological cycle with climate change. *Climatic Change*, **42,** 327-339.

Trenberth, K. E., A. Dai, R. M. Rasmussen, and D. B. Parsons, 2003: The changing character of precipitation. *B Am Meteorol Soc*, **84,** 1205-1217.

Trenberth, K. E., G. W. Branstator, D. Karoly, A. Kumar, N. C. Lau, and C. Ropelewski, 1998: Progress during TOGA in understanding and modeling global teleconnections associated with tropical sea surface temperatures. *J Geophys Res-Oceans*, **103,** 14291-14324.

Tuttle, J. D., and C. A. Davis, 2006: Corridors of warm season precipitation in the central United States. *Mon Weather Rev*, **134,** 2297-2317.

Vavrus, S. J., and R. J. Behnke, 2014: A comparison of projected future precipitation in Wisconsin using global and downscaled climate model simulations: implications for public health. *Int J Climatol*, **34,** 3106-3124.

Villarini, G., J. A. Smith, and G. A. Vecchi, 2012: Changing Frequency of Heavy Rainfall over the Central United States. *J Climate*, **26,** 351-357.

Villarini, G., J. A. Smith, M. L. Baeck, and W. F. Krajewski, 2011a: Examining Flood Frequency Distributions in the Midwest U.S. *J Am Water Resour As*, **47,** 447-463.

Villarini, G., J. A. Smith, M. L. Baeck, R. Vitolo, D. B. Stephenson, and W. F. Krajewski, 2011b: On the frequency of heavy rainfall for the Midwest of the United States. *J Hydrol*, **400,** 103-120.

Wallace, J. M., and P. V. Hobbs, 1977: *Atmospheric Science: An Introductory Survey.* Academic Press, 350 pp.

Wallace, J. M., and D. S. Gutzler, 1981: Teleconnections in the Geopotential Height Field during the Northern Hemisphere Winter. *Mon Weather Rev*, **109,** 784-812.

Wang, C. Z., D. B. Enfield, S. K. Lee, and C. W. Landsea, 2006: Influences of the Atlantic warm pool on western hemisphere summer rainfall and Atlantic hurricanes. *J Climate*, **19,** 3011-3028.

Wang, D. B., M. Hejazi, X. M. Cai, and A. J. Valocchi, 2011: Climate change impact on meteorological, agricultural, and hydrological drought in central Illinois. *Water Resour Res*, **47**.

Wang, J., P. M. Rich, and K. P. Price, 2003: Temporal responses of NDVI to precipitation and temperature in the central Great Plains, USA. *Int J Remote Sens*, **24,** 2345-2364.

Weaver, S. J., and S. Nigam, 2008: Variability of the great plains low-level jet: Large-scale circulation context and hydroclimate impacts. *J Climate*, **21,** 1532-1551.

Weaver, S. J., and S. Nigam, 2011: Recurrent Supersynoptic Evolution of the Great Plains Low-Level Jet. *J Climate*, **24,** 575-582.

Weaver, S. J., S. Schubert, and H. Wang, 2009: Warm Season Variations in the Low-Level Circulation and Precipitation over the Central United States in Observations, AMIP Simulations, and Idealized SST Experiments. *J Climate*, **22,** 5401-5420.

Wehner, M. F., 2013: Very extreme seasonal precipitation in the NARCCAP ensemble:

model performance and projections. *Climate Dynamics*, **40,** 59-80.

Wehner, M. F., R. L. Smith, G. Bala, and P. Duffy, 2010: The effect of horizontal resolution on simulation of very extreme US precipitation events in a global atmosphere model. *Climate Dynamics*, **34,** 241-247.

Weisman, M. L., and R. Rotunno, 2004: "A theory for strong long-lived squall lines" revisited. *Journal of the Atmospheric Sciences*, **61,** 361-382.

Wetherald, R. T., and S. Manabe, 2002: Simulation of hydrologic changes associated with global warming. *J Geophys Res-Atmos*, **107**.

Wilcox, E. M., and L. J. Donner, 2007: The frequency of extreme rain events in satellite rain-rate estimates and an atmospheric general circulation model. *J Climate*, **20,** 53-69.

Wu, W. L., A. H. Lynch, and A. Rivers, 2005: Estimating the uncertainty in a regional climate model related to initial and lateral boundary conditions. *J Climate*, **18,** 917-933.

Wuebbles, D., and Coauthors, 2014: Cmip5 Climate Model Analyses Climate Extremes in the United States. *B Am Meteorol Soc*, **95,** 571-583.

Xie, P. P., and P. A. Arkin, 1997: Global precipitation: A 17-year monthly analysis based on gauge observations, satellite estimates, and numerical model outputs. *B Am Meteorol Soc*, **78,** 2539-2558.

Yu, B., Y. M. Tang, X. B. Zhang, and A. Niitsoo, 2008: An analysis on observed and simulated PNA associated atmospheric diabatic heating. *Climate Dynamics*, **33,** 75-91.

Zhang, G. J., 2003: Roles of tropospheric and boundary layer forcing in the diurnal cycle of convection in the U.S. southern great plains. *Geophysical Research Letters*, **30**.

Zhang, X. B., and Coauthors, 2011: Indices for monitoring changes in extremes based on daily temperature and precipitation data. *Wires Clim Change*, **2,** 851-870.